



The  
University  
Of  
Sheffield.

Department of Mechanical Engineering

PhD Mechanical Engineering

PhD Thesis

**Aerodynamic Analysis on Modified  
Horizontal-Axis-Wind-Turbine**

Hassan Qansh

March 2022

**Supervisors: Dr. Andrew Nowakowski & Dr. Robert Howell**

PhD Thesis submitted to the Department of  
Mechanical Engineering, University of Sheffield in  
fulfilment of the requirement for the degree of PhD

---

## ABSTRACT

The increasing of lift force is an important task during the design process of wind turbines. This leads to a higher performance of wind turbines. The performance of wind turbines can be increased via either active or passive flow controllers. The aim of this work is to apply a passive flow controller, namely riblets, on the blades of National Renewable Energy Laboratory (NREL) phase II. The thesis consists of two main bodies: smooth and tripped study cases. The smooth study cases begin with studies on 2D aerofoils to investigate fluid domain geometry and turbulence models' effects on aerodynamic coefficients. A fixed blade is then simulated to determine the 2D aerodynamic forces and the pressure distribution for various angle of attacks (AOA). In addition, the torque of one-third scale rotor and full-scale rotor of the NREL phase II are computed separately.

Unlike the previous work on riblets, the riblets size of current work is in order of boundary layer thickness. First, a validation for large-scale riblets on DU 96-W-180 is performed to compare the results. The tripped cases begin with applying a riblet (step) with  $h^+ = 67 - 69$  on 2D S809. However, the result is unsatisfactory due to missing 3D effect. Different riblet configurations are then applied on the suction side of a 3D blade. The maximum increase in lift and reduction in drag occur at  $l^+ = 460$  for  $\alpha = 16^\circ$ . However, for a wider range of AOAs,  $l^+ = 104 - 157$  show an improved performance. The results show that riblets perform best at low  $Re$  and stall AOAs. Finally, riblets are placed on the blades' suction side of the NREL phase II. The riblets with  $l^+ = 114 - 140$  show an improvement in the performance, which varies between 1.32% and 0.51%, depending on tip speed ratio.

This work confirms that the large-scale riblets are not only able to reduce drag, but also can increase lift, and therefore improve the performance of wind turbines. Unlike the small-scale riblets, the large-scale ones act as a vortex generator and cause a recirculated zone in the wake of large riblets, which leads to delaying stall to a further chord location of the blade. In addition, and similar to small-scale riblets, the viscous sub-layer thickness of current tripped cases is increased, thus causing an upward shift of the log-law region and a reduction of the turbulence statistics. The drag reduction and lift increase depend on AOAs. However, the riblets positively affect more the skin-friction force for a larger number of riblets at a wider range of AOAs. This means the contribution of riblets in increasing the area of the blade is negligible because of the small riblets size compared to the blade size.

---

## **ACKNOWLEDGEMENT**

I would like to say special thanks to my family (parents, brothers, sisters, wife, and sons) for supporting and encouraging me all the time during my PhD degree at The University of Sheffield. The inspiration that I have received from them will always be appreciated. In addition, I would like to express my gratitude to King Abdulaziz University, Saudi Arabia, for giving me a chance to continue my higher education in The United Kingdom. Further, I would like to send my appreciation to Dr. Ahmed Bokhari and Dr. Majed Alhazmi who helped me through the early stages of my scholarship request.

I would like to express appreciation for my supervisor, Dr. Andrew Nowakowski, whose guidance, support, and encouragement has been invaluable throughout my PhD. Dr. Andrew has been always willing and enthusiastic to assist me throughout my project. For Dr. Robert Howell, I am still grateful for our little chat at the beginning of my PhD, Thank you. Many thanks to Dr. Radwan Addaiy and Dr. Ahmed Al-Mudhafar for sharing their knowledge and valuable information during my first year at the university. Finally, especial thanks to The University of Sheffield for providing me with access to supercomputers.

## **Nomenclature**

### **Case Letter**

EIA Energy Information Administration

IRENA International Renewable Energy Agency

GWEC Global Wind Energy Council

HAWT Horizontal-Axis Wind Turbine

VAWT Vertical-Axis Wind Turbine

CFD Computational Fluid Dynamics

NREL National Renewable Energy Laboratory

2D Two-dimensional

3D Three-dimensional

WT Wind Turbine

RANS Reynold's Averaged Navier-Stokes

URANS Unsteady Reynolds Averaged Navier-Stokes

NASA National Aeronautics and Space Administration

AOA Angle of attack

BEM Blade element momentum

LES Large eddies simulation

DNS Direct numerical simulation

MRF Multiple reference frame

MPM Mixing plane model

SMM Sliding mesh model

SIMPLE Semi-implicit method for pressure linked equation

QUICK Quadratic upstream interpolation for convective kinematics

$Ma$  Mach number

$Re$  Reynolds number

$SST$  Shear Stress Transport

$S - A$  Spalart-Allmaras

$\Delta h$  Protrusion height ( $m$ )

$h_l$  Protrusion height of the streamwise velocity profile ( $m$ )

$h_c$  Protrusion height of the spanwise velocity profile ( $m$ )

$l^+$  Non-dimensional square root of riblet's cross section

$A_b^+$  Non-dimensional riblet's base cross section

$A_b$  Area of riblet's base ( $m^2$ )

$A$  Blade area ( $m^2$ )

$C_L$  Lift force coefficient

$C_D$  Drag force coefficient

$\vec{n}$  Normal unit vector

$\vec{j}$  vertical unit vector

$\vec{i}$  parallel unit vector

$N$  Normal force ( $N$ )

$TN$  Tangent force ( $N$ )

$D$  Drag force ( $N$ )

$L$  Lift force ( $N$ )

$\vec{F}$  Resultant force ( $N$ )

## Nomenclature

---

$T$	Torque ( $N.m$ )
$\vec{V}_r$	Resultant velocity ( $m/s$ )
$N_B$	Number of blades
$\lambda$	Tip speed ratio
$G_\nu$	Production of turbulent viscosity
$p$	Pressure ( $Pa$ )
$T$	Temperature ( $^{\circ}C$ )
$\vec{M}$	Total moment ( $N.m$ )
$\vec{r}$	Position vector ( $m$ )
$\vec{F}_p$	Pressure force vector ( $N$ )
$\vec{F}_\nu$	Viscous force vector ( $N$ )
$C_p$	Power coefficient
$a$	Axial induction factor
$P_m$	Wind turbine mechanical power ( $W$ )
$P_g$	Wind turbine generator power ( $W$ )
$P_w$	Power of incoming wind ( $W$ )
$T_m$	Wind turbine mechanical torque ( $N.m$ )
$T_g$	Wind turbine electrical torque ( $N.m$ )
$S_A$	Rotor swept area ( $m^2$ )
$V_\infty$	Wind velocity ( $m/s$ )
$p_\infty$	Wind pressure ( $Pa$ )
$V_B$	Blade velocity ( $m/s$ )
$V_{tip}$	Velocity of blade tip ( $m/s$ )

## Nomenclature

---

$u$	Turbulence velocity ( $m/s$ )
$U$	Turbulence averaged velocity ( $m/s$ )
$u'$	Turbulence fluctuation velocity ( $m/s$ )
$\overline{u'_i u'_j}$	Reynold's (turbulent) stress
$t$	Time ( $s$ )
$d$	Blade diameter ( $m$ )
$R$	Blade radius ( $m$ )
$c$	Chord ( $m$ )
$k$	Turbulent kinetic energy ( $kg\ m^2/s^2$ )
$Y_\nu$	Destruction of turbulent viscosity
$f_{\nu 1}$	Viscous damping function
$\tilde{G}_k$	Generation of turbulence kinetic energy due to mean velocity gradient
$G_\omega$	Generation of $\omega$
$Y_\omega$	Dissipation of $\omega$
$D_\omega$	Cross-diffusion term $\omega$
$S$	Strain rate magnitude
$F_2$	Blending function
$G_k$	Generation of turbulence kinetic energy
$G_b$	Generation of turbulence kinetic energy due to buoyancy
$Y_M$	Contribution of the fluctuating dilatation in compressible turbulence to the overall dissipation rate
$v$	Absolute velocity ( $m/s$ )
$v_r$	Relative velocity ( $m/s$ )

$y^+$	Wall non-dimensional distance
$\tau_w$	Wall shear stress ( $Pa$ )
$y$	First layer thickness ( $m$ )
$s^+$	Non-dimensional rib lateral spacing
$h^+$	Non-dimensional rib height
$s_d$	Riblets' peak-to-peak distance ( $m$ )
$s$	Space between riblets ( $m$ )
$h$	Riblet height ( $m$ )
$h^*$	First layer length ( $m$ )
$H$	Thickness of specified layers ( $m$ )
$g$	Growth rate
$n$	number of layers
$u_\tau$	Shear velocity ( $m/s$ )
$\nabla$	Divergent operator $\left( \frac{\partial}{\partial x}, \frac{\partial}{\partial y}, \frac{\partial}{\partial z} \right)$

### **Greek symbols**

$\vec{\tau}$	Viscous stress vector ( $Pa$ )
$\phi$	Pitch angle
$\alpha$	Angle of attack
$\omega_B$	Blade rotation speed ( $rad/s$ )
$\Gamma_k$	Effective diffusivity of $k$
$\Gamma_\omega$	Effective diffusivity of $\omega$
$\sigma_k$	Turbulent Prandtl number for $k$
$\sigma_\omega$	Turbulent Prandtl number for $\omega$

## Nomenclature

---

$\epsilon$	Turbulence dissipation rate
$\omega$	Specific dissipation rate
$\mu$	Dynamic viscosity ( $kg/m \cdot s$ )
$\nu$	Kinematic viscosity ( $m^2/s$ )
$\tilde{\nu}$	Transported variable
$\alpha^*$	Damps the turbulent viscosity
$\rho$	Density ( $kg/m^3$ )
$\nu_t$	Turbulent viscosity ( $m^2/s$ )
$\delta$	Kronecker delta
$\bar{\tau}$	Absolute shear stress ( $Pa$ )
$\bar{\tau}_r$	Relative shear stress ( $Pa$ )

## Scripts

$p$	Pressure
$P$	Power
$\nu$	Viscous
$\tau$	Shear stress
+	Plus
$w$	Wind, wall
$k$	Turbulent kinetic energy
$\omega$	Specific dissipation rate
$\epsilon$	Turbulent dissipation rate
$b$	Buoyancy, base
$m$	Mechanical

## Nomenclature

---

$g$  Generator

$B$  Blade

$a$  Air

$D$  Drag

$L$  Lift

$max$  Maximum

$i, j, k$  x, y, z directions

$t$  Turbulent

$d$  Distance

# Contents

<b>Abstract</b>	<b>i</b>
<b>Acknowledgement</b>	<b>ii</b>
<b>Nomenclature</b>	<b>iii</b>
<b>Contents</b>	<b>x</b>
<b>List of Figures</b>	<b>xv</b>
<b>List of Tables</b>	<b>xxvii</b>
<b>1 INTRODUCTION</b>	<b>1</b>
1.1 Background . . . . .	1
1.2 Aims and Objectives . . . . .	3
1.3 Structure of the thesis . . . . .	5
1.4 Programs used for this work . . . . .	6
<b>2 LITERATURE REVIEW</b>	<b>7</b>
2.1 Horizontal Axis Wind Turbine . . . . .	7
2.2 NREL Phase II Wind Turbine Geometry . . . . .	9
2.2.1 NREL phase II rotor . . . . .	9
2.2.2 Aerofoil coordinates . . . . .	10
2.3 Wind Turbine Performance . . . . .	10

2.4	Computational Studies on HAWT . . . . .	14
2.5	Flow Controllers (Riblets) . . . . .	17
2.6	Challenges & Potential Work . . . . .	22
<b>3</b>	<b>SIMULATION SETUP</b>	<b>24</b>
3.1	Computational Fluid Domain . . . . .	24
3.2	Governing Equation . . . . .	24
3.2.1	Continuity Equation . . . . .	25
3.2.2	Reynold’s Averaged Navier-Stokes Equation . . . . .	25
3.2.3	Turbulence Models . . . . .	25
3.3	Mesh Generation . . . . .	27
3.4	Riblet Geometry . . . . .	28
<b>4</b>	<b>LARGE-SCALE RIBLETS VALIDATION</b>	<b>30</b>
4.1	Purpose . . . . .	30
4.2	Geometrical setup . . . . .	30
4.3	Mesh & computational setup . . . . .	30
4.4	Results and discussion . . . . .	36
<b>5</b>	<b>TRIPPED STUDY CASES</b>	<b>39</b>
5.1	Study Case 6 (2D, URANS, S809, $Re_c = 6.5 \times 10^5$ , Riblet) . . . . .	39
5.1.1	Purpose . . . . .	39
5.1.2	Geometrical setup . . . . .	39

5.1.3	Mesh & computational setup . . . . .	39
5.1.4	Results & discussion . . . . .	44
5.2	Study Case 7 (3D, URANS, S809, $Re_c = 6.5 \times 10^5$ , Riblets) . . . . .	54
5.2.1	Purpose . . . . .	54
5.2.2	Geometrical Setup . . . . .	54
5.2.3	Mesh & computational setup . . . . .	56
5.2.4	Results & discussion . . . . .	62
5.3	Study Case 8 (3D, URANS, NREL phase II, SMM, $Re_c = 9.4 \times 10^5$ , Riblets) . . . . .	94
5.3.1	Purpose . . . . .	94
5.3.2	Geometrical setup . . . . .	94
5.3.3	Mesh & computational setup . . . . .	96
5.3.4	Results & discussion . . . . .	101
<b>6</b>	<b>IMPROVING PERFORMANCE OF NREL PHASE II</b>	<b>117</b>
6.1	Number of riblets . . . . .	117
6.1.1	Geometrical setup . . . . .	117
6.1.2	Mesh element number . . . . .	117
6.1.3	Result & discussion . . . . .	117
6.2	Riblets Only on Pressure Side . . . . .	120
6.2.1	Geometrical setup . . . . .	120
6.2.2	Mesh element number . . . . .	121
6.2.3	Result & discussion . . . . .	122

6.3	Riblets on Both Blade Sides . . . . .	124
6.3.1	Geometrical setup . . . . .	124
6.3.2	Mesh element number . . . . .	124
6.3.3	Result & discussion . . . . .	126
6.4	Changing Riblets' Orientation . . . . .	128
6.4.1	Geometrical setup . . . . .	128
6.4.2	Mesh element number . . . . .	129
6.4.3	Result & discussion . . . . .	132
<b>7</b>	<b>CONCLUSION &amp; FUTURE WORK</b>	<b>140</b>
	<b>References</b>	<b>142</b>
	<b>Appendix A (Smooth Study Cases)</b>	<b>151</b>
<b>8</b>	<b>SMOOTH STUDY CASES</b>	<b>151</b>
8.1	Study Case 1 (2D, RANS, NACA 4412, $Re_c = 1.64 \times 10^6$ ) . . . . .	151
8.1.1	Purpose . . . . .	151
8.1.2	Geometrical setup . . . . .	151
8.1.3	Mesh study & simulation setup . . . . .	151
8.1.4	Results & discussion . . . . .	158
8.2	Study Case 2 (2D, URANS, S809, $Re_c = 6.5 \times 10^5$ ) . . . . .	162
8.2.1	Purpose . . . . .	162
8.2.2	Geometrical setup . . . . .	162

8.2.3	Mesh study & computational setup . . . . .	163
8.2.4	Results & discussion . . . . .	168
8.3	Study Case 3 (3D, URANS, S809, $Re_c = 6.5 \times 10^5$ ) . . . . .	171
8.3.1	Purpose . . . . .	171
8.3.2	Geometrical setup . . . . .	171
8.3.3	Mesh study & computational setup . . . . .	171
8.3.4	Results & discussion . . . . .	177
8.4	Study Case 4 (3D, RANS, NREL phase II, MRF, $Re_c = 9.4 \times 10^5$ ) . . .	183
8.4.1	Purpose . . . . .	183
8.4.2	Geometrical Setup . . . . .	183
8.4.3	Mesh study & computational setup . . . . .	183
8.4.4	Results & discussion . . . . .	189
8.5	Study Case 5 (3D, URANS, NREL phase II, SMM, $Re_c = 9.4 \times 10^5$ ) . .	196
8.5.1	Purpose . . . . .	196
8.5.2	Geometrical setup . . . . .	197
8.5.3	Mesh study & computational setup . . . . .	198
8.5.4	Results & discussion . . . . .	204
	<b>Appendix B (Aerofoil Coordinates)</b>	<b>207</b>
	<b>Appendix C (Turbulence Models)</b>	<b>212</b>

## List of Figures

1	<b>World renewable energy demands and its projection [7]</b> . . . . .	2
2	<b>General configuration of HAWT &amp; VAWT</b> . . . . .	3
3	<b>Anatomy of HAWT [13]</b> . . . . .	7
4	<b>The NREL phase II blade platform</b> . . . . .	9
5	<b>The NREL phase II hub</b> . . . . .	10
6	<b>The applied aerodynamic force on an aerofoil</b> . . . . .	12
7	<b>Ideal wind turbine model</b> . . . . .	14
8	<b>Shark dunticle shape on the blade [44]</b> . . . . .	18
9	<b>Microtabs on the pressure side of aerofoil [53]</b> . . . . .	18
10	<b>Mechanism of drag by riblets for (a) drag increase (b) drag reduction [61]</b> . . . . .	19
11	<b>Streamwise and spanwise velocity profiles of tripped surface [64]</b> . . . . .	20
12	<b>The fluid domain of large-scale riblets validation</b> . . . . .	31
13	<b>The top view of the simulated blade with employed riblets for validation case (not to scale)</b> . . . . .	31
14	<b>Triangular riblets' configuration for validation case</b> . . . . .	31
15	<b>Riblets' configuration for validation case (side view)</b> . . . . .	32
16	<b>Mesh dependency for large-scale riblet validation</b> . . . . .	32
17	<b><math>y^+</math> values for different meshes of large-scale riblets validation</b> . . . . .	33
18	<b>The skewness of large-scale riblet validation</b> . . . . .	33
19	<b>The orthogonality of large-scale riblet validation</b> . . . . .	33

20	<b>The generated mesh of fluid domain for large-scale riblets validation</b> . . . . .	34
21	<b>The generated mesh of blade for large-scale riblets validation</b> . . . . .	34
22	<b>The generated mesh of blade and riblets for large-scale riblets validation</b> . . . . .	35
23	<b>The generated mesh of riblets for large-scale riblets validation</b> . . . . .	35
24	<b>The convergence history of large-scale riblets validation</b> . . . . .	37
25	<b>The <math>y^+</math> distribution of large-scale riblets validation</b> . . . . .	37
26	<b>Lift coefficient difference versus angle of attack for validation case</b> . . . . .	38
27	<b>Drag coefficient difference versus angle of attack for validation case</b> . . . . .	38
28	<b>A tripped 2D aerofoil geometry with riblet on the suction side (not to scale)</b> . . . . .	40
29	<b>Mesh dependency for study case 6</b> . . . . .	40
30	<b><math>y^+</math> values for different meshes of study case 6</b> . . . . .	41
31	<b>The skewness of study case 6</b> . . . . .	41
32	<b>The orthogonality of study case 6</b> . . . . .	42
33	<b>Mesh visualisation of the riblet (study case 6)</b> . . . . .	42
34	<b>Mesh visualisation of the riblet tip (study case 6)</b> . . . . .	43
35	<b>The convergence history of study case 6</b> . . . . .	44
36	<b>The <math>y^+</math> distribution of study case 6</b> . . . . .	45
37	<b>Comparison of the smooth and tripped aerofoils' lift coefficient against angle of attacks</b>	46
38	<b>Comparison of the smooth and tripped aerofoils' drag coefficient against angle of attacks</b>	46
39	<b>The pressure contour at <math>\alpha = 0^\circ</math> of the smooth case (study case 2)</b> . . . . .	49
40	<b>The pressure contour at <math>\alpha = 0^\circ</math> of the tripped case (study case 6)</b> . . . . .	49

41	<b>The wall shear stress of the smooth and tripped cases at <math>\alpha = 0^\circ</math></b> . . . . .	50
42	<b>The velocity contour at <math>\alpha = 0^\circ</math> of the smooth case (study case 2)</b> . . . . .	51
43	<b>The velocity contour at <math>\alpha = 0^\circ</math> of the tripped case (study case 6)</b> . . . . .	51
44	<b>The velocity profile of the smooth and tripped cases at <math>\alpha = 0^\circ</math></b> . . . . .	52
45	<b>The velocity vector at <math>\alpha = 0^\circ</math> of the smooth case (study case 2)</b> . . . . .	52
46	<b>The velocity vector at <math>\alpha = 0^\circ</math> of the tripped case (study case 6)</b> . . . . .	53
47	<b>The velocity vector at <math>\alpha = 0^\circ</math> of the tripped case (zoom-in)</b> . . . . .	53
48	<b>The top view of the simulated blade with employed riblets for study case 7 (not to scale)</b>	54
49	<b>Triangular riblets' configuration for fixed blade</b> . . . . .	55
50	<b>Riblets' configuration (side view)</b> . . . . .	55
51	<b>The skewness of study case 7</b> . . . . .	59
52	<b>The orthogonality of study case 7</b> . . . . .	59
53	<b>The generated mesh of riblets and tripped blade for case 7</b> . . . . .	60
54	<b>The generated mesh of the riblets on the blade for case 7</b> . . . . .	60
55	<b>The generated mesh of the riblets for case 7</b> . . . . .	61
56	<b>The generated mesh of riblet with inflation layers for case 7</b> . . . . .	61
57	<b>The simulated time of study case 7</b> . . . . .	62
58	<b>The <math>y^+</math> distribution of study case 7</b> . . . . .	63
59	<b>Lift coefficient versus AOAs for the smooth and tripped blades</b> . . . . .	64
60	<b>Drag coefficient versus AOAs for the smooth and tripped blades</b> . . . . .	65
61	<b>Lift-to-drag ratio versus AOAs for the smooth and tripped blades</b> . . . . .	65

62	The lift coefficient due to pressure versus angle of attacks . . . . .	68
63	The lift coefficient due to surface skin-friction versus angle of attacks . . . . .	68
64	The drag coefficient due to pressure versus angle of attacks . . . . .	69
65	The drag coefficient due to surface skin-friction versus angle of attacks . . . . .	69
66	The wall shear stress distribution at $\alpha = 0^\circ$ . . . . .	71
67	The skin friction coefficient of riblet at $\alpha = 0^\circ$ . . . . .	72
68	The velocity contour of the tripped blade at $\alpha = 0^\circ$ in spanwise direction . . . . .	72
69	The boundary layer thickness of the tripped and smooth blades at $\alpha = 0^\circ$ . . . . .	73
70	The velocity profile of the tripped and smooth blades at $\alpha = 0^\circ$ . . . . .	74
71	The turbulence intensity of the tripped and smooth blades at $V_\infty = 6m/s$ ( $\alpha = 0^\circ$ )	74
72	The turbulence intensity of the tripped and smooth blades at $V_\infty = 26m/s$ ( $\alpha = 0^\circ$ )	75
73	The pressure distribution of smooth and tripped blades at $\alpha = 16^\circ$ . . . . .	76
74	The pressure contour of the smooth blade at $\alpha = 16^\circ$ . . . . .	77
75	The pressure contour of the tripped blade at $\alpha = 16^\circ$ . . . . .	77
76	The velocity contour of the smooth blade at $\alpha = 16^\circ$ . . . . .	78
77	The velocity contour of the tripped blade at $\alpha = 16^\circ$ . . . . .	78
78	The streamlines of the smooth blade at $\alpha = 16^\circ$ . . . . .	79
79	The streamlines of the tripped blade at $\alpha = 16^\circ$ . . . . .	79
80	The velocity vector of the smooth blade at $\alpha = 16^\circ$ . . . . .	80
81	The velocity vector of the tripped blade at $\alpha = 16^\circ$ . . . . .	80
82	The velocity vector of the tripped blade at $\alpha = 16^\circ$ (zoom-in) . . . . .	81

83	The streamwise vorticity of the tripped blade at $\alpha = 16^\circ$ . . . . .	81
84	The crossflow streamlines of the tripped blade at $t = 0.12s$ ( $\alpha = 16^\circ$ ) . . . . .	83
85	The crossflow streamlines of the tripped blade at $t = 0.96s$ ( $\alpha = 16^\circ$ ) . . . . .	83
86	The crossflow streamlines of the tripped blade at $t = 3.6s$ ( $\alpha = 16^\circ$ ) . . . . .	84
87	The streamlines and pressure contour of the smooth blade at $\alpha = 12^\circ$ . . . . .	86
88	The streamlines and pressure contour of the tripped blade at $\alpha = 12^\circ$ . . . . .	86
89	The velocity contour of the smooth blade at $\alpha = 12^\circ$ . . . . .	87
90	The velocity contour of the tripped blade at $\alpha = 12^\circ$ . . . . .	87
91	Lift coefficient versus AOAs for different number of riblets . . . . .	91
92	Drag coefficient versus AOAs for different number of riblets . . . . .	91
93	Lift-to-drag ratio versus AOAs for different number of riblets . . . . .	92
94	Surface pressure drag force versus AOAs for different number of riblets . . . . .	93
95	Skin-friction drag force versus AOAs for different number of riblets . . . . .	93
96	The top view of NREL phase II blade with riblets (not to scale) . . . . .	95
97	Triangular riblets on NREL phase II blade's suction side . . . . .	95
98	The riblets on the suction side of the blade at the tip . . . . .	95
99	The skewness of study case 8 . . . . .	96
100	The orthogonality of study case 8 . . . . .	97
101	The generated mesh of the full blade and riblets for case 8 . . . . .	98
102	The generated mesh of the the blade and riblets for case 8 (zoom-in) . . . . .	98
103	The generated mesh of the 40 riblets on the blade for case 8 . . . . .	99

104	<b>The simulated orientation of the blade and riblets for case 8</b> . . . . .	99
105	<b>The generated mesh of a cross section of the riblets for case 8</b> . . . . .	100
106	<b>The generated mesh of one riblet for case 8</b> . . . . .	100
107	<b>The simulated time of study case 8</b> . . . . .	101
108	<b>The simulated time of study case 8 (zoom-in)</b> . . . . .	102
109	<b>The <math>y^+</math> distribution of study case 8</b> . . . . .	102
110	<b>Power coefficient versus tip speed ratio for the smooth and tripped wind turbines</b> . .	103
111	<b>The pressure contour of the smooth WT at 30% span at <math>V_\infty = 7m/s</math></b> . . . . .	105
112	<b>The pressure contour of the tripped WT at 30% span at <math>V_\infty = 7m/s</math></b> . . . . .	105
113	<b>The pressure contour of the smooth WT at 99.7% span (riblets' location) at <math>V_\infty = 7m/s</math></b>	106
114	<b>The pressure contour of the tripped WT at 99.7% span (riblets' location) at <math>V_\infty = 7m/s</math></b>	106
115	<b>The velocity contour of the smooth WT at 30% span at <math>V_\infty = 7m/s</math></b> . . . . .	107
116	<b>The velocity contour of the tripped WT at 30% span at <math>V_\infty = 7m/s</math></b> . . . . .	107
117	<b>The velocity contour of the smooth WT at 99.7% span (riblets' location) at <math>V_\infty = 7m/s</math></b>	108
118	<b>The velocity contour of the tripped WT at 99.7% span (riblets' location) at <math>V_\infty = 7m/s</math></b>	108
119	<b>The velocity vector of the smooth WT at 99.7% span (riblets' location) at <math>V_\infty = 7m/s</math></b>	109
120	<b>The velocity vector of the tripped WT at 99.7% span (riblets' location) at <math>V_\infty = 7m/s</math></b>	109
121	<b>The velocity vector of the tripped WT at 99.7% span (zoom-in) at <math>V_\infty = 7m/s</math></b> . .	110
122	<b>The streamline of the tripped WT at 80% span at <math>V_\infty = 7m/s</math></b> . . . . .	110
123	<b>The streamline of the smooth WT at 80% span at <math>V_\infty = 7m/s</math></b> . . . . .	111
124	<b>The streamline of the smooth WT at 80% span at <math>V_\infty = 7m/s</math> (zoom-in)</b> . . . . .	111

125	The streamlines (spanwise) of the smooth WT at $V_\infty = 7m/s$ (top: suction, bottom: pressure) . . . . .	112
126	The streamlines (spanwise) of the tripped WT at $V_\infty = 7m/s$ (top: suction, bottom: pressure) . . . . .	112
127	The streamline & pressure contour of the smooth WT at 80% span at $V_\infty = 18m/s$	114
128	The streamline & pressure contour of the tripped WT at 80% span at $V_\infty = 18m/s$	114
129	The velocity contour of the smooth WT at 80% span at $V_\infty = 18m/s$ . . . . .	115
130	The velocity contour of the tripped WT at 80% span at $V_\infty = 18m/s$ . . . . .	115
131	The streamlines (spanwise) of the smooth WT at $V_\infty = 18m/s$ (top: suction, bottom: pressure) . . . . .	116
132	The streamlines (spanwise) of the tripped WT at $V_\infty = 18m/s$ (top: suction, bottom: pressure) . . . . .	116
133	Power coefficient versus tip speed ratio for different number of riblets . . . . .	119
134	Triangular riblets on the NREL phase II blade's pressure side . . . . .	120
135	The riblets on the pressure side of the blade at the tip . . . . .	120
136	Power coefficient versus tip speed ratio for different riblets's locations on the blade . . . . .	122
137	Triangular riblets on both NREL phase II blade sides . . . . .	124
138	The riblets on both sides of the blade at the tip . . . . .	125
139	Power coefficient versus tip speed ratio for different riblets' configurations . . . . .	126
140	Riblets on the NREL phase II blade in the chordwise direction (not to scale) . . . . .	128
141	Riblets on the NREL phase II blade in the spanwise direction . . . . .	129
142	The generated mesh of the riblet for the new orientation . . . . .	130
143	The generated mesh of the riblet for the new orientation (zoom-in) . . . . .	130

144	The generated mesh of the riblet's face for the new orientation . . . . .	131
145	The generated mesh of the riblet and aerofoil for the new orientation . . . . .	131
146	The generated mesh of the riblet on the blade for the new orientation . . . . .	132
147	Power coefficient versus tip speed ratio for two orientations of riblets in comparison with the smooth WT . . . . .	133
148	The pressure contour of the smooth WT at 99.7% span (riblets' location) at $V_\infty = 7m/s$	135
149	The pressure contour of the new riblet's orientation at 99.7% span (riblets' location) at $V_\infty = 7m/s$ . . . . .	135
150	The velocity contour of the smooth WT at 99.7% span (riblets' location) at $V_\infty = 7m/s$	136
151	The velocity contour of the new riblet's orientation at 99.7% span (riblets' location) at $V_\infty = 7m/s$ . . . . .	136
152	The velocity vector of the smooth WT at 99.7% span at $V_\infty = 7m/s$ . . . . .	137
153	The velocity vector of the new riblet's orientation at 99.7% span at $V_\infty = 7m/s$ . . .	137
154	The velocity vector of the new riblet's orientation at 99.7% span (zoom-in) at $V_\infty = 7m/s$	138
155	The streamlines of the smooth WT at 99.7% span at $V_\infty = 7m/s$ . . . . .	138
156	The streamlines of the new riblet's orientation at 99.7% span at $V_\infty = 7m/s$ . . . .	139
157	The streamlines (spanwise) of smooth WT at $V_\infty = 7m/s$ (top: suction, bottom: pres- sure) . . . . .	139
158	The streamlines (spanwise) of new riblet's orientation at $V_\infty = 7m/s$ (top: suction, bottom: pressure) . . . . .	139
159	Study case 1 rectangular shape fluid domain (not to scale) . . . . .	152
160	Study case 1 C-shaped fluid domain (not to scale) . . . . .	152
161	Mesh dependency for study case 1 . . . . .	153

162	$y^+$ values for different meshes of study case 1 . . . . .	154
163	The skewness of study case 1 . . . . .	154
164	The orthogonality of study case 1 . . . . .	154
165	The generated mesh of fluid domain and aerofoil for case 1 . . . . .	155
166	The generated mesh of the aerofoil for case 1 . . . . .	155
167	The generated mesh of the aerofoil's leading edge for case 1 . . . . .	156
168	The generated mesh of the aerofoil's trailing edge for case 1 . . . . .	156
169	The convergence history of study case 1 . . . . .	158
170	The $y^+$ distribution of study case 1 . . . . .	159
171	Lift coefficient versus angle of attack for study case 1 . . . . .	160
172	Lift coefficient versus angle of attack for different pressure-velocity couplings (study case 1) . . . . .	160
173	Drag coefficient versus angle of attack for study case 1 . . . . .	161
174	Study case 2 rectangular fluid domain (not to scale) . . . . .	162
175	Mesh dependency for study case 2 . . . . .	163
176	$y^+$ values for different meshes of study case 2 . . . . .	164
177	The skewness of study case 2 . . . . .	164
178	The orthogonality of study case 2 . . . . .	164
179	The generated mesh of fluid domain and aerofoil for case 2 . . . . .	165
180	The generated mesh of the aerofoil for case 2 . . . . .	165
181	The generated mesh of the aerofoil's leading edge for case 2 . . . . .	166

182	The generated mesh of the aerofoil's trailing edge for case 2 . . . . .	166
183	The simulated time of study case 2 . . . . .	168
184	The $y^+$ distribution of study case 2 . . . . .	169
185	Lift coefficient against angle of attacks for study case 2 . . . . .	170
186	Pressure drag coefficient against angle of attacks for study case 2 . . . . .	170
187	Study case 3 fluid domain (not to scale) . . . . .	172
188	Study case 3 simulated blade (not to scale) . . . . .	172
189	Mesh dependency for study case 3 . . . . .	173
190	$y^+$ values for different meshes of study case 3 . . . . .	173
191	The skewness of study case 3 . . . . .	174
192	The orthogonality of study case 3 . . . . .	174
193	The generated mesh of fluid domain and blade for case 3 . . . . .	174
194	The generated mesh of the blade for case 3 . . . . .	175
195	The inflation layers on the blade for case 3 . . . . .	175
196	The generated mesh of the cross section of the blade for case 3 . . . . .	176
197	The simulated time of study case 3 . . . . .	177
198	The $y^+$ distribution of study case 3 . . . . .	178
199	Drag coefficient against angle of attack for study case 3 . . . . .	179
200	Lift coefficient against angle of attack for study case 3 . . . . .	179
201	Drag-to-lift ratio against angle of attack for study case 3 . . . . .	180
202	Pressure distribution along the blade chord at $\alpha = 6^\circ$ (pre-stall) . . . . .	181

203	<b>Pressure distribution along the blade chord at <math>\alpha = 18^\circ</math> (post-stall)</b> . . . . .	181
204	<b>Pressure distribution along the blade chord at <math>\alpha = 16^\circ</math> (stall)</b> . . . . .	182
205	<b>Study case 4 fluid domain (not to scale)</b> . . . . .	184
206	<b><math>y^+</math> values for different meshes of study case 4</b> . . . . .	185
207	<b>The skewness of study case 4</b> . . . . .	185
208	<b>The orthogonality of study case 4</b> . . . . .	185
209	<b>The generated mesh of fluid domain and blade for case 4</b> . . . . .	186
210	<b>The generated mesh of the cross plane of the blade for case 4</b> . . . . .	186
211	<b>The inflation layers around the blade for case 4</b> . . . . .	187
212	<b>The generated mesh of the blade for case 4</b> . . . . .	187
213	<b>The convergence history of study case 4</b> . . . . .	189
214	<b>The <math>y^+</math> distribution of study case 4</b> . . . . .	190
215	<b>Study case 4: the blade velocity at different spanwise locations</b> . . . . .	191
216	<b>Study case 4: the velocity streamlines</b> . . . . .	192
217	<b>Relative velocity vector at 30% span for case 4</b> . . . . .	193
218	<b>Relative velocity vector at 80% span for case 4</b> . . . . .	193
219	<b>Pressure contour at 30% span for case 4</b> . . . . .	194
220	<b>Pressure contour at 80% span for case 4</b> . . . . .	194
221	<b>Study case 5 fluid domain (not to scale)</b> . . . . .	197
222	<b>Mesh dependency of fluid domain (study case 5)</b> . . . . .	199
223	<b>Mesh dependency of rotating body (study case 5)</b> . . . . .	199

224	<b><math>y^+</math> values for different meshes of study case 5</b>	200
225	<b>The skewness of study case 5</b>	200
226	<b>The orthogonality of study case 5</b>	200
227	<b>The generated mesh of fluid domain and rotor for case 5</b>	201
228	<b>The generated mesh of the rotor for case 5</b>	201
229	<b>The generated mesh of the hub and one blade for case 5</b>	202
230	<b>The generated mesh of a cross section with one blade for case 5</b>	202
231	<b>The inflation layers around the blade for case 5</b>	203
232	<b>The simulated time of study case 5</b>	204
233	<b>The simulated time of study case 5 (zoom-in)</b>	205
234	<b>The <math>y^+</math> distribution of study case 5</b>	205
235	<b>The velocity of the blades (study case 5)</b>	206
236	<b>Rotor torque for different wind speeds (study case 5)</b>	207
237	<b>Power coefficient versus tip speed ratio (study case 5)</b>	208

## List of Tables

1	<b>The simulation setting of large-scale riblet validation</b> . . . . .	36
2	<b>Lift-to-drag ratio increase comparison with the 2D smooth aerofoil</b> . . . . .	47
3	<b>Pressure drag coefficient for the smooth and tripped aerofoils</b> . . . . .	47
4	<b>Skin-friction drag coefficient for the smooth and tripped aerofoils</b> . . . . .	48
5	<b>Wall unit for each riblets' configuration</b> . . . . .	56
6	<b>Number of inflation layers above the riblets</b> . . . . .	57
7	<b>Number of nodes on each base and top of riblets</b> . . . . .	57
8	<b>Number of nodes on each edge of riblets</b> . . . . .	57
9	<b>Meshing for each riblets' configuration</b> . . . . .	58
10	<b>Total number of mesh (triangular faces)</b> . . . . .	59
11	<b>Total number of mixed cells</b> . . . . .	59
12	<b>Lift increase of the tripped blades in comparison with the smooth blade (<math>26m/s</math>)</b> . . . . .	66
13	<b>Drag reduction of the tripped blades in comparison with the smooth blade (<math>26m/s</math>)</b> . . . . .	66
14	<b>Lift-to-drag ratio increase of the tripped blades in comparison with the smooth blade (<math>26m/s</math>)</b> . . . . .	67
15	<b>Pressure drag reduction of the tripped blades in comparison with the smooth blade (<math>26m/s</math>)</b> . . . . .	70
16	<b>Skin-friction drag reduction of the tripped blades in comparison with the smooth blade (<math>26m/s</math>)</b> . . . . .	70
17	<b>Lift increase comparison of configuration II with smooth blade</b> . . . . .	88

18	<b>Drag reduction comparison of configuration II with smooth blade</b> . . . . .	89
19	<b>Lift-to-drag ratio increase comparison of configuration II with smooth blade</b> . . . . .	89
20	<b>Total number of mesh (triangular faces)</b> . . . . .	90
21	<b>Total number of mixed cells</b> . . . . .	90
22	<b>Average number of the mesh triangular faces</b> . . . . .	97
23	<b>Total number of the mixed cells</b> . . . . .	97
24	<b>Percentage change in power coefficient of the tripped WT compared to the smooth WT</b>	104
25	<b>Average number of the mesh (triangular faces)</b> . . . . .	118
26	<b>Total number of mixed cells</b> . . . . .	118
27	<b>Percentage change in power coefficient for different number of riblets compared to the smooth WT</b> . . . . .	119
28	<b>Average number of the mesh (triangular faces)</b> . . . . .	121
29	<b>Total number of the mixed cells</b> . . . . .	121
30	<b>Percentage change in power coefficient of riblets only on suction or pressure side compared to the smooth side</b> . . . . .	123
31	<b>Average number of the mesh (triangular faces)</b> . . . . .	125
32	<b>Total number of mixed cells</b> . . . . .	125
33	<b>Percentage change in power coefficient for different riblets' configurations compared to the smooth WT</b> . . . . .	127
34	<b>Average number of the mesh (triangular faces)</b> . . . . .	129
35	<b>Total number of the mixed cells</b> . . . . .	129
36	<b>Percentage change in power coefficient of two different orientations of riblets compared to the smooth WT</b> . . . . .	133

37	<b>Study case 1 simulation algorithm</b>	157
38	<b>Simulation settings for study case 2</b>	167
39	<b>Study case 3 simulation algorithm</b>	176
40	<b>Study case 4 simulation algorithm</b>	188
41	<b>Study case 4: torque (<math>N.m</math>) at <math>10.5m/s</math> calculation comparison</b>	195
42	<b>Study case 5 Simulation Algorithm</b>	203
43	<b>Steady and transient torques validated against experiment</b>	208
44	<b>Effect of hub on the computed mechanical torque</b>	209
45	<b>The 21% chord aerofoil coordinates</b>	210
46	<b>The 43% chord aerofoil coordinates</b>	211
47	<b><math>S - A</math> turbulence model constants</b>	213
48	<b><math>SST k - \omega</math> turbulence model constants</b>	216
49	<b><math>k - \epsilon</math> turbulence model constants</b>	217

# 1 INTRODUCTION

## 1.1 Background

Fossil-fuel energy, such as natural gas, coal, and crude oil, has been the dominant energy across world in the past decade [1, 2]. However, its harmful impacts to humanity and the environment, including air pollution [3], climate change [4], and global warming [5] have led to the requirement of using renewable energy. Furthermore, the availability of renewable energy is greater than the actual energy used globally. For example in 2005, wind energy that was available was 5 times greater than the consumed worldwide energy [6].

In the last decade, the world demand for renewable energy has increased and this is expected to grow in the future, as shown in Figure 1 [7], which is based on studies by the U.S. Energy Information Administration (EIA) [8–10], the International Renewable Energy Agency (IRENA), and the Global Wind Energy Council (GWEC) statistics. Figure 1 also shows the projection of the high contribution of wind energy as part of the total world energy. This means further analysis and investigation of wind energy are required.

The total energy consists of the fossil-fuel energy and renewable energy that are consumed in the U.S. over the years. For example in 2006, about 20% of the total energy used was renewable energy. However, the percentage of relying on renewable energy will be increased and expected to be the only reliable source in the future. The wind energy will be expected to contribute to about 25% of the renewable energy in 2040, as shown in Figure 1.

A wind turbine (WT) system is defined as a machine that converts wind energy (kinetic energy) into mechanical energy using a rotor. Then the energy is transported using shafts to produce electrical energy via a generator. Generally, a WT is classified either as a horizontal axis wind turbine (HAWT) or a vertical axis wind turbine (VAWT); Figure 2 shows the general configuration of both systems.

The main difference between HAWT and VAWT is the rotation axis of the rotor. It is parallel to the ground in HAWT, whereas it is perpendicular to the ground in VAWT. Of course, there are other distinctions between the two machines, such as the yaw system and maintenance costs. Recently, HAWT has been commonly used due to its functionality and production of higher output power compared to VAWT [11, 12].

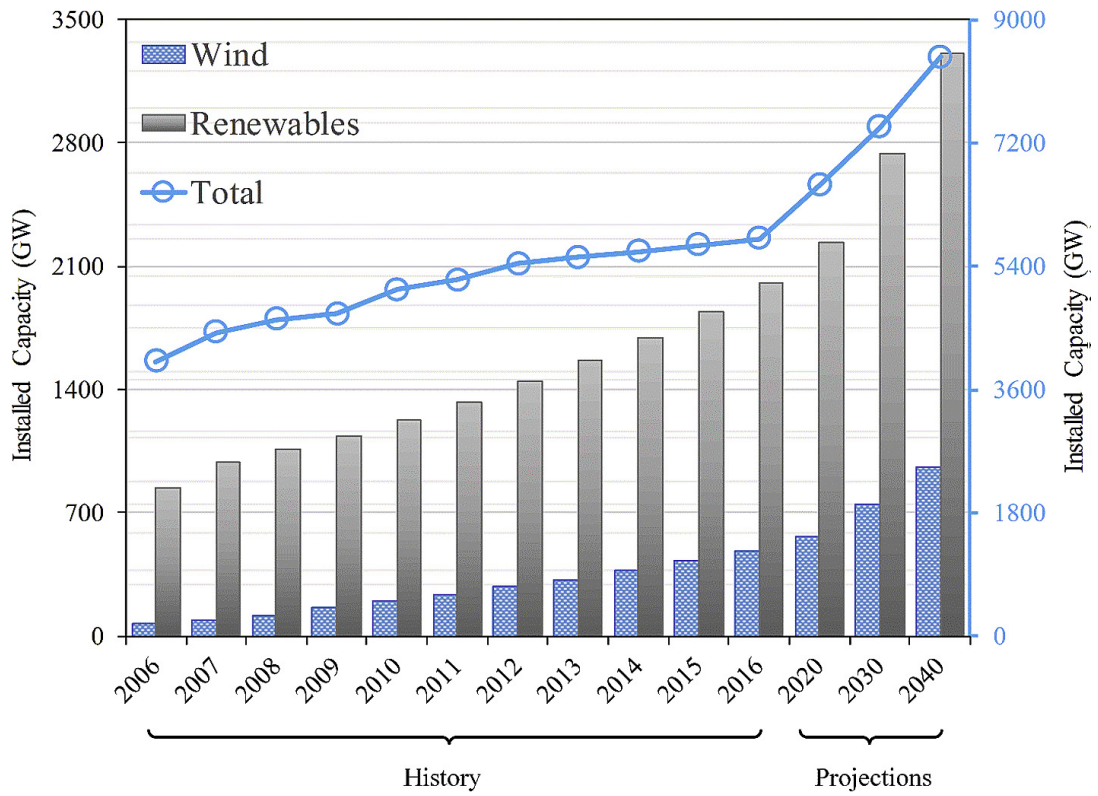


Figure 1: World renewable energy demands and its projection [7]

There are some advantages and disadvantages of using VAWT in comparison with HAWT. For example, VAWT produces a small level of noise because it is exposed to a lower tip speed ratio. However, this causes some difficulty in the starting of vertical turbines. One of the major advantages of VAWT is that the heavy components, such as generator, are placed on the ground, therefore easier access for maintenance and replacement. For VAWT, yaw system can be discarded so lower mass and cost.

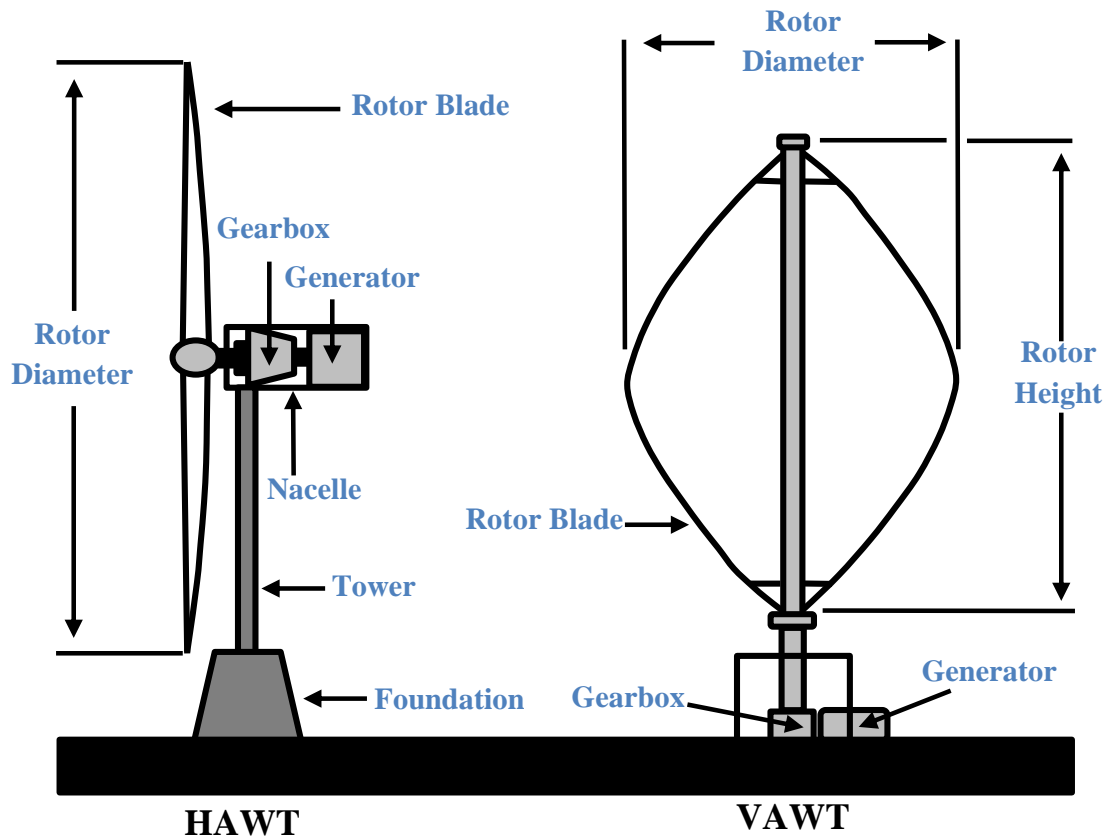


Figure 2: General configuration of HAWT & VAWT

## 1.2 Aims and Objectives

Computational Fluid Dynamics (CFD) studies are less expensive and more attainable compared to experiments because of their availability. Modelling can produce rich and detailed results with consistency however, it is based on assumptions and needs validation. On the other hand, experiments deal with real problem analysis and produce gold standard data however, experiments require repeatability and scaling.

As such, this work only focuses on computational analysis. Geometry is created in Auto-desk Inventor and then imported into Ansys Workbench, followed by generating mesh via Ansys Meshing and finally domains are numerically simulated using Ansys Fluent. The aim of this PhD project is to modify the National Renewable Energy Laboratory (NREL) phase II by adding a passive flow controller, namely riblets, on the blade surface, then to examine the change in its performance.

The aim of this project is achieved via two main bodies, which are simulating smooth and then tripped blades. In total, there are five study cases for smooth blades that are validated

against experimental work to achieve the first stage of the project. Smooth study cases start with very simple simulations of a steady and transient two-dimensional (2D) flow, followed by an unsteady three-dimensional (3D) flow on a S809 aerofoil profile as well as simulating the NREL phase II. All the smooth cases validation can be found in Appendix A. Each smooth study case has its own objective as follows:

- Study case 1 is simulated to observe the effect of fluid domain geometry of a rectangular shape and C-shape at an inlet on the lift and drag coefficients of a 2D NACA 4412 aerofoil using Reynolds Averaged Navier-Stokes (RANS) equations.
- Study case 2 is based on selecting appropriate turbulence models via simulating a 2D Unsteady Reynolds Averaged Navier-Stokes (URANS) on a S809 aerofoil by validating lift and pressure drag coefficients against experiment.
- Study case 3 is about simulating a 3D URANS S809 blade by showing lift and drag coefficients and drag-to-lift ratio. Additionally, it focuses on determining the flow separation point on a S809 aerofoil along the chordwise direction.
- Study case 4 is a periodic simulation of one-third of the NREL phase II with an offset angle of  $120^\circ$  and implementation of the multiple reference frame (MRF) model to compute the mechanical torque using two different turbulence models.
- Study case 5 is about applying the sliding mesh model (SMM) on a full rotor scale of the NREL phase II to compute its mechanical torque and power coefficient at various tip speed ratios. In addition, it examines separately the effect of including the hub and time calculation in the simulation.

The tripped blade section has four study cases. Each study case has its own riblet configuration based on the geometry of the blade. The simulation starts with a validation for large-scale riblets on DU 96-W-180 aerofoil profile. Then, a very simple 2D flow on a tripped S809 aerofoil profile followed by a 3D flow on a tripped fixed blade with the same aerofoil profile are simulated. Finally, the simulation of the tripped NREL phase II is performed. Each tripped study case is compared to its similar setting of smooth ones. The objective of the tripped study cases are as follows:

- Large-scale riblets validation against recent experimental work is performed to compare the effect of large-scale riblets on the aerodynamic coefficients. The simulation is done on a 3D fixed blade with a DU 96-W-180 aerofoil profile due to the lack of previous work on a tripped fixed blade with a S809 aerofoil profile.
- Study case 6 has the objective to simulate a 2D rectangular riblet (step) on the suction side of the S809 aerofoil to observe the riblet effect on the 2D lift and drag coefficients. It also shows separately the effect of the 2D riblet on pressure and skin-friction drags. In addition, it displays the flow physics for degradation of the performance.
- Study case 7 computes the aerodynamic forces and pressure distribution on a fixed 3D blade for different triangular riblet configurations at various wind speeds to record the riblets' effect. In addition, the aim is to observe how riblets change the pressure and skin-friction drags. It also shows the flow physics and turbulence level for drag reduction and lift increase cases.
- Study case 8 is done to observe triangular riblets' effect on the NREL phase II performance via simulating riblet on the blade's suction side. The flow physics are also shown to determine the behaviour of riblets in improving the performance of wind turbine.

Finally, four new riblet configurations are established to further improve the performance of the NREL phase II. The new riblet configurations include changing the riblets number, creating riblets only on the pressure side of the NREL phase II, applying riblets on both blade sides of the wind turbine and finally the riblets are orientated by  $90^\circ$  with respect to the incoming wind.

### **1.3 Structure of the thesis**

The content of this thesis is as follows: first, a literature review is undertaken covering the components of HAWTs, particularly the NREL phase II blade and hub geometries. Computational studies on HAWTs are then described showing the most suitable turbulence model to be employed. In addition, the history and previous conclusions resulting from applying riblets on flat plates and fixed blades are given. Second, this work defines the pre-processing of the study cases. This includes describing the governing equations that are

used for simulating HAWT and the generated mesh. Additionally, general riblet geometry is shown.

Third, a validation for large-scale riblets on a 3D fixed blade with DU 96-W-180 against recent experimental work. Fourth, the tripped study cases are described for applying triangular riblets on S809 aerofoil, fixed blade and the NREL phase II. The results of the tripped study cases are compared to the smooth ones. The smooth study cases validation against experimental and computational works can be found in Appendix A. Finally, improving further the performance of the NREL phase II by showing four new different riblet configurations and their effects on the wind turbine performance.

### **1.4 Programs used for this work**

Various programs are used for this research to achieve the required outcome of the results. Texmaker (Latex) has been used to write up this thesis and to ensure a professional writing style. In addition, Excel is employed to issue x-y plots and the graphs are then converted to pdf files for better visualization via Word, and finally imported into Latex. Few pictures of mesh and simulation are improved by Paraview for better visualisation.

The geometry of the blades is created in Auto-desk Inventor and imported into Ansys Modelling for further commands. Each case is then meshed in Ansys Meshing and forwarded into the solver. All the computational work is simulated using Ansys Fluent with running aid of The University of Sheffield high performance computer (Iceberg & Sharc). Finally, the results are extracted using CFD-post processing.

## 2 LITERATURE REVIEW

### 2.1 Horizontal Axis Wind Turbine

The primary components of the HAWT are the rotor (blades and hub), nacelle (shafts, gearbox and generator) and tower, as shown in Figure 3 [13]. Generally, the resultant force on the blades is generated by incoming wind causing rotation of the rotor and resulting in spinning a low-speed shaft that is connected to a gearbox. The gearbox's function is to increase the speed of spinning to match generator's rotational speed via a high-speed shaft. Eventually, the mechanical energy is converted into the electrical energy using a generator.

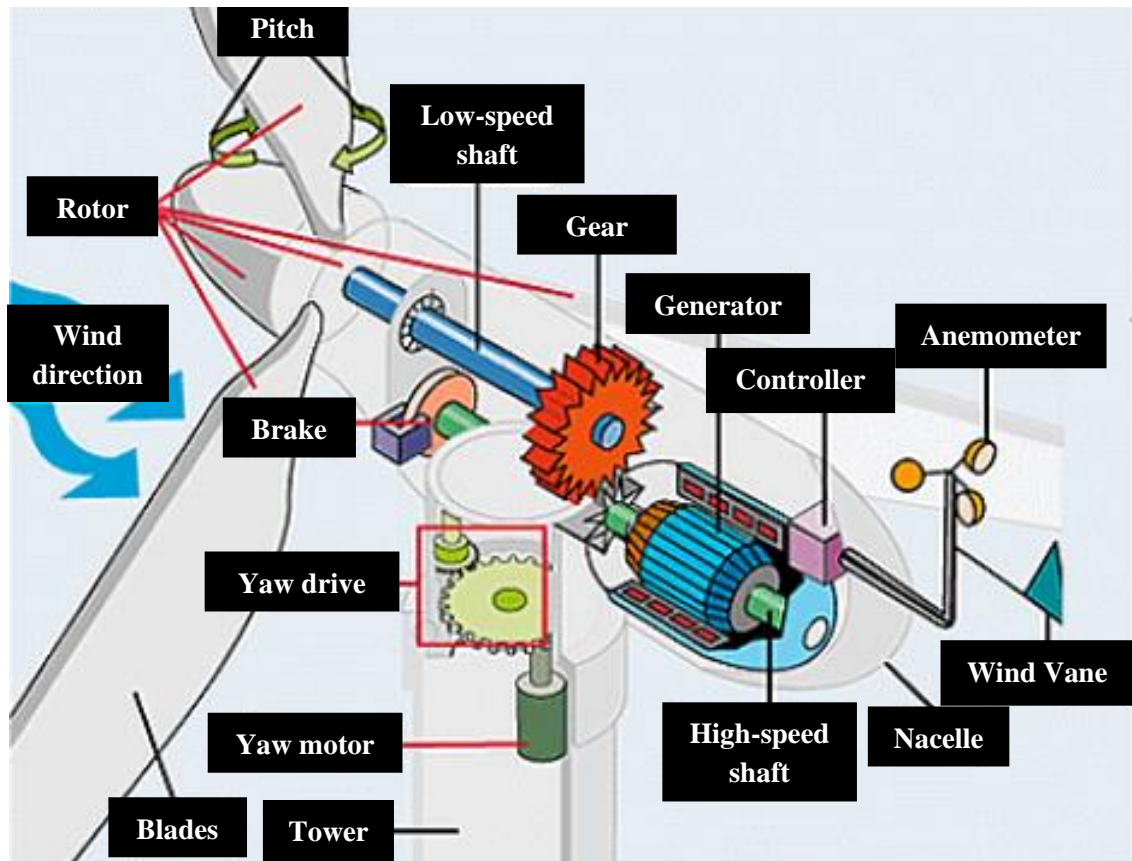


Figure 3: Anatomy of HAWT [13]

Based on the rotor and tower locations, with respect to wind direction, HAWT is classified into upwind and downwind HAWTs. The rotor faces the wind in the upwind type, whereas the wind hits the tower first in a downwind HAWT. Currently, most HAWTs are manufactured as upwind types due to the advantage of avoiding the shadow of wind behind the tower, which

causes turbulence and fatigue, as in downwind turbines. However, the yaw system can be discarded in a downwind turbine, thereby leading to lower mass and cost [14].

Regarding the torque of upwind and downwind turbines, Larwood and Chow [14] compared the performance of both upwind and downwind NREL phase VI. It was shown that the downwind type can achieve approximately the same torque for a pre-stall condition. However, the upwind turbine can produce higher power at high wind speeds. The blade flap-bending is avoided for downwind turbines due to lower aerodynamic loads that are highly exposed to upwind turbines [14].

One of the largest HAWT full-scale projects in early 1990s was the IEA Annex XIV, which was then followed by the IEA Annex XVIII. Seven organisations participated and collaborated to determine the aerodynamic quantities in flow field conditions. Each organisation tested different type of wind turbines including un-tapered and un-twisted blades, a blade with twist but not tapered, and tapered and twisted blades. The list below shows all participants of the IEA Annex XIV/XVIII [15]:

1. Netherlands Energy Research Foundation (Operating Agent).
2. Centre for Renewable Energy Systems, only participated in IEA Annex XVIII.
3. Delft University of Technology.
4. Imperial College, together with Rutherford Appleton Laboratory, only participated in Annex XIV.
5. Mie University, only participated in IEA Annex XVIII.
6. NREL.
7. Risø National Laboratory.

## 2.2 NREL Phase II Wind Turbine Geometry

### 2.2.1 NREL phase II rotor

One WT phase that was experimented by NREL in EIA Annex XIV is NREL phase II, which was performed in field conditions in the north of Golden, United States. It is the same version of the Grumman turbine, but replaced the Grumman aerofoil with the S809 aerofoil for all blade profiles. The NREL phase II has a fixed rotor geometry, as it has a constant pitch angle of  $12^\circ$  along the blades. The blade is not tapered and is un-twisted, with dimensions of  $5.05m$  and  $0.457m$  in radius and chord respectively [16].

The aerofoil, with a thickness of 43% chord, begins at a 14.4% span then its thickness is linearly reduced until a 30% span. However, the thickness of a 21% chord is maintained for the rest of the blade. The NREL phase II is a three bladed, downwind turbine. In addition, it has a rotational speed of  $71.63rpm$  ( $7.50rad/s$ ) and rotates clockwise, as seen from downwind looking upwind, with a rated power of  $19.8kW$  and a cut-in speed of  $6m/s$ . Due to having a constant pitch angle, the NREL phase II has a stall regulated power [16]. Figure 4 represents the blade platform of the NREL phase II.

The spar of an approximated length of  $0.51m$  is attached to the blade at about 25% chord from the leading edge with diameter of  $0.08m$ . The root length of  $0.22m$  is estimated for smoother simulation however, spar extends to 30% span in reality. The hub of the NREL phase II is shown in Figure 5. The features of the hub have been estimated by the author due to lack information on the hub dimensions in either the report by Schepers *et al.* [15] or by Simms *et al.* [16]; however, the effect of the hub on the mechanical torque will be studied later in the results (section 8.5).

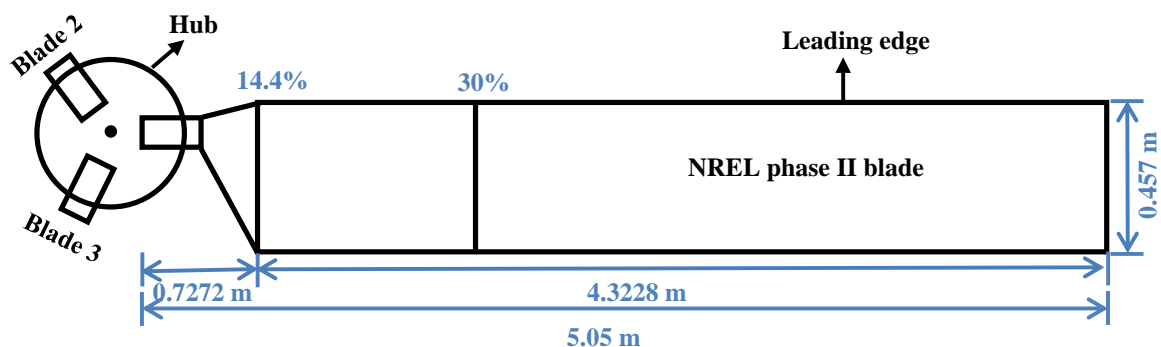


Figure 4: The NREL phase II blade platform

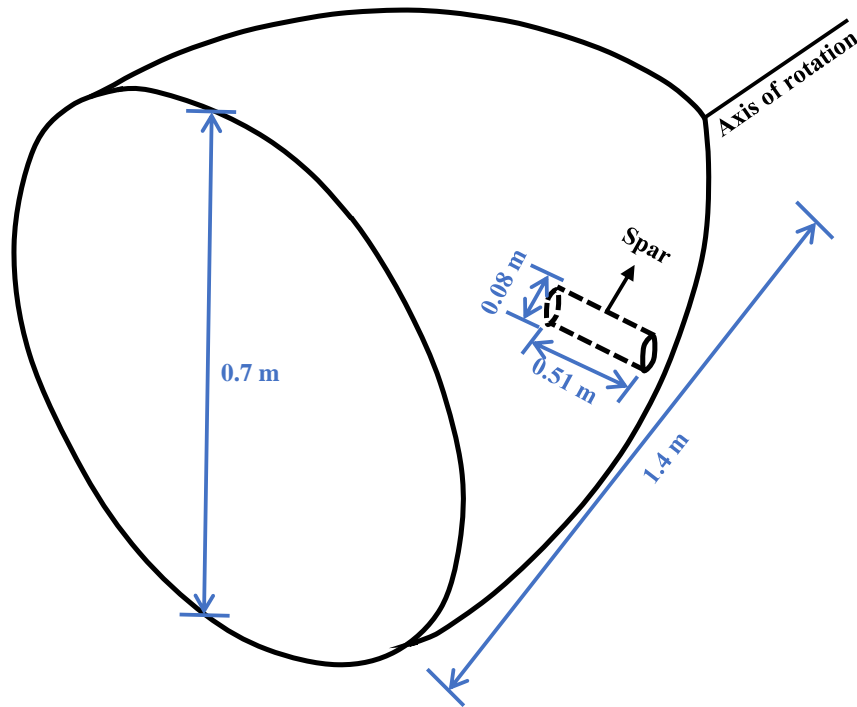


Figure 5: The NREL phase II hub

### 2.2.2 Aerofoil coordinates

As previously stated, the S809 aerofoil profile, with two different thicknesses, forms the NREL phase II blade. The two aerofoil coordinates are shown in Appendix B [17].

## 2.3 Wind Turbine Performance

First, it is important to fully state the acting aerodynamic force on an aerofoil as shown in Figure 6. When the wind hits the blades, a difference in pressure between the upper side and lower side of the blade creates the lift force. The drag force is a force that acts opposite to the object direction. The resultant force ( $\vec{F}$ ) of lift and drag is causing a net positive torque ( $T$ ) on the shaft, and therefore rotation of the blades. This leads to mechanical power production which turns into electricity via the generator.

Both lift and drag forces can be computed directly in Fluent by integrating pressure and stress tensors over the aerofoil area stating the desired direction of force with respect to relative wind flow. Equations (1) and (2) illustrate how the components of the resultant force, that are lift and drag forces, are generally computed respectively [18]. Computing the lift and drag

forces makes it possible to calculate the lift and drag coefficients as in Equations (3) and (4) respectively [18].

$$L = \oint p \vec{n} \cdot \vec{j} dA + \oint \vec{\tau} \cdot \vec{j} dA \quad (1)$$

$$D = \oint p \vec{n} \cdot \vec{i} dA + \oint \vec{\tau} \cdot \vec{i} dA \quad (2)$$

$$C_L = \frac{L}{\frac{1}{2} \rho V_r^2 A} \quad (3)$$

$$C_D = \frac{D}{\frac{1}{2} \rho V_r^2 A} \quad (4)$$

Where:  $L$  is the lift force ( $N$ ),  $D$  is drag force ( $N$ ),  $\vec{F}$  is resultant force ( $N$ ),  $A$  is blade area ( $m^2$ ),  $\vec{n}$  is normal unit vector,  $\vec{j}$  is vertical unit vector,  $\vec{i}$  is parallel unit vector,  $p$  is pressure ( $Pa$ ),  $\vec{\tau}$  is viscous stress vector ( $Pa$ ),  $\phi$  is pitch angle,  $\alpha$  is angle of attack (AOA),  $N$  is normal force ( $N$ ),  $TN$  is tangent force ( $N$ ),  $T$  is torque ( $N.m$ ),  $\vec{V}_r$  is resultant velocity ( $m/s$ ),  $C_L$  is lift coefficient,  $C_D$  is drag coefficient,  $V_\infty$  is wind velocity ( $m/s$ ), and  $\rho$  is air density ( $kg/m^3$ ).

However, normal and tangent coefficients are initially calculated from pressure measurements in experiment [16]. Other forces are then calculated from normal and tangent forces. Each two forces are related by a special reference, for example, lift and drag forces are referenced by the resultant velocity, effective force and torque are referenced by the axis of rotation, and normal and tangent forces are referenced by the chord line.

The two most important parameters when determining the WT performance are mechanical torque by rotor and WT power coefficient. This is because mechanical torque is a measure of how efficient the design of blades is to extract energy from wind. Furthermore, the generator is a measure of how much electricity can be produced after energy losses. The WT mechanical torque can be measured experimentally, either by calculating a torque coefficient, being determined from normal and tangent force coefficients of the blade [16], or directly by placing torque sensors along the blades [11]. However, it also could be calculated computationally, as in Ansys Fluent [19] (Equation (5)):

$$\vec{M} = \vec{r} \times \vec{F}_P + \vec{r} \times \vec{F}_v \quad (5)$$

Where:  $\vec{M}$  is the total moment ( $N.m$ ),  $\vec{r}$  is position vector ( $m$ ),  $\vec{F}_P$  is pressure force vector ( $N$ ), and  $\vec{F}_v$  is viscous force vector ( $N$ ).

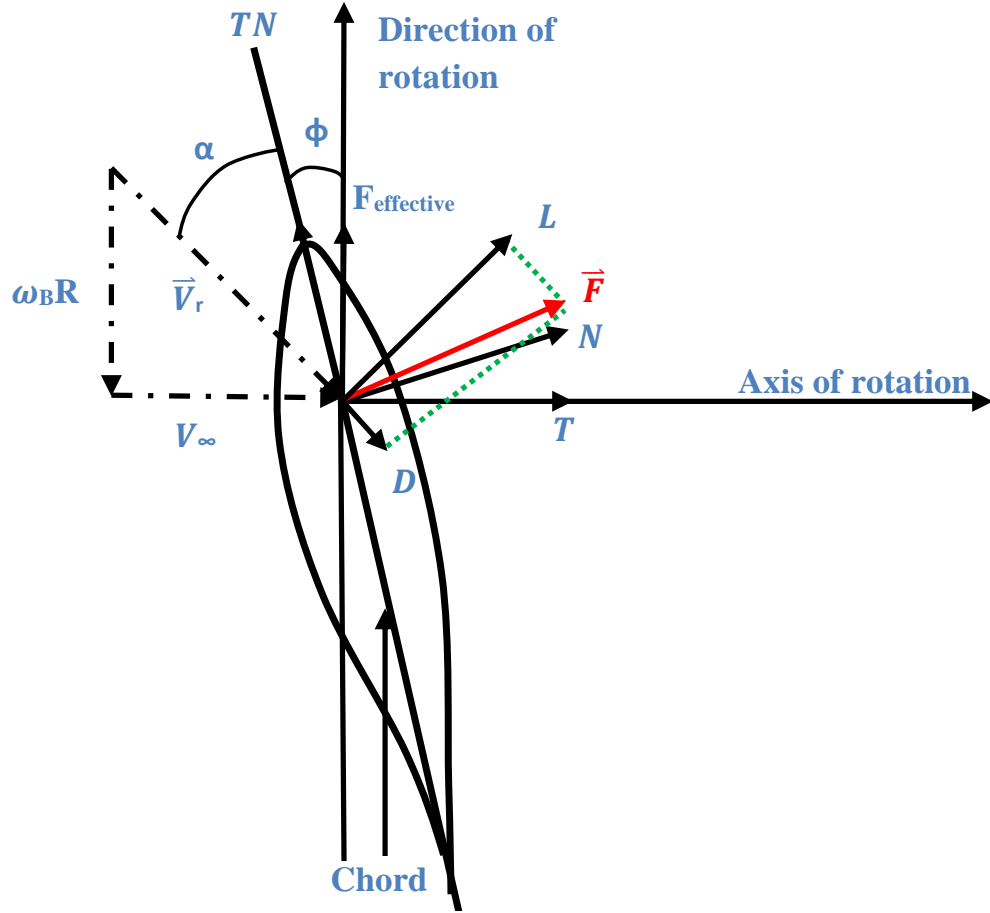


Figure 6: The applied aerodynamic force on an airfoil

In addition, the WT power coefficient, or in other words, the WT efficiency, can be expressed either by mechanical power or electrical power using Equations (6) and (7) respectively [20]:

$$C_P = \frac{P_m}{P_w} = \frac{T_m \omega_B}{\frac{1}{2} S_A \rho V_\infty^3} \quad (6)$$

$$C_P = \frac{P_g}{P_w} = \frac{T_g \omega_B}{\frac{1}{2} S_A \rho V_\infty^3} \quad (7)$$

Where:  $P_m$  is the wind turbine mechanical power (W),  $P_g$  is wind turbine generator power (W),  $P_w$  is power of incoming wind (W),  $T_m$  is wind turbine mechanical torque (N.m),  $T_g$  is wind turbine electrical torque (N.m),  $\omega_B$  is speed rotation of blade (rad/s),  $S_A$  is rotor swept area =  $\pi \frac{d^2}{4}$  ( $m^2$ ), and  $d$  is blade diameter (m).

Another important parameter is the tip speed ratio of the wind turbine, which is a ratio of wind speed to the rotation rate of the wind turbine. This parameter is usually plotted against the power coefficient of a wind turbine to determine the best operation condition that can be achieved with respect to a specific wind speed. The tip speed ratio can be calculated as per

Equation (8) [20]:

$$\lambda = \frac{V_{tip}}{V_{\infty}} = \frac{\omega_B R}{V_{\infty}} \quad (8)$$

Where:  $V_{tip}$  is the velocity of blade tip ( $m/s$ ) and  $R$  is blade radius ( $m$ ).

From Figure 7, the maximum possible efficiency of the wind turbine is  $16/27 = 59.3\%$  and it is known as Betz's limit [21]. This limit is based on the following assumptions:

- Homogeneous, steady state and incompressible flow.
- Infinite number of blades.
- No frictional drag is considered ( $V_2 = V_3$ ).
- The thrust is uniform over the rotor.
- Non-rotating flow at the wake of the rotor.
- The inlet static pressure equals the outlet static pressure of the slipstream ( $p_1 = p_4$ )

The calculation of Betz's limit starts by applying the momentum theory to the control volume so the thrust:

$$Thrust = \rho S_A V_2 (V_1 - V_4) \quad (9)$$

The thrust can also be found from the pressure difference across the rotor:

$$Thrust = S_A (p_2 - p_3) \quad (10)$$

Because the flow is assumed incompressible, steady and inviscid, Bernoulli's equation can be applied upstream and downstream the rotor as follows:

$$p_2 - p_1 = \frac{1}{2} \rho (V_1^2 - V_2^2) \quad (11)$$

$$p_3 - p_4 = \frac{1}{2} \rho (V_4^2 - V_3^2) \quad (12)$$

After simple algebra the following is resulted:

$$Thrust = S_A (p_2 - p_3) = \frac{1}{2} \rho S_A (V_1^2 - V_4^2) \quad (13)$$

Now defining the axial induction factor ( $a$ ) as follows:

$$a = \frac{V_1 - V_2}{V_1} \quad (14)$$

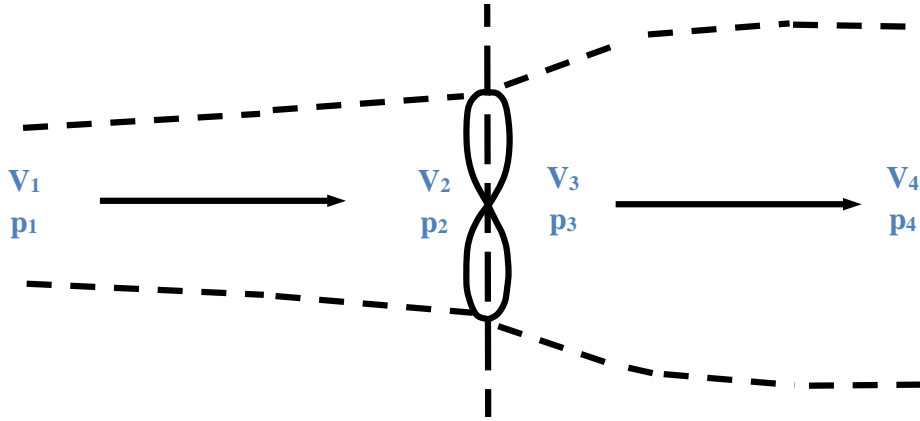


Figure 7: Ideal wind turbine model

The wind turbine power coefficient ( $C_P$ ) can be calculated as follows:

$$C_P = 4a(1 - a)^2 \quad (15)$$

The maximum wind turbine power ( $dC_p/da = 0$ ) is obtained at  $a = 1/3$  and therefore  $C_P = 59.3\%$ .

The pressure distribution along the blade chord is also an important parameter to determine the starting point of flow separation at certain AOA's of the blade, particularly when the pressure gradient is positive. The stall condition occurs when the blade experiences a sudden lift reduction as AOA increases, thereby flow separation occurs as the boundary layer is no longer attached to the blade surface. The pressure distribution is expressed in terms of the pressure coefficient ( $C_p$ ), and it is calculated as in Equation (16) [18], where  $p_\infty$  is the wind pressure ( $Pa$ ).

$$C_p = \frac{p - p_\infty}{\frac{1}{2}\rho V_r^2} \quad (16)$$

## 2.4 Computational Studies on HAWT

There are several computational studies for predicting aerodynamic forces on WT, therefore, in the author's opinion, numerical studies can be classified into three categories. First, the blade element momentum (BEM) method, which is very simple and efficient approach used by Glauert in 1935 [22]. The BEM method equates two theories (momentum theory and blade element theory). It can estimate the performance of WTs from aerodynamic coefficients that

are obtained either from experimental data or mathematical models [11].

Modifications have been made to the BEM method by introducing new corrections and models to account for 3D effects and improve the outcome results, such as, Prandtl's tip-loss factor [23], improved tip-loss model [24], dynamic stall correction [25], and stall delay model [26]. Despite its low cost and simplicity in terms of calculations, the BEM method is unable to resolve viscous flow and thus this technique fails to accurately predict flow separation points over the aerofoils [27].

The next complexity level in computing acting aerodynamics forces on WT is solving RANS equations, which simulate 3D viscous flow and therefore can predict flow separation points over the blades of WTs. However, the accuracy of computing the flow separations points depends on the turbulence models used. Commercial CFD solvers, for example, Fluent and CFX, solve RANS equations using the finite volume method as a numerical discretization scheme [11].

Finally, large eddies simulation (LES) and direct numerical simulation (DNS) are more advanced levels in terms of accuracy for simulating WT. However, cost and time are critical as both methods hugely depend on the power of Reynolds number ( $Re$ ) due to its requirement in refining all flow direction. Therefore, a CFD hybrid RANS-LES, such as detached eddy simulation, is considered a compromise solution, but the computational cost and time needed are still higher than for the RANS simulation [28].

Due to its reasonable cost, time, and accuracy in predicting characteristics of external flow, RANS equations are modelled using the CFD Fluent solver for this work. Since the flow around a HAWT is considered turbulent, three different turbulence models are used to close RANS equations throughout this project. The following list of turbulence models shows other researchers' work and the conclusions of the best one to be used for simulating flow over the blades of WTs.

- **The  $S - A$  turbulence model**

The main purpose of developing the  $S - A$  model is so it can be used on aerodynamic applications. Previous researchers, such as Song and Perot [29], simulated the NREL phase VI and concluded that the  $S - A$  model showed good agreement of the theory with the experiment at the pre-stall condition; however, a large difference in results was observed for higher velocities. In addition, a similar conclusion was obtained by You *et al.* [30].

Moreover, a simulation of periodic one-third of the NREL phase II blades was previously performed by Mansour and Yahyazade [31] and Tachos *et al.* [32] using the  $S - A$  turbulence model. As a result, the  $S - A$  turbulence model does not have the ability to accurately predict the mechanical torque of the NREL phase II at the flow separation region, but performed well at low wind velocities.

- **The  $k - \epsilon$  turbulence model**

Of all the turbulence models used for closing RANS equations, the  $k - \epsilon$  model is considered the most frequently simulated model in many engineering applications. However, a very large error in computing the power coefficient of the NREL phase II was reported by Mansour and Yahyazade [31], using the standard  $k - \epsilon$  model, due to its low effectiveness in handling highly recirculated flow such as the flow around WTs.

Nevertheless, the standard  $k - \epsilon$  turbulence model was simulated by Thumthae and Chitsomboon [33] and acceptable accuracy was shown in low and mid wind speed regimes. Furthermore, Elfarra *et al.* [34] showed that the  $k - \epsilon$  Launder–Sharma turbulence model performed well at pre-stall and stall regions, but inaccurate results were shown at high wind speed regions for the NREL phase VI.

- **The  $SST k - \omega$  turbulence model**

The  $SST k - \omega$  turbulence model is widely used in aerodynamic applications, including WT, due to its advantages over other RANS turbulence models [35]. According to Sørensen and Michelsen [36], who simulated a steady flow around the NREL phase II, good accuracy in mechanical power production was found at low wind speeds. However, increasing the wind speed resulted in less agreement with experiment, but results were improved by assuming transient state.

Moreover, results can be improved further at a flow separation region by applying a transitional  $SST$  turbulence model, as reported by Lanzafame *et al.* [37]. Nevertheless, the  $SST k - \omega$  turbulence model performed better in all other flow conditions compared to the transitional  $SST$  turbulence model. Therefore, combining both models might result in better agreement with experiment, as noted by Sørensen *et al.* [38]. For this model,  $y^+$  should be below 5 ( $y^+ = yu_\tau/\nu$  [39]), where  $y$  is first layer thickness,  $u_\tau$  is shear velocity ( $u_\tau = \sqrt{\tau_w/\rho}$ ), and

$\nu$  is kinematic viscosity, to resolve sub-viscous region.

In terms of pressure distribution along the blade, Chen and Qin [40] and Sørensen *et al.* [41] showed successful accuracy in all flow conditions, except at  $10m/s$ . As such, the *SST*  $k - \omega$  is unable to accurately predict pressure distribution near the root at a flow separation region on the blade's suction side. In summary, the *SST*  $k - \omega$  shows the best prediction for the power coefficient of WTs. However, all three models referred will be tested within this thesis.

## 2.5 Flow Controllers (Riblets)

Lift-to-drag ratio is an important factor in aeroplane designs. This is because increasing this ratio leads to a reduction in the fuel consumption of aeroplanes [42]. However, for other aerodynamic applications, such as wind turbines, increasing lift force is more important than reducing drag force. This is because the lift force is the main driving force in wind turbines [33, 40, 43]. This means new blade designs should focus on maximise the lift force to increase the performance of wind turbines.

The lift-to-drag ratio of aerodynamic systems can be simply increased by either using active or passive flow controllers. Passive flow controllers are widely used due to its low cost and easier implementation compared to the active technique [44]. Active flow controllers such as, jet actuators [40, 45] act as an external power, while passive flow controllers, for example, divergent trailing-edge [40], shark denticle [44], riblets [46–50], and winglets [51, 52], require geometrical change of wind turbine blades.

Domel *et al.* [44] experimented using the shark denticle effect on a NACA 0012 aerofoil profile, as shown in Figures 8a and 8b. The shark denticle height ranges between  $0.7mm$  and  $2mm$  which corresponds to the order of 100 in a wall unit. They observed a recirculation zone in the form of separation bubbles behind the denticle. This alters the pressure distribution, and therefore enhances lift. The shark denticle also generates streamwise vortices, which recover the momentum loss because of skin friction, and therefore the reduction of drag. Given this, their configuration could help increase the efficiency of wind turbines.

Other researchers, such as Van Dam *et al.* [53] deployed small tabs, normally to the surface of aerofoils at about  $95\%c$ , as displayed in Figure 9. The optimum height of the tabs are in the order of boundary layer thickness. The tabs are able to increase the lift force if they are placed on the pressure side by causing a recirculation zone on the wake of the tabs. Similarly, Chen

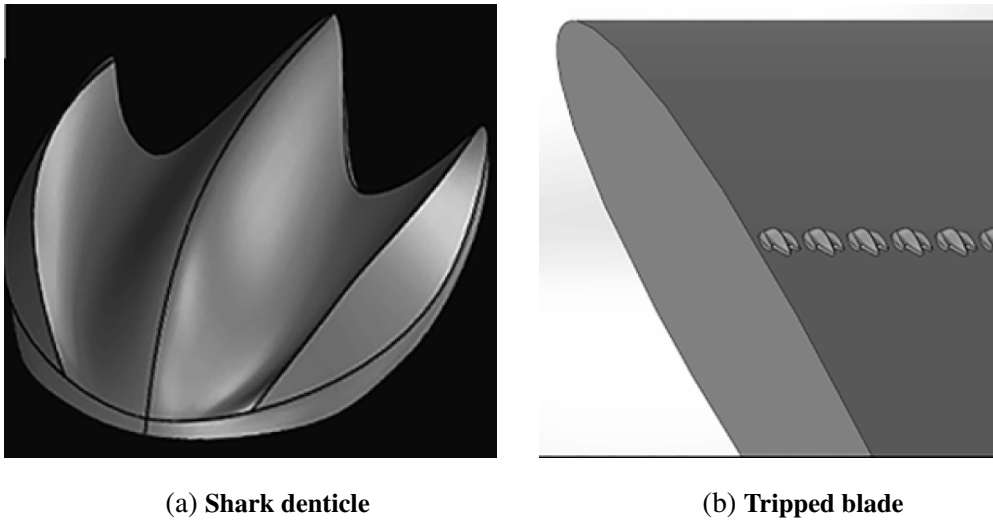


Figure 8: Shark denticle shape on the blade [44]

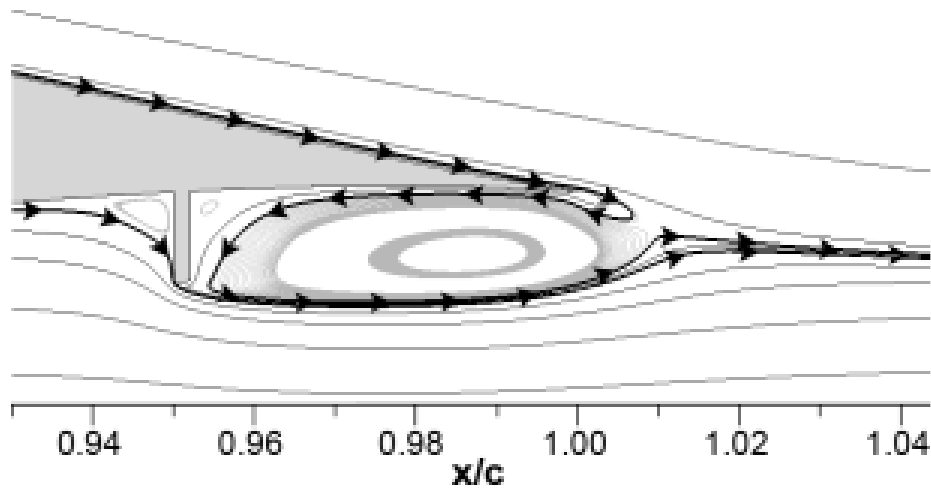


Figure 9: Microtabs on the pressure side of aerofoil [53]

and Qin [40] deployed microtabs on the pressure side of the NREL phase VI. The length and position of the microtabs are were  $2\%c$  and  $90\%c$ , respectively. An improved wind turbine performance at high wind speeds was reported, when microtabs were applied.

A passive flow controller's effect, namely riblets, was investigated first by the National Aeronautics and Space Administration (NASA) in the 1970s and applied on aircrafts. However, riblets' technology was further developed by the 3M company and its application was widely spread among other aerodynamic machines in the 1980s [47]. Riblets, inspired by shark skin, have proven their ability in reducing drag, ranging from 4% to 10% depending on geometrical factors, as reported by previous researchers [54–60].

The mechanism of drag reduction by riblets is still ambiguous. However, there are two

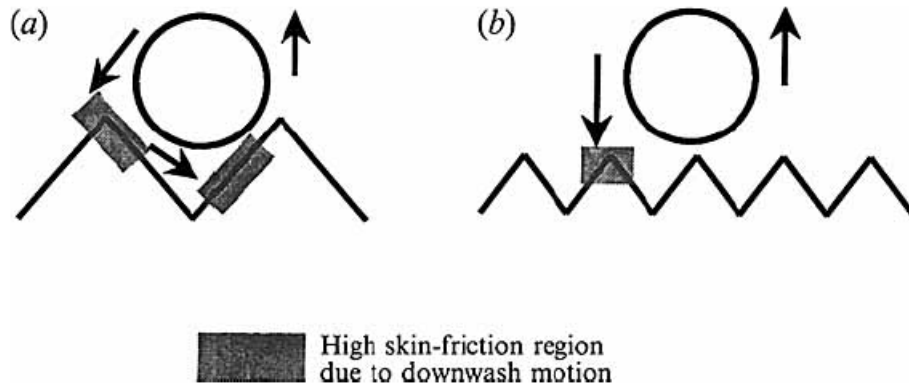


Figure 10: Mechanism of drag by riblets for (a) drag increase (b) drag reduction [61]

common hypotheses in the literature that riblets force streamwise vortices to only occur on a small wetted area, limited by riblet tips, and allow low flow velocity to act only on riblets' valleys; therefore, a viscous drag reduction is observed. This was computationally observed by Choi *et al* [61], such that the high wall shear rate was only found near the riblet tips for drag reduction cases. However, the sides and tip of riblets were both exposed to a high wall shear rate for drag increasing cases [61].

Turbulence statistics, such as turbulence intensity and turbulence stresses, are reduced for the tripped plate in comparison with the smooth one [61]. In 2020, Tiainen *et al.* [62] undertook experimental work on a tripped blade for different AOAs and wind speeds. Their result confirms a reduction of turbulence statistics and an upward shift of the log-law region, because of the thicker viscous layer, as previously reported by Choi *et al.* [61]. Furthermore, they added that the effect of riblets can be clearly seen at low  $Re$  and a positive AOA [62].

The second hypothesis was observed by Bechert and Bartenwerfer [63], such that the flow in the spanwise direction is impeded by riblets; therefore, momentum transport is reduced, leading to drag reduction. They introduced a protrusion height ( $\Delta h$ ) that was analytically defined as the distance between the riblet tip and the virtual origin of the streamwise velocity profile. However, Luchini *et al.* [64] theoretically suggested that the protrusion height depends on the origin of both streamwise ( $h_l$ ) and spanwise ( $h_c$ ) velocity profiles. Choi *et al.* [61] defined the origin at the maximum transfer of turbulent kinetic energy of the flow.

The spanwise flow is generated by the streamwise vortices at the viscous sub-layer. However, because of the riblets, the streamwise vortices are lifted away from the wall due to high elevation of the spanwise flow origin, causing a thicker viscous region [63, 64]. More recent computational research, by Martin and Bhushan [65], on blade-shaped riblets over a flat plate

confirms that the longitudinal vortex are displaced further away from the wall, leading to a thicker viscous sub-layer for drag reduction cases.

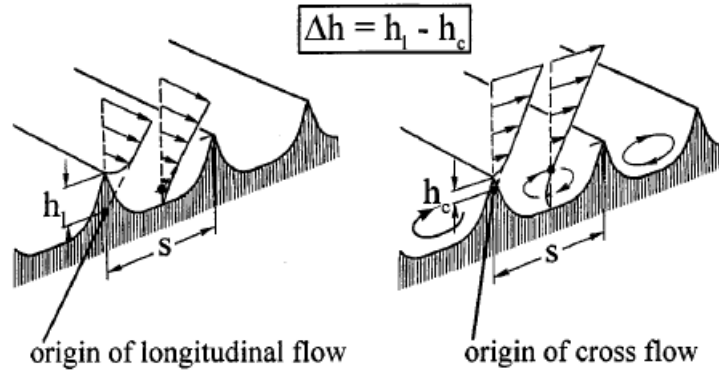


Figure 11: Streamwise and spanwise velocity profiles of tripped surface [64]

The behaviour at which the drag is reduced by the riblets was well explained by García-Mayoral and Jiménez [66], in that drag is reduced as riblet size increases in the viscous sublayer and then, at a certain point, the drag is increased as riblet size increases. This is the maximum point that could have a drag reduction and it varies from 10 to 20 in wall unit ( $s^+ = s_d u_\tau / \nu = 10$  to 20, where  $s^+$  is non-dimensional rib lateral spacing and  $s_d$  is riblets' peak-to-peak distance) depending on riblet configuration [67]. The breakdown comes from drag that is provided by spanwise vortices below the buffer region of the flow [66].

A better scaling was proposed by García-Mayoral and Jiménez [66] to express the optimum drag reduction in terms of the non-dimensional square root of a riblet's cross section ( $l^+ = \sqrt{A_b^+} = A_b^{1/2} u_\tau / \nu$ , where  $A_b$  is the area of riblet's base). They found that, regardless of riblets' shape, the optimum drag reduction occurred at  $l^+ \simeq 10.7 \pm 1.0$  [66]. The tested riblet geometries were triangular riblets, trapezoid base, scalloped base, and blades. According to their findings, Chamorro *et al.* [47] obtained an approximated expression for calculating optimum riblet size as a function of viscous drag and  $Re$ .

There are different types of riblet shapes, including V-base and blade. Launder and Li [68] concluded that the L-shaped obtained the best drag reduction for a flat plate, while the V-base was the poorest for size ratio ( $s_d/h$ ) of 1.6 ( $h$  is riblet height). Nevertheless, Yang [50] reported that the V and trapezoidal bases showed the best drag reduction for  $s_d/h = 1$  and 2, respectively. The best performance of riblets, on an aerofoil, is obtained for V-base of size of  $s_d/h = 1$ , as found by Chamorro *et al.* [47]. In summary, drag reduction by riblets is highly dependent on AOA,  $Re$ , and riblet configurations [46].

Experimentally, Sareen *et al.* [46] and Chamorro *et al.* [47] performed an investigation of triangular riblets on a DU 96-W-180 aerofoil, which is used for wind turbine blades, then reported a reduction of drag to a maximum of 5% compared to a clean blade. However, the optimum riblet height was different for both works because of using different Reynolds numbers. They both applied riblets on partial coverage of a blade, particularly to the last 60% and 30% of chord on the suction and pressure sides respectively, where this region is believed to be the starting point of flow transition to turbulence.

In terms of computational work, Choi *et al.* [61] performed DNS on channel with smooth and tripped flat sides for two different riblet sizes ( $s^+ = 20, 40$ ) at  $Re = 4200$ . The reported drag reduction was in good agreement with experiment. Other researchers such as, Chu and Karniadakis [69] previously applied DNS on V and rounded riblets with  $s^+ = 17.1$  and  $20.3$ , respectively for various Reynolds numbers ranging from 500 to 3500. The results were also validated against experiment.

RANS simulation was also modelled by Beibei *et al.* [70] on a flat plate with thin triangular riblets using the standard  $k - \epsilon$  model. Furthermore, Launder and Li [68] examined a curvilinear mesh on a flat plate with separately three different riblet shapes using the standard  $k - \epsilon$  model. The results showed good agreement with experiment, but the optimum reduction in drag occurred at larger riblet size than those stated by experiment, due to insufficient simulation of the model used as reported [68]. A similar conclusion was reached earlier by Djenidi *et al.* [71] using a mixed length-eddy viscosity model.

RANS simulation on tripped aerofoils has also been discussed in the literature, for example, the NACA 0026 aerofoil with triangular riblets was simulated via Fluent by Ghazali *et al.* [49] using the standard  $k - \epsilon$  model, and reported a drag reduction of 11.8% and 1.64% at  $\alpha = 0^\circ$  and  $\alpha = 30^\circ$ , respectively. In addition, Sidhu *et al.* [48] optimised the riblet performance on the NACA 0012 using the Taguchi method at  $\alpha = 0^\circ$ , and concluded that riblet spacing has a dominant impact on drag reduction compared to height and angle of riblets.

Early in 2020, and during this work, Leidl *et al.* [72] conducted an experiment using a trapezoidal base applied on the blade's suction side, and reported a lift increase and drag reduction. Moreover, they simulated a full-scale wind turbine with three different riblet configurations via Fluent, using MRF. The best configuration of riblet effect showed an increase in WT power of 0.8% and 1.2% at  $8m/s$  and  $11m/s$ , applying the same riblet size with  $s_d/h = 2$  all over the blade's top side. Finally, an experimental tripped WT was performed and showed

a higher WT power than the simulation due to the indirect riblet effect [72].

Later in 2020, Tiainen *et al.* [62] experimentally tested the non-ideal manufactured riblets, using nano-second pulse laser on a blade with a NACA 0024 aerofoil profile. As a result of applying low quality riblets, the design parameters are deformed with time; for example, the riblet angle changed by 93%. However, the results agreed with previous research in terms of velocity profile and turbulence statistics. In addition, the wake thickness of the smooth blade is larger than that of the tripped blade. This means riblets are able to weaken the mixing process in the wake of the blade [62].

## 2.6 Challenges & Potential Work

Applying riblets on blades has already been tested experimentally. However, performing a numerical simulation of riblet effects lacks published evidence. In addition, to the author's knowledge and apart from recent work by Leitl *et al.* [72], no experiment has been conducted in term of applying riblets on wind turbine blades and involving the rotation of the blades. Furthermore, most researchers have tested the effect and arrangement of riblets on stationary blade. Therefore, studying the riblets orientation effects on wind turbine performance is also considered in this present work.

The riblet geometry for this work is potentially able to increase lift and reduce drag, thereby, increasing the performance of WT. Previously, most researchers have been able to decrease drag, although lift remained unchanged. This work uses a millimetre scale instead of micrometre scale for riblet sizes. In comparison with Leitl *et al.* [72] work, riblets are either applied on suction or pressure side, and on both blade's sides. Moreover, riblets are only placed on the outboard section of the blades where most power is produced [40, 47]. Other distinctions, such as riblet heights, WTs (aerofoils), AOAs, rotational technique, and generated mesh show different conclusion.

In some published papers, the conventional terminology "riblets" is not the same as this work's riblets in terms of geometry. For example, some of the previous works on riblets assumed that riblets are fully immersed in the viscous sub-layer. This is due to using a very small scale of riblets. In addition, some of those riblets are just cut on the surface (grooves). The previous results showed a reduction in drag, while the lift force was unchanged. However,

for the present contribution, riblets are not restricted in the viscous sub-layer because of their size. They are not also grooves on the blade's surface, and they are just created on the surface. The riblets in this thesis can be considered as surface perturbations.

## 3 SIMULATION SETUP

### 3.1 Computational Fluid Domain

Each study case requires a different fluid domain depending on the assumed simulation conditions. For fluid domain dimension, study cases 1, 2, and 6 have 2D fluid domains, while study cases 3, 4, 5, 7, and 8 have 3D fluid domains. Each study case's fluid domain is described separately (in detail in sections 5 and 8) along either the aerofoil or blade characteristics. For all study cases' fluid domains, the domains are created in Ansys Workbench.

### 3.2 Governing Equation

Throughout this thesis, three different turbulence models are used to compute the aerodynamic forces on a 2D aerofoil, a 3D stationary blade, and the NREL phase II via Ansys Fluent solver. Equation (17) is substituted on Navier-Stokes equations in Fluent to obtain RANS equations:

$$u = U + u' \quad (17)$$

Where:  $u$  is the turbulence velocity ( $m/s$ ),  $U$  is turbulence averaged velocity ( $m/s$ ), and  $u'$  is turbulence fluctuation velocity ( $m/s$ ).

To describe the flow condition around wind turbines mathematically, assumptions must first be stated:

- Compressibility effect is negligible as the Mach number ( $Ma$ ) does not exceed 0.12 for NREL phase II.
- Based on  $Re$  and other flow conditions, the flow around WTs is assumed to be fully turbulent.
- Turbulent viscosity is isotropic as Boussinesq's hypothesis is assumed for all turbulence models used [19].
- No body force is applied including gravitational force.

### 3.2.1 Continuity Equation

$$\frac{\partial U_i}{\partial x_i} = 0 \quad (18)$$

Where:  $U_i$  is the averaged air velocity components ( $U_x, U_y, U_z$ ) ( $m/s$ ), and  $x_i$  is coordinate system ( $x, y, z$ ).

### 3.2.2 Reynold's Averaged Navier-Stokes Equation

$$\rho \left( \frac{\partial U_i}{\partial t} + U_j \frac{\partial U_i}{\partial x_j} \right) = -\frac{\partial p}{\partial x_i} + \frac{\partial}{\partial x_j} \left( \mu \frac{\partial U_i}{\partial x_j} - \rho \overline{u'_i u'_j} \right) \quad (19)$$

Where:  $t$  is the time ( $s$ ),  $\mu$  is the air dynamic viscosity ( $kg/m \cdot s$ ), and  $\overline{u'_i u'_j}$  is Reynolds (turbulent) stress. Equations (17), (18), and (19) are taken from Pope [73].

### 3.2.3 Turbulence Models

To close RANS equations, Reynold's stresses must be modelled using an appropriate turbulence model. One of the most often used methods is Boussinesq hypothesis which assumes turbulent viscosity is an isotropic scalar quantity. However, this assumption is not entirely true because it is not valid for all flow types, particularly intensive swirling flow [19]. The Reynold's stresses are directly related to the mean velocity gradient as stated by Boussinesq hypothesis (Equation (20)) [74].

$$-\overline{u'_i u'_j} = \nu_t \left( \frac{\partial U_i}{\partial x_j} + \frac{\partial U_j}{\partial x_i} \right) - \frac{2}{3} k \delta_{ij} \quad (20)$$

Where:  $\nu_t$  is the turbulent viscosity ( $m^2/s$ ),  $k$  is turbulence kinetic energy ( $kg \ m^2/s^2$ ), and  $\delta_{ij}$  is Kronecker delta ( $\delta_{ij} = 1$  if  $i = j$  otherwise  $\delta_{ij} = 0$ ).

Employing turbulence models is essentially required to model the turbulent viscosity and therefore, solve Reynold's stresses. Three different turbulence models ( $S - A$ ,  $SST \ k - \omega$ , standard  $k - \epsilon$ ) are simulated throughout this work, to compare with either each other's or with other researchers' simulations. In this section, only the general formulations of the three turbulence models are demonstrated. However, a clearer explanation of each turbulence model terms can be found in Appendix C.

- **The  $S - A$  model by Spalart and Allmaras (Equation (21)) [75]:**

$$\frac{\partial}{\partial t}(\rho\tilde{\nu}) + \frac{\partial}{\partial x_i}(\rho\tilde{\nu}u_i) = G_\nu + \frac{1}{\sigma_{\tilde{\nu}}} \left[ \frac{\partial}{\partial x_j} \left\{ (\mu + \rho\tilde{\nu}) \frac{\partial\tilde{\nu}}{\partial x_j} \right\} + C_{b2}\rho \left( \frac{\partial\tilde{\nu}}{\partial x_j} \right)^2 \right] - Y_\nu \quad (21)$$

Where  $S - A$  model's turbulent viscosity is defined as in Equation (22):

$$\nu_t = \tilde{\nu}f_{\nu1} \quad (22)$$

Where:  $\tilde{\nu}$  is the transported variable,  $G_\nu$  is production of turbulent viscosity,  $\sigma_{\tilde{\nu}}$  and  $C_{b2}$  are constants,  $Y_\nu$  is destruction of turbulent viscosity that occurs in the near-wall region due to wall blocking and viscous damping, and  $f_{\nu1}$  is viscous damping function.

- **The  $SST k - \omega$  model by Menter (Equation (23) and (24)) [76]:**

$$\frac{\partial}{\partial t}(\rho k) + \frac{\partial}{\partial x_i}(\rho k u_i) = \frac{\partial}{\partial x_j} \left( \Gamma_k \frac{\partial k}{\partial x_j} \right) + \tilde{G}_k - Y_k \quad (23)$$

$$\frac{\partial}{\partial t}(\rho\omega) + \frac{\partial}{\partial x_i}(\rho\omega u_i) = \frac{\partial}{\partial x_j} \left( \Gamma_\omega \frac{\partial\omega}{\partial x_j} \right) + G_\omega - Y_\omega + D_\omega \quad (24)$$

Where  $SST k - \omega$  model's turbulent viscosity is defined as in Equation (25):

$$\nu_t = \frac{k}{\omega} \frac{1}{\max\left[\frac{1}{\alpha^*}, \frac{sF_2}{a_1\omega}\right]} \quad (25)$$

Where:  $\Gamma_k$  is the effective diffusivity of  $k$ ,  $\tilde{G}_k$  is generation of turbulence kinetic energy due to mean velocity gradients,  $Y_k$  is dissipation of  $k$ ,  $\omega$  is specific dissipation rate,  $\Gamma_\omega$  is effective diffusivity of  $\omega$ ,  $G_\omega$  is generation of  $\omega$ ,  $Y_\omega$  is dissipation of  $\omega$ ,  $D_\omega$  is cross-diffusion term,  $\alpha^*$  damps turbulent viscosity causing a low-Reynolds-number correction,  $s$  is strain rate magnitude, and  $F_2$  is blending function.

- **The standard  $k - \epsilon$  model by Launder and Spalding (Equation (26) and (27)) [77]:**

$$\frac{\partial}{\partial t}(\rho k) + \frac{\partial}{\partial x_i}(\rho k u_i) = \frac{\partial}{\partial x_j} \left[ \left( \mu + \frac{\mu_t}{\sigma_k} \right) \frac{\partial k}{\partial x_j} \right] + G_k - \rho\epsilon \quad (26)$$

$$\frac{\partial}{\partial t}(\rho\epsilon) + \frac{\partial}{\partial x_i}(\rho\epsilon u_i) = \frac{\partial}{\partial x_j} \left[ \left( \mu + \frac{\mu_t}{\sigma_\epsilon} \right) \frac{\partial\epsilon}{\partial x_j} \right] + C_{1\epsilon} \frac{\epsilon}{k} G_k - C_{2\epsilon} \rho \frac{\epsilon^2}{k} \quad (27)$$

Where standard  $k - \epsilon$  model's turbulent viscosity is defined as in Equation (28):

$$\nu_t = C_\mu \frac{k^2}{\epsilon} \quad (28)$$

Where:  $\sigma_k$  is the turbulent Prandtl numbers for  $k$ ,  $G_k$  is generation of turbulence kinetic energy due to the mean velocity gradients,  $\epsilon$  is turbulence dissipation rate,  $\sigma_\epsilon$  is turbulent Prandtl numbers for  $\epsilon$ , and  $C_{1\epsilon}$ ,  $C_{2\epsilon}$ ,  $C_\mu$  are constants.

### 3.3 Mesh Generation

The solution reliability primarily depends on the mesh accuracy near the rotor to fully capture the flow characteristics. The two most important parameters for mesh accuracy are skewness and non-orthogonality. Both should be minimised, as much as possible, to have a reliable solution [7]. Therefore, the aerofoil is cut-off at the trailing edge, specifically at 99% of the chord length. This modification process causes a blunt instead of a sharp trailing edge and leads to achieving a better mesh accuracy. In the literature, a blunt aerofoil has been used by many other researchers, including Song and Perot [29] and Mo *et al.* [78].

In all study cases, unstructured mesh is mostly generated for rotor and fluid domain via Ansys Meshing; however, mesh size gradually decreases towards the rotor. Finer mesh near the rotor means resolving flow characteristics at the viscous sub-layer (i.e.  $y^+ < 5$  [39]), therefore, inflation layers on the rotor surface are applied. Applying inflation layers near the blade surface leads to constructing wedge elements (prisms) for capturing the boundary effect. For tripped cases, the generated mesh is finer around the riblets region, particularly at the riblets' tips, to observe the riblets' effect. Mesh dependency study and mesh images for each study case are provided in sections 5 and 8.

Regarding rotational techniques, only study cases 4, 5, and 8 involve rotation of the blades, moving reference frame equations must be employed to account for rotational effect, while Equations (18) and (19) are used for the stationary part. The momentum equation can be written in either absolute velocity formulation, as in Equation (29), which is used for this work's rotational cases, or as relative velocity formulation, as in Equation (30). However, the continuity (Equation (31)) is the same for both formulations [79].

$$\rho \left( \frac{\partial}{\partial t} \vec{v} + \nabla \cdot (\vec{v}_r \vec{v}) + (\vec{\omega}_B \times \vec{v}) \right) = -\nabla p + \nabla \bar{\tau} \quad (29)$$

$$\rho \left( \frac{\partial}{\partial t} \vec{v}_r + \nabla \cdot (\vec{v}_r \vec{v}_r) + (2\vec{\omega}_B \times \vec{v}_r + \vec{\omega}_B \times \vec{\omega}_B \times \vec{r}) \right) = -\nabla p + \nabla \bar{\bar{\tau}}_r \quad (30)$$

$$\nabla \cdot \vec{v}_r = 0 \quad (31)$$

Where relative velocity ( $\vec{v}_r$ ) and absolute velocity ( $\vec{v}$ ) can be related as in Equation (32):

$$\vec{v}_r = \vec{v} - (\vec{\omega}_B \times \vec{r}) \quad (32)$$

Where:  $\nabla$  is the divergent operator  $\left( \frac{\partial}{\partial x}, \frac{\partial}{\partial y}, \frac{\partial}{\partial z} \right)$ ,  $\bar{\bar{\tau}}$  is absolute shear stress (Pa), and  $\bar{\bar{\tau}}_r$  is relative shear stress (Pa).

Referring to Ansys Fluent [19], there are three different approaches for modelling a rotational zone: MRF, mixing plane model (MPM), and SMM. The main difference between these techniques is how Equations (29), (30), and (31) are implemented at the interface between inertia and moving zones. Steady state approximation is preferred for both MRF and MPM, while SMM is only applicable for transient state because of mesh movement as a function of time. In the current work, MRF is applied for all rotational cases while SMM is only applied for study cases 5 and 8.

MRF was proposed by Luo and Gosman [80], and it should be used where interaction between moving and stationary zones is weak. However, SMM performs well where unsteady and high interaction exist at the interface. For MRF, the change of vector quantities depends on the reference frame, although, scalar quantities are maintained unchanged. Nevertheless, SMM requires a motion of the grid at the interface with respect to the specified angular velocity. Due to applying unsteady state for SMM, it is computationally more expensive and requires more processing time compared to the other two models.

### 3.4 Riblet Geometry

For all tripped cases, riblets start at the maximum node of the S809 aerofoil and extend towards the trailing edge for the desired distance. This applies to either the suction or pressure side and both blade sides depend on the study case. In all 3D cases, riblet troughs are equally spaced with a distance of one riblet height. For example, if the riblet height is  $1mm$  then the distance is also  $1mm$ . Although the in-flow aligned V-base may produce better results, it has more aggressive mesh therefore, it is decided not to perform it. In addition, the peak to peak

distance is twice the height of riblets for all 3D tripped cases ( $s_d/h = 2$ ).

The trapezoidal riblets' base shape with different riblet configurations are examined on a fixed blade. The best resulted configuration is applied on NREL phase II. Other riblet configurations are only applied on the NREL phase II blades. This is because the core of this work is to increase the performance of WT by creating triangular riblets on its blades. Every case's configuration and results are detailed in sections 5 and 6. The velocity variation is also tested on a tripped fixed blade to observe the effect of different wind speeds for further study on the NREL phase II.

## 4 LARGE-SCALE RIBLETS VALIDATION

### 4.1 Purpose

A validation against experimental work for large-scale riblets that was recently performed by Leitl *et al.* [72] is carried out in this section. The DU 96-W-180 aerofoil profile is simulated for this study case instead of S809 aerofoil as there is no experimental or computational study that has been yet conducted by applying riblets on S809 aerofoil. The difference in lift and drag coefficients between smooth and unclean blades are computed separately and validated against calculated values.

### 4.2 Geometrical setup

The fluid domain of this study case is displayed in Figure 12. The no-slip boundary condition is set for both blade and riblets. The trapezoidal riblets have streamwise and spanwise lengths of  $22mm$  and  $180mm$ , respectively for 20 riblets, as shown in Figures 13, 14 and 15. In comparison with experiment, the streamwise and spanwise distances of trapezoidal riblets are  $510mm$  and  $1.5m$  respectively for 160 riblets. The riblets start at about 32% of the chord for both works. The ratios of riblets size are 0.145 and 0.12 for chordwise and crosswise directions, respectively. The  $h^+$  is between 389 and 606 based on wall shear stress of the smooth blade. Based on the chord length, the Reynolds number is  $2.2 \times 10^6$ .

### 4.3 Mesh & computational setup

The domains are refined in all directions to have a negligible mesh effect in lift and drag coefficients. Figures 16 and 17 show how the lift and drag coefficients change as the number of mesh elements and  $y^+$  change, respectively. The selected mesh of  $1.6 \times 10^6$  and  $y^+ = 0.035$  has 20, 20 and 250 nodes in the spanwise, normal and streamwise directions of the freestream, respectively. There are 60 and 400 nodes on the blade chordwise and spanwise directions, respectively. The blade has also 30 inflation layers in the normal direction with growth rate of 1.2 with first layer at  $1\mu m$  above the fixed blade.

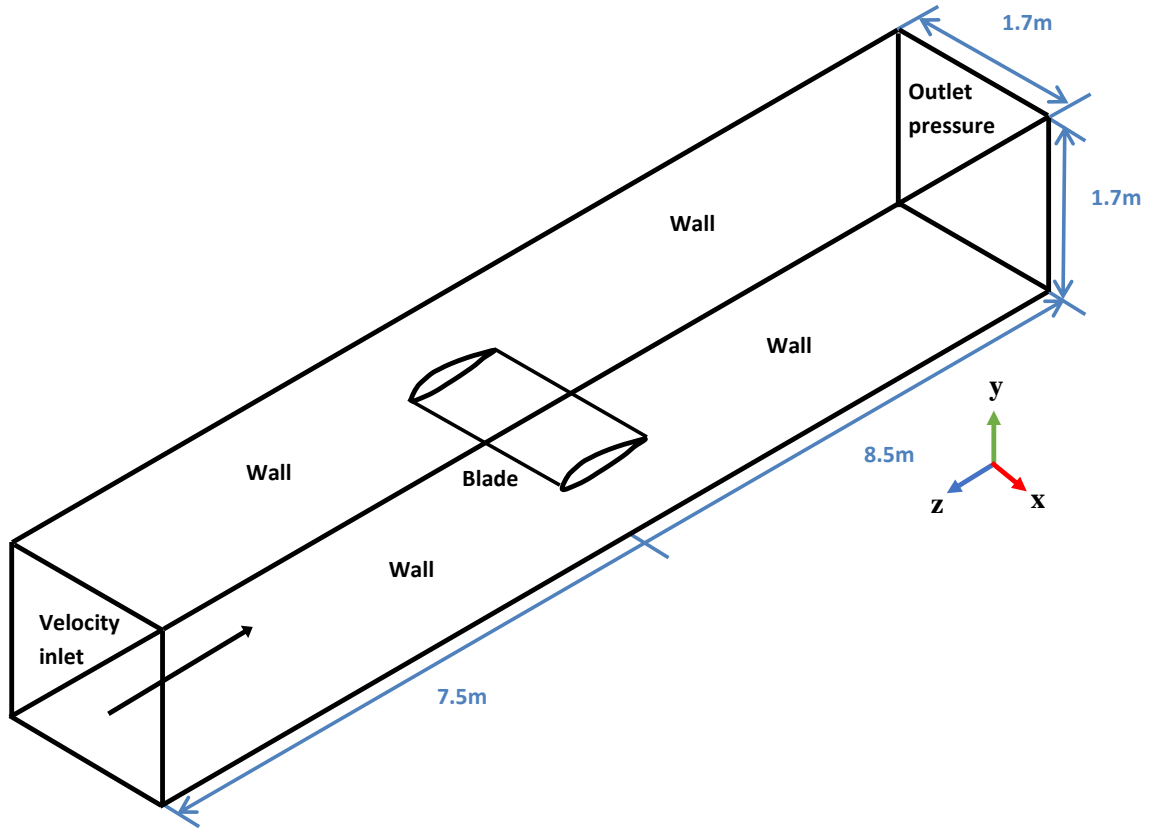


Figure 12: The fluid domain of large-scale riblets validation

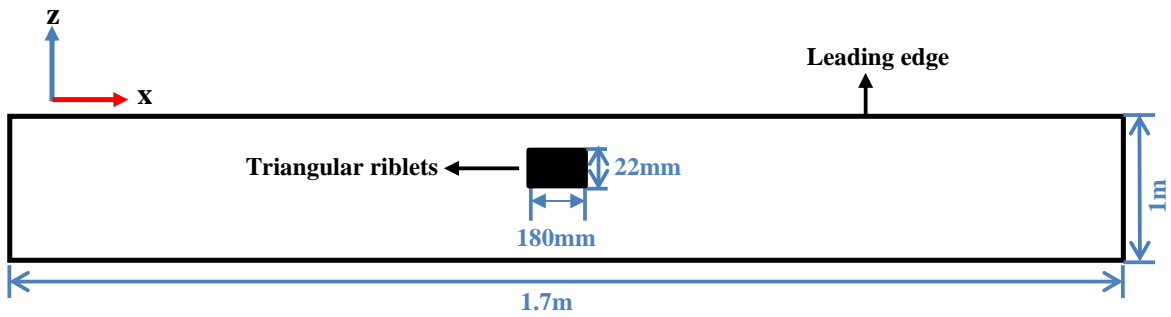


Figure 13: The top view of the simulated blade with employed riblets for validation case (not to scale)

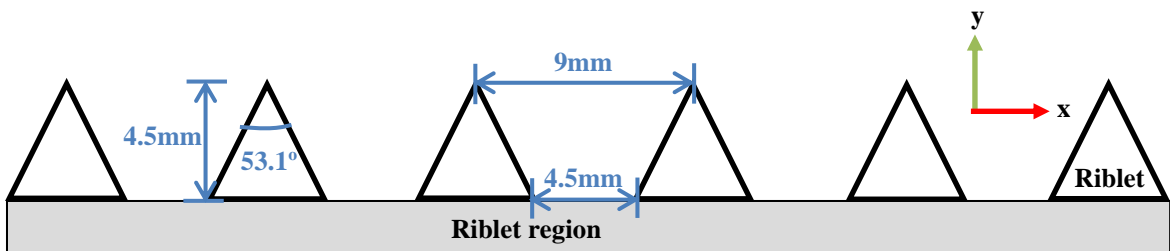


Figure 14: Triangular riblets' configuration for validation case

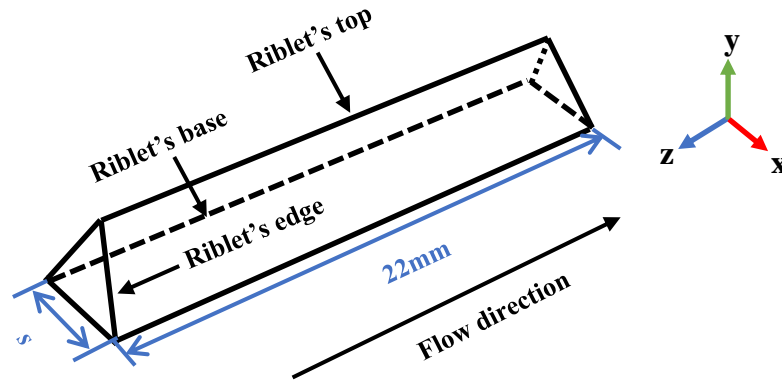


Figure 15: Riblets' configuration for validation case (side view)

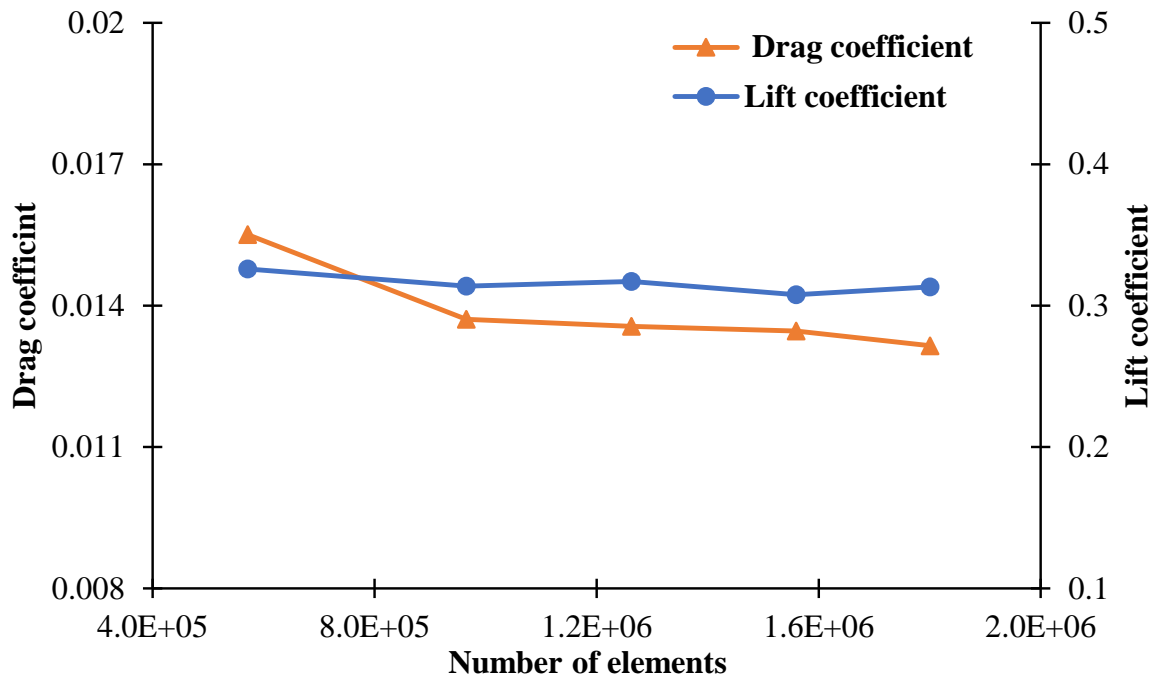


Figure 16: Mesh dependency for large-scale riblet validation

The mesh node numbers are 31 and 21 on each riblet's edge in chordwise and spanwise directions, respectively. Increasing the node number negligibly affect the force coefficients of the blade. The mesh metric of this study case such as, skewness and orthogonality are shown in Figures 18 and 19, respectively. Figures 20-23 display the mesh resolution for the fluid domain, blade and trapezoidal riblets. Table 1 shows the simulation setting of large-scale riblets validation.

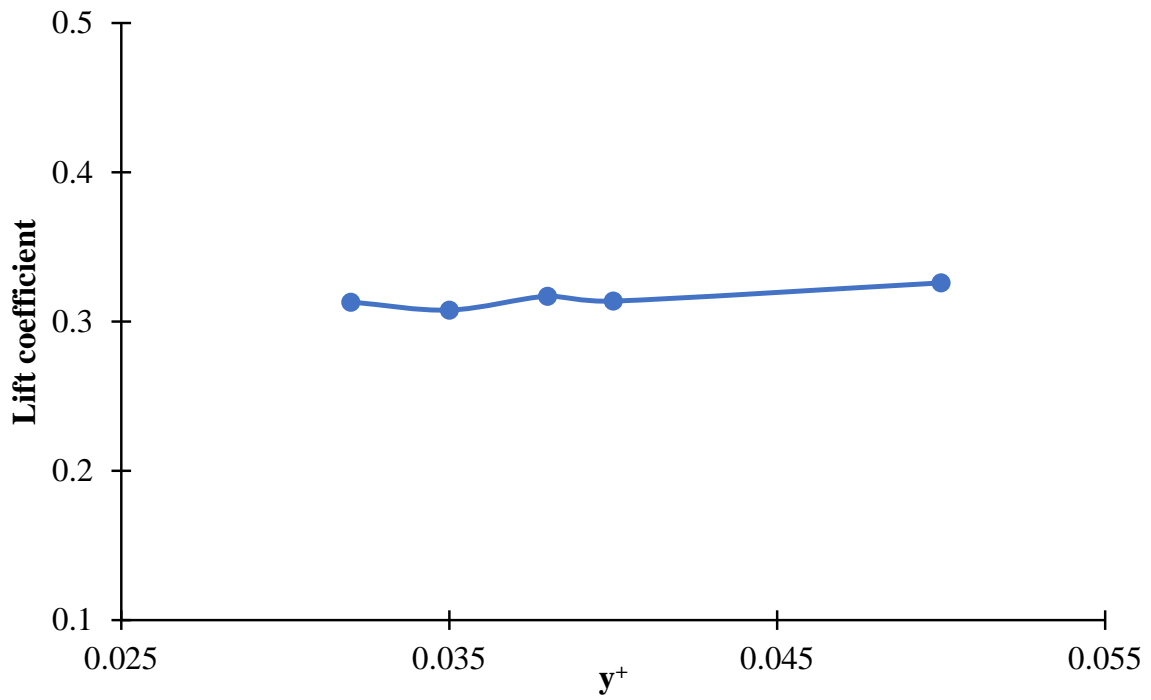


Figure 17:  $y^+$  values for different meshes of large-scale riblets validation

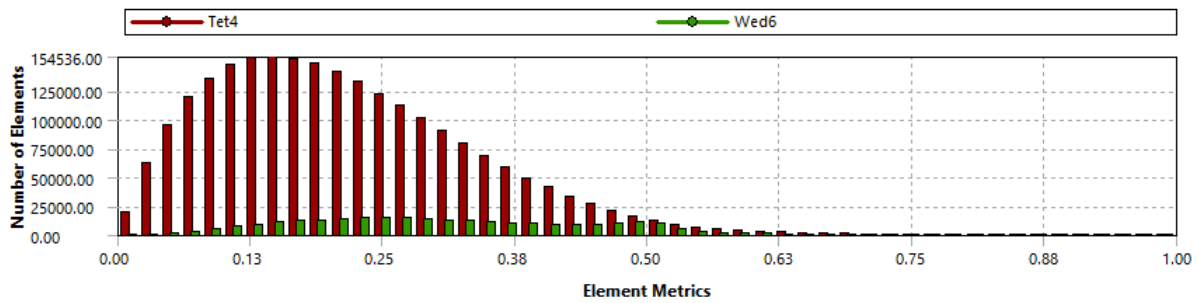


Figure 18: The skewness of large-scale riblet validation

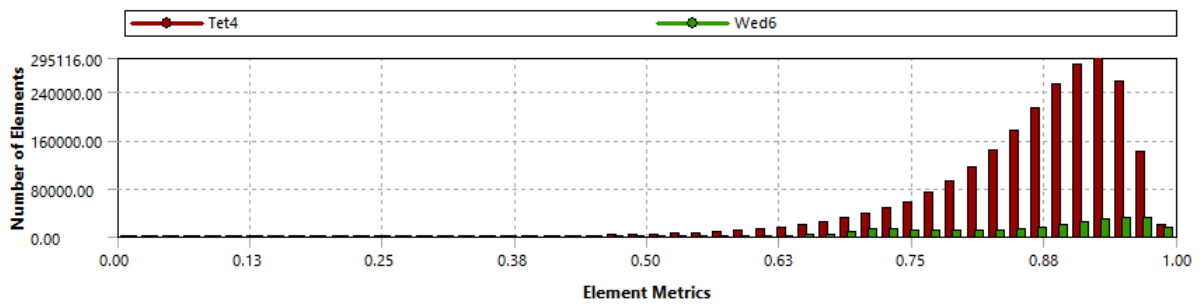


Figure 19: The orthogonality of large-scale riblet validation

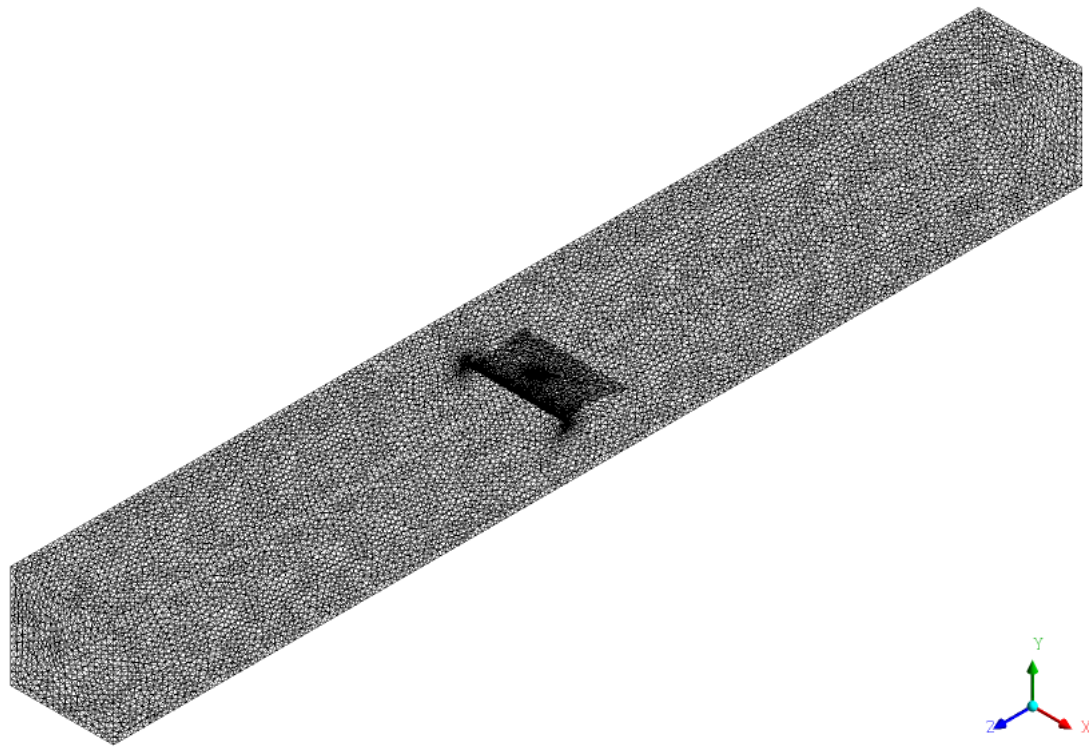


Figure 20: The generated mesh of fluid domain for large-scale riblets validation

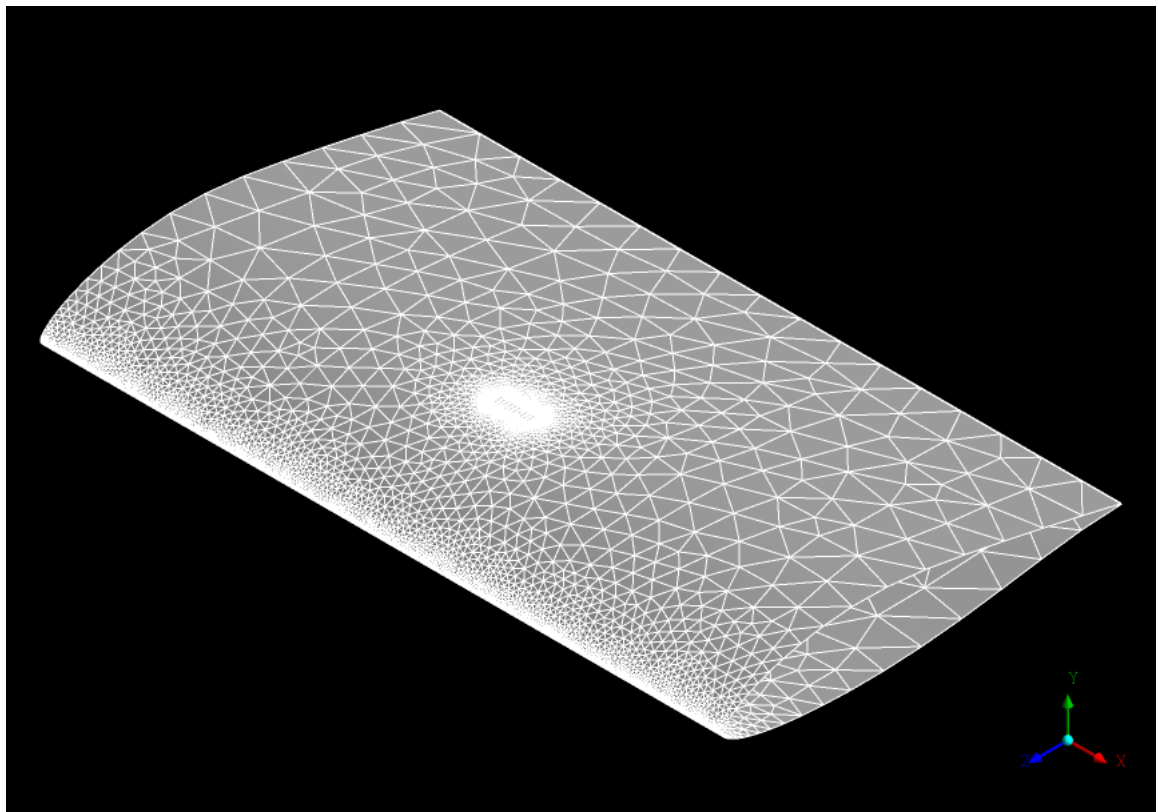


Figure 21: The generated mesh of blade for large-scale riblets validation

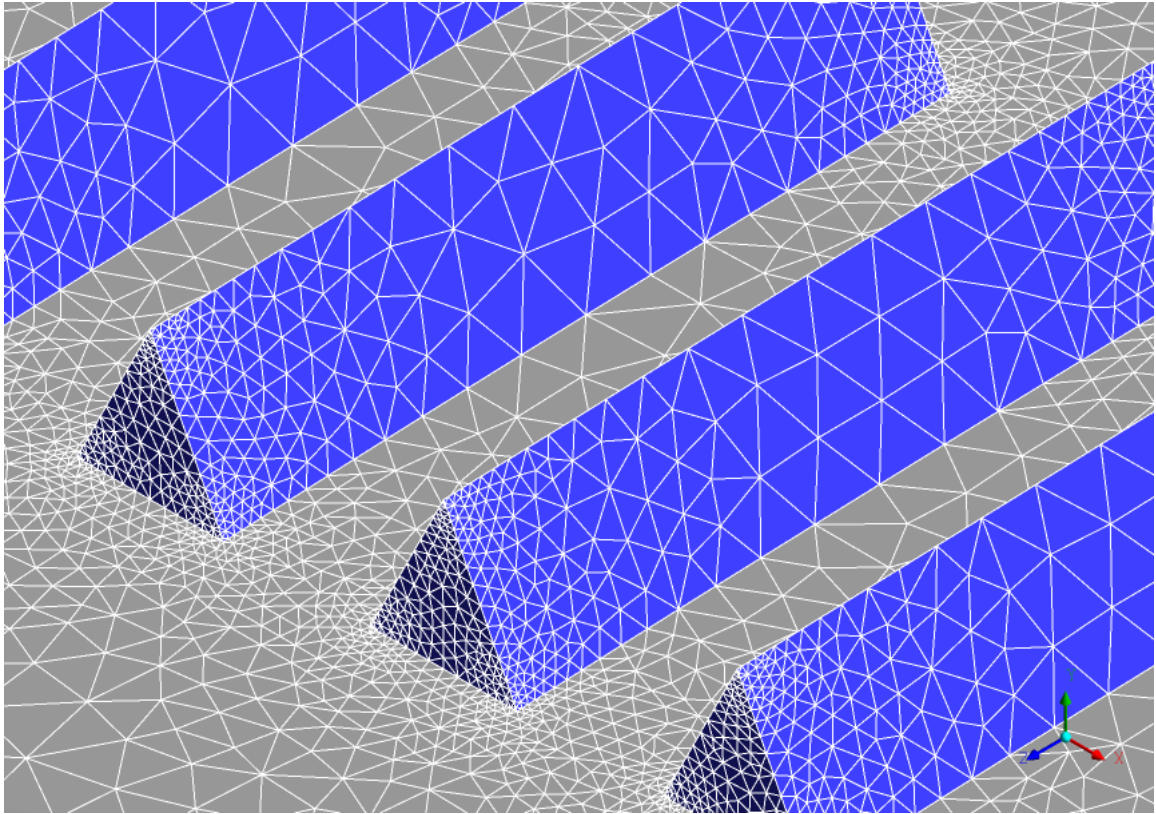


Figure 22: The generated mesh of blade and riblets for large-scale riblets validation

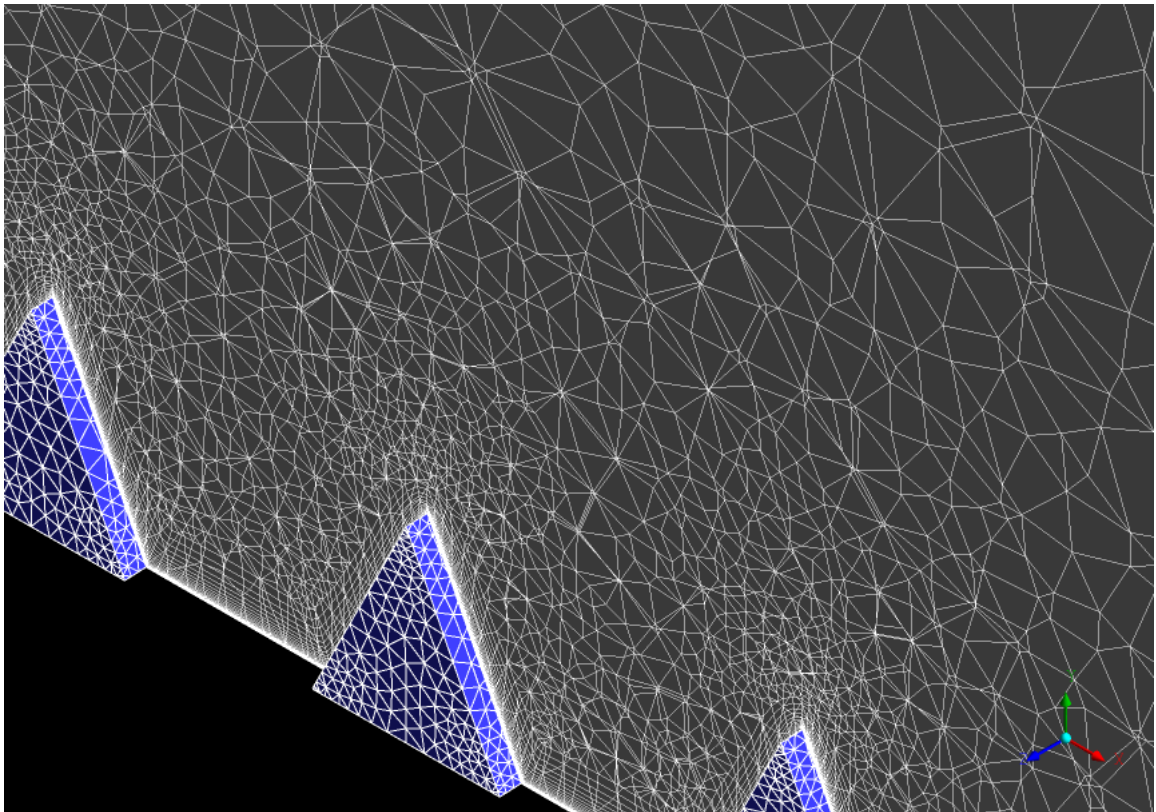


Figure 23: The generated mesh of riblets for large-scale riblets validation

Table 1: The simulation setting of large-scale riblet validation

Algorithm	Function Used
Turbulence Model	<i>SST</i> $k - \omega$
Turbulence Intensity	$I = 0.2\%$
Length Scale	$l = 0.02m$
Operating Pressure	$p = 1ATM$
Wind Velocity	$V = 33.2m/s$
Pressure-Velocity Coupling	Simple
Interpolating Scheme	2 <sup>st</sup> Order Upwind

#### 4.4 Results and discussion

The convergence history of the lift coefficient for large-scale riblets validation at AOA of  $10^\circ$  is shown in Figure 24. At about 1500 iterations, the lift coefficient does not change as the simulation continues to run therefore, this study case is converged. The  $y^+$  distribution along the chord line of the aerofoil at about 50% of the span length is displayed in Figure 25. The values of  $y^+$  at different aerofoil locations are below 0.2, which means the generated mesh is able to resolve the viscous sub-layer. The large-scale riblets start at 32% of the chord length and extend for about 22mm.

The difference in lift and drag coefficients of the smooth and unclean blades are shown in Figures 26 and 27, respectively. The effect of riblets depend on AOAs, as various AOAs show different percentage change in both coefficients. Because more riblets can possibly created experimentally, there is discrepancy between computational and experimental results. Adding more riblets computationally is not possible at this stage due to the limitation of computer resources. However, 20 riblets converge better with experiment, which means increasing length of riblets computationally is going to match the experimental calculated values. According to both works, applying large-scale riblets confirms an increase in lift and a reduction in drag and therefore, improving the performance of wind turbines.

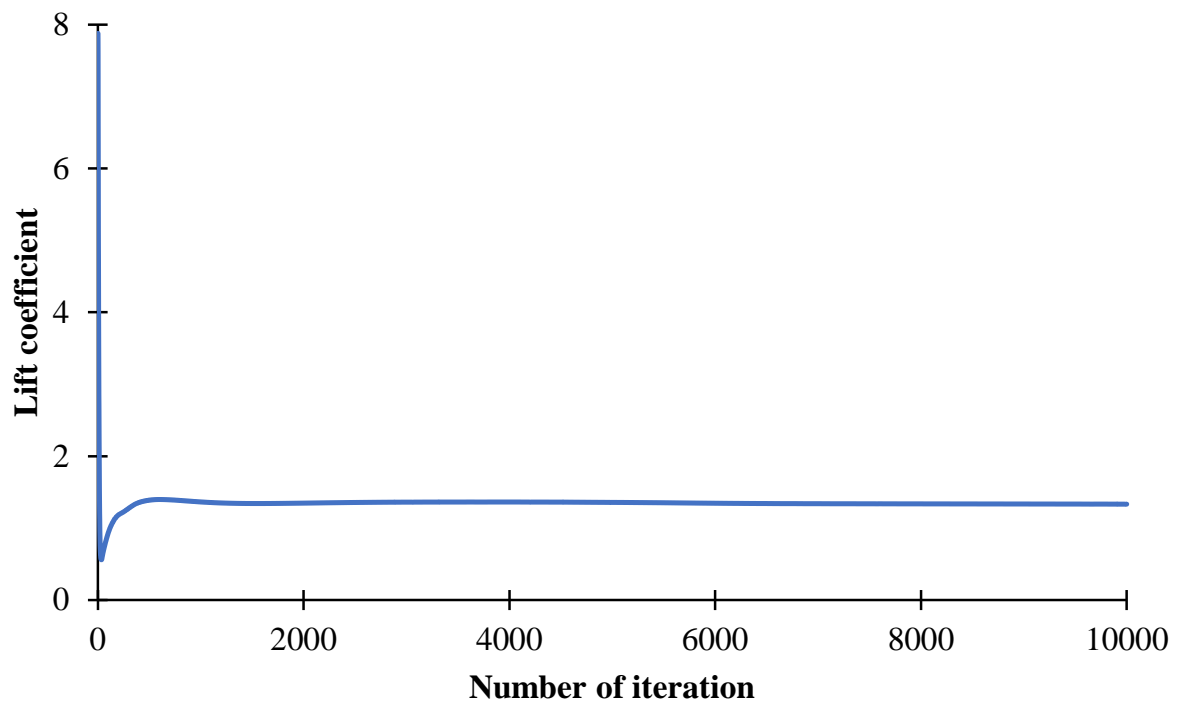


Figure 24: The convergence history of large-scale riblets validation

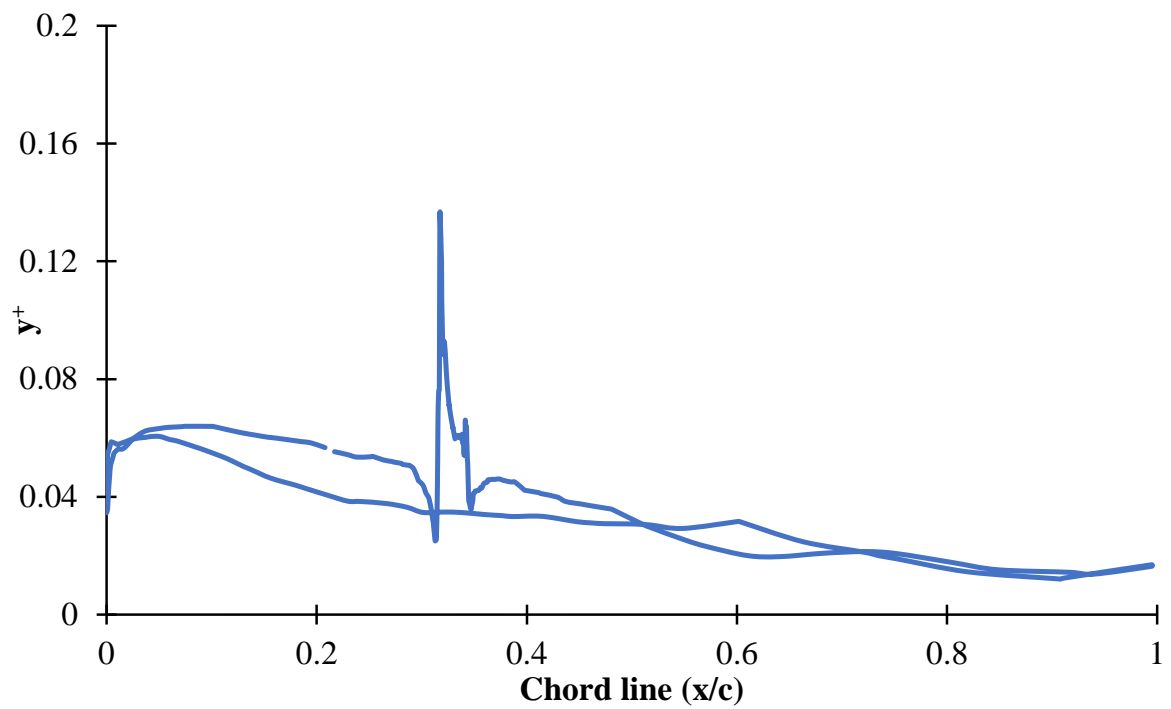


Figure 25: The  $y^+$  distribution of large-scale riblets validation

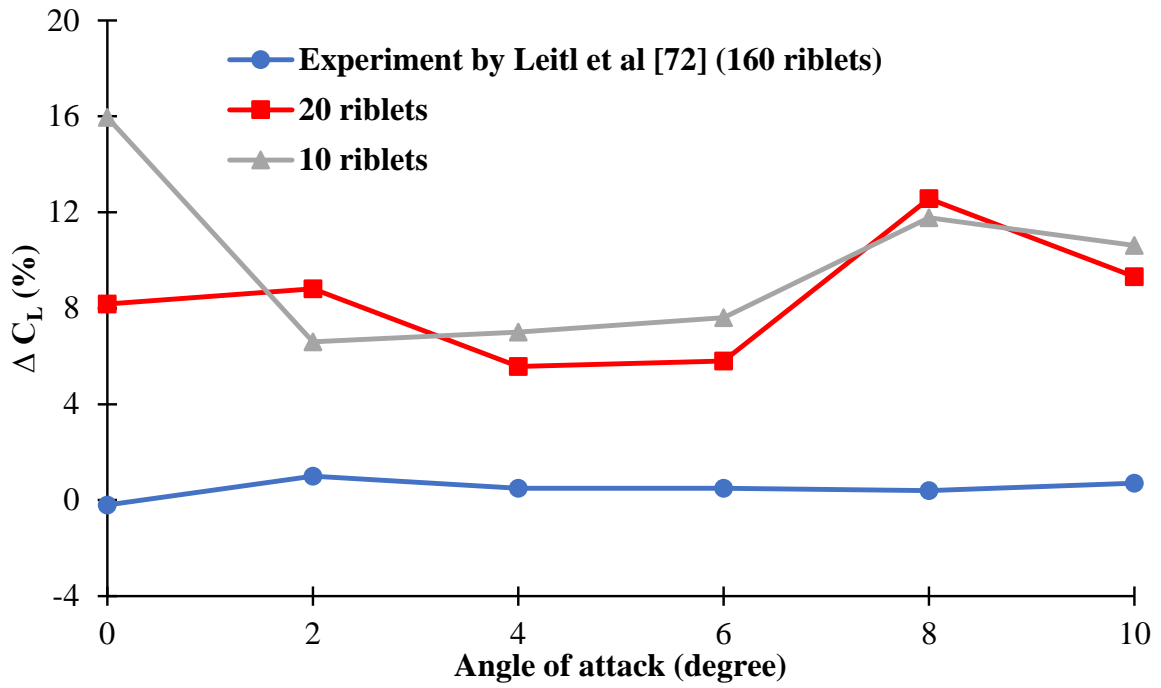


Figure 26: Lift coefficient difference versus angle of attack for validation case

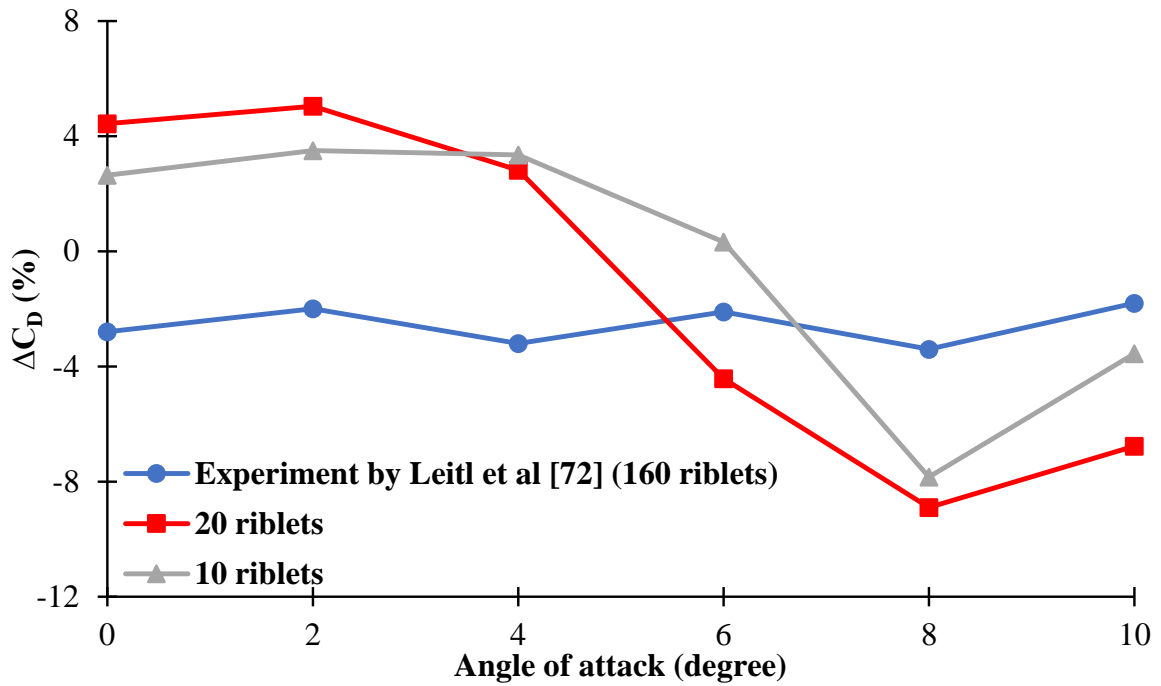


Figure 27: Drag coefficient difference versus angle of attack for validation case

## 5 TRIPPED STUDY CASES

The validation of smooth cases against experimental and computational works are shown in Appendix A. The smooth cases contain five study cases with different objectives. Study cases 2, 3 and 5 are compared to study cases 6, 7 and 8, respectively.

### 5.1 Study Case 6 (2D, URANS, S809, $Re_c = 6.5 \times 10^5$ , Riblet)

#### 5.1.1 Purpose

This study case is the same as study case 2 (section 8.2) in terms of computational settings. However, the difference between the two cases is that one riblet (step) on the upper aerofoil edge is created for study case 6. Study case 6 examines a riblet effect on 2D lift and drag coefficients and lift-to-drag ratio of S809 aerofoil. The effect of riblet on pressure and skin friction drags are also shown for further observation. Some flow physics are also shown.

#### 5.1.2 Geometrical setup

A tripped 2D S809 aerofoil is displayed in Figure 28. The riblet is created on the maximum node of the aerofoil upper edge with streamwise length of  $21mm$  and  $h^+ = hu_\tau/\nu = 67 - 69$ , where  $h = 1mm$ . The values of  $h^+$  are calculated based on the average wall shear stress of the tripped aerofoil. The riblet is viewed as a rectangular in a 2D flow. However, it is represented as triangular riblets in a 3D flow. In additions, the number of riblets in the 3D flow are much more than in the 2D flow and therefore, this might affect the results significantly. The fluid domain for this study case is the same as the fluid domain used in study case 2 (Figure 174).

#### 5.1.3 Mesh & computational setup

Figure 29 represents how drag coefficient changes as mesh elements number change at AOA of  $\alpha = 0^\circ$ . A mesh of about  $1.26 \times 10^5$  elements is selected, as the result becomes independent

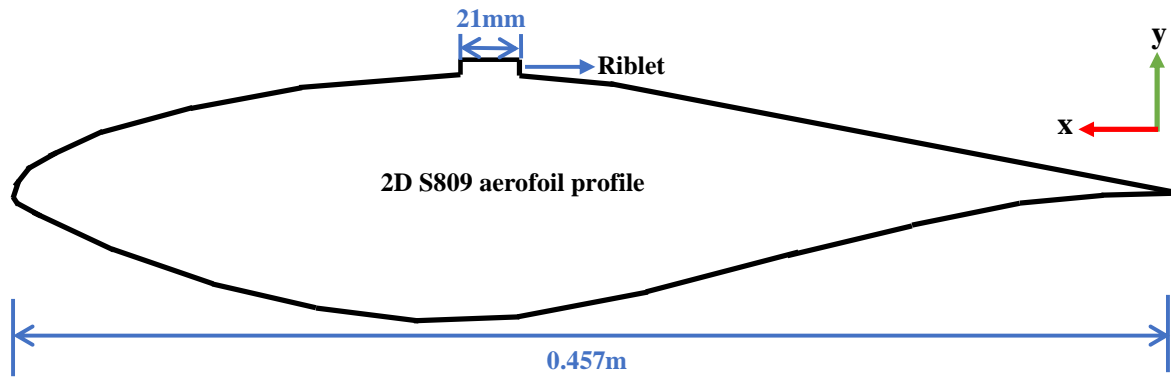


Figure 28: A tripped 2D aerofoil geometry with riblet on the suction side (not to scale)

on mesh elements number. Figure 30 displays how the  $y^+$  changes with drag coefficient. The selected mesh has an average value of  $y^+ = 1.57$ . The mesh changes as the number of nodes changes. The mesh is refined in the normal and parallel directions of the flow. The selected mesh has 80 and 300 nodes in the normal and parallel directions to the freestream, respectively.

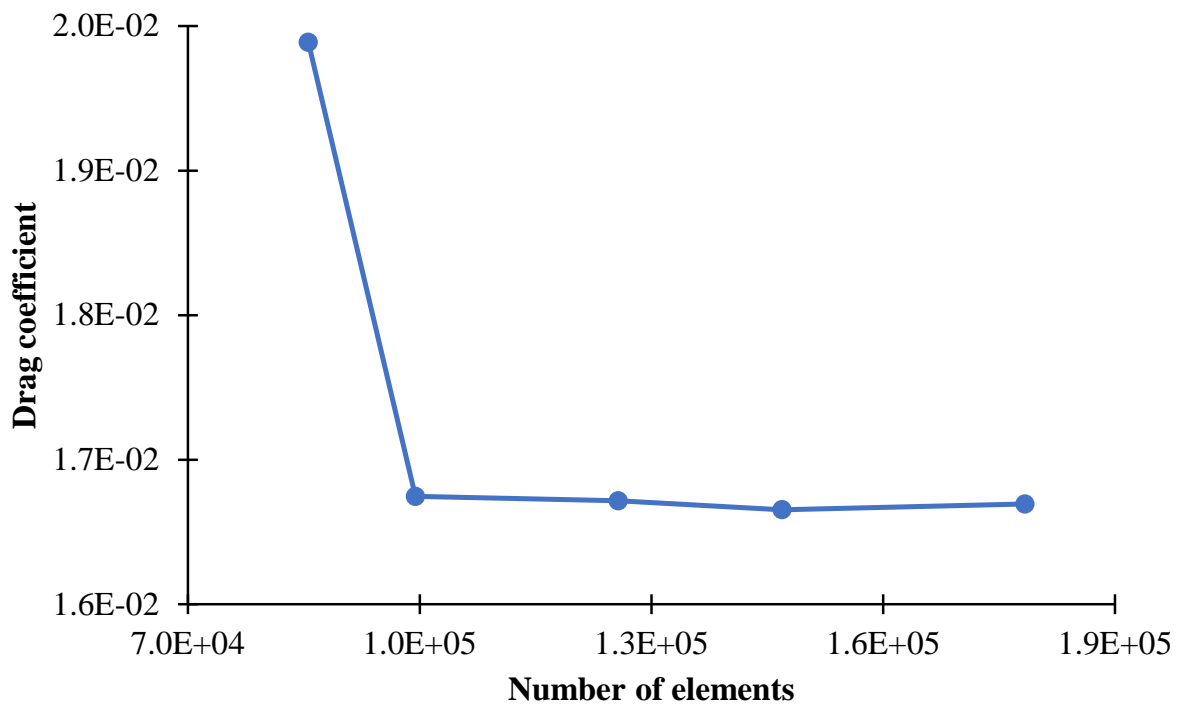


Figure 29: Mesh dependency for study case 6

The first layer of mesh above the aerofoil is placed at  $50\mu m$  and the aerofoil edge has about 400 nodes with 30 inflation layers and growth rate of 1.2. The step has 5 nodes on each vertical edge and 50 nodes on the top edge. The mesh metric of this study case for skewness

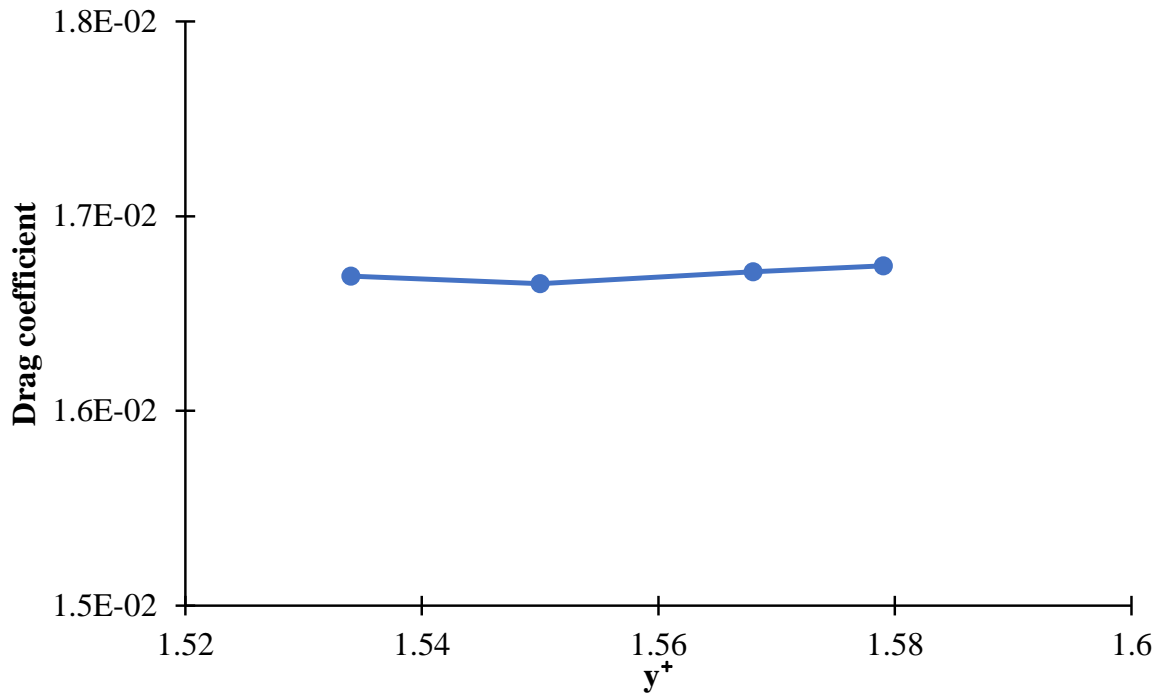


Figure 30:  $y^+$  values for different meshes of study case 6

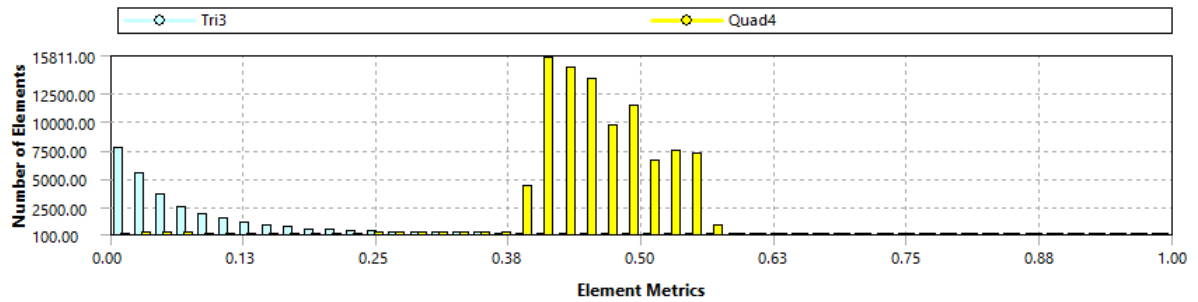


Figure 31: The skewness of study case 6

and orthogonality are shown in Figures 31 and 32, respectively. The generated mesh of the fluid domain and aerofoil are shown in Figures 179-182. The generated mesh of the step is visualised in Figures 33 and 34. The simulation settings for this study case are displayed in Table 38.

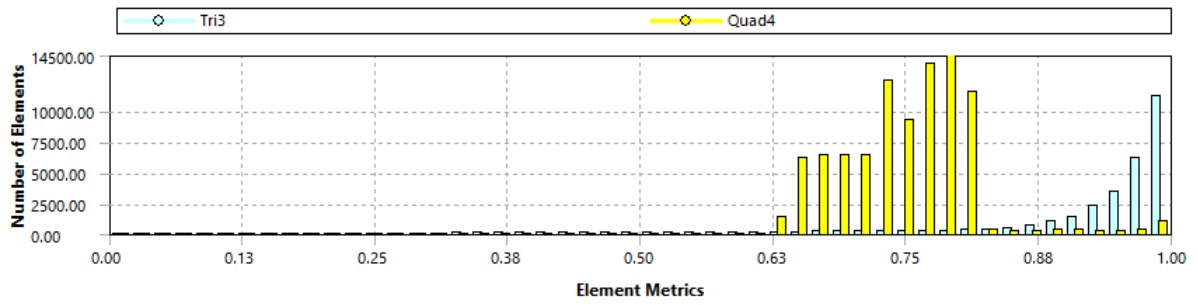


Figure 32: The orthogonality of study case 6

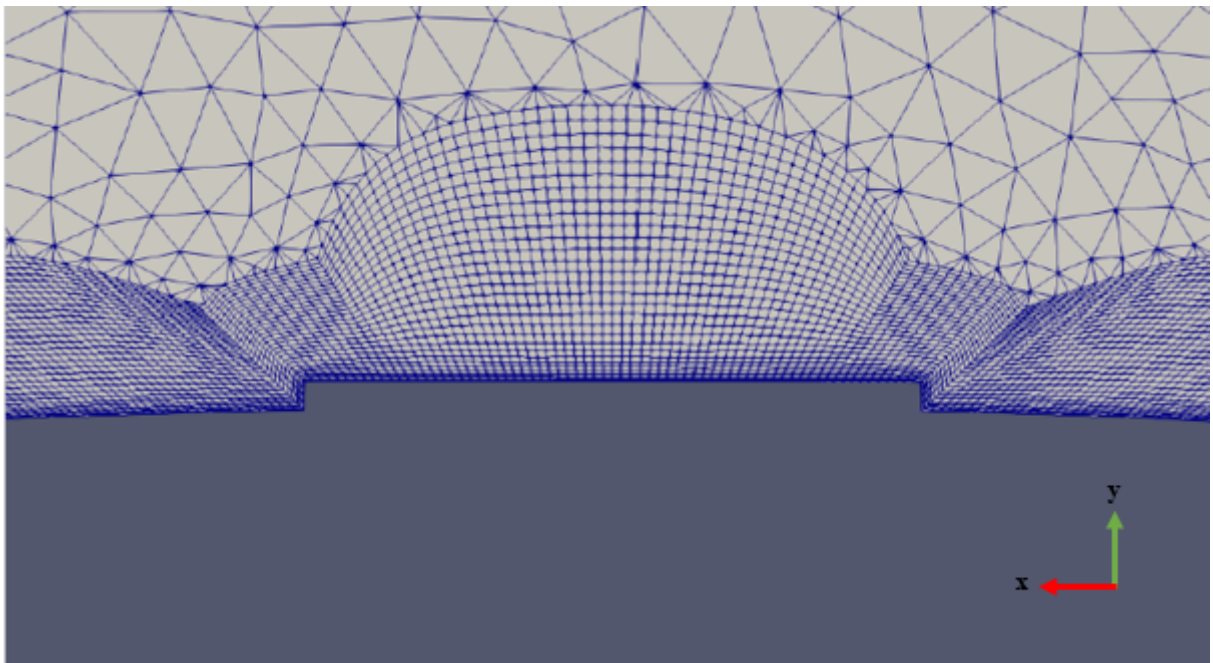


Figure 33: Mesh visualisation of the riblet (study case 6)

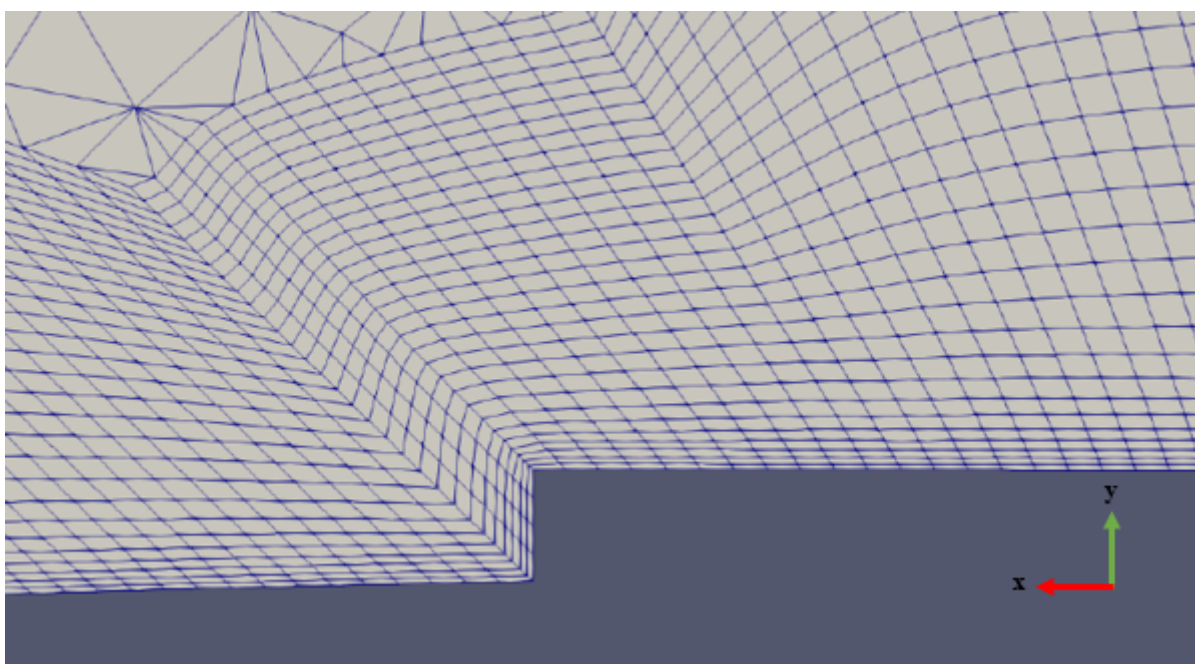


Figure 34: Mesh visualisation of the riblet tip (study case 6)

### 5.1.4 Results & discussion

The convergence history of the lift coefficient is shown in Figure 35. At about 2000 iterations, the lift coefficient does not change as the simulation continues to run therefore, study case 6 is converged. The  $y^+$  distribution along the chord line of the aerofoil is displayed in Figure 36. The values of  $y^+$  at different aerofoil locations are below 3, which means the generated mesh is able to resolve the viscous sub-layer.

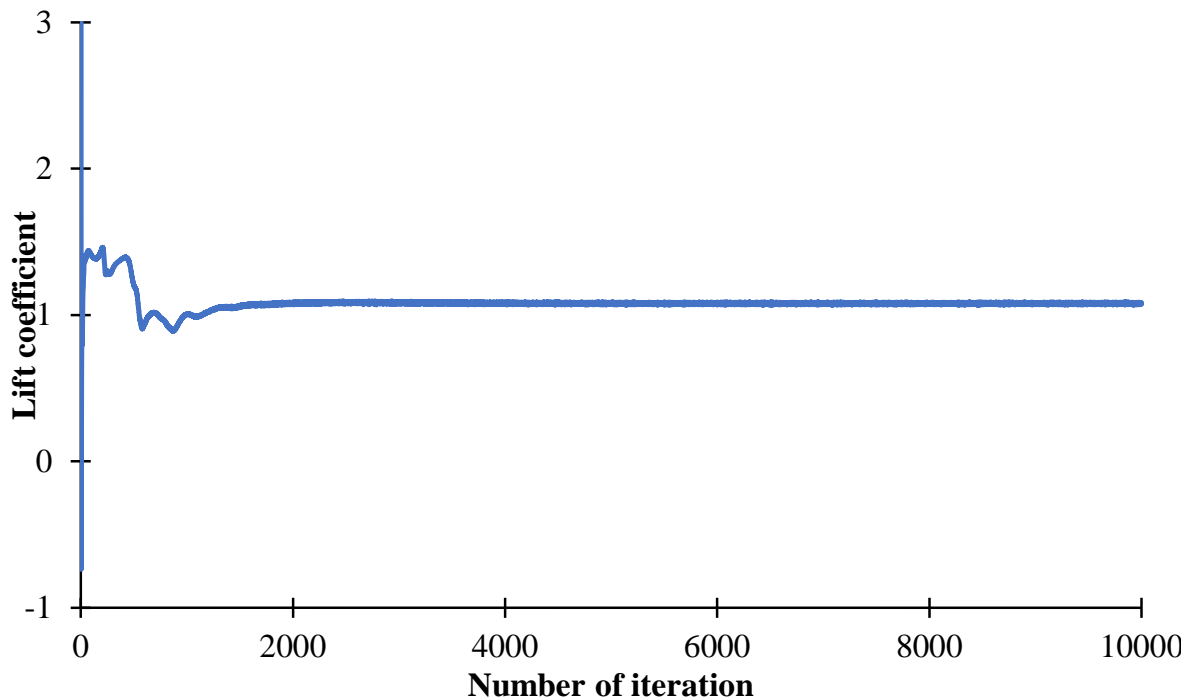


Figure 35: The convergence history of study case 6

The simulation settings for this study case is the same as the simulation settings that used in study case 2. Therefore, the *SST*  $k - \omega$  turbulence model is used for this computational study case. The computed smooth aerofoil's force coefficients are validated against experiment and compared computationally in section 8.2.4. Based on this experimental validation, the computed tripped lift and drag coefficients for a range of AOAs are confidently compared to the smooth aerofoil of study case 2 at wind speed of  $26m/s$ .

Figures 37 and 38 show a comparison of the clean and modified aerofoils' lift and drag coefficients versus various AOAs, respectively. Broadly, no improvement is recorded at all available AOAs for both forces. Table 2 shows the comparison of tripped and clean aerofoils in terms of the difference percentage of lift-to-drag ratio. The minus sign means that the

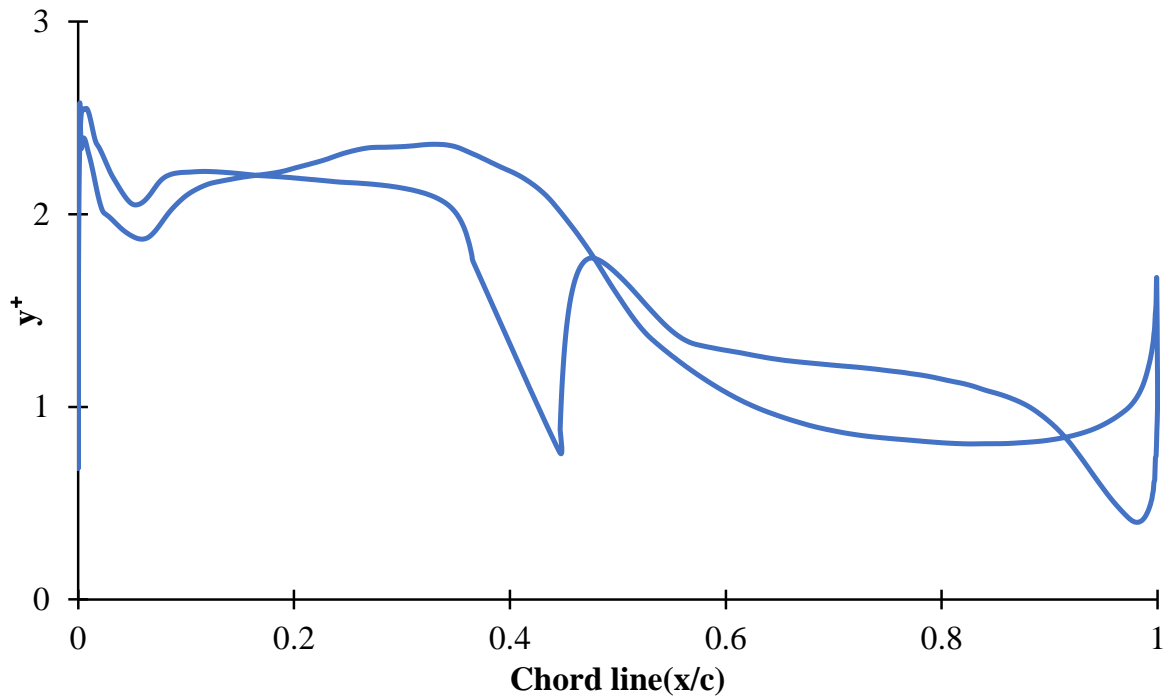


Figure 36: The  $y^+$  distribution of study case 6

existence of riblet on the 2D aerofoil negatively affect the aerofoil forces. At AOA of  $\alpha = 12^\circ$ , the maximum decrease in lift-to-drag ratio's difference percentage is recorded.

This massive decrease in the tripped aerofoil forces is believed due to two reasons. First, the mechanism of drag reduction by riblets is to force streamwise vortices to only occur on a small wetted area limited by riblet tips and allow low flow velocity to act on riblets valleys. This obviously cannot be achieved at this stage as this is a 2D problem therefore, no drag or lift force improvement is observed. Second reason is that the spanwise length of riblets is limited in 2D flow, which can affect the results. Increasing the length in spanwise direction requires multiple riblets to be created. Consequently, improvement will be significant, and obviously this only can be done in a 3D flow.

Tables 3 and 4 display the pressure and skin-friction drag coefficients, respectively for the clean and unclean aerofoils. Both tables also show the comparison between the two aerofoils in terms of the percentage error. Two observations about both aerofoils can be concluded from Tables 3 and 4. First observation is about the effect of riblet on both pressure and skin-friction drags, that riblet is able to reduce the skin-friction drag, while the pressure drag is raised. This is because applying riblet on the upper aerofoil edge will make the aerofoil larger in size, and therefore blocking the air flowing.

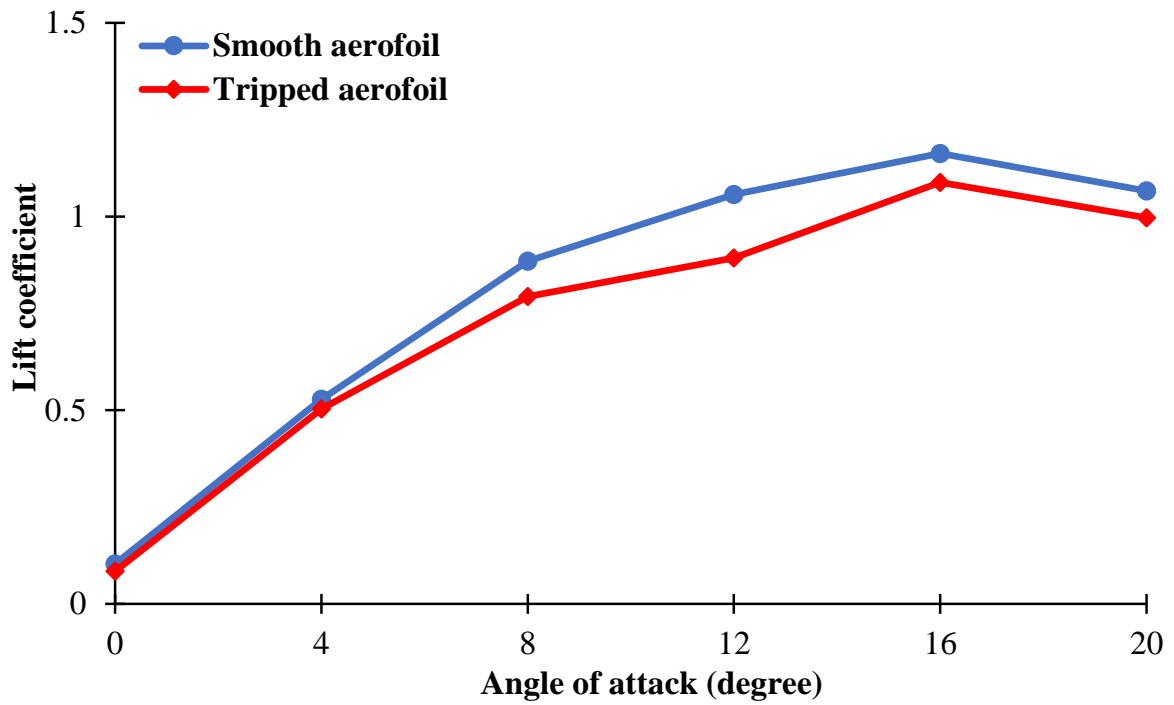


Figure 37: Comparison of the smooth and tripped aerofoils' lift coefficient against angle of attacks

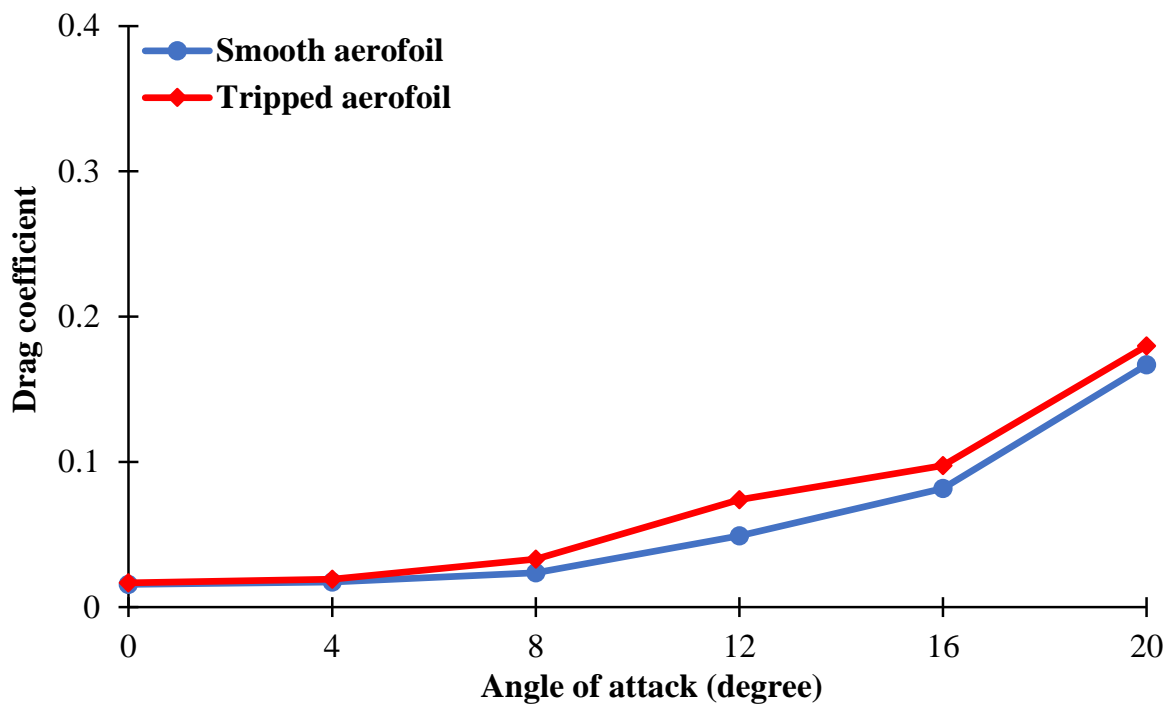


Figure 38: Comparison of the smooth and tripped aerofoils' drag coefficient against angle of attacks

Table 2: Lift-to-drag ratio increase comparison with the 2D smooth aerofoil

AOA	Tripped aerofoil
0°	−23.6%
4°	−14.2%
8°	−35.6%
12°	−43.9%
16°	−21.6%
20°	−13.3%

Another observation is that higher AOAs will increase the pressure drag for smooth and tripped aerofoils due to changing their position in reference to the direction of wind. This means both aerofoils act as an obstacle and prevent air flowing toward the desired direction. Although, the skin-friction is reduced by the existence of riblet, the total drag of the tripped aerofoil is increased compared to the smooth aerofoil due to a large rise in the pressure drag. Consequently, in a 2D flow, riblet negatively affect the lift-to-drag ratio. Further analysis via flow physics pictures will be shown.

Table 3: Pressure drag coefficient for the smooth and tripped aerofoils

AOA	Smooth aerofoil	Tripped aerofoil	Difference
0°	0.0061	0.0079	29.9%
4°	0.0077	0.0107	38.3%
8°	0.0151	0.0255	69.1%
12°	0.0419	0.0677	61.5%
16°	0.0756	0.0917	21.3%
20°	0.1624	0.1758	8.22%

The pressure contour of the smooth case (study case 2) and tripped case (study case 6) are shown in Figures 39 and 40, respectively. The step increases the pressure of the upper edge of the aerofoil leading to increasing the pressure drag and reducing the lift force compared to the smooth aerofoil. The wall shear stress of the smooth case and tripped cases are displayed in

Table 4: Skin-friction drag coefficient for the smooth and tripped aerofoils

AOA	Smooth aerofoil	Tripped aerofoil	Difference
0°	0.0095	0.0088	-8.00%
4°	0.0095	0.0085	-10.8%
8°	0.0087	0.0076	-12.4%
12°	0.0073	0.0064	-12.1%
16°	0.0061	0.0058	-4.86%
20°	0.0043	0.0041	-6.50%

Figure 41. The wall shear stress is higher for the tripped case. However, the wind velocity above the tripped aerofoil is increased due to the step, which leads to lower skin-friction drag, as shown in Table 4.

The velocity contour of the smooth and tripped cases is displayed in Figures 42 and 43, respectively. The velocity is reduced just before the step and then increased resulting in a higher velocity above the step compared to the smooth case at the same location. The velocity at 90% of the step length, for smooth and tripped cases, is shown in Figure 44. The velocity curve is shifted up due to the step and therefore, increases the flow velocity.

The velocity vector of the smooth and tripped aerofoils is shown in Figures 45 and 46, respectively. The velocity of the flow is clearly affected by the step. The step acts as an obstacle causing a flow separation just behind the step, as shown in Figure 47. The reduction in lift and increase in drag that are shown in Figures 37 and 38 are the result of the flow separation caused by the step.

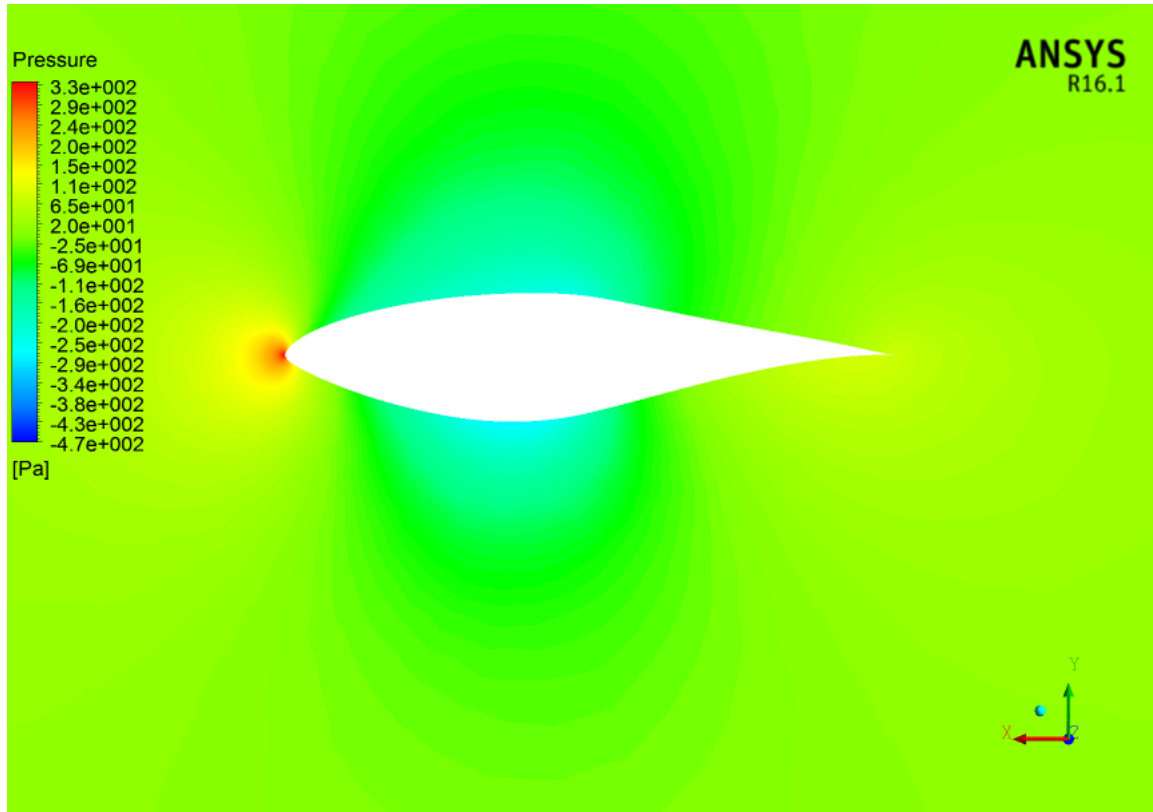


Figure 39: The pressure contour at  $\alpha = 0^\circ$  of the smooth case (study case 2)

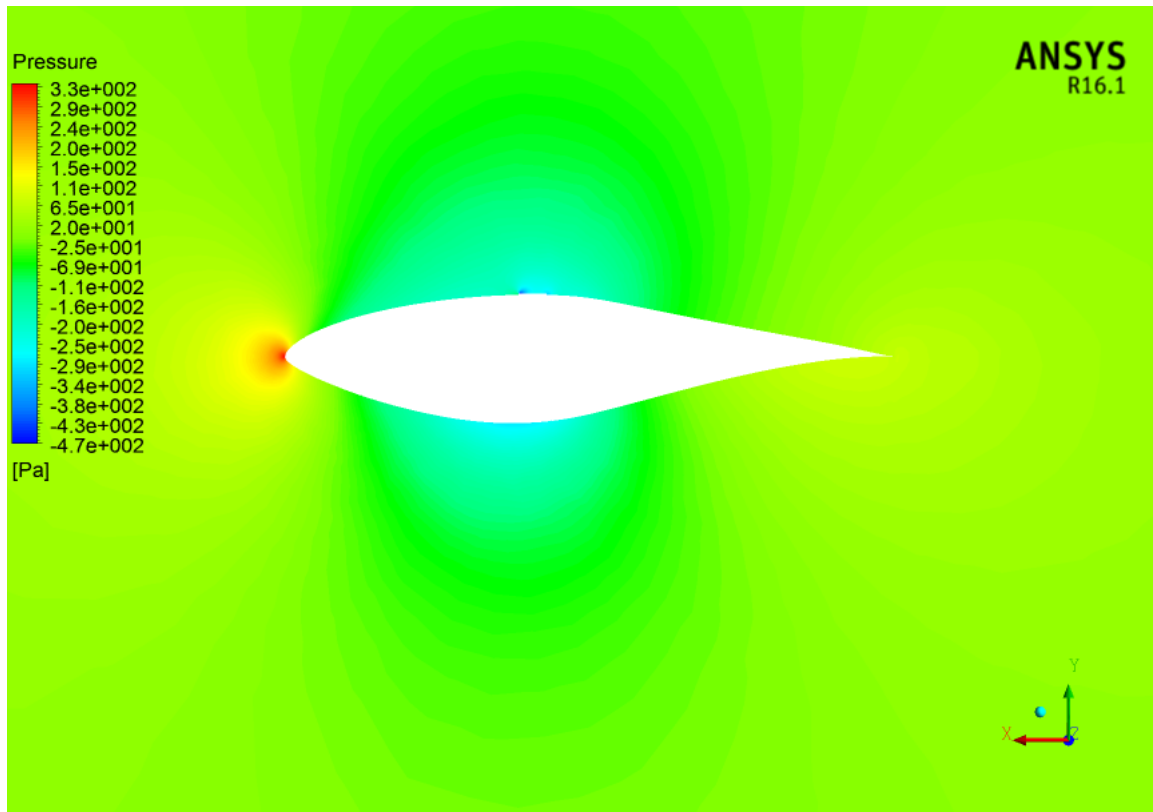


Figure 40: The pressure contour at  $\alpha = 0^\circ$  of the tripped case (study case 6)

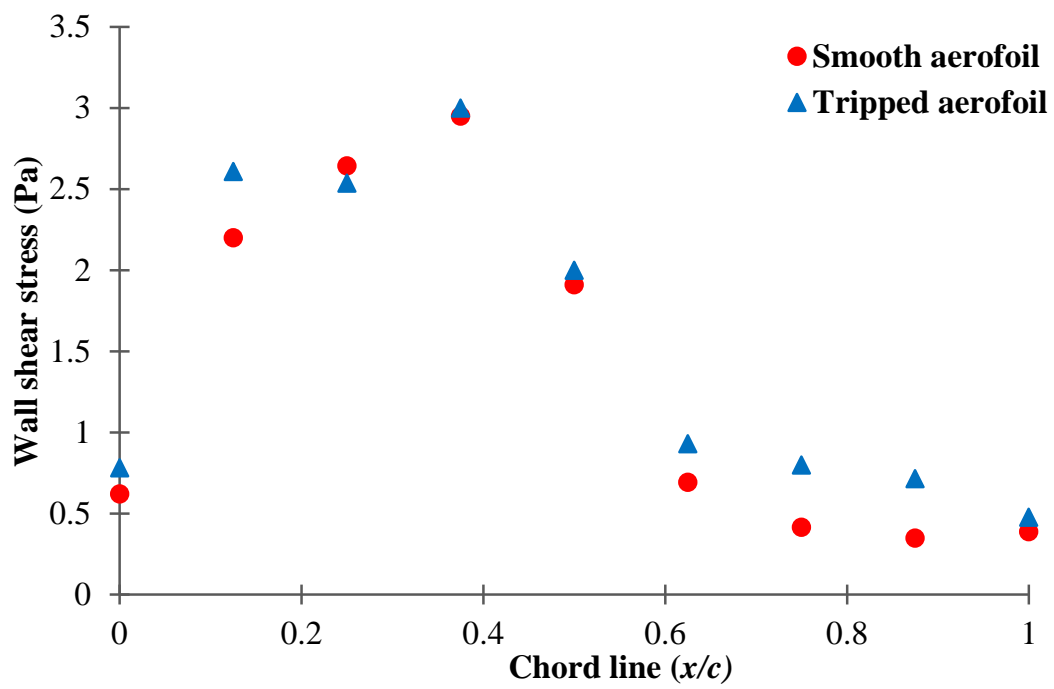


Figure 41: The wall shear stress of the smooth and tripped cases at  $\alpha = 0^\circ$

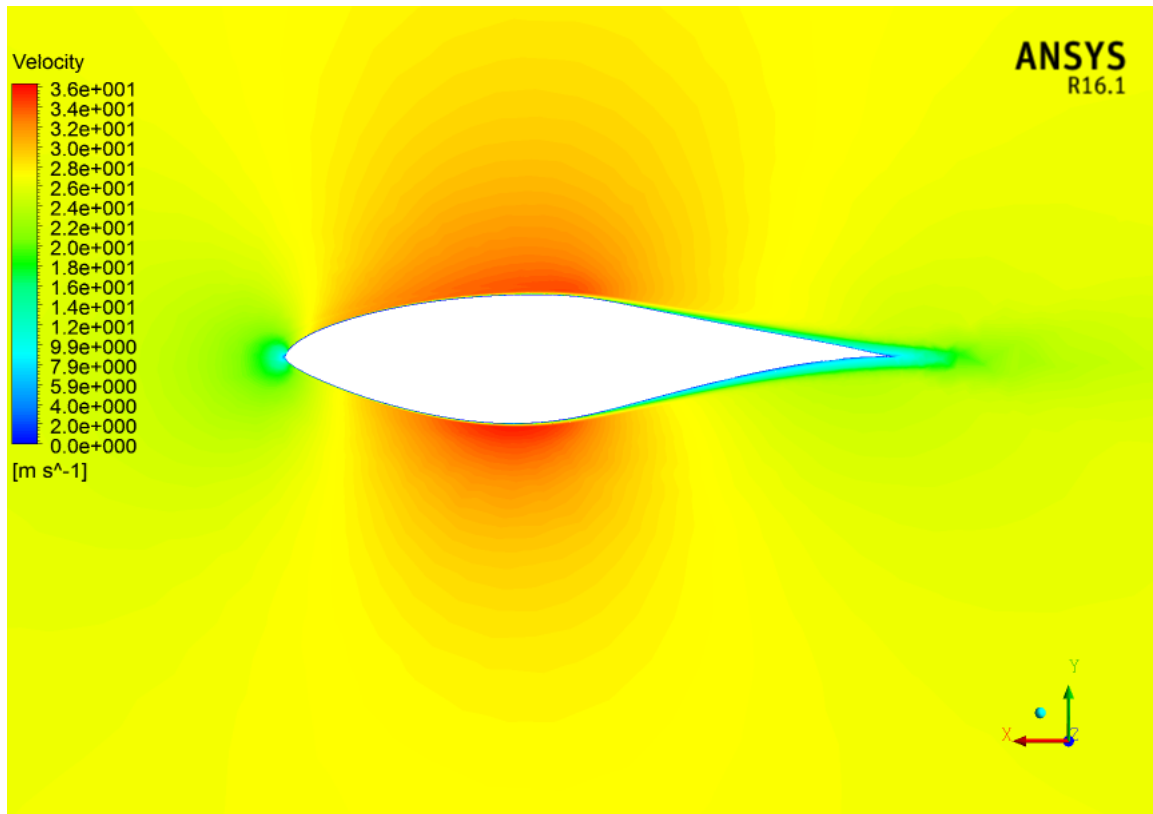


Figure 42: The velocity contour at  $\alpha = 0^\circ$  of the smooth case (study case 2)

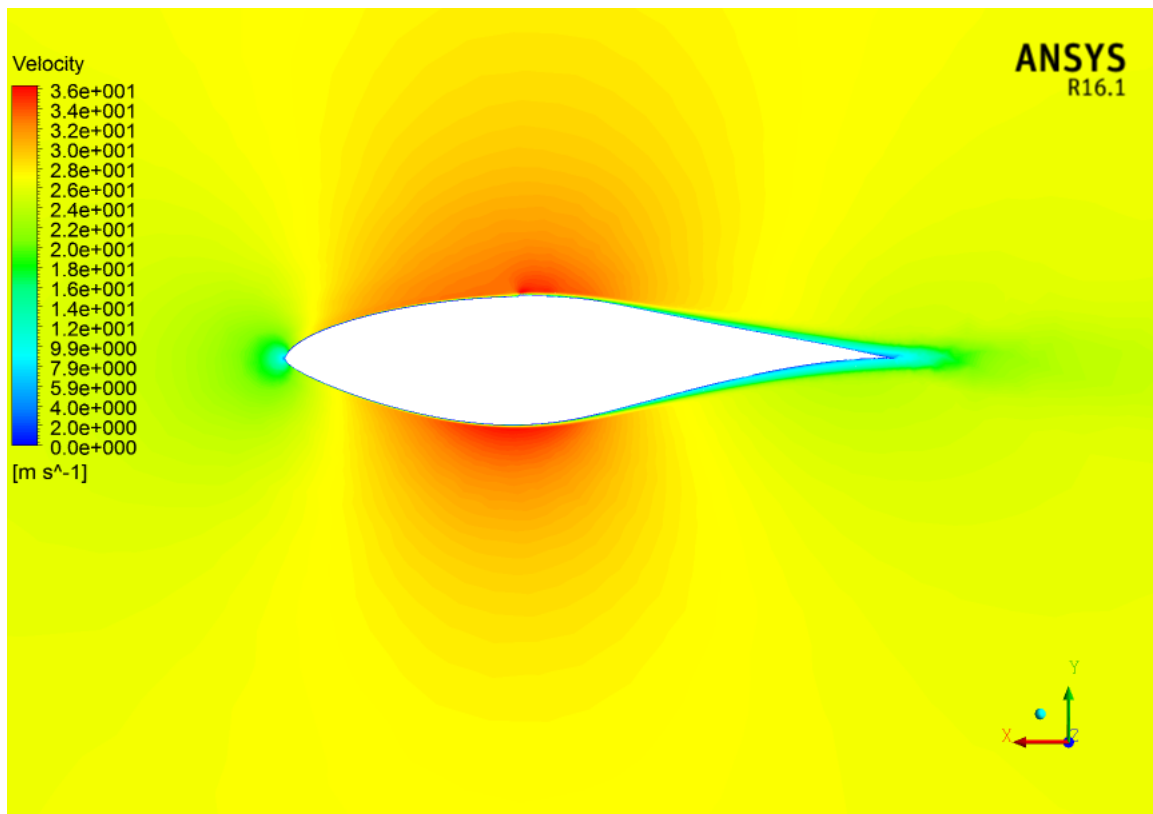


Figure 43: The velocity contour at  $\alpha = 0^\circ$  of the tripped case (study case 6)

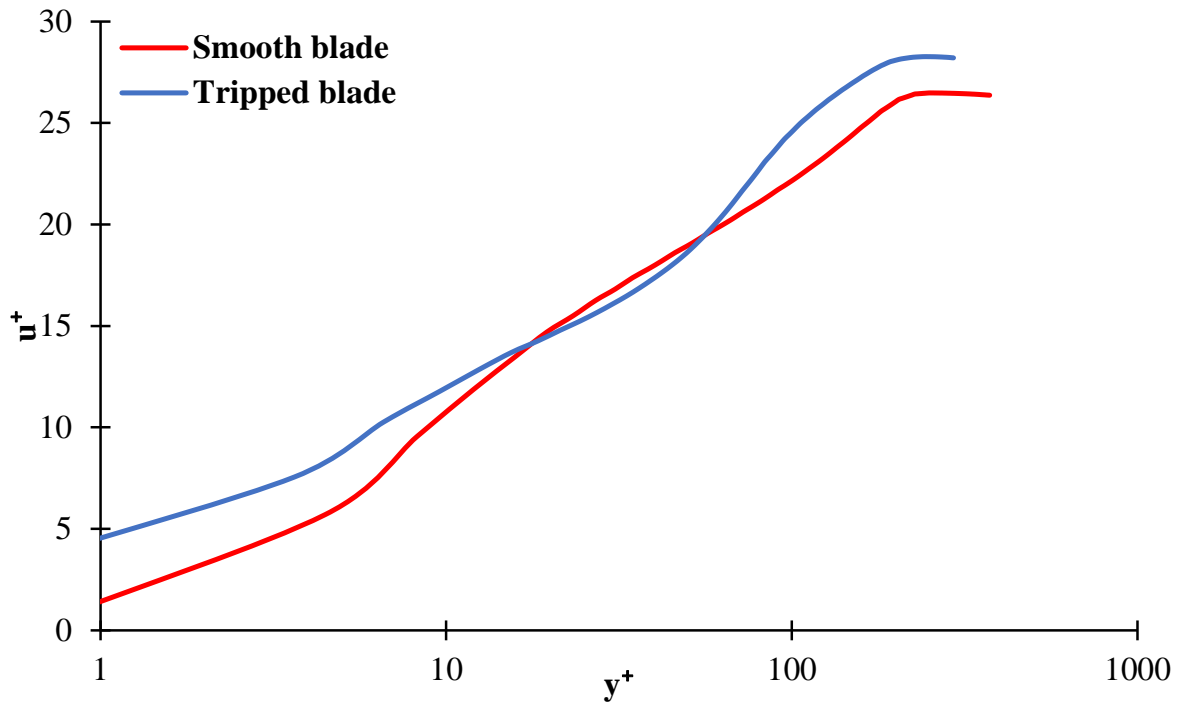


Figure 44: The velocity profile of the smooth and tripped cases at  $\alpha = 0^\circ$



Figure 45: The velocity vector at  $\alpha = 0^\circ$  of the smooth case (study case 2)

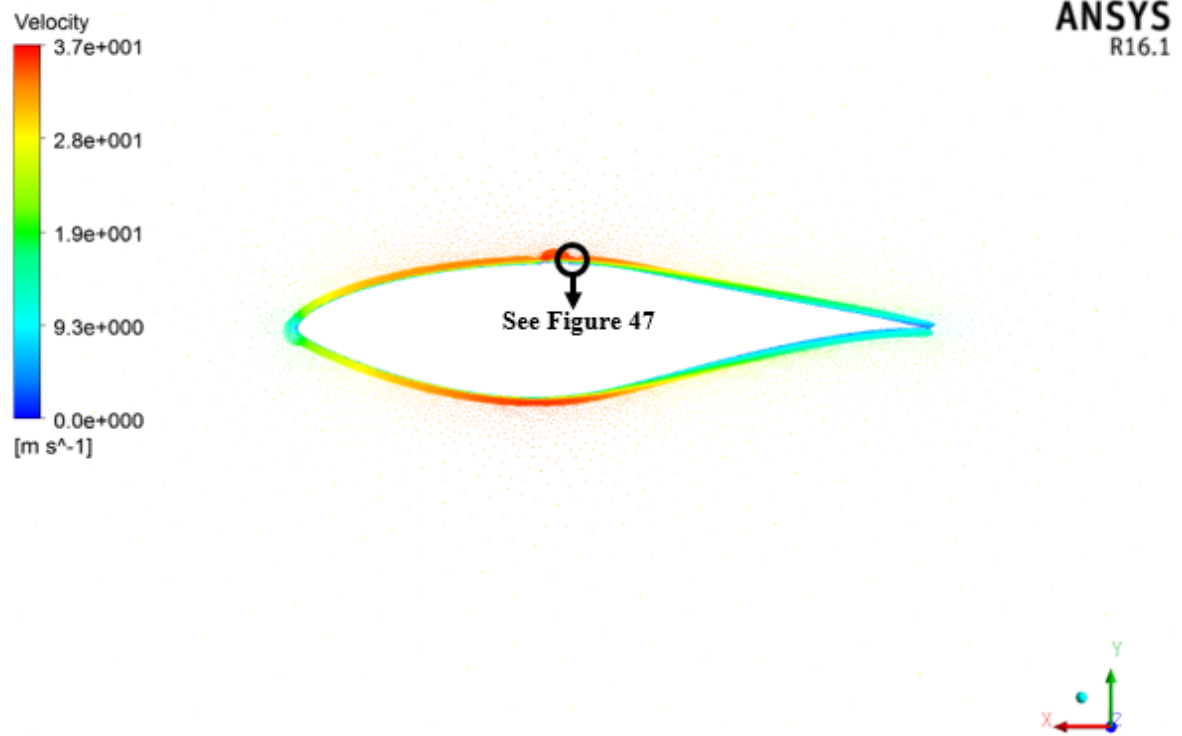


Figure 46: The velocity vector at  $\alpha = 0^\circ$  of the tripped case (study case 6)

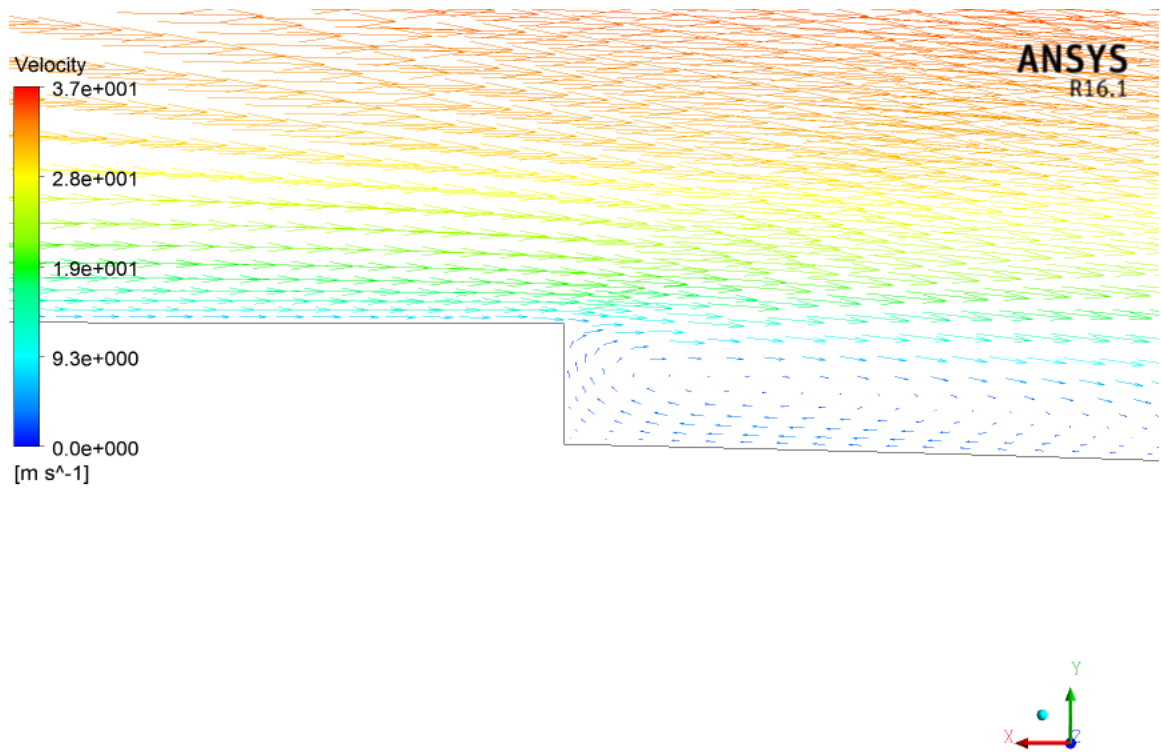


Figure 47: The velocity vector at  $\alpha = 0^\circ$  of the tripped case (zoom-in)

## 5.2 Study Case 7 (3D, URANS, S809, $Re_c = 6.5 \times 10^5$ , Riblets)

### 5.2.1 Purpose

The purpose of study case 7 is to observe the effect of applying riblets on the upper side of the fixed blade with S809 aerofoil profile. The process starts by applying three different configurations on the blade's suction side. The results (including: The aerodynamic coefficients, flow physics and turbulence statistic) of the tripped blade are compared to the smooth blade from section 8.3. Various wind speeds and changing number of riblets tests are then done, and the results are compared to the clean blade.

### 5.2.2 Geometrical Setup

The simulated fluid domain is the same as the conducted wind tunnel by Butterfield *et al.* [84], and it is already described in section 8.3.2, as seen in Figure 187. The dimension of the blade with S809 aerofoil profile that used is already illustrated in section 8.3.2, as seen in Figure 188. The boundary conditions are as following: lateral and vertical faces of the fluid domain as well as the blade are assumed as stationary with no slip wall. The rest of faces are velocity inlet and pressure outlet, as displayed in Figure 187.

As previously described in study case 3 (section 8.3.2), the simulated fixed blade is divided into three parts, as seen in Figure 188. The riblets are only applied onto the small section of the middle part. However, riblets could have been placed in any upper blade region because the air attacks the whole blade at the same angle. Figure 48 shows the blade with riblets configuration.

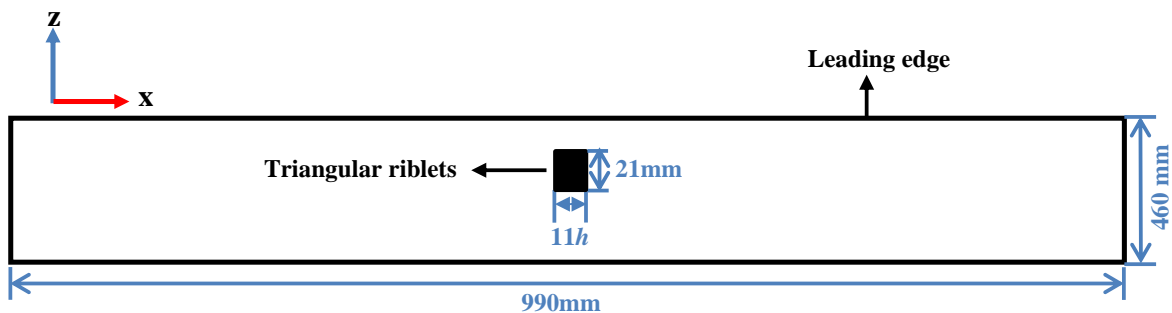


Figure 48: The top view of the simulated blade with employed riblets for study case 7 (not to scale)

Six triangular riblets with three different riblet configurations are separately created on the maximum node of the blade suction side. The maximum thickness of S809 aerofoil is located more towards the leading edge, as displayed in Figure 48. Referring to Table 45, riblets start at  $0.04664m$  and extends to  $0.04661m$  for a streamwise length of  $21mm$ . This means riblets start at about  $40\%c$  where flow is already separated, as previously shown in Figure 204. Figures 49 and 50 show the riblets' configuration.

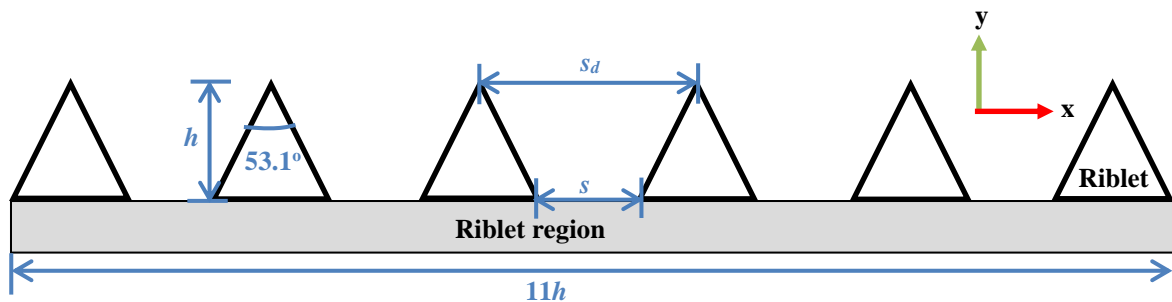


Figure 49: Triangular riblets' configuration for fixed blade

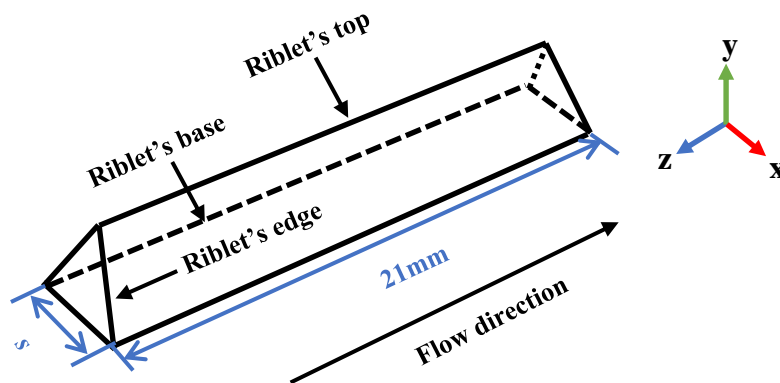


Figure 50: Riblets' configuration (side view)

As mentioned previously in section 3.4, all the simulated cases for the fixed blade assume that each riblet height equals the space between two riblets ( $h = s = 0.5s_d$ ), as shown in Figures 49 and 50. However, particularly for study case 7, zero space configuration is already attempted, but unfortunately the simulation process diverged. Table 5 shows the three riblet configurations with details in the wall units.  $l^+$  is preferable for use in further studies, as it concerns the shape and size of the base of riblets.

According to Table 5, the configurations of this work are considered as large-scale riblets, and those in the previous work are considered as small-scale ones. This is because this

work's riblets are beyond the range of  $s^+$  that were used in experiments undertaken by other researchers. The previous riblets' scale is up to  $s^+ = 40$ . However, this work's range of riblets is between 120 and 750 for  $s^+$ , while  $h^+$  is between 60 and 375. One interesting conclusion could be to follow the increase of riblets' size on changing the lift force, so not only altering the drag force as previously reported.

Table 5: Wall unit for each riblets' configuration

Riblets configuration	$h$	$h^+$ $h^+ = hu_\tau/\nu$	$s^+$ $s^+ = s_d u_\tau/\nu$	$l^+$ $l^+ = A_b^{\frac{1}{2}} u_\tau/\nu$
Configuration I	3mm	260 – 375	520 – 750	319 – 460
Configuration II	1mm	85 – 122	170 – 244	104 – 157
Configuration III	0.7mm	60 – 87	120 – 174	74 – 106
Sareen <i>et al.</i> [46]	44 – 150 $\mu$ m	-	-	-
Chamorro <i>et al.</i> [47]	40 – 225 $\mu$ m	-	-	10
Sidhu <i>et al.</i> [48]	44 – 152 $\mu$ m	-	-	-
Choi <i>et al.</i> [61]	-	10 – 34	20, 40	-
Bechert & Bartenwerfer [63]	-	-	5 – 40	5 – 20
Launder & Li [68]	-	0 – 50	-	-
Chu & Karniadakis [69]	-	17, 18	17, 20	-

### 5.2.3 Mesh & computational setup

Based on the validation of the smooth blade in section 8.3.4 against experimental results, this study case's mesh confidently employs the same mesh method used in study case 3. This means the mesh maximum and minimum element sizes are the same for both cases. This is because there is no experimental or computational references to validate the mesh for the tripped blade with S809 aerofoil profile.

Regarding meshing of riblets, different mesh studies are carried out for riblet's edges and bases. The following mesh study is for riblet configuration II however, the mesh of all simulated riblet configurations are studied in the same procedure.

- **The mesh resolution of riblet in normal direction.** The number of inflation layers above the riblet are studied as shown in Table 6.

Table 6: Number of inflation layers above the riblets

No. layers	$C_L$
10	1.31
20	1.14
30	1.14

- **Number of nodes on each base and top of riblets.** The riblets are simulated using different number of nodes on each base and top of the triangular riblets in the chordwise direction, as shown in Table 7.

Table 7: Number of nodes on each base and top of riblets

No. nodes	$C_D$
21	0.121
31	0.119
51	0.118

- **Number of nodes on each edge of riblets.** The riblets are simulated using different number of nodes on each edge of the triangular riblets, as shown in Table 8.

Table 8: Number of nodes on each edge of riblets

No. nodes	$C_D$
5	0.124
8	0.119
11	0.122
14	0.122

From Tables 6, 7 and 8, the number of nodes on each riblet’s edge, top and base are 11, 31 and 31 respectively and 30 inflation layers above the riblets are selected for meshing of riblet configuration II. The first layer of mesh is place at  $50\mu m$  with growth rate of 1.2 to be able to resolve the viscous sub-layer. Table 9 show the number of nodes in all directions of riblet for each riblet’s configuration. The mesh metric of this study case for skewness and orthogonality are shown in Figures 51 and 52, respectively. The generated mesh of the blade and riblets are displayed in Figures 53-56.

Even though the mesh minimum and maximum element sizes are the same for both smooth and tripped blades, the number of mesh elements for each case is not the same. This also applies to all simulated tripped cases due to the difference in riblet’s configurations. Table 10 shows the number of triangular mesh faces on the surface of the smooth and tripped blades, including all different riblets’ configurations. However, the number of the triangular mesh faces for the fluid domain is not included in Table 10.

Table 11 shows the total number of the mesh elements for all different simulated riblet configurations. The shown mixed mesh cells include all the tetrahedral elements as well as the wedge elements. Therefore, Table 11 represents the exact number of elements for each simulation. From Tables 10 and 11, the existence of riblets requires more mesh cells to be generated. The larger riblet’s height, the more mesh elements are needed. The simulation settings for this study case are displayed in Table 39.

Table 9: Meshing for each riblets’ configuration

Meshing of riblets	Configuration I	Configuration II	Configuration III
No. nodes on base & top	31	31	31
No. nodes on edge	21	11	8

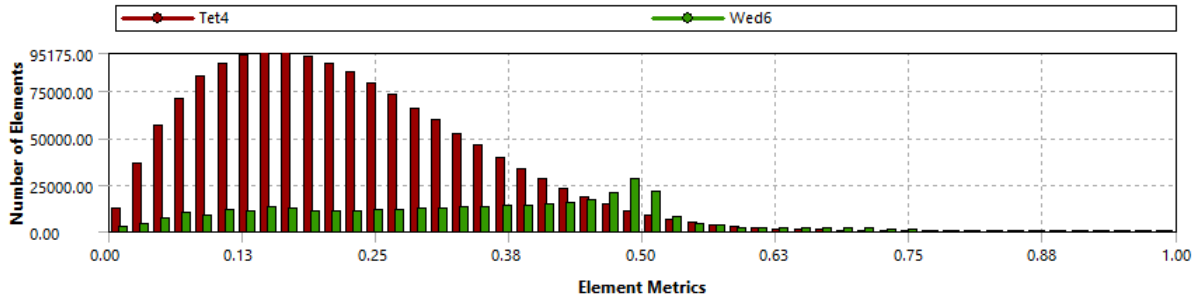


Figure 51: The skewness of study case 7

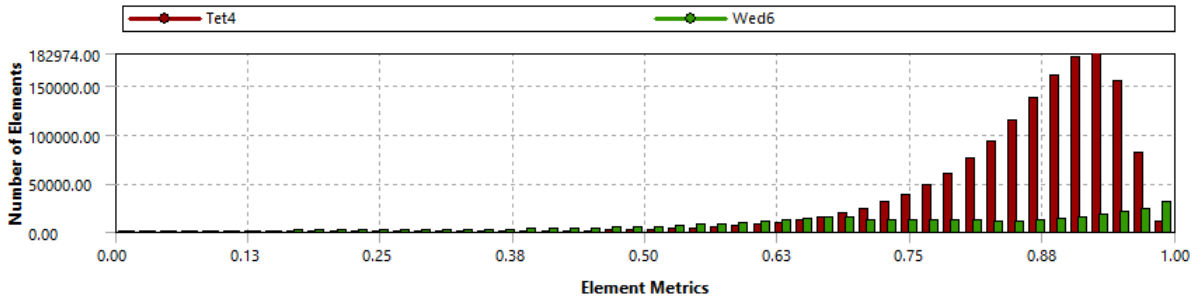


Figure 52: The orthogonality of study case 7

Table 10: Total number of mesh (triangular faces)

Configurations	Number of triangular mesh faces
Smooth blade	13,410
Configuration I	21,204
Configuration II	19,000
Configuration III	18,156

Table 11: Total number of mixed cells

Configurations	Number of mixed cells
Smooth blade	1,483,050
Configuration I	2,124,955
Configuration II	1,879,532
Configuration III	1,772,393

ANSYS  
R16.1

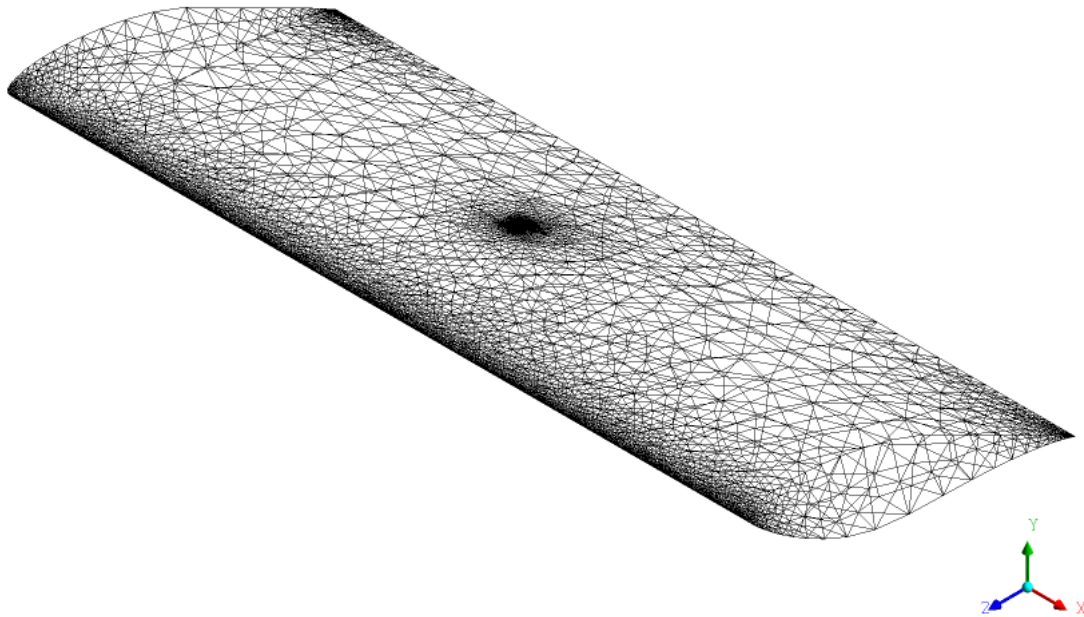


Figure 53: The generated mesh of riblets and tripped blade for case 7

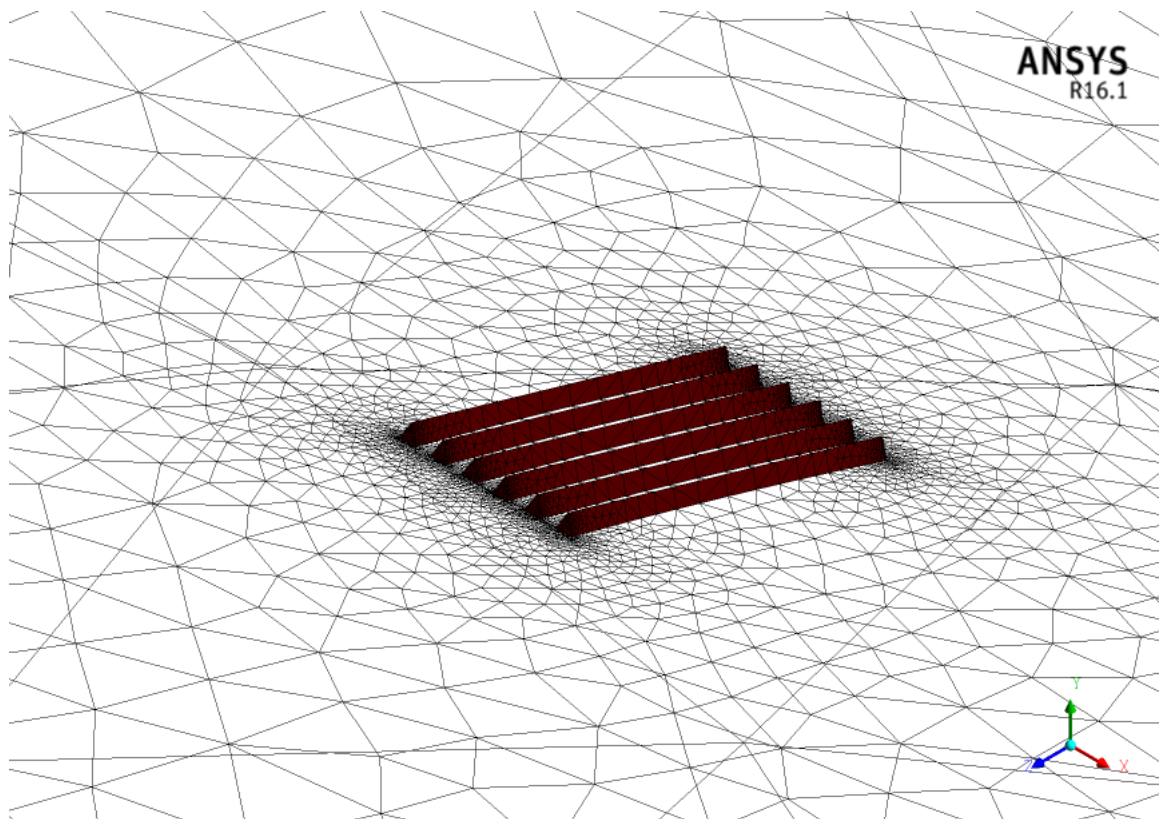


Figure 54: The generated mesh of the riblets on the blade for case 7

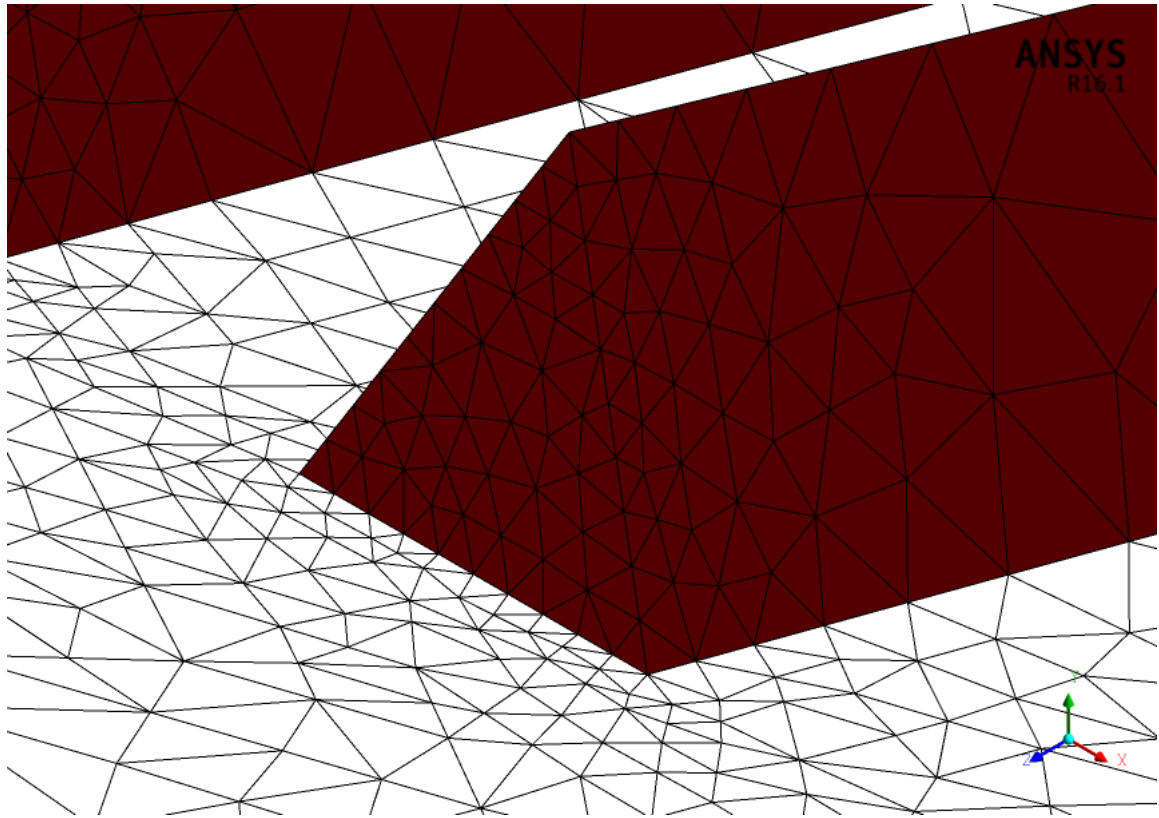


Figure 55: The generated mesh of the riblets for case 7

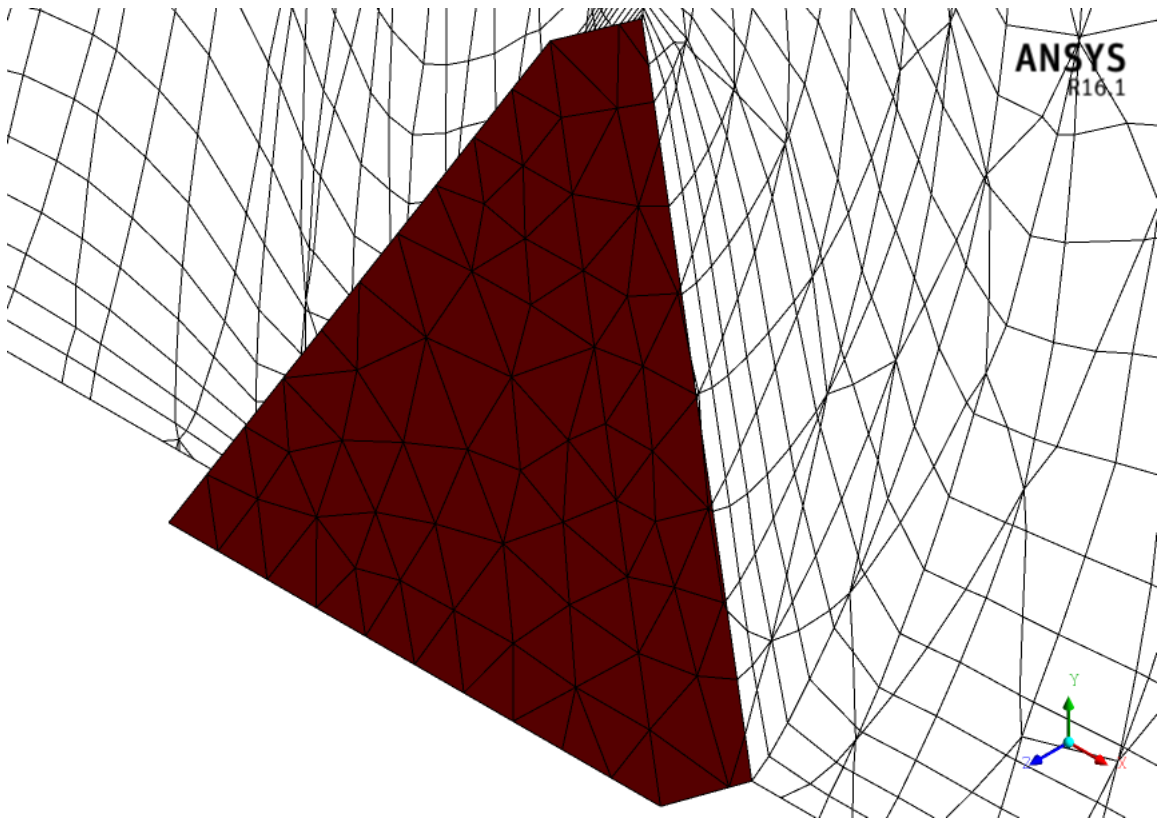


Figure 56: The generated mesh of riblet with inflation layers for case 7

### 5.2.4 Results & discussion

The simulated time of the lift coefficient for study case 7 is shown in Figure 57. The calculation of the aerodynamic coefficients is based on calculating the average of the last circle of the simulated time, as shown in Figure 57. The  $y^+$  distribution along the chord line of the blade's cross section at 50% span is displayed in Figure 58. The values of  $y^+$  at different locations are below 3, which means the generated mesh is able to resolve the viscous sub-layer.

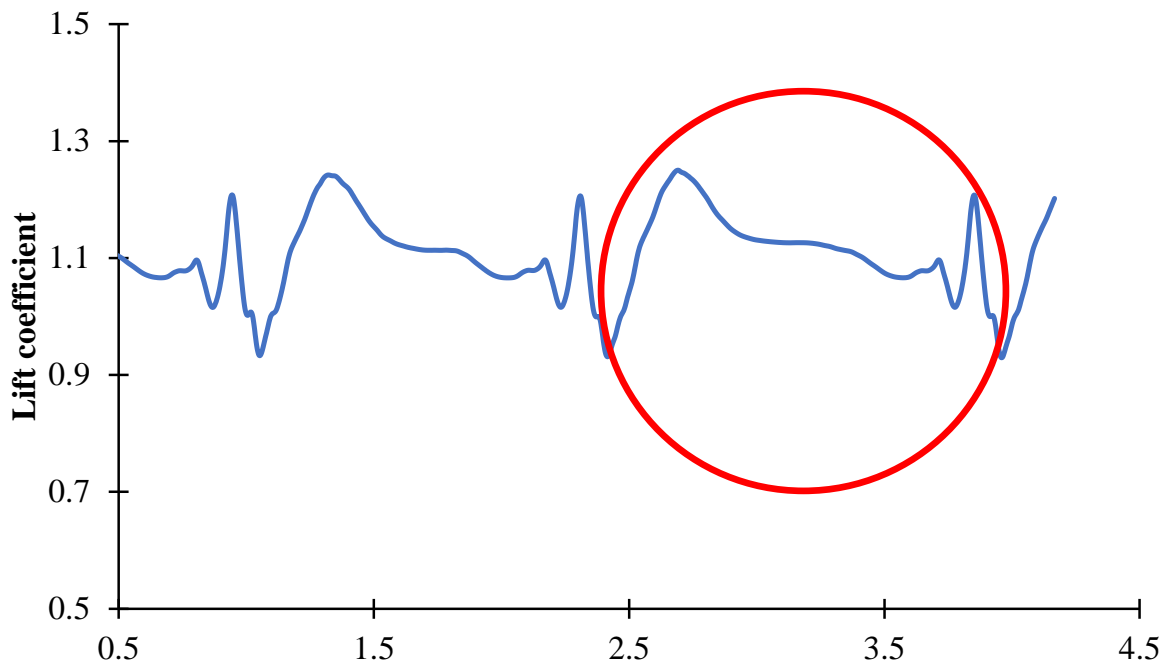


Figure 57: The simulated time of study case 7

Three separate examinations (different riblet configurations, wind speeds and number of riblets) are carried out for the tripped blade at different AOAs. The computed results of the unclean blade is compared to the smooth one from section 8.3.4. Each simulation is firstly run as a steady state for 10000 iterations to ensure solution stability. Then it is simulated as a transient state with time step of  $0.002s$ . The simulation is run using 40 processors with assistance of supercomputer, and it is approximately lasted for 5 hours per case.

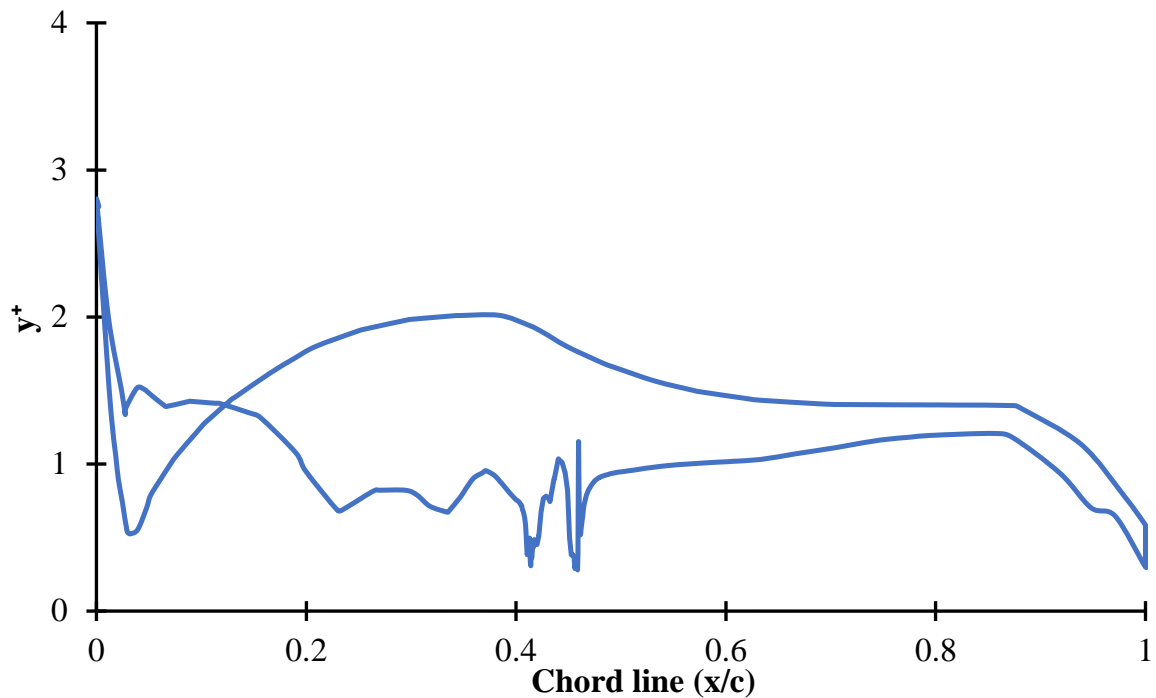


Figure 58: The  $y^+$  distribution of study case 7

- **Different riblet configurations.**

Three different riblet configurations are simulated separately at a wind speed of  $26\text{m/s}$  to observe the riblets' effect on increasing lift, reducing drag and increasing lift-to-drag ratio. Beside studying riblets' effect, they are simulated to conclude which riblet configuration performs better for a blade with S809 aerofoil profile. Therefore, the best riblet's configuration effect will be applied on the blades of the NREL phase II. The three simulated riblet configurations are already shown in Table 5.

Figure 59 displays the lift coefficient against AOAs for the smooth and tripped blades with different riblet configurations. At  $\alpha = 0^\circ$ , riblets' effect on the lift seems to be undesirable for all simulated riblets' configurations. However, the effect of riblets on increasing lift force is shown clearly at stall and post-stall AOAs for all simulated riblet's configurations. The best performance is obtained at stall ( $\alpha = 16^\circ$ ) for configuration I and II. Of all simulated riblet heights, Configuration III shows an increase in lift at wider range of AOAs.

Referring to Figure 60, the drag coefficient of the tripped and smooth blades is shown at different AOAs. At low AOAs ( $\alpha \leq 4^\circ$ ), the three configurations show a drag reduction. The maximum drag reduction is obtained at stall ( $\alpha = 16^\circ$ ) for configuration I. However, the maximum drag increase is also obtained for configuration I at  $\alpha = 8^\circ$ . At a wider range of

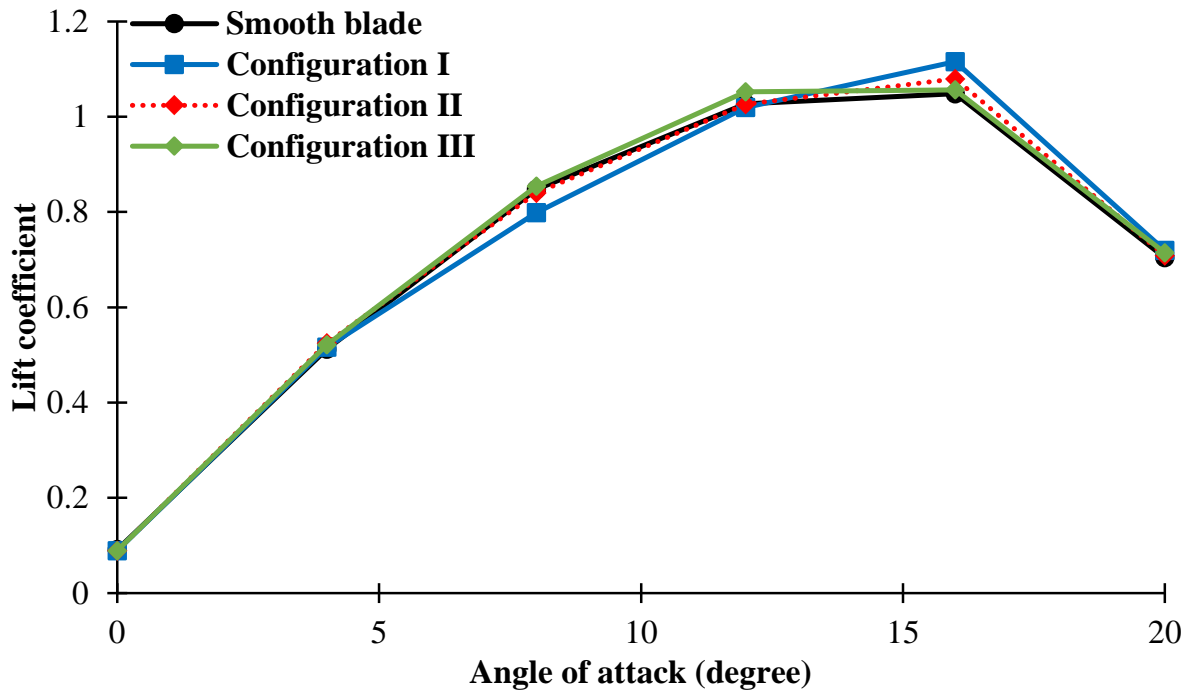


Figure 59: Lift coefficient versus AOAs for the smooth and tripped blades

AOAs, riblets' configuration II shows the best percentage of drag reduction compared to the other two configurations.

Lift-to-drag ratio of the tripped blades are also compared to the clean blade as shown in Figure 61. At AOA of  $\alpha = 4^\circ$ , the ratio is increased by riblets for all simulated riblet's configurations. However, the ratio starts to decrease at higher AOAs. At stall, the riblets are clearly able to increase lift-to-drag ratio for configurations I and II. Because configuration I shows a large decrease in lift-to-drag ratio at  $\alpha = 8^\circ$ , configuration II is considered the best configuration compared to the other two configurations.

Table 12 shows the percentage of increasing lift in comparison of different riblets' configurations with the clean blade at air velocity of  $26m/s$ . At  $\alpha = 0^\circ$ , the largest decrease in lift force is recorded for configurations II and III. However, the largest decrease of lift is obtained at  $\alpha = 8^\circ$  for configuration I. Increasing lift force by riblets hugely depend on the AOAs and configuration of riblets, such that the influenced of riblets can be clearly seen at high AOAs for all simulated riblets' configurations.

The drag reduction percentage of the tripped blades in comparison with the smooth one is shown in Table 13 for wind speed of  $26m/s$ . The minus sign indicates a reduction in drag, which is preferable for this work. At just pre-stall condition, the three riblets' configurations

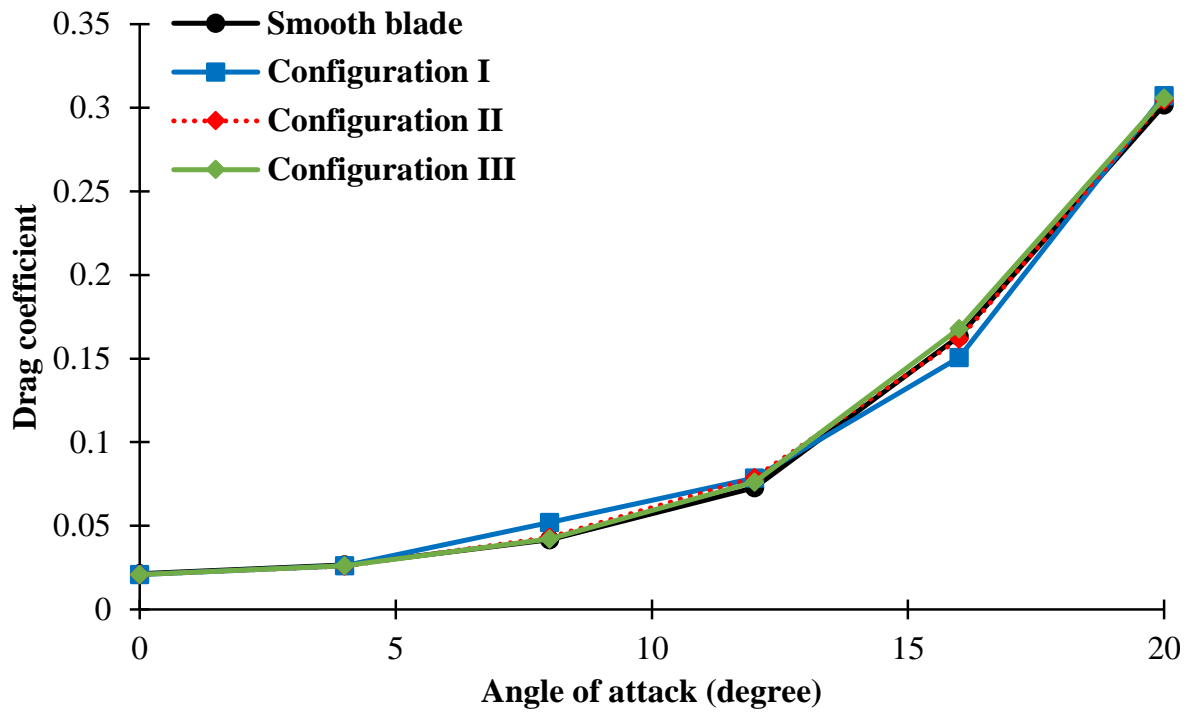


Figure 60: Drag coefficient versus AOAs for the smooth and tripped blades

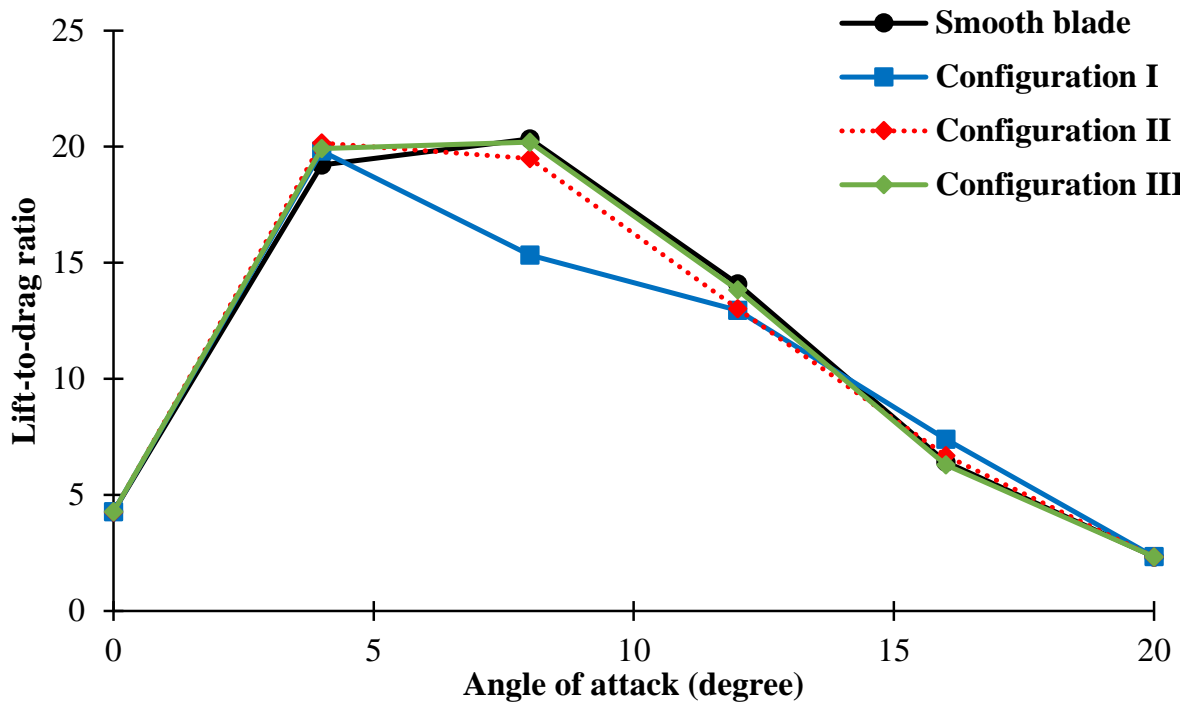


Figure 61: Lift-to-drag ratio versus AOAs for the smooth and tripped blades

Table 12: Lift increase of the tripped blades in comparison with the smooth blade ( $26m/s$ )

AOA	Configuration I	Configuration II	Configuration III
$0^\circ$	-2.23%	-2.52%	-2.23%
$4^\circ$	0.88%	2.42%	1.83%
$8^\circ$	-5.70%	-0.85%	0.79%
$12^\circ$	-0.76%	-0.08%	2.48%
$16^\circ$	6.41%	2.98%	0.76%
$20^\circ$	2.19%	0.62%	1.45%

Table 13: Drag reduction of the tripped blades in comparison with the smooth blade ( $26m/s$ )

AOA	Configuration I	Configuration II	Configuration III
$0^\circ$	-2.24%	-2.09%	-2.24%
$4^\circ$	-2.15%	-2.38%	-1.81%
$8^\circ$	25.0%	3.47%	1.48%
$12^\circ$	7.94%	8.21%	4.39%
$16^\circ$	-7.80%	-1.13%	2.69%
$20^\circ$	1.88%	1.00%	1.36%

show an increase in drag force. However, the drag is reduced at stall by 7.8% and 1.13% for riblets' configurations I and II, respectively. At post-stall, there is a sudden drag increase for all simulated riblets' configurations, but it is lower than the pre-stall values.

Referring to Table 14, a comparison between the tripped and the smooth blades in increasing percentage of lift-to-drag ratio at wind speed of  $26m/s$  is displayed. In comparison with all obtained riblet's configurations, the optimum riblet's configuration should be either configuration I or configuration II, as both record the best performance in increasing lift-to-drag ratio at stall. However, configuration II shows a better performance at other AOAs. Consequently, configuration II is selected for applying riblets on NREL phase II.

A study is performed to determine whether the surface-skin friction or the pressure lift is increased more by riblets. Figures 62 and 63 show the lift force due to pressure and skin-

Table 14: Lift-to-drag ratio increase of the tripped blades in comparison with the smooth blade ( $26m/s$ )

AOA	Configuration I	Configuration II	Configuration III
$0^\circ$	0.01%	-0.45%	0.01%
$4^\circ$	3.10%	4.92%	3.70%
$8^\circ$	-24.6%	-4.17%	-0.68%
$12^\circ$	-8.06%	-7.66%	-1.83%
$16^\circ$	15.4%	4.16%	-1.88%
$20^\circ$	0.30%	-0.38%	0.09%

friction, respectively. The improvement or degradation of the performance depends on AOAs more than on the pressure or viscous force. However, the lift force due to surface skin-friction shows a higher increase of lift force in comparison with pressure force. For example, at an AOA of  $16^\circ$ , the lift force is increased by 22% due to skin-friction, while it is increased by 3% due to pressure of configuration II.

A similar study is carried out to further analyse which components (that is pressure or skin-friction) of drag forces are reduced more by riblets. The pressure and skin-friction drags against AOAs are displayed in Figures 64 and 65, respectively. The behaviour is still similar to the previous result of lift forces, namely that the improvement or degradation of performance depends on AOAs. However, the reduction of skin-friction drag is shown at a wider range of AOAs in comparison with pressure drag. From this, it is concluded that riblets are more able to alter the viscous sub-layer behaviour.

For further comparison of a tripped blade with smooth blade, Tables 15 and 16 represent the difference between the smooth and tripped blades in terms of the pressure and skin-friction drag coefficients, respectively. The pressure drag is generally increased at just the pre-stall condition for all configurations. However, at an AOA of  $\alpha \leq 4^\circ$ , the riblets can reduce pressure drag for the three configurations. The maximum pressure drag reduction occurs at different AOAs for each riblet's configuration.

According to Table 16, riblets can reduce the skin-friction drag for all configurations at most AOAs. The maximum decrease in skin-friction drag is obtained at an AOA of  $\alpha = 12^\circ$  for configurations II and III, while it occurs at  $\alpha = 8^\circ$  for configuration I. The skin-friction drag

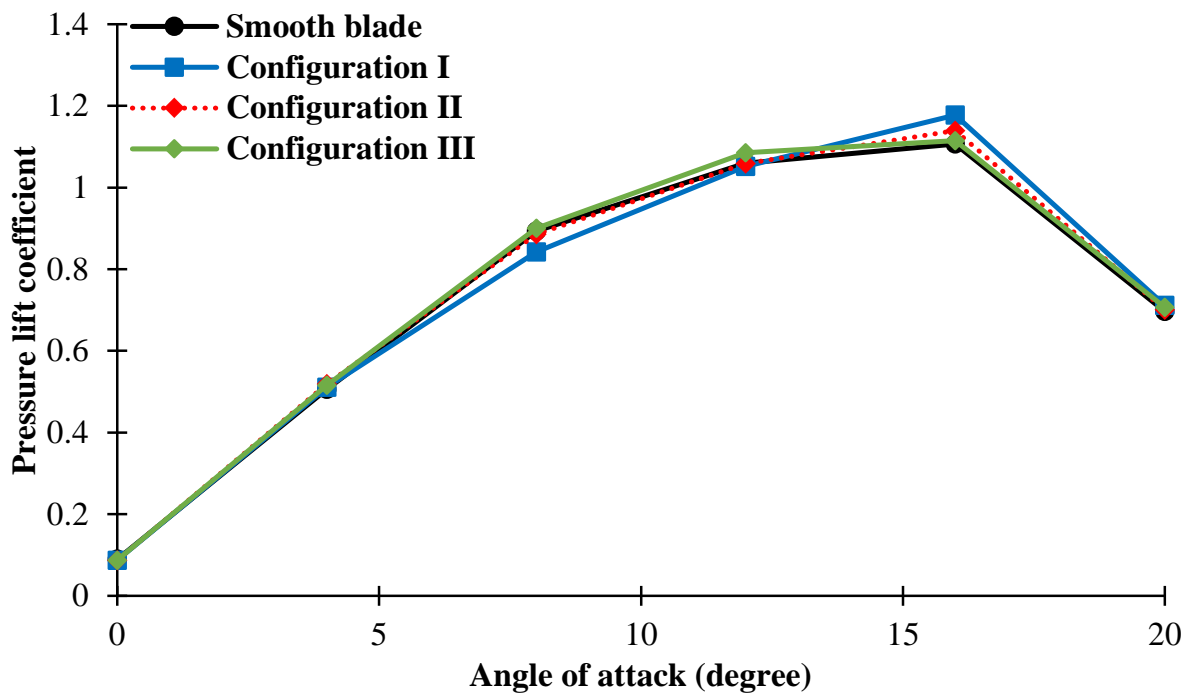


Figure 62: The lift coefficient due to pressure versus angle of attacks

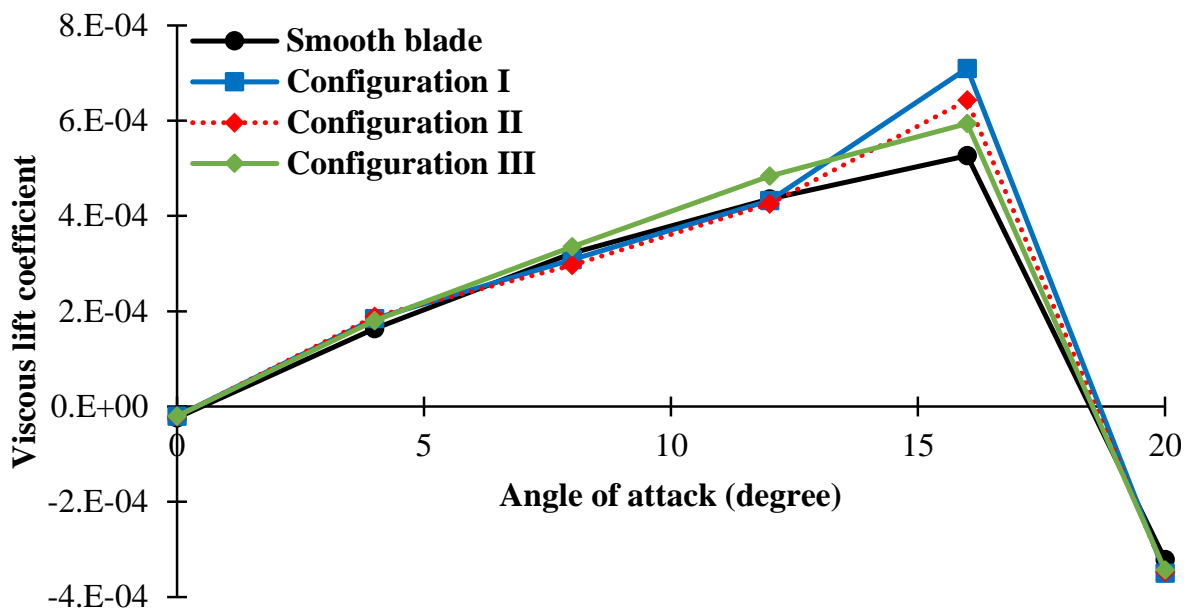


Figure 63: The lift coefficient due to surface skin-friction versus angle of attacks

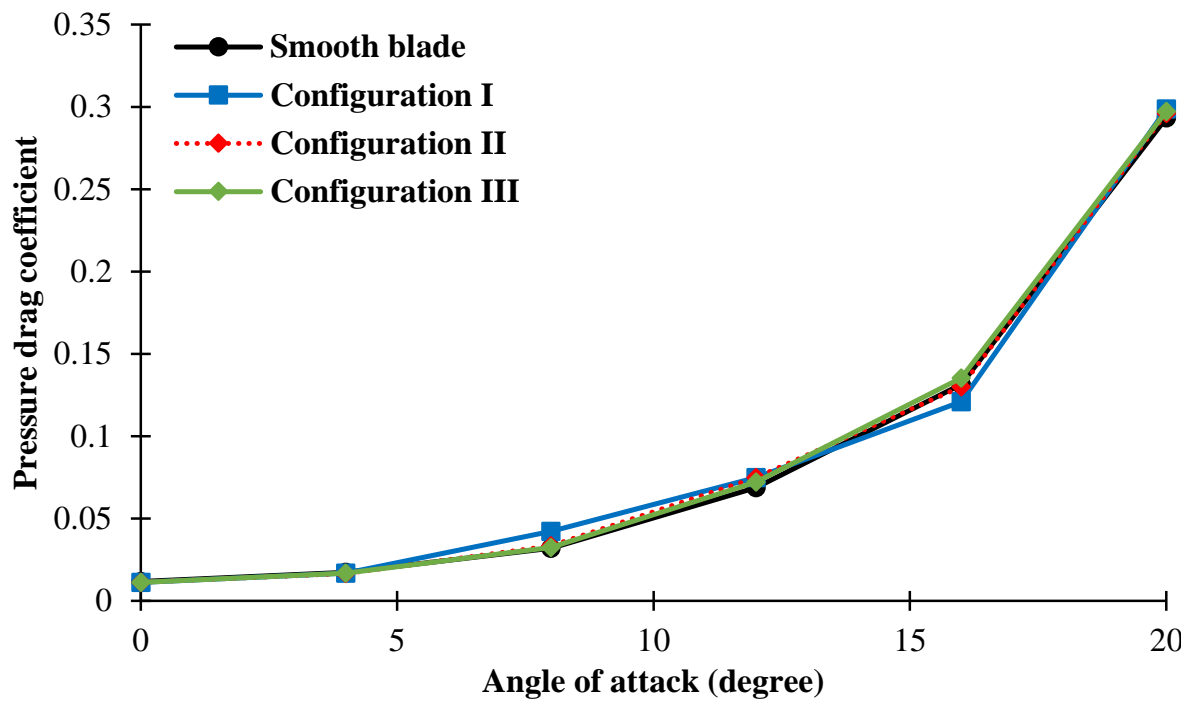


Figure 64: The drag coefficient due to pressure versus angle of attacks

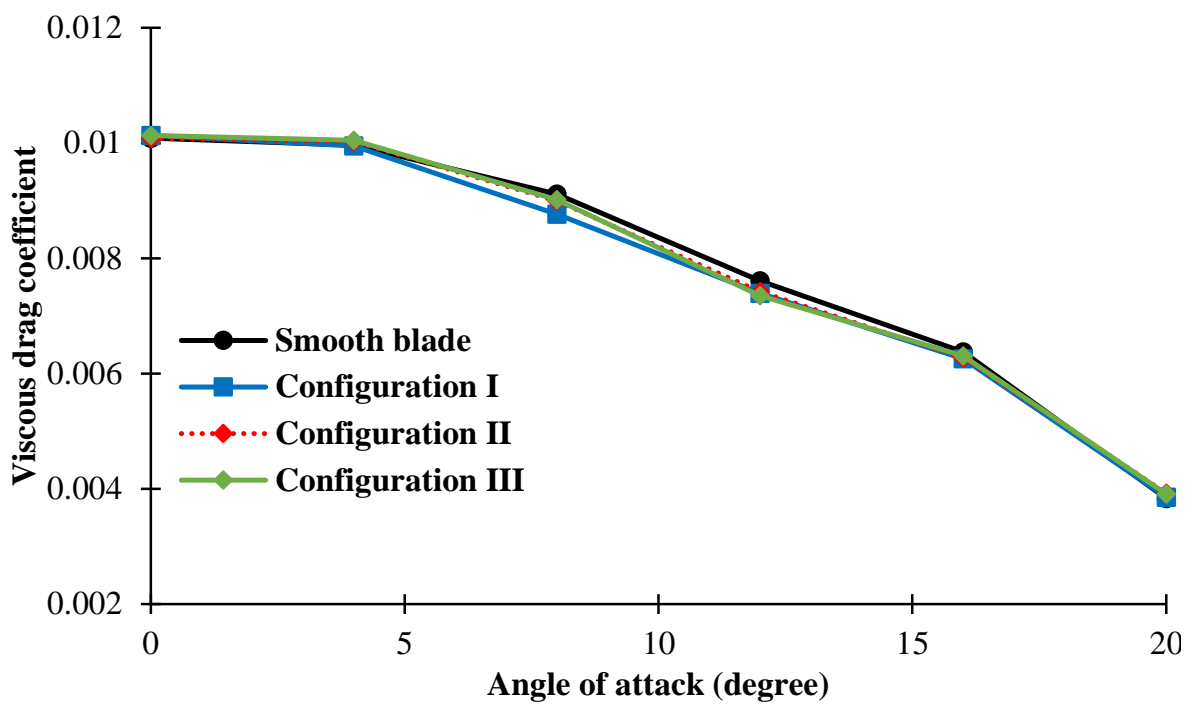


Figure 65: The drag coefficient due to surface skin-friction versus angle of attacks

is decreased at flow separation, while it is increased at the post-stall condition for all riblets' configurations. Generally, riblets are more able to reduce the skin-friction drag rather than the pressure drag at a wider range of AOAs.

Table 15: Pressure drag reduction of the tripped blades in comparison with the smooth blade ( $26m/s$ )

AOA	Configuration I	Configuration II	Configuration III
0°	-4.60%	-3.88%	-4.60%
4°	-3.27%	-4.08%	-3.50%
8°	32.8%	4.83%	2.20%
12°	8.87%	9.13%	5.00%
16°	-8.09%	-1.10%	2.88%
20°	1.90%	0.99%	1.35%

Table 16: Skin-friction drag reduction of the tripped blades in comparison with the smooth blade ( $26m/s$ )

AOA	Configuration I	Configuration II	Configuration III
0°	0.46%	-0.04%	0.46%
4°	-0.16%	0.63%	0.79%
8°	-3.83%	-1.33%	-1.07%
12°	-2.85%	-2.45%	-3.42%
16°	-1.93%	-1.72%	-1.10%
20°	0.55%	2.29%	1.98%

The discussion about the effect of riblets on lift and drag forces for configuration II at different AOAs and wind speed of  $26m/s$  can be summarised as follows:

- \* **Drag reduction case:** There are some cases where drag is reduced because of applying riblets. Configuration II at AOA of  $\alpha = 0^\circ$  is studied as an example of drag reduction case to show the flow physics and turbulence statistics compared to the smooth blade. The same behaviour is expected for all drag reduction cases.

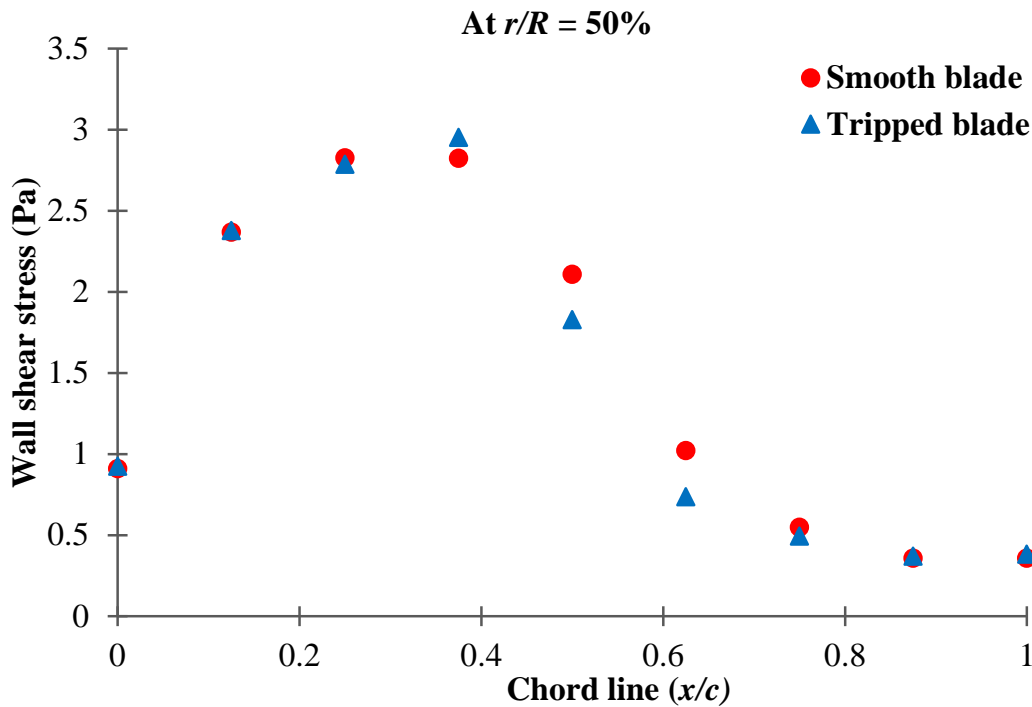


Figure 66: The wall shear stress distribution at  $\alpha = 0^\circ$

1. **Wall shear stress.** For the drag reduction case ( $\alpha = 0^\circ$ ), the wall shear stress of the tripped blade is reduced compared to the smooth blade, as shown in Figure 66. The data is taken at the middle of the blade ( $r/R = 50\%$ ) and the riblets are located at about  $40\%c$ . Once the flow reaches the riblets the wall shear stress is reduced thereby reducing the skin friction drag. Figure 67 shows the skin-friction on one riblet at  $\alpha = 0^\circ$ . For the drag reduction case, it was previously observed by Choi *et al.* [61] that the skin-friction is higher at the tip compared to the sides and the base of riblet.
2. **Velocity contour.** Figure 68 shows the velocity contour in the spanwise direction at  $\alpha = 0^\circ$  for the drag reduction case. The riblets can impede the flow in the spanwise direction resulting in the reduction of momentum transport of the flow and therefore reducing drag force. This supports what was previously observed by Bechert and Bartenwerfer [63] for riblets over the plate.
3. **Boundary layer thickness.** Figure 69 shows the velocity profile of the tripped blade in comparison with the smooth blade. The thickness of the boundary layer is increased by a distance of  $1mm$  due to the riblets. The velocity of the flow for the tripped blade is increased by about  $2.1\%$  above the boundary layer region.

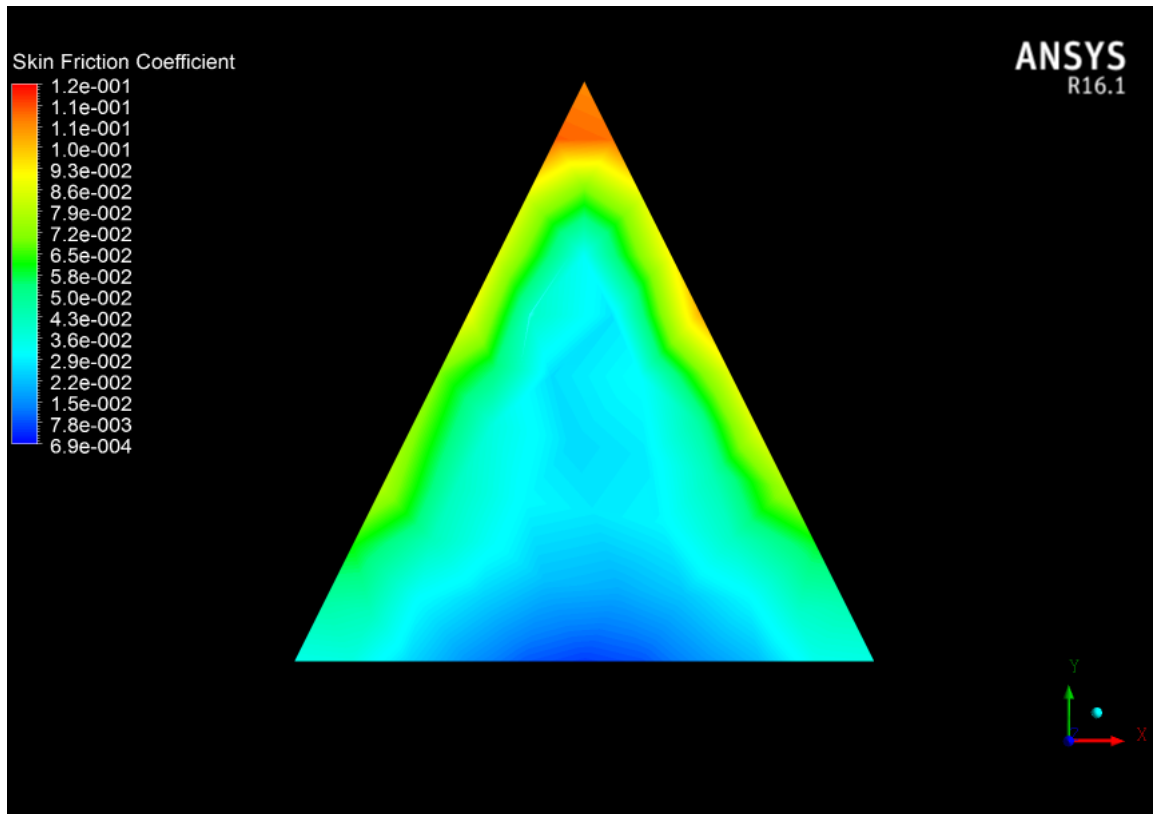


Figure 67: The skin friction coefficient of riblet at  $\alpha = 0^\circ$

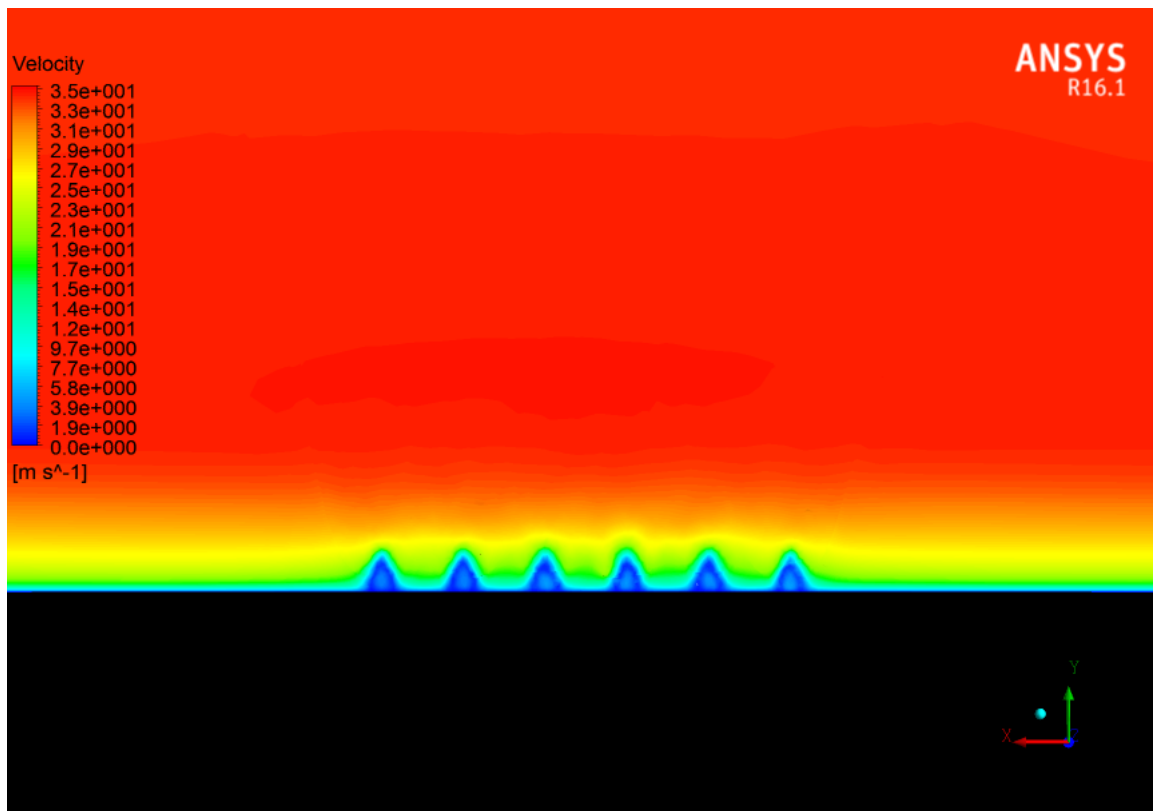


Figure 68: The velocity contour of the tripped blade at  $\alpha = 0^\circ$  in spanwise direction

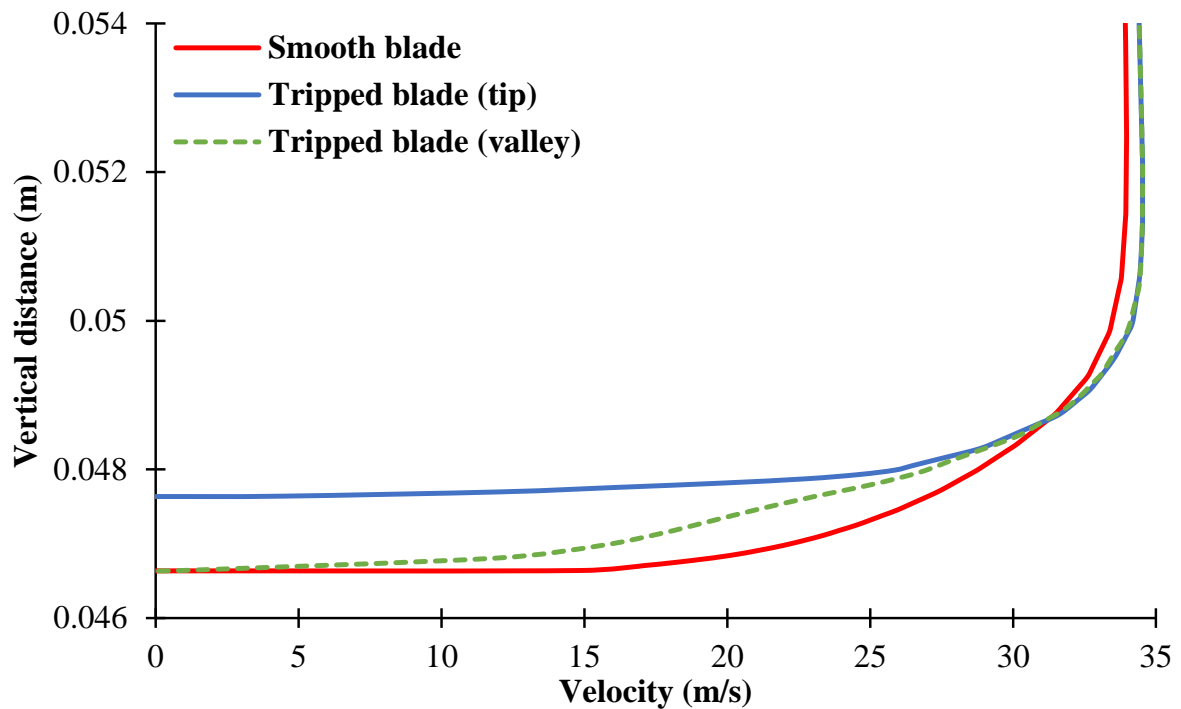


Figure 69: The boundary layer thickness of the tripped and smooth blades at  $\alpha = 0^\circ$

4. **Velocity profile.** Due to the riblets, the velocity profile at the log-law region is shifted upward, while the velocity at the viscous sub-layer region is shifted downward, as shown in Figure 70. This means the viscous sub-layer thickness is increased. This was previously observed by Choi *et al.* [61] for the drag reduction case of the tripped plate.
5. **Turbulence intensity.** Figures 71 and 72 show the turbulence intensity of the smooth and tripped blades at wind speeds of  $6m/s$  and  $26m/s$ , respectively. The turbulence intensity is reduced for tripped blade because of the riblets. The reduction is observed clearly at low  $Re$ . This was also shown previously by Choi *et al.* [61] for a drag reduction case of the tripped plate.

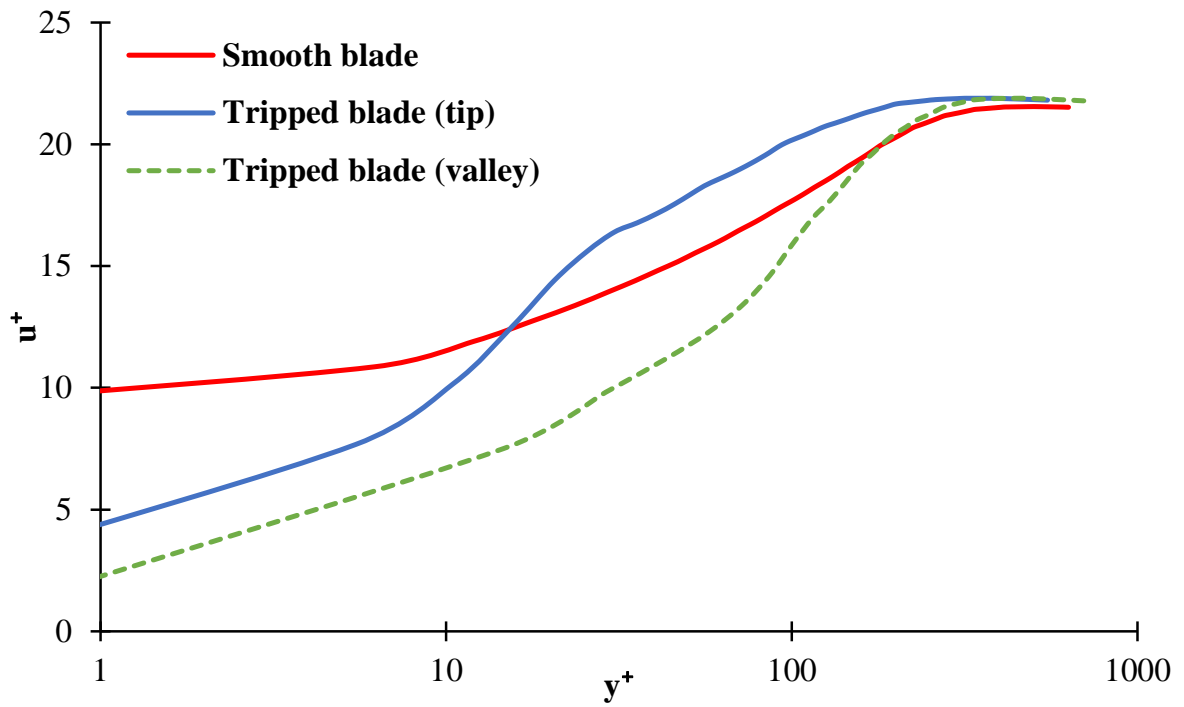


Figure 70: The velocity profile of the tripped and smooth blades at  $\alpha = 0^\circ$

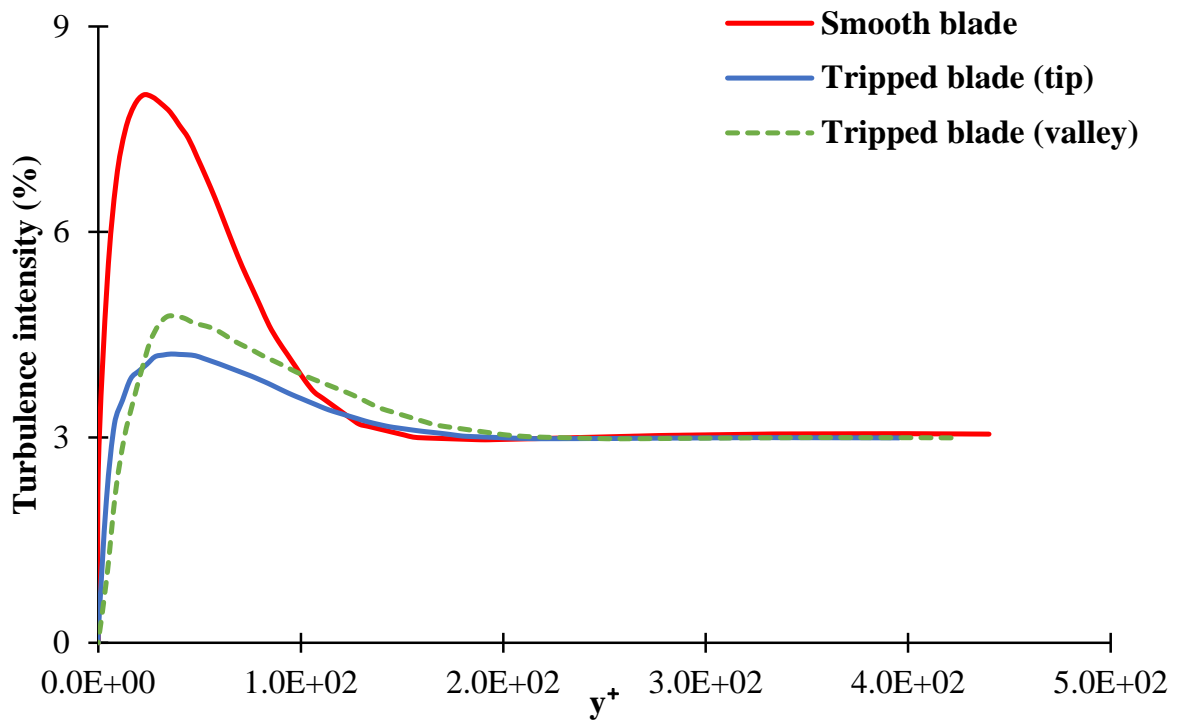


Figure 71: The turbulence intensity of the tripped and smooth blades at  $V_\infty = 6m/s$  ( $\alpha = 0^\circ$ )

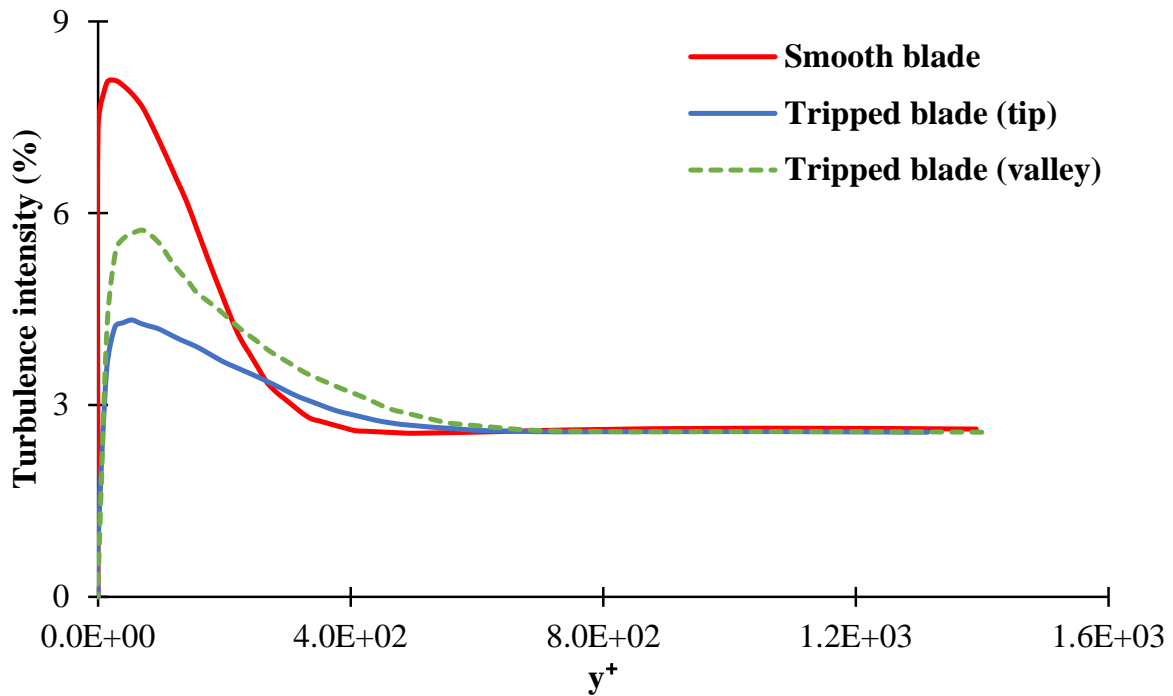


Figure 72: The turbulence intensity of the tripped and smooth blades at  $V_\infty = 26\text{m/s}$  ( $\alpha = 0^\circ$ )

\* **Lift increase case:** There are some cases where lift is increased because of riblets. An example is shown here is for lift increase at  $\alpha = 16^\circ$  (configuration II).

1. **The pressure distribution.** The pressure distribution of the smooth and tripped blades is shown in Figure 73 at the blade's mid span for  $\alpha = 16^\circ$ . The flow separation of the blade's upper side occurs at a further chord location for the tripped blade, as it occurs at  $21\%c$  and  $50\%c$  for smooth and tripped blades, respectively. The result proves that riblets are able to delay flow separation over the blade.
2. **Pressure contour.** The pressure contours of the smooth and tripped blades at  $\alpha = 16^\circ$  are shown in Figures 74 and 75, respectively. The pressure on the blade's upper side is affected by the riblets. This leads to a higher difference in pressure between both blade sides for the tripped blade compared to smooth one. As a result, the riblets are able to alter the pressure distribution, and therefore enhance lift.
3. **Velocity contour.** The velocity contours of the smooth and tripped blades at  $\alpha = 16^\circ$  are shown in Figures 76 and 77, respectively. As this is the stall AOA for *S809*, the riblets accelerate the flow. This leads to a higher resistance to the flow separation, and therefore higher lift occurs as shown on the blade's suction side.

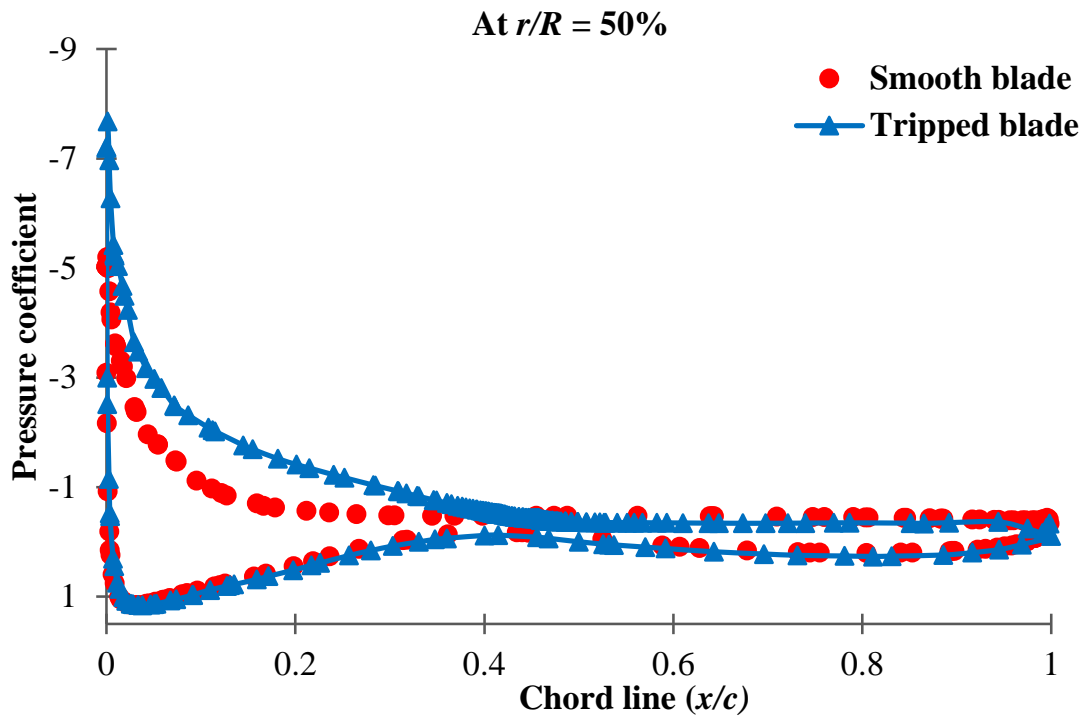


Figure 73: The pressure distribution of smooth and tripped blades at  $\alpha = 16^\circ$

4. **Streamwise streamlines.** The streamlines of the smooth and tripped blades at  $\alpha = 16^\circ$  are displayed in Figures 78 and 79, respectively. The smooth blade is exposed to larger flow separation compared to the tripped blade. It is believed that riblets' work is to prevent the flow separation zone to propagate further towards the leading edge for this study case.
5. **Velocity vector.** Figures 80 and 81 show the velocity vectors of the smooth and tripped blades, respectively at  $\alpha = 16^\circ$ . This is the stall angle for *S809* aerofoil, and the flow separation is expected. The flow separation causes a back flow for both smooth and tripped cases. The difference is that the riblets cause a circulation zone by preventing a back flow, as shown in Figure 82. This circulation zone improves the performance by increasing the lift force.
6. **Streamwise vorticity.** The streamwise vorticity of the tripped blade is shown in Figure 83. The large-scale riblets are able to generate streamwise vorticity, therefore providing high momentum flow from outer wall region into inner wall region. As a result, the stall is delayed leading to increasing lift and reducing drag of the tripped blade compared to the smooth one.

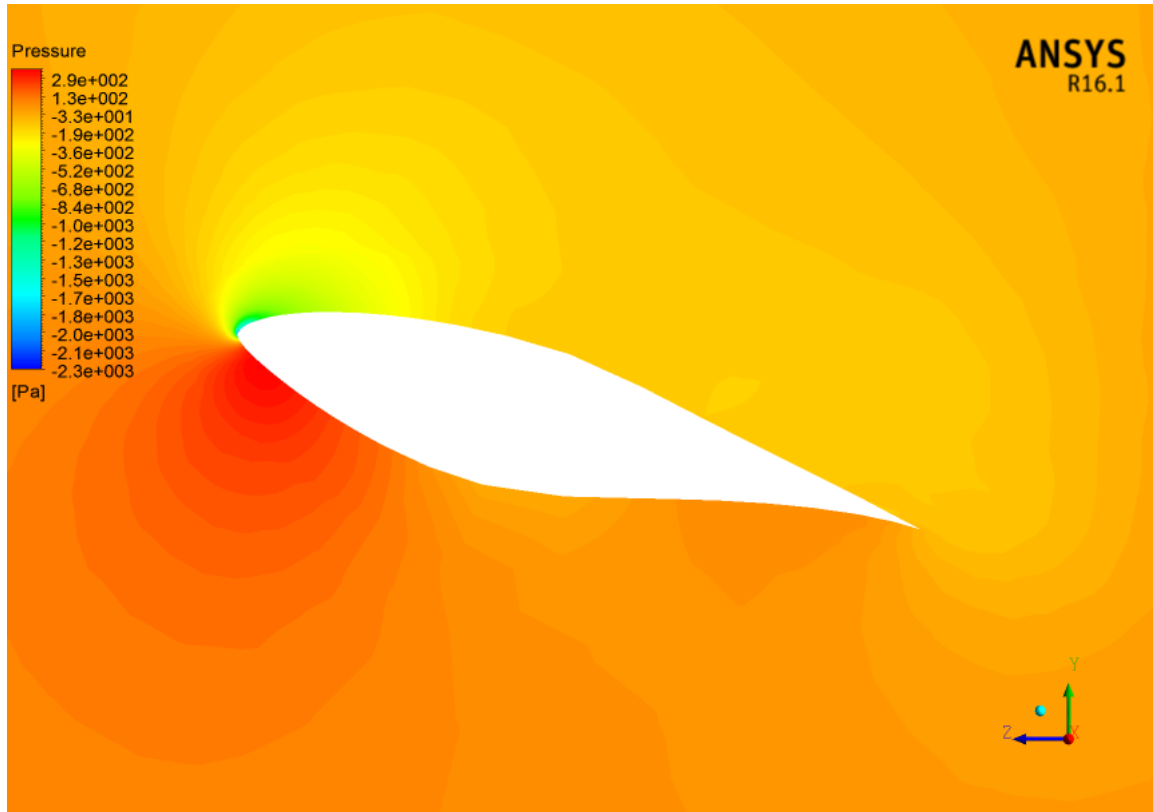


Figure 74: The pressure contour of the smooth blade at  $\alpha = 16^\circ$



Figure 75: The pressure contour of the tripped blade at  $\alpha = 16^\circ$

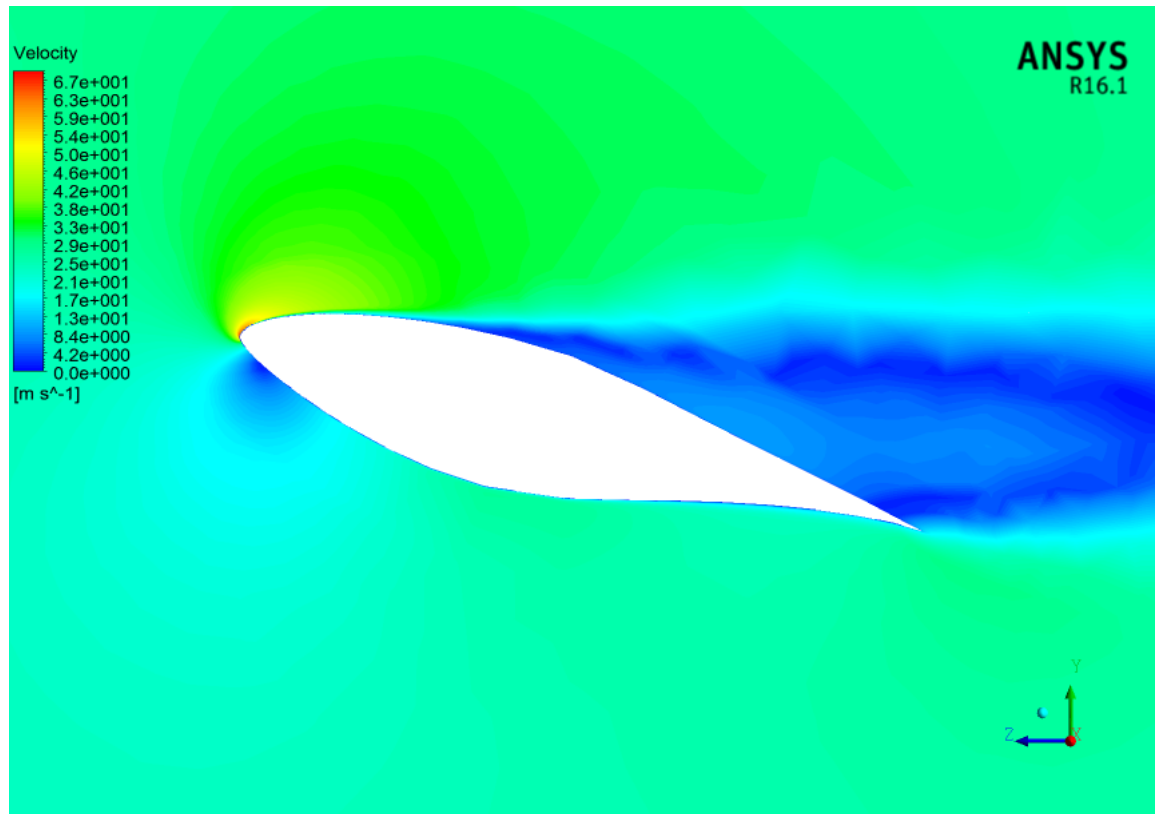


Figure 76: The velocity contour of the smooth blade at  $\alpha = 16^\circ$

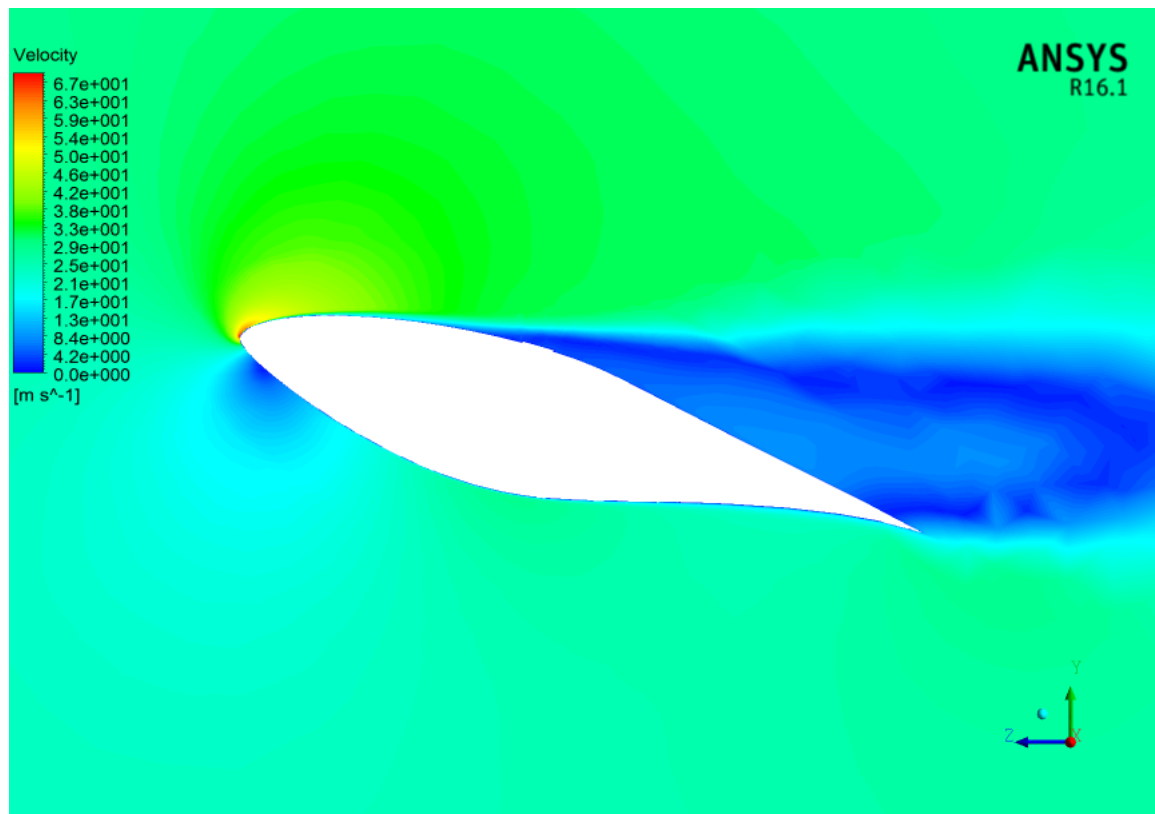


Figure 77: The velocity contour of the tripped blade at  $\alpha = 16^\circ$

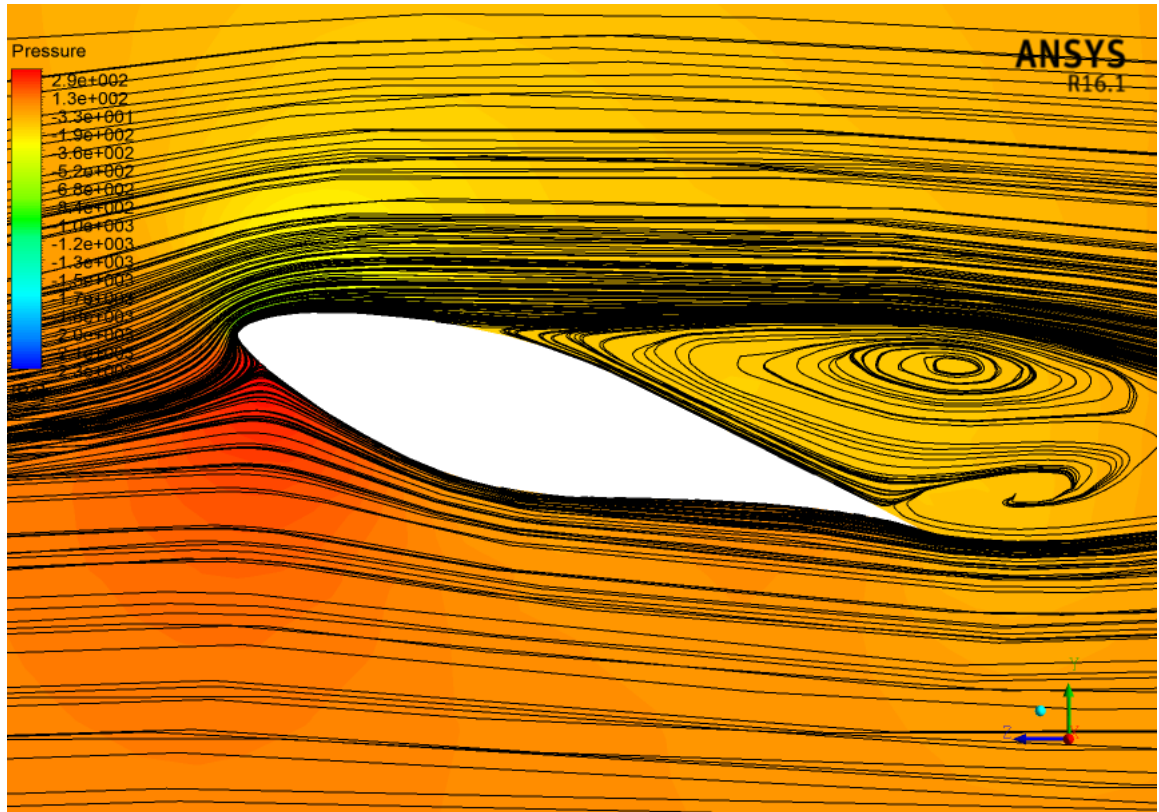


Figure 78: The streamlines of the smooth blade at  $\alpha = 16^\circ$

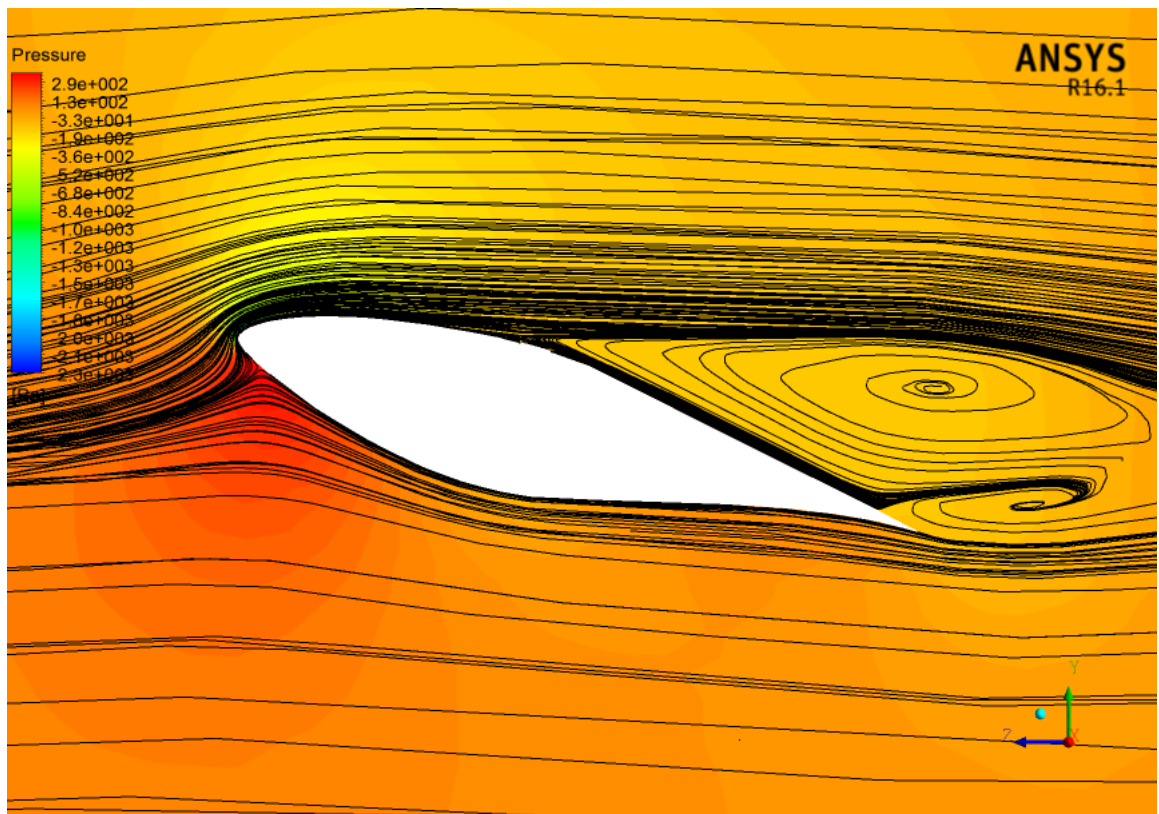


Figure 79: The streamlines of the tripped blade at  $\alpha = 16^\circ$

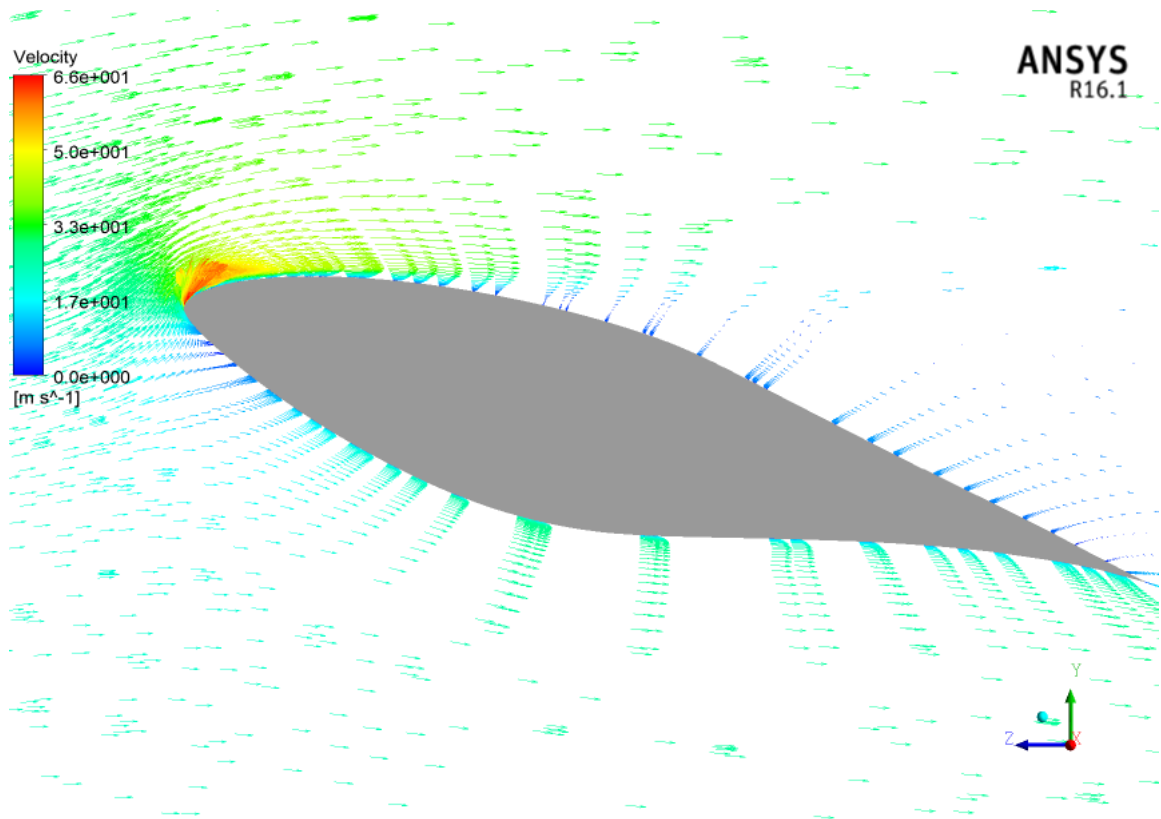


Figure 80: The velocity vector of the smooth blade at  $\alpha = 16^\circ$

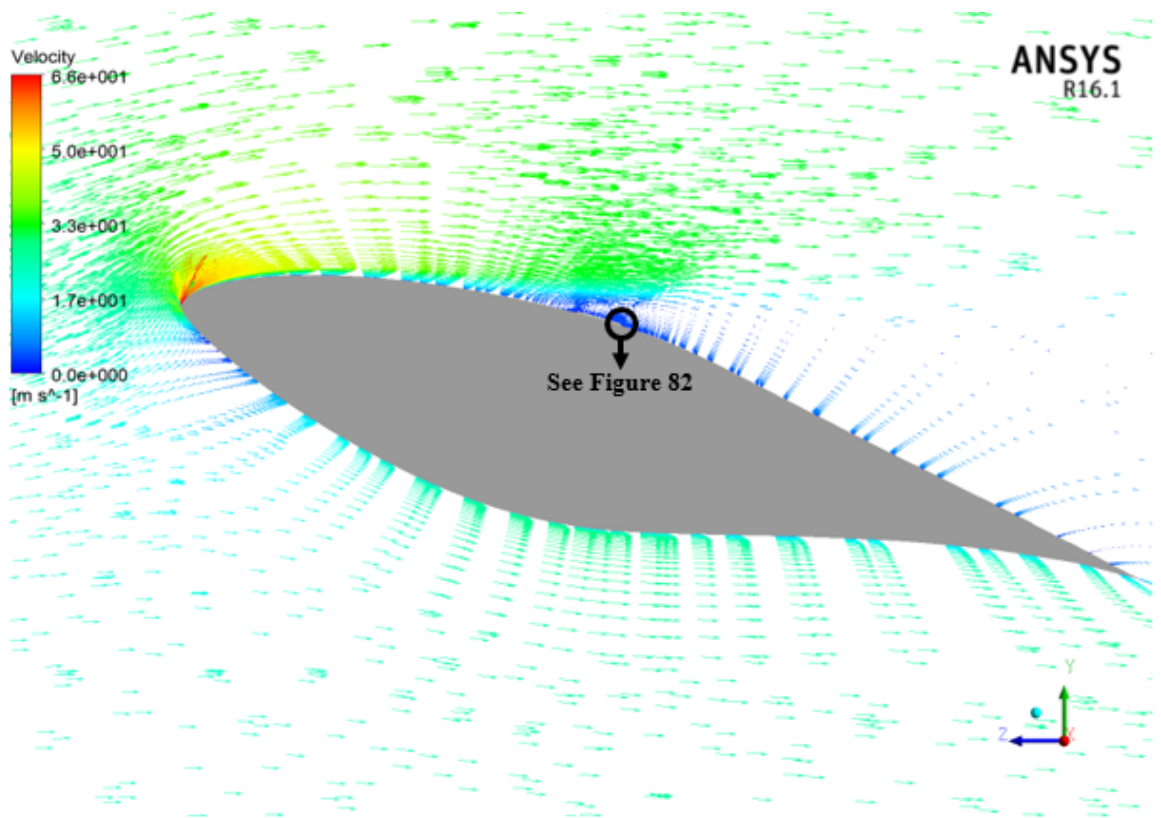


Figure 81: The velocity vector of the tripped blade at  $\alpha = 16^\circ$

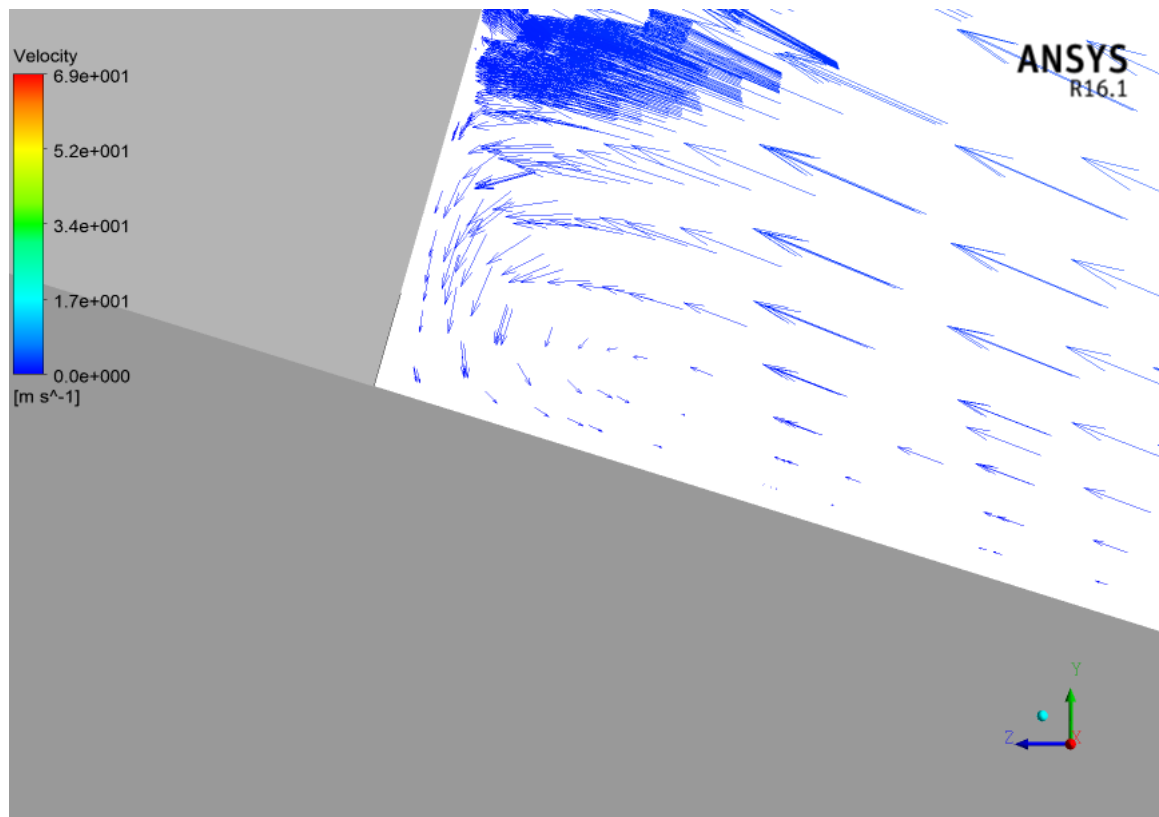


Figure 82: The velocity vector of the tripped blade at  $\alpha = 16^\circ$  (zoom-in)

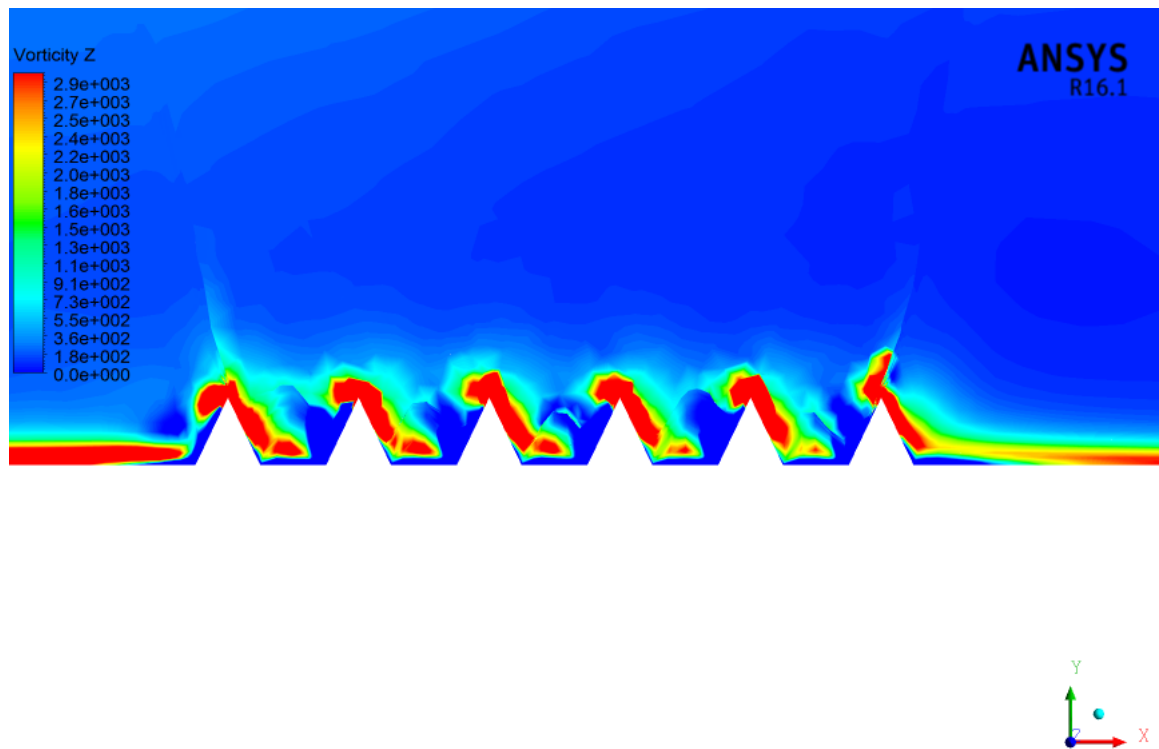


Figure 83: The streamwise vorticity of the tripped blade at  $\alpha = 16^\circ$

7. **Crossflow streamlines.** The crossflow streamlines of the tripped blade are shown at different simulated times in Figures 84, 85 and 86 at  $\alpha = 16^\circ$ . The large riblets cause a recirculated flow at the valley, which leads to an increase in lift force. The spanwise flow is impeded by the riblets causing a reduction of drag force. However, the streamwise vortices are not lifted away from the wall due to the size of the riblets' valley.

According to this work's results, the large-scale riblets are not only able to reduce drag but also to increase lift. This is done by eliminating an earlier flow separation and causing a recirculated flow behind the riblets at high AOAs. This leads to delaying the stall of the blade to a further chord location, as shown in Figures 81 and 82. In addition, the large-scale riblets are able to generate streamwise vortices at all AOAs, as shown in Figure 83. This means high momentum flow is provided into the inner wall region, thereby recovering the loss that is caused by skin friction.

Furthermore, it has been proven that the skin-friction is higher at the riblet tip, compared to the sides and bottom of the riblets. This means a high down-wash flow speed is only exposed to small limited area, that are riblet tips. This was also supported by showing an upward shift of the log-law region (Figure 70) and the reduction of turbulence statistics (Figure 71) for the tripped blade, as has been previously reported [61, 62]. The viscous sub-layer thickness of the tripped case is increased due to a decrease of flow speed. For example at  $\alpha = 16^\circ$ , the viscous layer thickness is roughly  $41\mu m$  and  $33\mu m$  for tripped and smooth blades, respectively.

The difference in operation between large-scale riblets and small-scale ones is that the former are able to cause a recirculated zone and generate streamwise vortices in the wake of large riblets, as shown in Figures 82 and 83 respectively. These events are believed to be the reason why stall is delayed, thus leading to the increase of lift and reduction of drag forces. For other flow controllers with similar scale to large riblets, such as the shark denticle shape, the upward shift of the log-law region, as a result of a thicker viscous sub-layer, higher wall shear stress at the riblet tips and reduction of turbulence statistics were not reported.

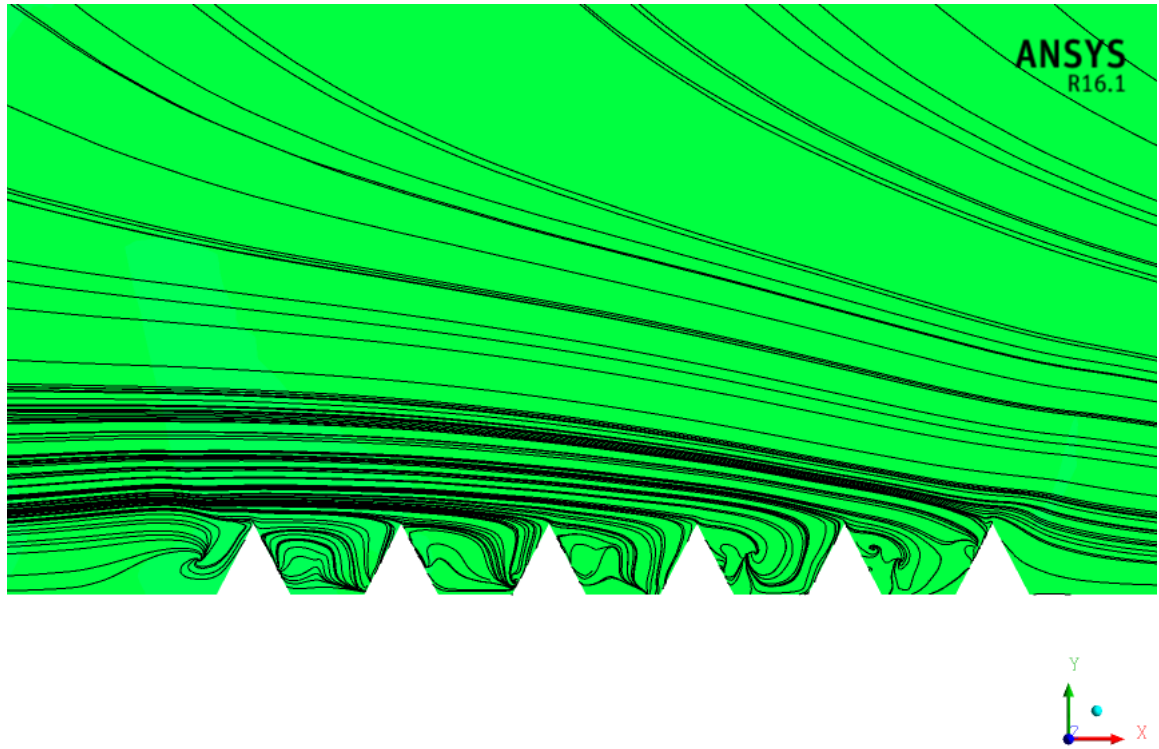


Figure 84: The crossflow streamlines of the tripped blade at  $t = 0.12s$  ( $\alpha = 16^\circ$ )

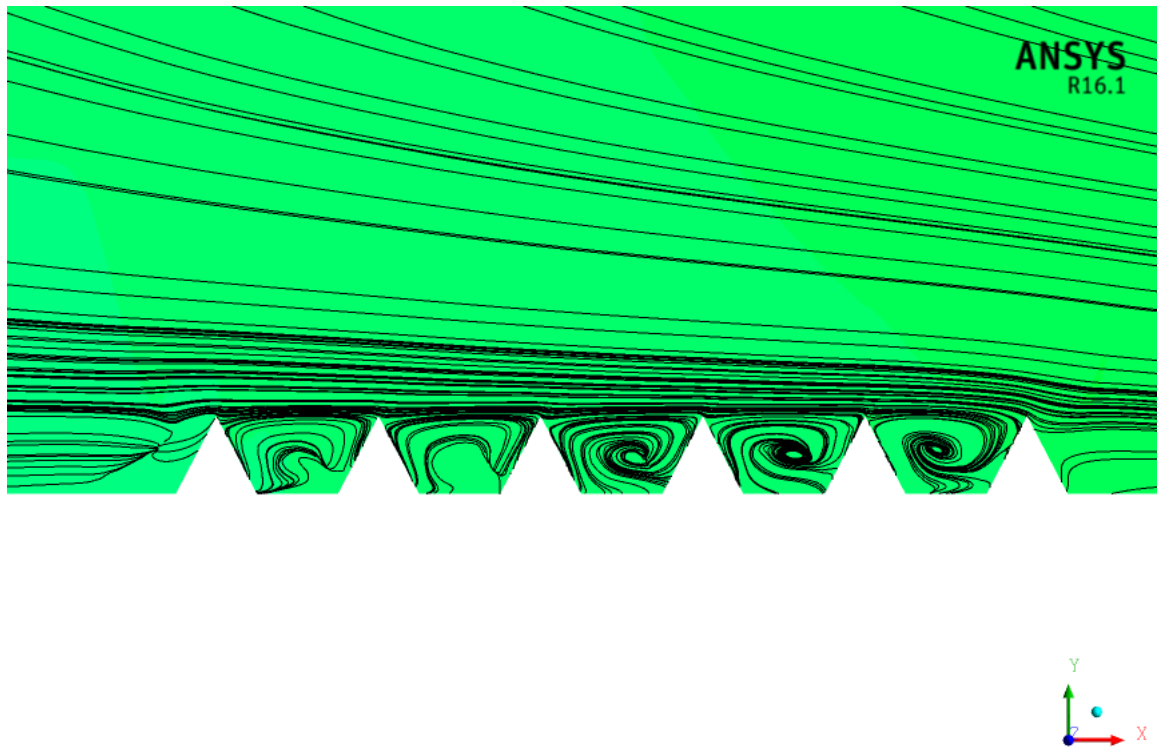


Figure 85: The crossflow streamlines of the tripped blade at  $t = 0.96s$  ( $\alpha = 16^\circ$ )

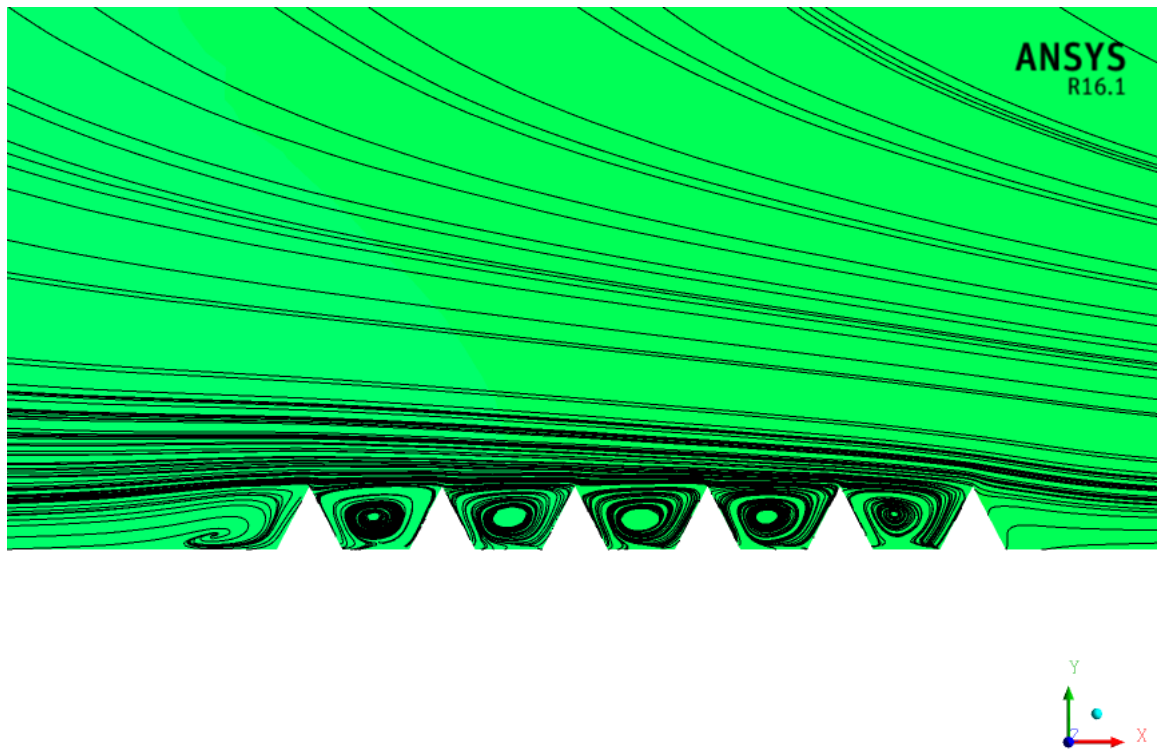


Figure 86: The crossflow streamlines of the tripped blade at  $t = 3.6s$  ( $\alpha = 16^\circ$ )

\* **Lift reduction & drag increase case:** There are some cases where lift is reduced and drag is increased because of riblets. An example is shown here is for lift reduction and drag increase at  $\alpha = 12^\circ$  (configuration II).

1. **Pressure contour and streamlines.** Figures 87 and 88 show the pressure contour and streamlines of the smooth and tripped blades at  $\alpha = 12^\circ$ , respectively. The riblets negatively affect the performance of the blade causing a flow separation. This leads to a reduction in lift and an increase in drag compared to the smooth blade.
2. **Velocity contour.** The velocity contours of the smooth and tripped blades at  $\alpha = 12^\circ$  are displayed in Figures 89 and 90. It is clearly shown that the flow of the smooth blade is more resistant to flow separation. The riblets decrease the lift by 0.08% and increase the drag by 8.21% at this AOA. This means riblets can also degrade the blade performance, depending on AOAs.

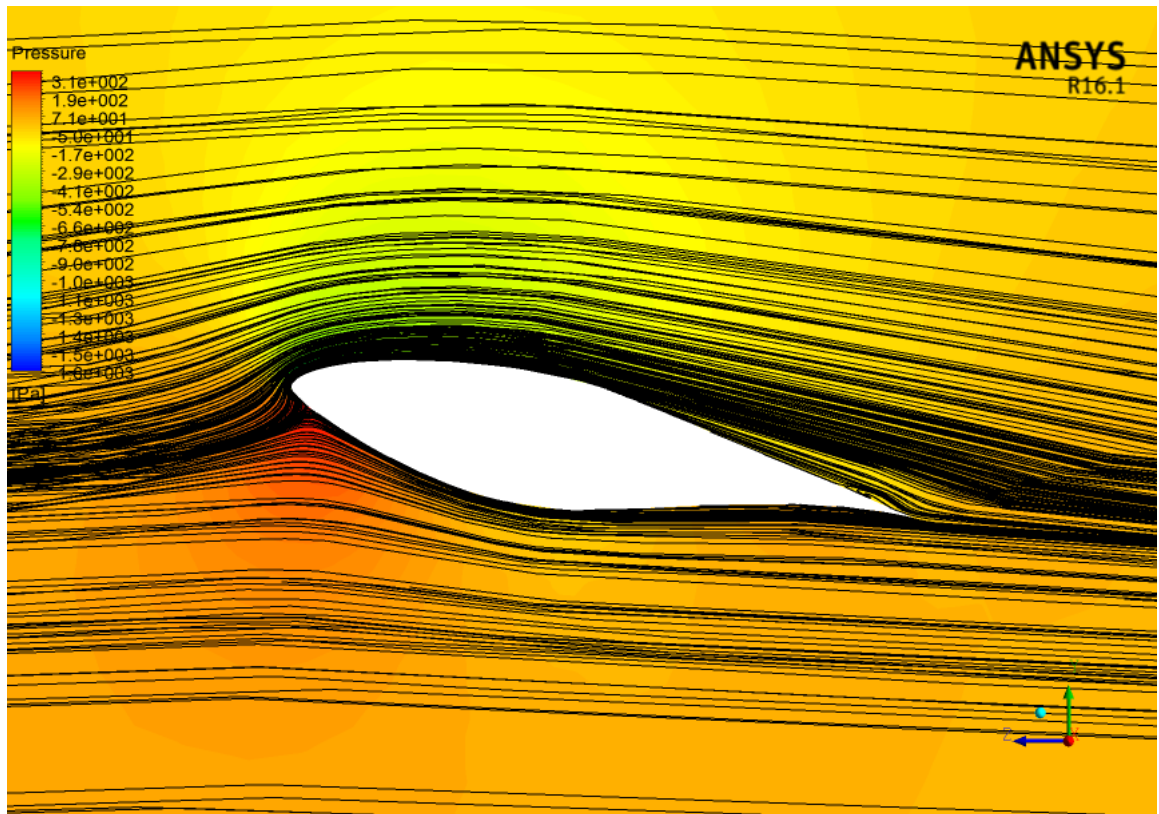


Figure 87: The streamlines and pressure contour of the smooth blade at  $\alpha = 12^\circ$

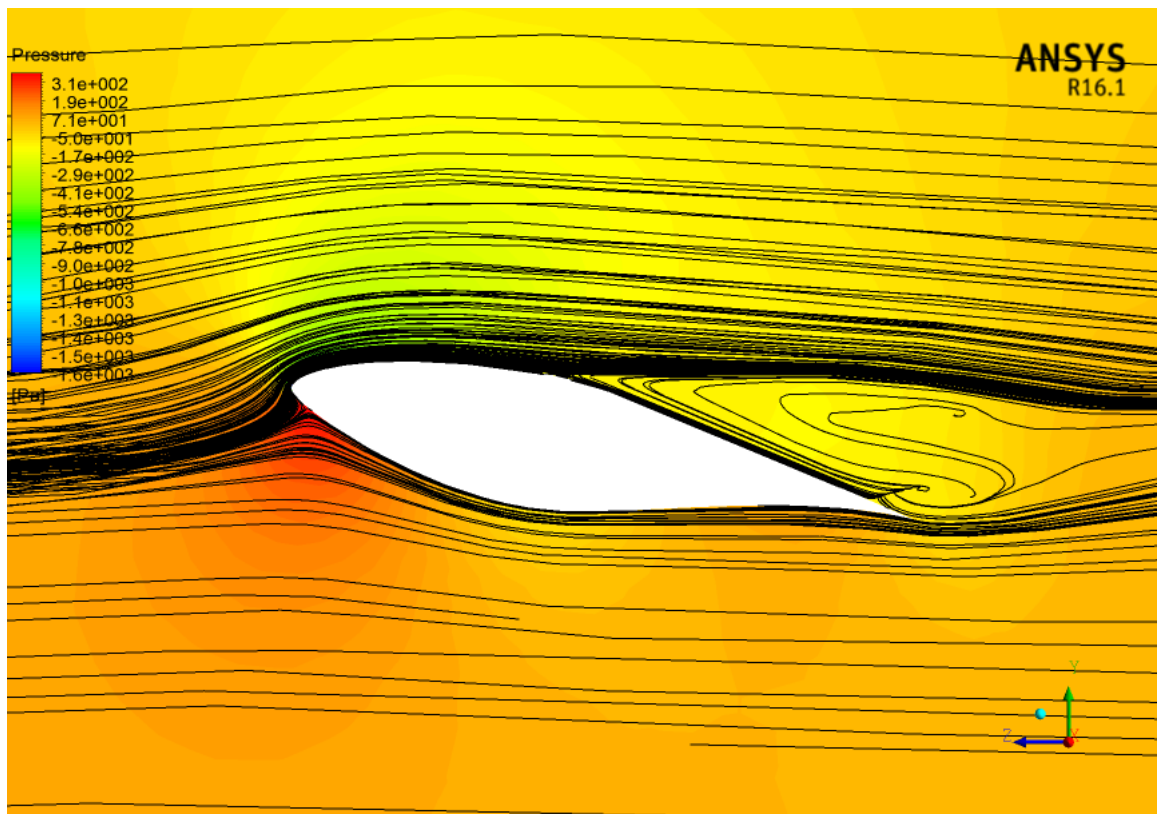


Figure 88: The streamlines and pressure contour of the tripped blade at  $\alpha = 12^\circ$

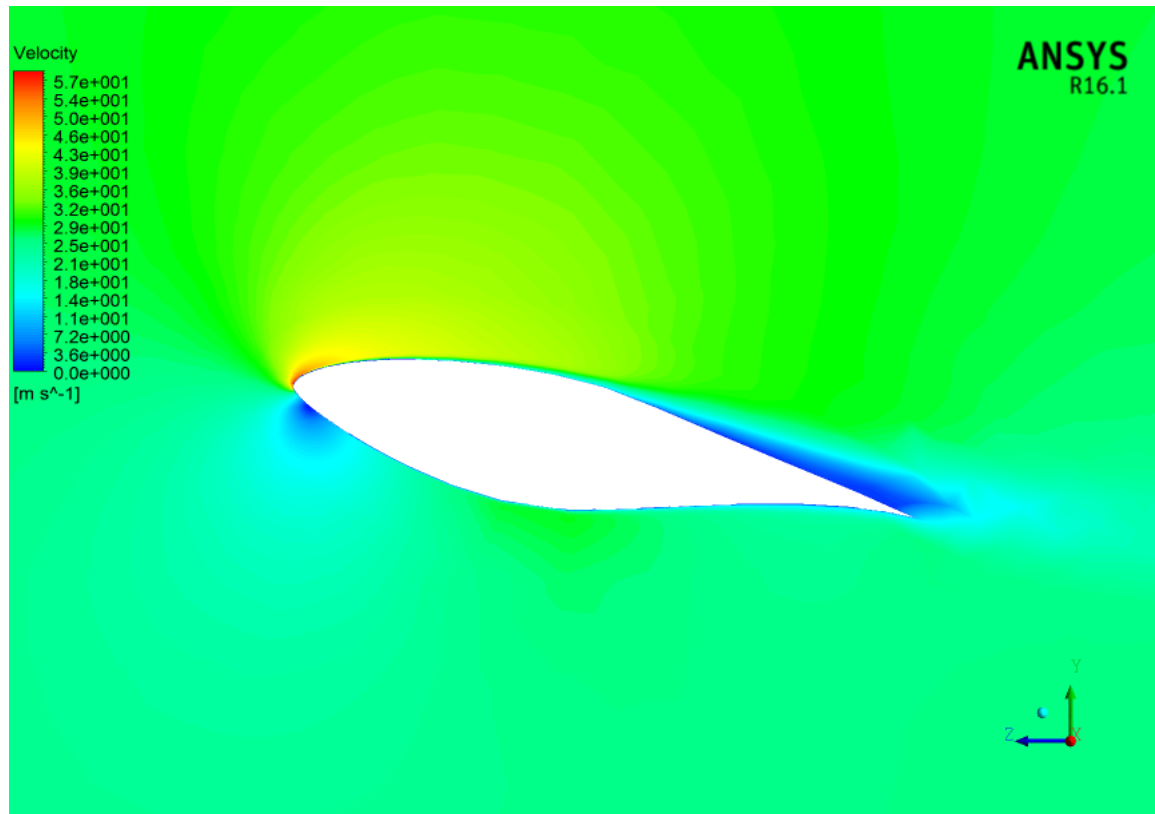


Figure 89: The velocity contour of the smooth blade at  $\alpha = 12^\circ$

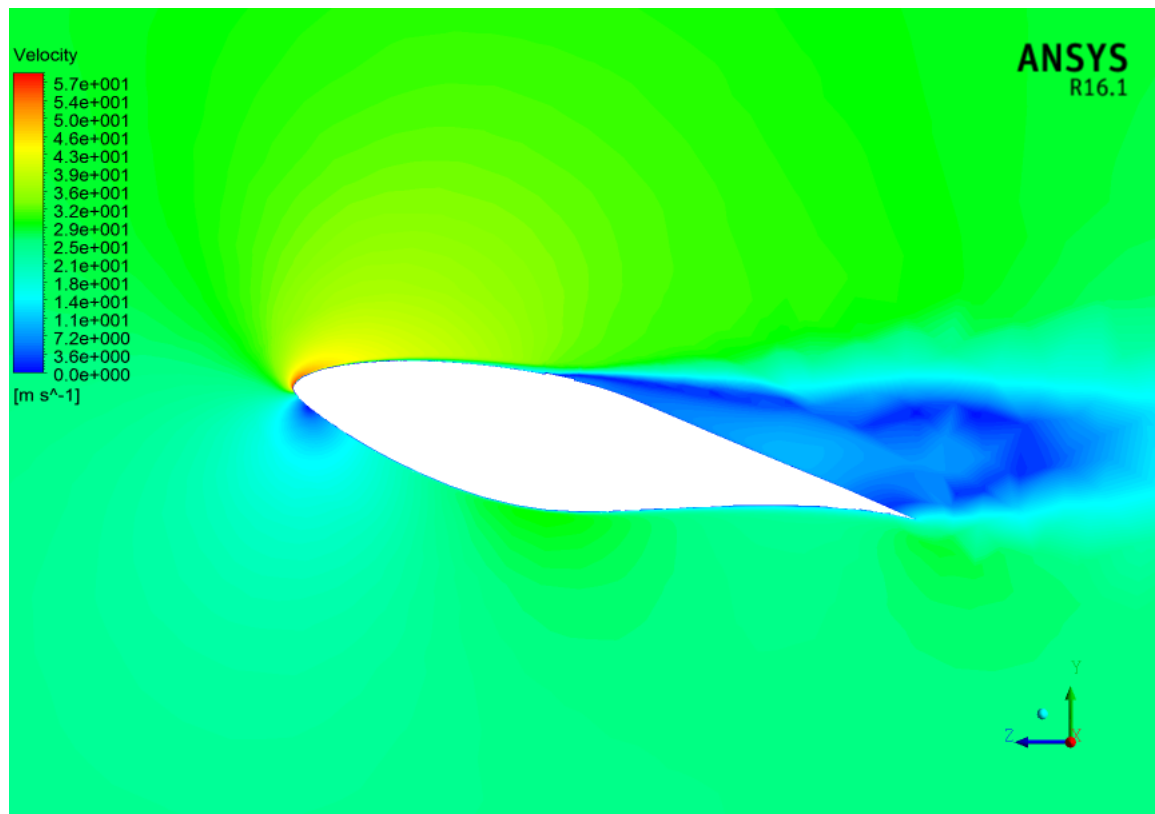


Figure 90: The velocity contour of the tripped blade at  $\alpha = 12^\circ$

- **Various wind speeds.**

Because wind turbines generally are exposed to various wind speeds during the year, an essential study is performed to observe the effect of riblets on aerodynamic coefficients at different air velocities. Table 17 shows the effect of configuration II on lift force at wind speeds of  $6m/s$ ,  $11m/s$ ,  $16m/s$  and  $21m/s$  compared to smooth blade. At low wind speeds ( $V_\infty \leq 11m/s$ ), riblets can perform better on increasing lift. For example, the maximum increase percentage in lift coefficient occurs at  $V_\infty = 6m/s$  by 9%. For all simulated wind speeds, riblets can improve the performance at flow separation.

Table 18 represents the percentage of drag reduction of configuration II compared to smooth blade. The drag reduction is recorded at low AOAs ( $\alpha \leq 4^\circ$ ) for all wind speeds. The same behaviour is noticed for all cases at flow separation by showing a decrease in drag. According to Table 19, higher lift-to-drag ratio is recorded for low wind speeds at low AOAs. At stall, riblets are able to increase the ratio. In summary, riblets' effect on lift and drag forces can be clearly observed at low  $Re$  and stall AOAs, in which they perform best. The effect of riblets also depends on riblets' configurations.

Table 17: **Lift increase comparison of configuration II with smooth blade**

<b>AoA</b>	$l^+$	$6ms^{-1}$	$11ms^{-1}$	$16ms^{-1}$	$21ms^{-1}$
<b>0°</b>	32 – 88	9.03%	2.66%	-1.89%	-2.34%
<b>4°</b>	35 – 97	4.51%	3.25%	2.84%	2.62%
<b>8°</b>	37 – 106	-3.63%	-1.16%	-0.91%	-0.94%
<b>12°</b>	39 – 112	-0.53%	-0.54%	-0.41%	0.07%
<b>16°</b>	46 – 134	4.21%	4.89%	3.78%	2.71%
<b>20°</b>	34 – 92	-0.25%	-0.56%	0.52%	-0.03%

Table 18: Drag reduction comparison of configuration II with smooth blade

<b>AoA</b>	$l^+$	$6ms^{-1}$	$11ms^{-1}$	$16ms^{-1}$	$21ms^{-1}$
<b>0°</b>	32 – 88	–1.74%	–1.72%	–1.81%	–2.00%
<b>4°</b>	35 – 97	–1.57%	–1.96%	–2.19%	–2.32%
<b>8°</b>	37 – 106	12.1%	3.97%	3.74%	3.71%
<b>12°</b>	39 – 112	6.80%	7.16%	6.52%	2.76%
<b>16°</b>	46 – 134	–0.64%	–3.61%	–1.83%	–1.92%
<b>20°</b>	34 – 92	0.39%	0.27%	0.97%	0.47%

Table 19: Lift-to-drag ratio increase comparison of configuration II with smooth blade

<b>AoA</b>	$l^+$	$6ms^{-1}$	$11ms^{-1}$	$16ms^{-1}$	$21ms^{-1}$
<b>0°</b>	32 – 88	11.0%	4.45%	–0.08%	–0.35%
<b>4°</b>	35 – 97	6.17%	5.32%	5.15%	5.05%
<b>8°</b>	37 – 106	–14.0%	–4.93%	–4.48%	–4.48%
<b>12°</b>	39 – 112	–6.87%	–7.19%	–6.51%	–2.61%
<b>16°</b>	46 – 134	4.88%	8.82%	5.71%	4.73%
<b>20°</b>	34 – 92	–0.63%	–0.83%	–0.45%	–0.50%

- **Number of riblets.**

The number of riblets is also studied. The number of riblets are increased from 6 to 14 and 20 riblets. Tables 20 and 21 show the mesh number of triangular faces and the total number of the mesh elements for all configurations, respectively. The higher number of riblets the larger number of mesh elements needed. Figure 91 displays the lift coefficient of different number of riblets at  $V_\infty = 26m/s$ . A similar behaviour is shown as stated early however, increasing the number of riblets does not show a better performance.

Figure 92 shows the drag coefficient of different number of riblets at  $V_\infty = 26m/s$ . Increasing the number of riblets proves its advantage in reducing drag, particularly at stall and post-stall conditions. According to Figure 93, the lift-to-drag ratio is also improved for higher number of riblets at wider range of AOAs. For example, the ratio is increased by 17% for 20 riblets, while it is increased by 4% for 6 riblets at stall compared to smooth blade. In summary, Increasing the number of riblets improves the lift-to-drag ratio and increases the drag reduction. However, it does not show any further increase for the lift force.

Table 20: Total number of mesh (triangular faces)

<b>Configurations</b>	<b>Number of triangular mesh faces</b>
Smooth blade	13, 410
20 riblets	28, 690
14 riblets	24, 662
6 riblets	19, 000

Table 21: Total number of mixed cells

<b>Configurations</b>	<b>Number of mixed cells</b>
Smooth blade	1, 483, 050
20 riblets	2, 540, 376
14 riblets	2, 249, 613
6 riblets	1, 879, 532

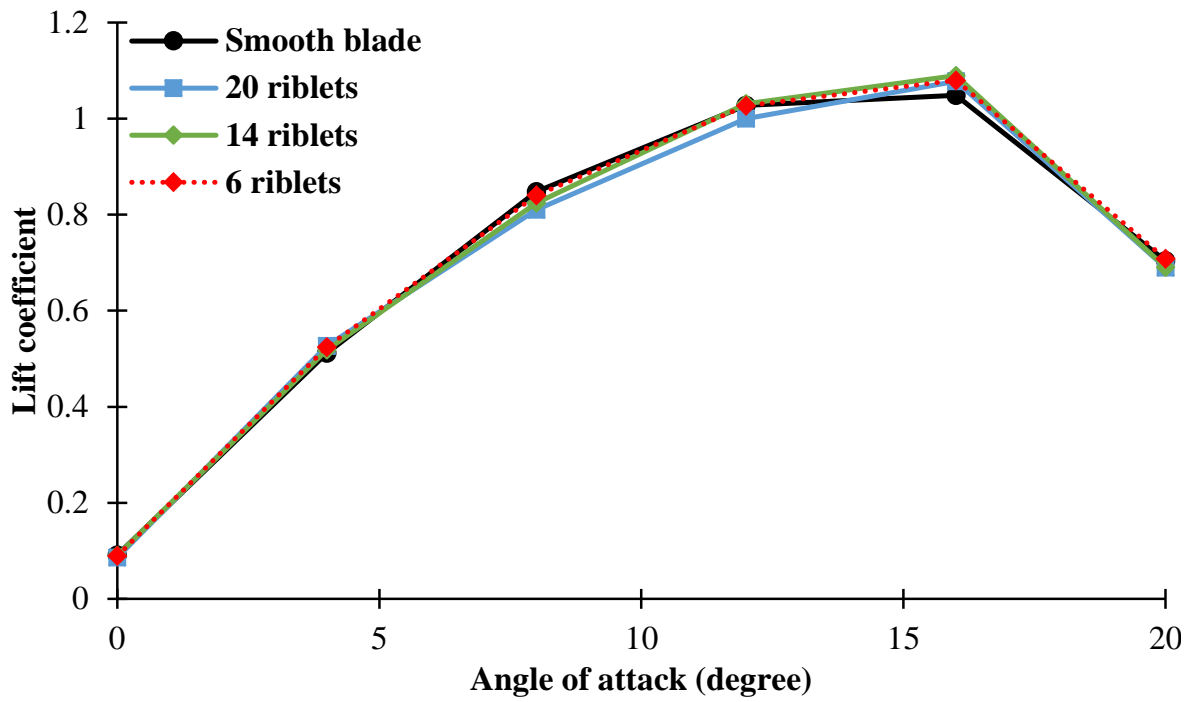


Figure 91: Lift coefficient versus AOAs for different number of riblets

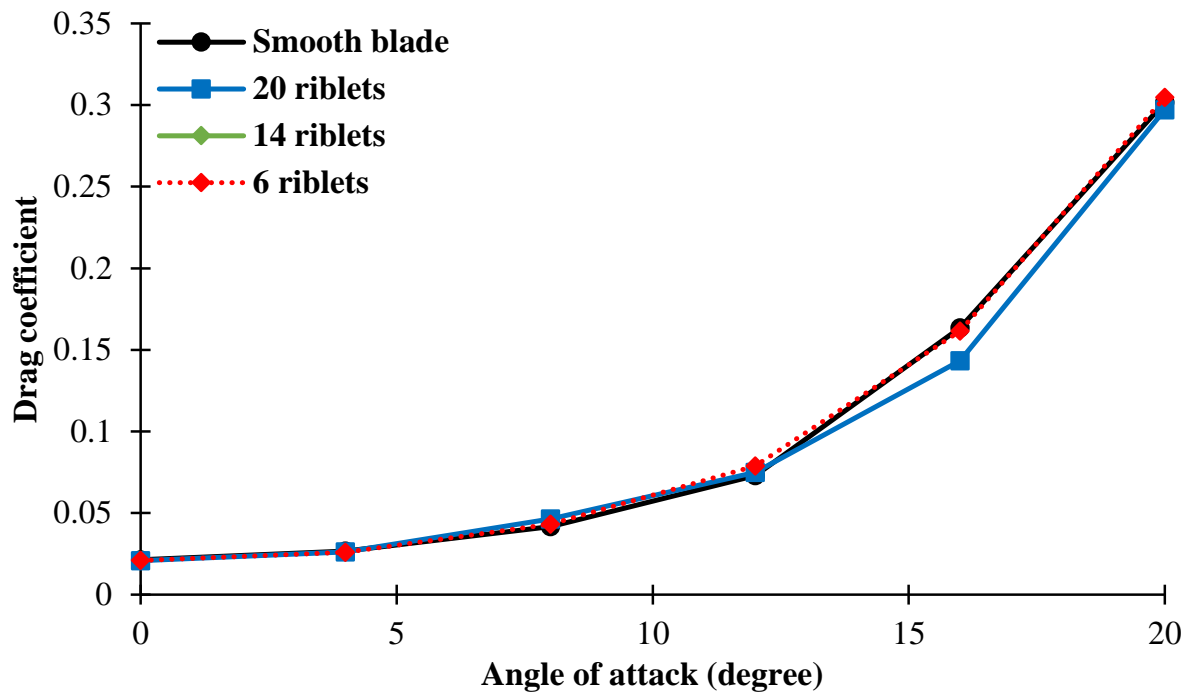


Figure 92: Drag coefficient versus AOAs for different number of riblets

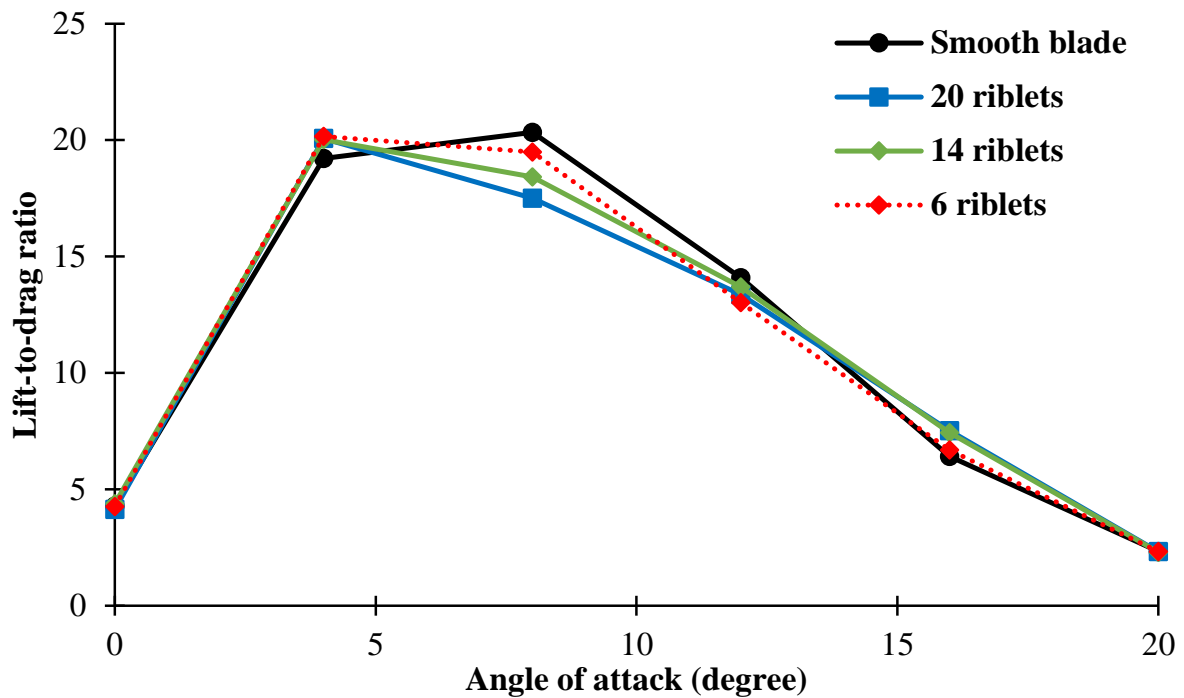


Figure 93: Lift-to-drag ratio versus AOAs for different number of riblets

The surface pressure and skin-friction drag forces for different numbers of riblets are shown in Figures 94 and 95, respectively. The pressure drag force is hugely decreased at stall for all configurations. The maximum decrease is shown for a larger number of riblets. This is because a larger amount of flow is recirculated and more streamwise vortices are generated. Similarly, the viscous drag force is reduced more for a larger number of riblets at a wider range of AOAs, even though the area of the blade is increased. It is believed that the contribution of riblets in increasing the area is negligible, due to the riblets' size.

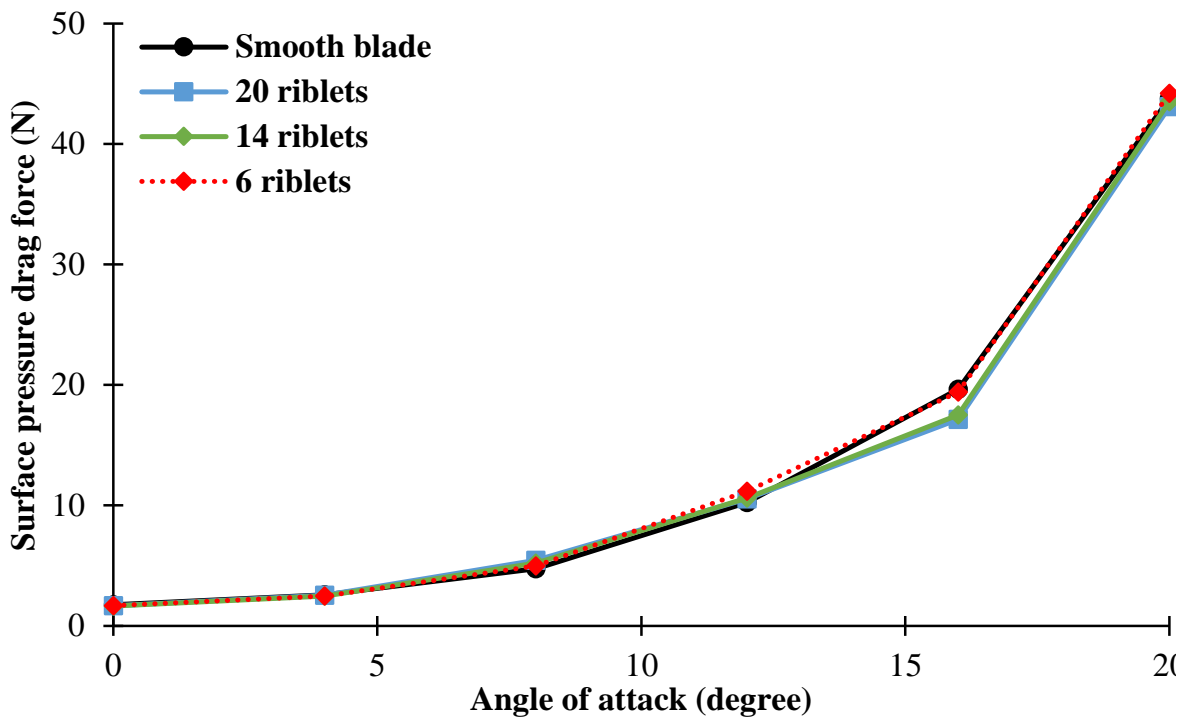


Figure 94: Surface pressure drag force versus AOAs for different number of riblets

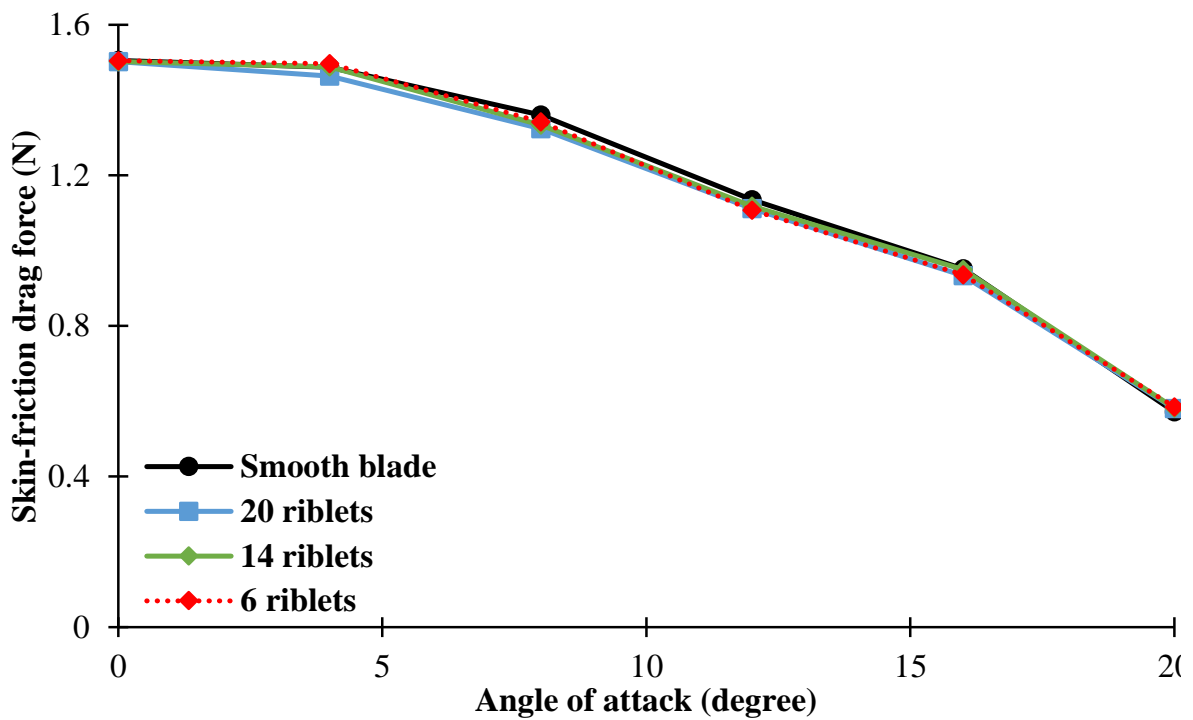


Figure 95: Skin-friction drag force versus AOAs for different number of riblets

### 5.3 Study Case 8 (3D, URANS, NREL phase II, SMM, $Re_c = 9.4 \times 10^5$ , Riblets)

#### 5.3.1 Purpose

Study case 8 is the core of the author's PhD research, as it examines the effect of trapezoidal base on improving the performance of the NREL phase II. The study contains 40 riblets with  $l^+ = 114 - 140$ , that are applied on the upper side of the NREL phase II blades. The modified WT performance is shown in terms of power coefficient versus various tip speed ratios. The tripped WT results are also compared to the smooth WT from study case 5 (section 8.5.4).

#### 5.3.2 Geometrical setup

The well-known NASA Ames wind tunnel that was described by Hand *et al.* [89] is considered as the fluid domain of study case 8. It is the same fluid domain that is used for study case 5 (Figure 221). In additions, the blades' and hub's geometries are already described in section 2.2.1, as in Figures 4 and 5, respectively. The boundary conditions are also shown in Figure 221. The triangular riblets are considered as part of the blades.

For the NREL phase II blade, the riblets are located near the blade tip as shown in Figure 96. This is because about 50% of wind turbine power is produced near the tip region that is about 25% of latter blade area [47]. The riblets begin at the maximum upper node of S809 aerofoil then extends towards trailing edge for 21mm. The spanwise length of riblets is 80mm. Figures 97 and 98 displays the triangular riblets on the blade latter section.

Viewing Figure 6, AOAs at riblets' region are calculated as in Equation (33):

$$\alpha = \tan^{-1} \left[ \frac{V_\infty}{\omega_B r} \right] - \phi \quad (33)$$

Where  $r$  is the local blade radius. It is a function of the total blade length (5.05m). The pitch angle ( $\phi$ ) is  $12^\circ$  and the angular velocity ( $\omega_B$ ) is 71.63rpm for the NREL phase II. According to Equation (33), and realizing that riblets spanwise length is 80mm, then the maximum AOA exists in this region is about  $16^\circ$ , while the minimum is  $1.2^\circ$ . Therefore, the computed results of tripped fixed blade with S809 aerofoil profile (study case 7) should be applicable for this work as its simulated AOAs are between  $0^\circ$  and  $20^\circ$ .

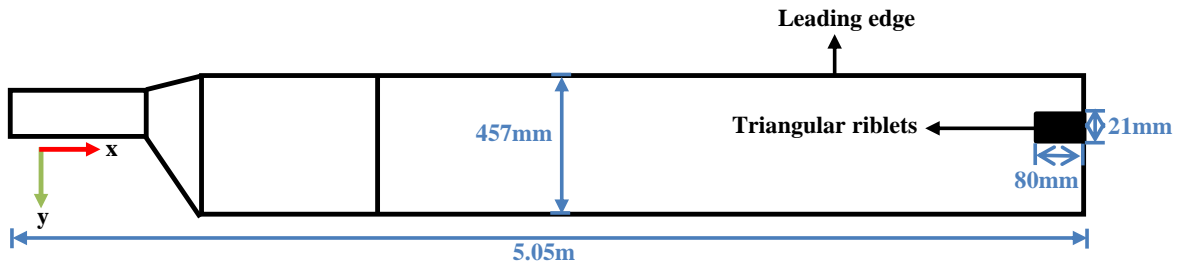


Figure 96: The top view of NREL phase II blade with riblets (not to scale)

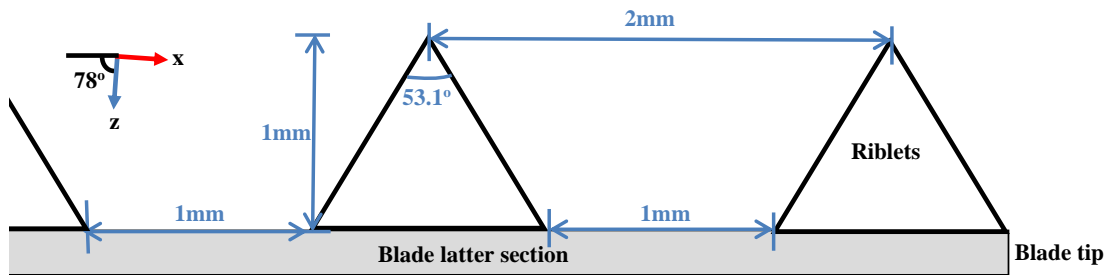


Figure 97: Triangular riblets on NREL phase II blade's suction side

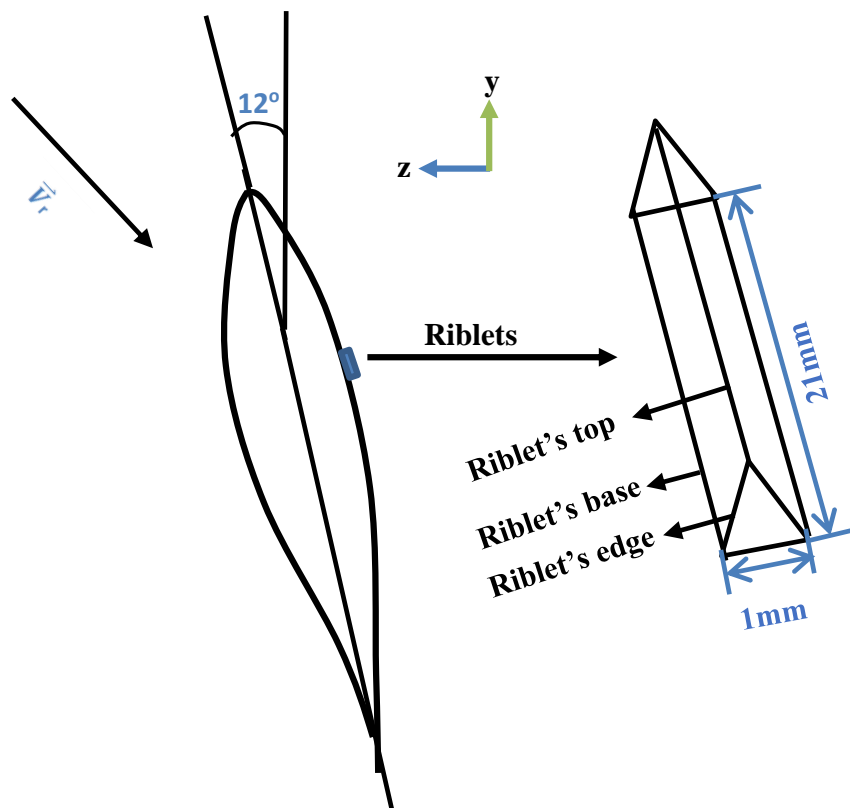


Figure 98: The riblets on the suction side of the blade at the tip

### 5.3.3 Mesh & computational setup

The mesh setting of study case 8 is the same mesh as study case 5 (section 8.5.3), as based on the validation of study case 5 against experiment. This indicates of applying the same maximum and minimum mesh element sizes. However, denser mesh is generated on the riblets region compared to other blade regions. This confidence of applying the same mesh size due to two reasons: first, there is no available experiment of the tripped NREL phase II to be validated against. Another reason is that the mesh size as well as inflation layers of study case 5 should also resolve the trapezoidal base.

For riblets' resolution. The selected mesh of riblets has 11 nodes for each edge of riblets. This includes the edges of the frontal and back sides of the riblets. The number of nodes of each base and top in the chordwise direction of riblets are 31 and 31 nodes, respectively. The first layer of mesh is placed at  $50\mu m$  above the riblets. The mesh metrics of study case 8 are shown in Figures 99 and 100 for skewness and orthogonality, respectively. The generated mesh of riblets in different directions are displayed in Figures 101-106.

Table 22 shows the average number of triangular mesh faces of each blade for the tripped and smooth NREL phase II. Table 23 represents the number of mesh cells for the tripped and smooth NREL phase II. This number includes the fluid domain mesh elements as well as the rotational body mesh elements. There are about 550 mesh faces for each riblet. In total, there are about  $22 \times 10^3$  mesh faces for 40 riblets on each blade. The simulation settings and air properties for this study case are displayed in Table 42.

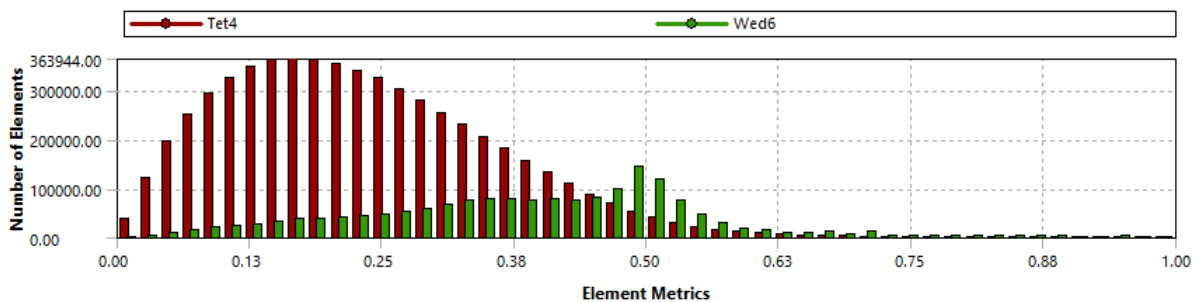


Figure 99: The skewness of study case 8

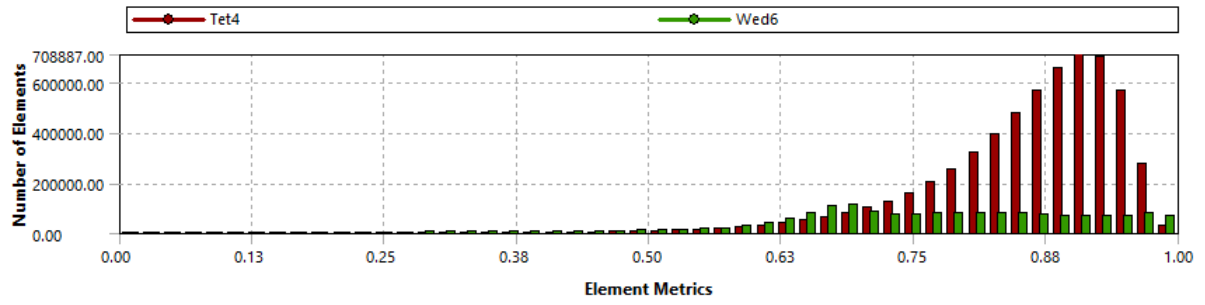


Figure 100: The orthogonality of study case 8

Table 22: Average number of the mesh triangular faces

NREL phase II	Average number of triangular mesh faces
Smooth	27, 228
Tripped	53, 666

Table 23: Total number of the mixed cells

NREL phase II	Number of mixed cells
Smooth	4, 726, 267
Tripped	8, 215, 682

ANSYS  
R16.1

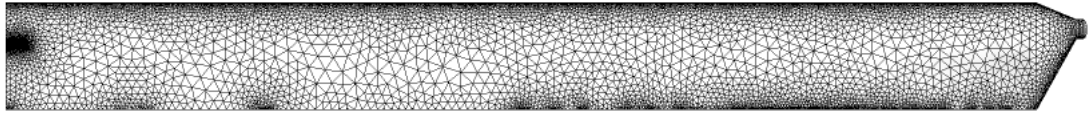
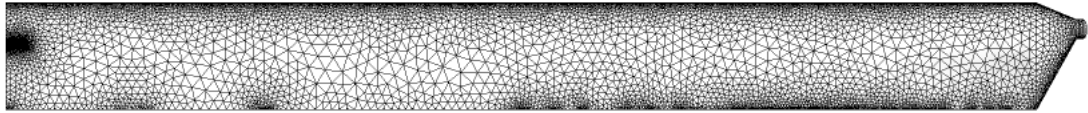


Figure 101: The generated mesh of the full blade and riblets for case 8

ANSYS  
R16.1

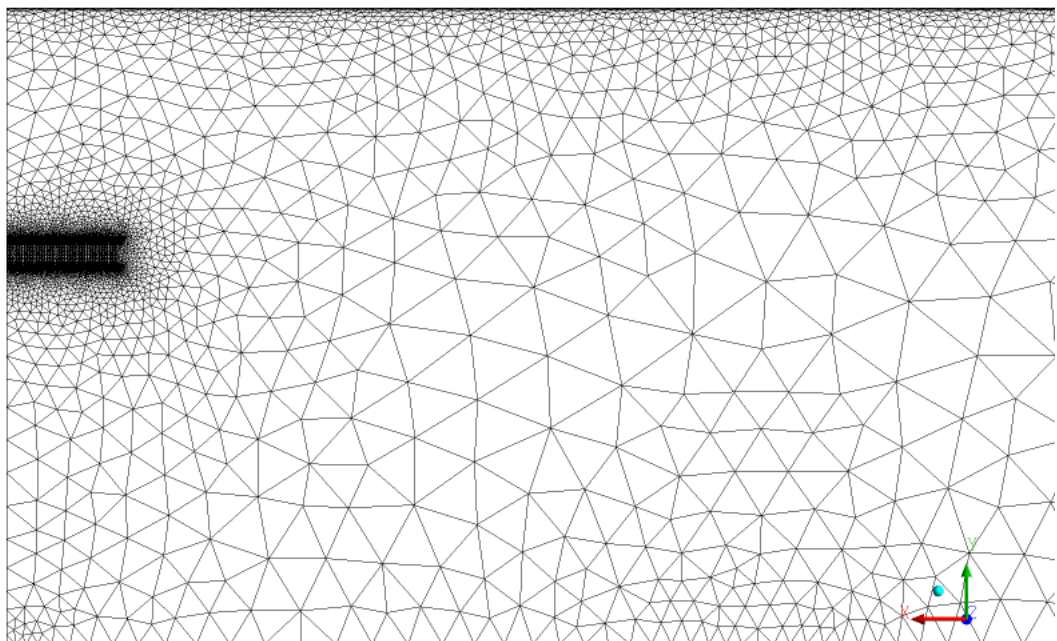


Figure 102: The generated mesh of the the blade and riblets for case 8 (zoom-in)

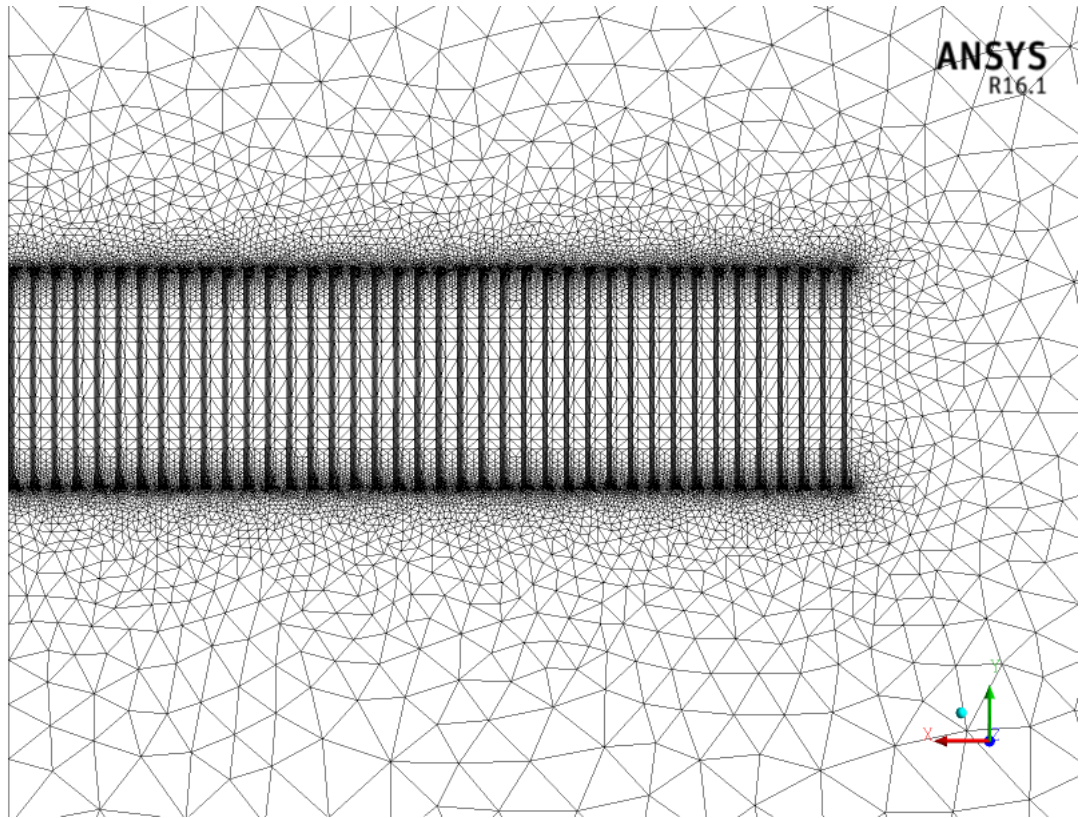


Figure 103: The generated mesh of the 40 riblets on the blade for case 8

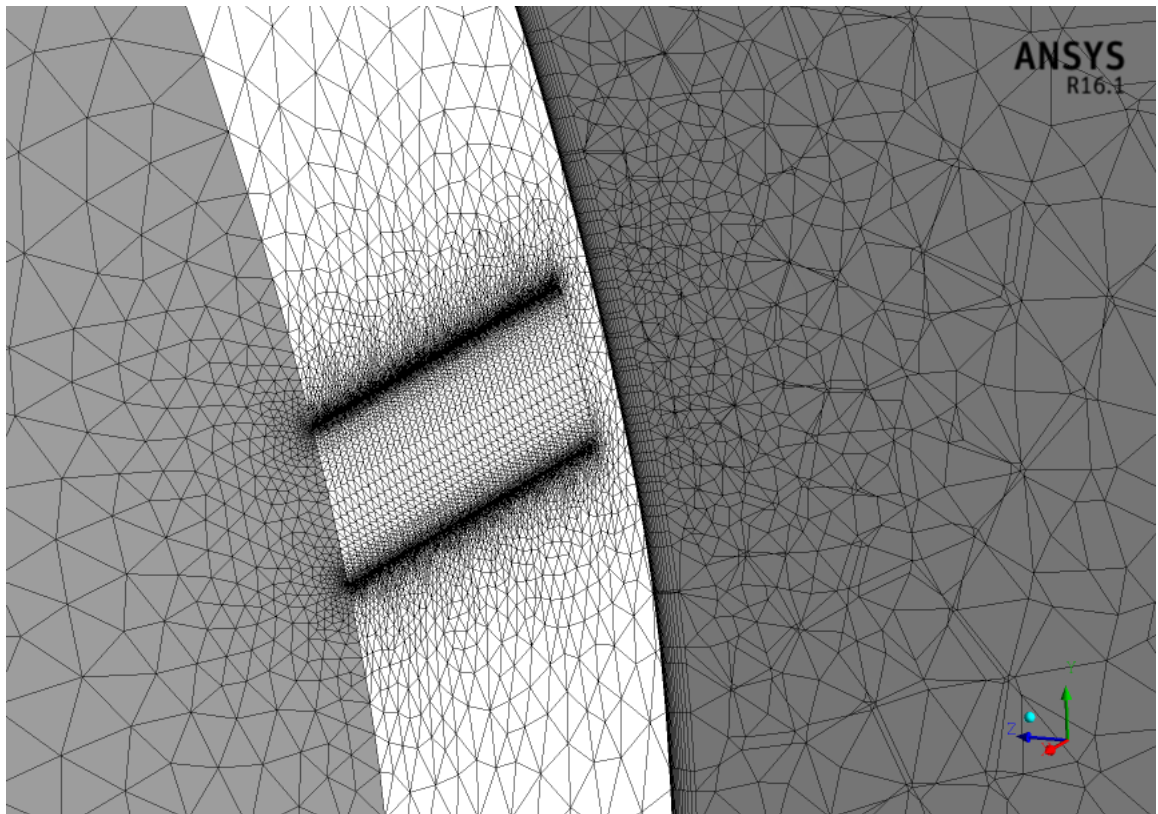


Figure 104: The simulated orientation of the blade and riblets for case 8

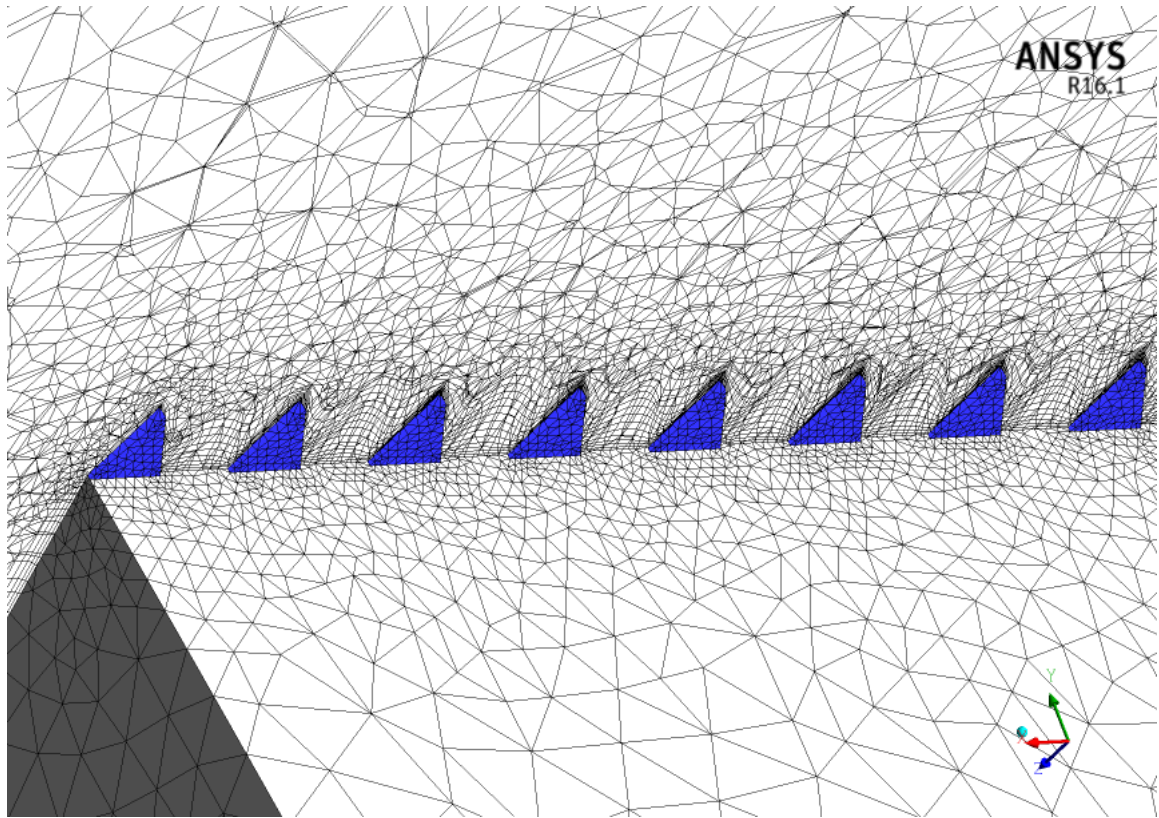


Figure 105: The generated mesh of a cross section of the riblets for case 8

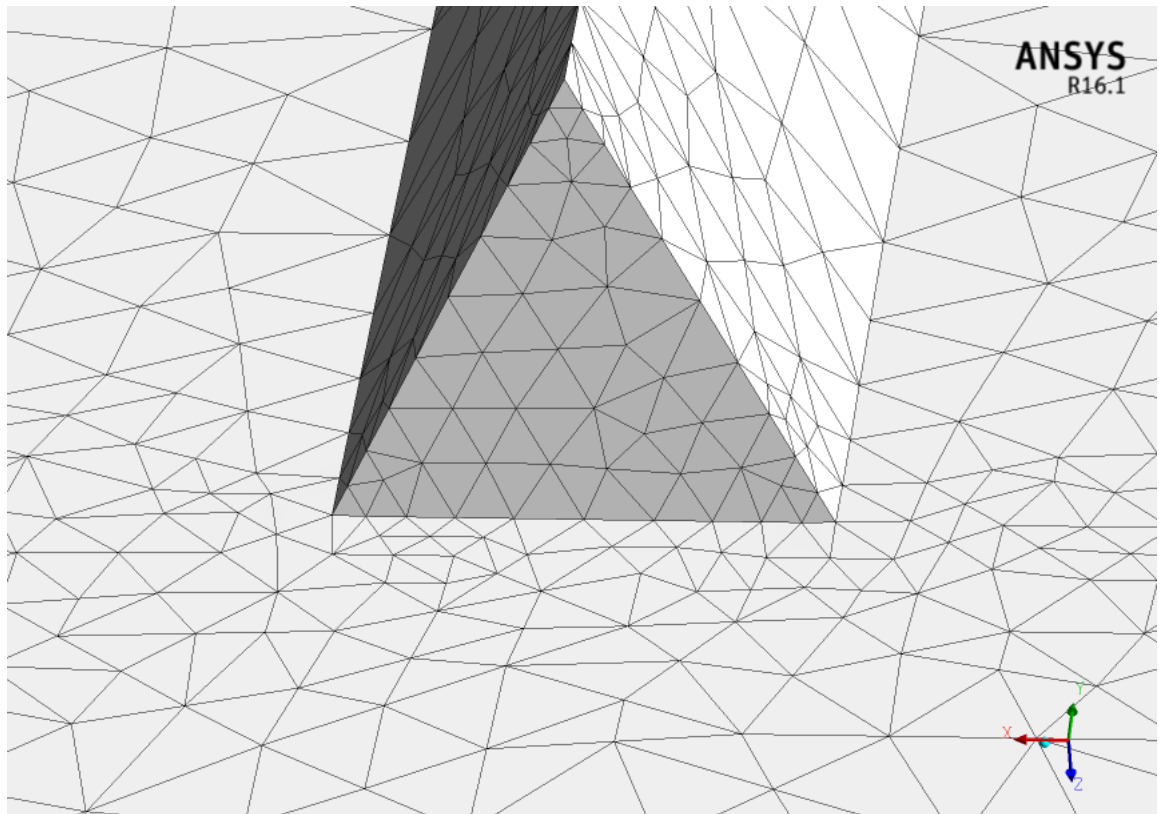


Figure 106: The generated mesh of one riblet for case 8

### 5.3.4 Results & discussion

The simulated time of study case 8 for torque coefficient is shown in Figures 107 and 108. The calculation of the torque coefficient is based on averaging the last circle of the simulated time, as marked in Figure 108. The  $y^+$  distribution over the chord line of the tripped blade at 99.7% span (location of riblets on the blade) is displayed in Figure 109. The  $y^+$  is less than 3 at all blade locations therefore, resolving viscous sub-layer. The riblets are located at about  $40\%c$  where  $y^+ < 2$ .

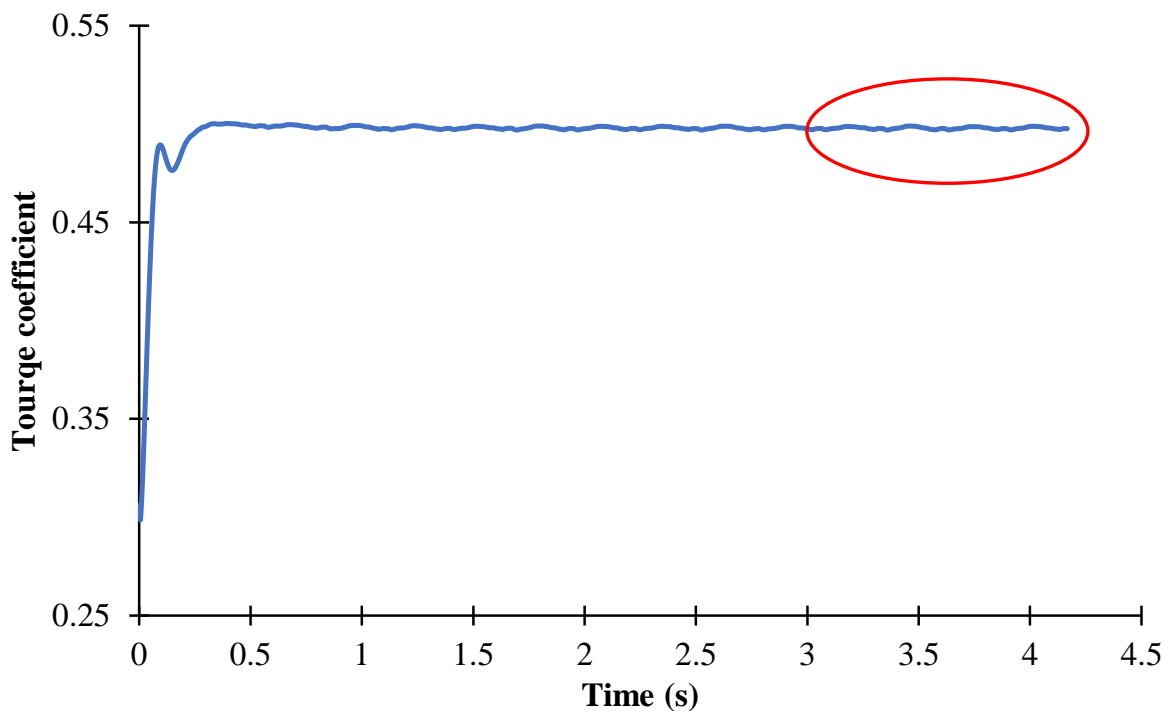


Figure 107: The simulated time of study case 8

Based on study case 7 (section 5.2.4), configuration II outperforms the other two configurations. Because both study cases experience the same range of AOAs and wind speeds, configuration II is applied on the wind turbine. Study case 8 is simulated using the *SST*  $k - \omega$  turbulence model to observe riblets' effect on the performance of the NREL phase II. The computed result is compared to the smooth NREL phase II (study case 5, section 8.5.4) by showing a change of the power coefficient at various wind speeds.

Figure 110 shows the power coefficient of the smooth and tripped NREL phase II. The tripped wind turbine shows an improvement at most simulated tip speed ratios. The influence of riblets can be clearly seen at high tip speed ratio. As wind speeds increases, the difference in

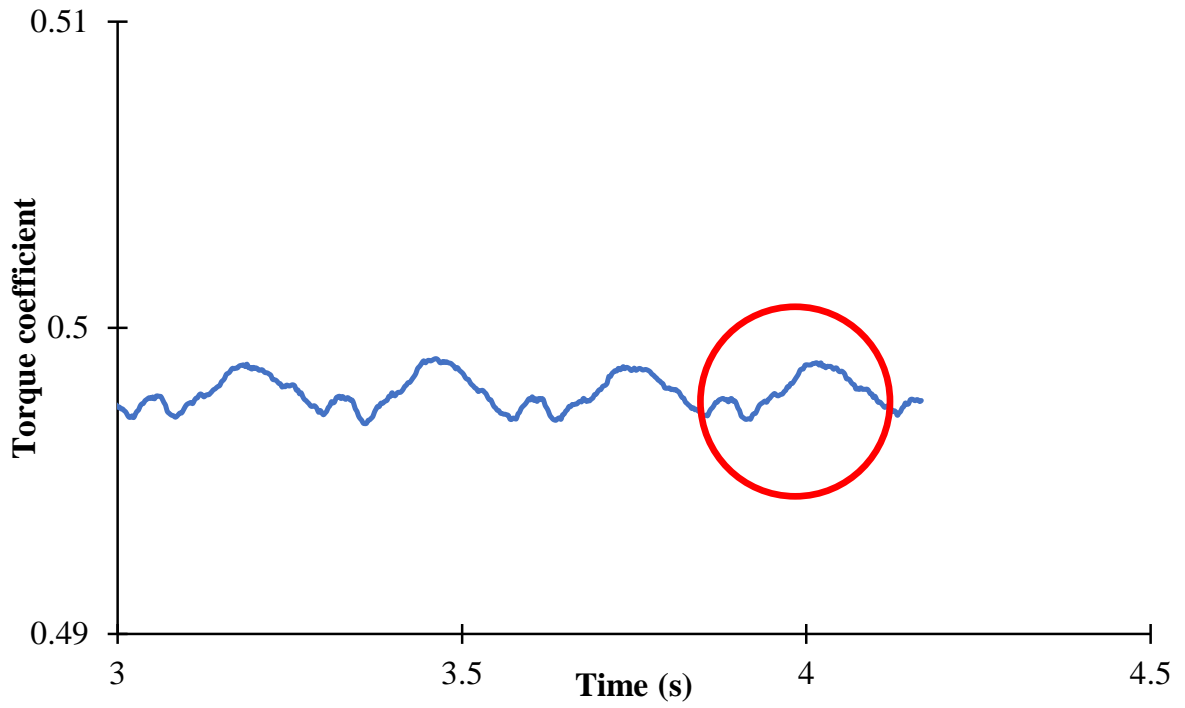


Figure 108: The simulated time of study case 8 (zoom-in)

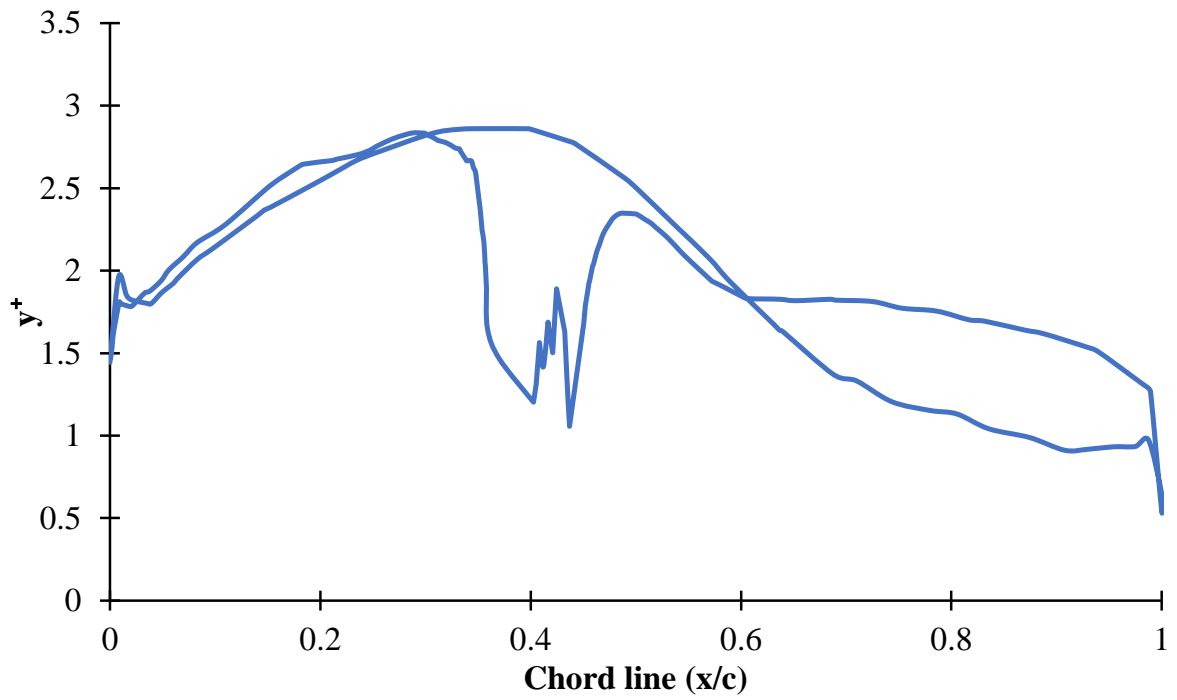


Figure 109: The  $y^+$  distribution of study case 8

performance is decreased, as shown in Table 24. The maximum increase of power coefficient is at  $7m/s$ , while the minimum increase is at  $12.5m/s$ . In summary, The effect of riblets on the wind turbine performance depends on the riblets' configuration and tip speed ratio.

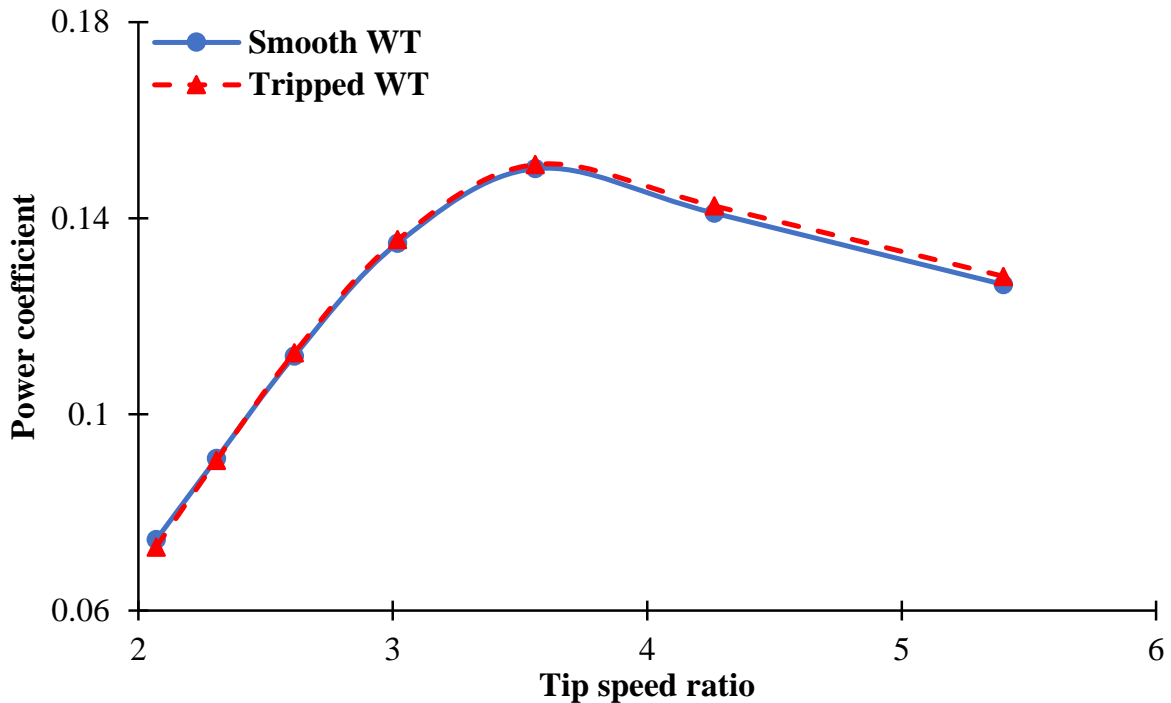


Figure 110: Power coefficient versus tip speed ratio for the smooth and tripped wind turbines

The explanation on how riblets improve (at low wind speed) or degrade (at high wind speed) the performance of wind turbine is shown as follows:

\* **Wind turbine performance improvement:** there are some cases where wind turbine performance is improved because of applying riblets. At wind speed of  $V_\infty = 7m/s$ , the performance of the tripped wind turbine is increased by 1.32%. Therefore, this case is taken as an example for wind turbine performance improvement.

1. **Pressure Contour.** Figures 111 and 112 show the pressure contour of the smooth and tripped WTs at 30% span, respectively. The tripped blade experiences a lower pressure on the suction side, which leads to increasing the lift force and therefore, better wind turbine performance. The pressure contours of the smooth and tripped WTs at 99.7% span (location of riblets) are displayed in Figures 113 and 114, respectively. The tripped blade's pressure of the lower side is higher than that of the smooth blade. This means riblets can change the pressure distribution over the blade.

Table 24: Percentage change in power coefficient of the tripped WT compared to the smooth WT

Tip speed ratio	Smooth WT ( $C_P$ )	Tripped WT ( $C_P$ )	Difference
5.40	12.6%	12.8%	1.32%
4.26	14.1%	14.3%	1.03%
3.56	15.0%	15.1%	0.57%
3.02	13.5%	13.6%	0.51%
2.61	11.2%	11.3%	0.54%
2.31	9.10%	9.06%	-0.41%
2.07	7.45%	7.30%	-2.02%

- 2. Velocity contour & velocity vector.** The velocity contours at 30% span of the smooth and tripped WTs are shown in Figures 115 and 116, respectively. The flow separation occurs earlier for the smooth WT. This means the centrifugal force is higher for the tripped WT resulting in more resistance flow to boundary layer separation. Figures 117 and 118 display the velocity contour at the riblets' location for smooth and tripped WTs, respectively. Because of the riblets, the flow speed is increased leading to a better wind turbine performance. This can be clearly seen as velocity vectors in Figures 119 and 120 for both WTs. A very small circulation zone is observed behind the riblet, as shown in Figure 121, thereby, improving the wind turbine performance.
- 3. Chordwise's streamlines.** Figures 122 and 123 show the streamlines of the tripped and smooth wind turbines at 80% span, respectively. The difference between the two figures is that there is a flow separation zone on the pressure side of the smooth blade, as shown in Figure 124. This flow separation zone is completely removed from the tripped wind turbine. It is believed that riblets are able to prevent flow separation and therefore enhance the wind turbine performance.
- 4. Spanwise's streamlines.** The streamlines in the spanwise direction of the smooth and tripped WTs are displayed in Figures 125 and 126, respectively. The same flow is shown for both WTs on the blade's suction side. Similarly, the pressure side is exposed to the same flow for both WTs. However, there is an observable flow separation zone near the tip of the smooth blade. This leads to a higher tripped wind turbine performance.

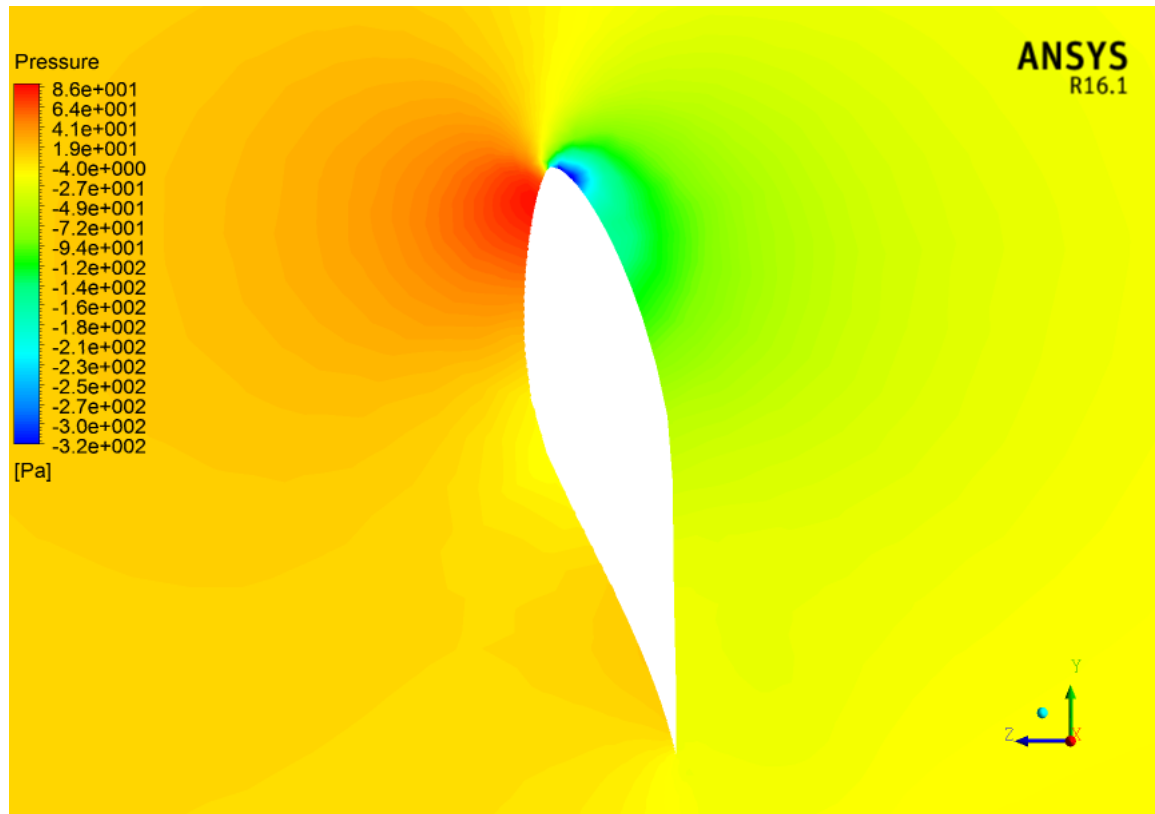


Figure 111: The pressure contour of the smooth WT at 30% span at  $V_\infty = 7m/s$

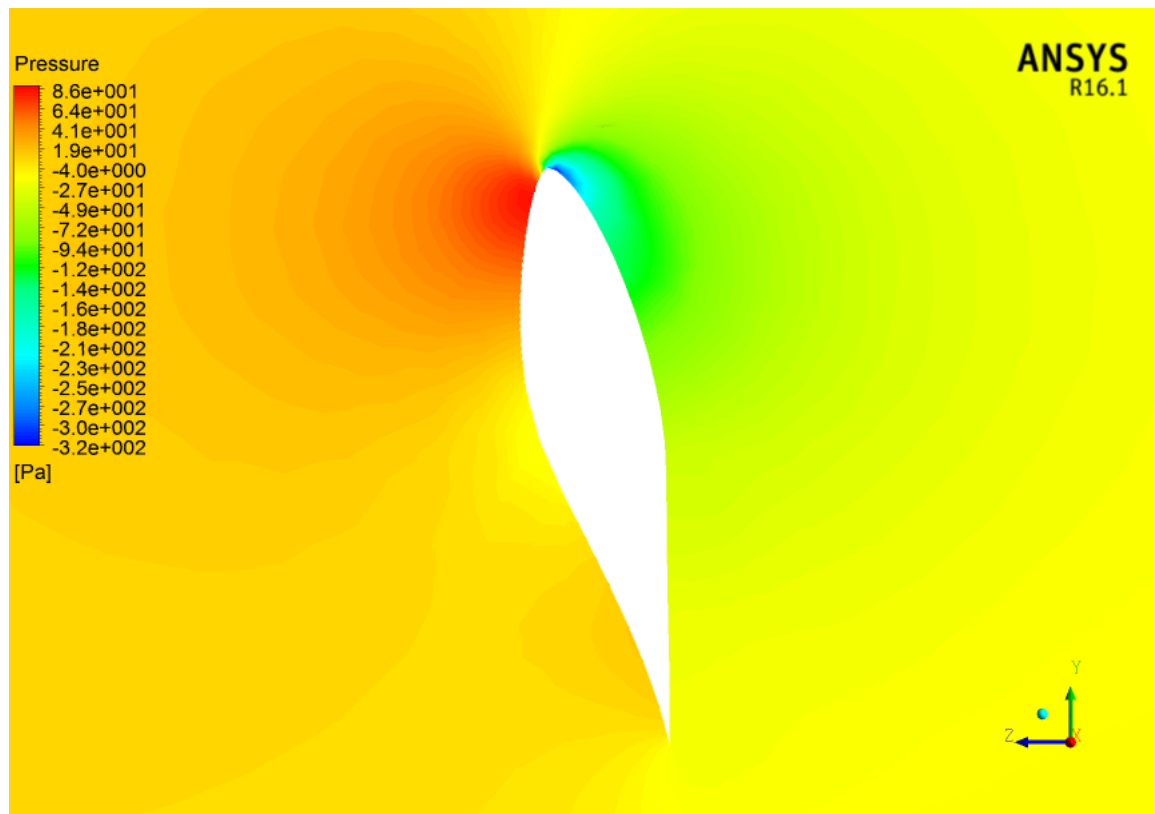


Figure 112: The pressure contour of the tripped WT at 30% span at  $V_\infty = 7m/s$

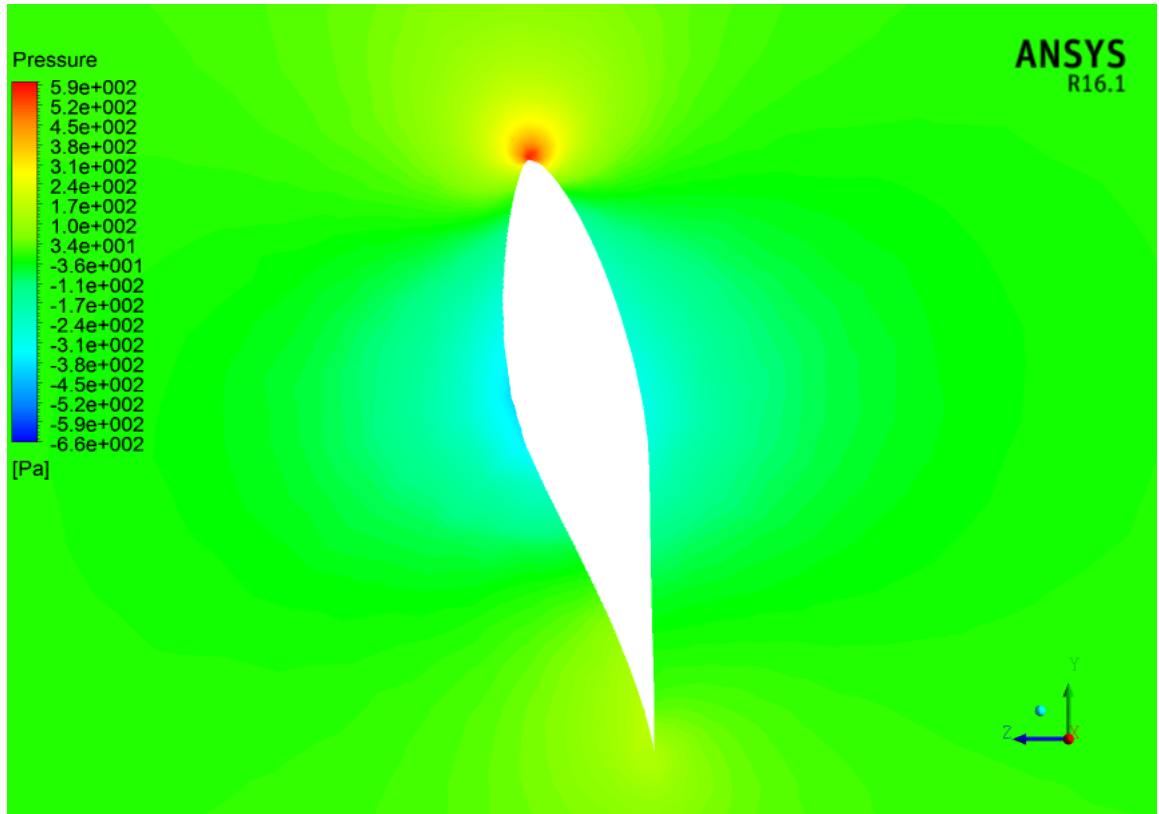


Figure 113: The pressure contour of the smooth WT at 99.7% span (riblets' location) at  $V_\infty = 7m/s$

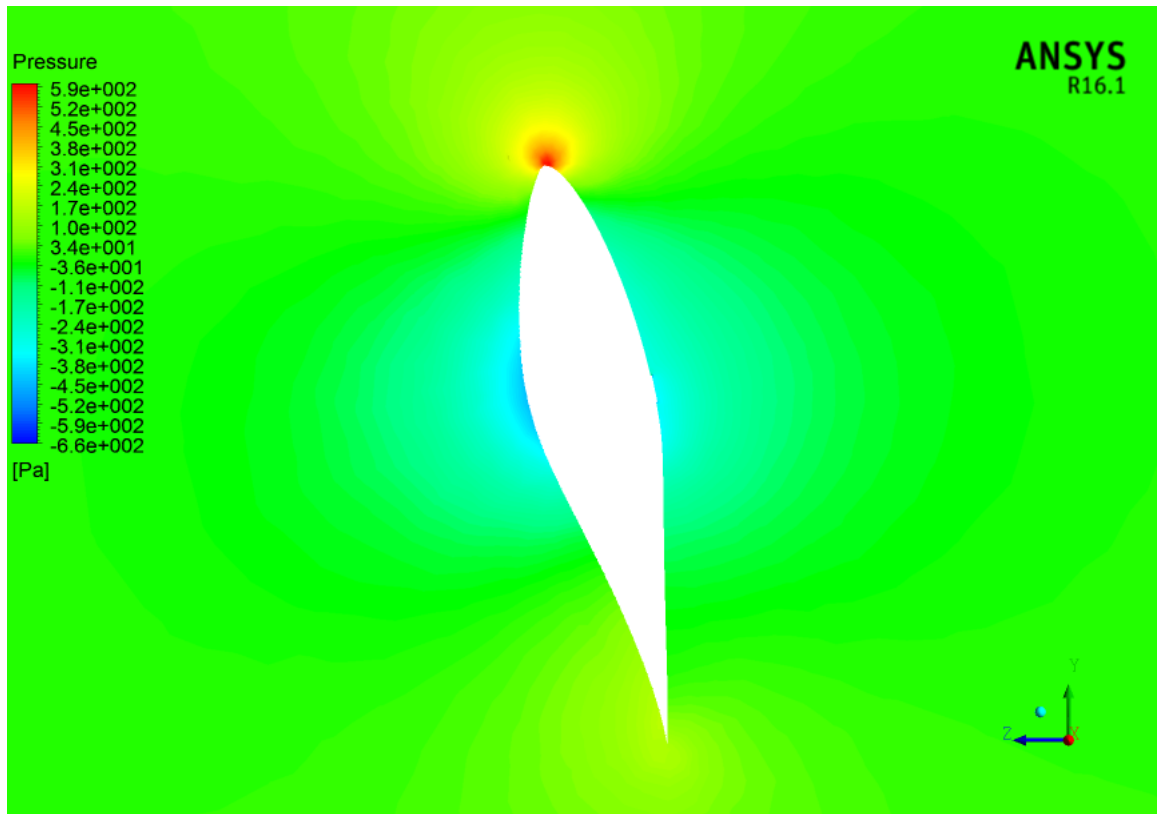


Figure 114: The pressure contour of the tripped WT at 99.7% span (riblets' location) at  $V_\infty = 7m/s$

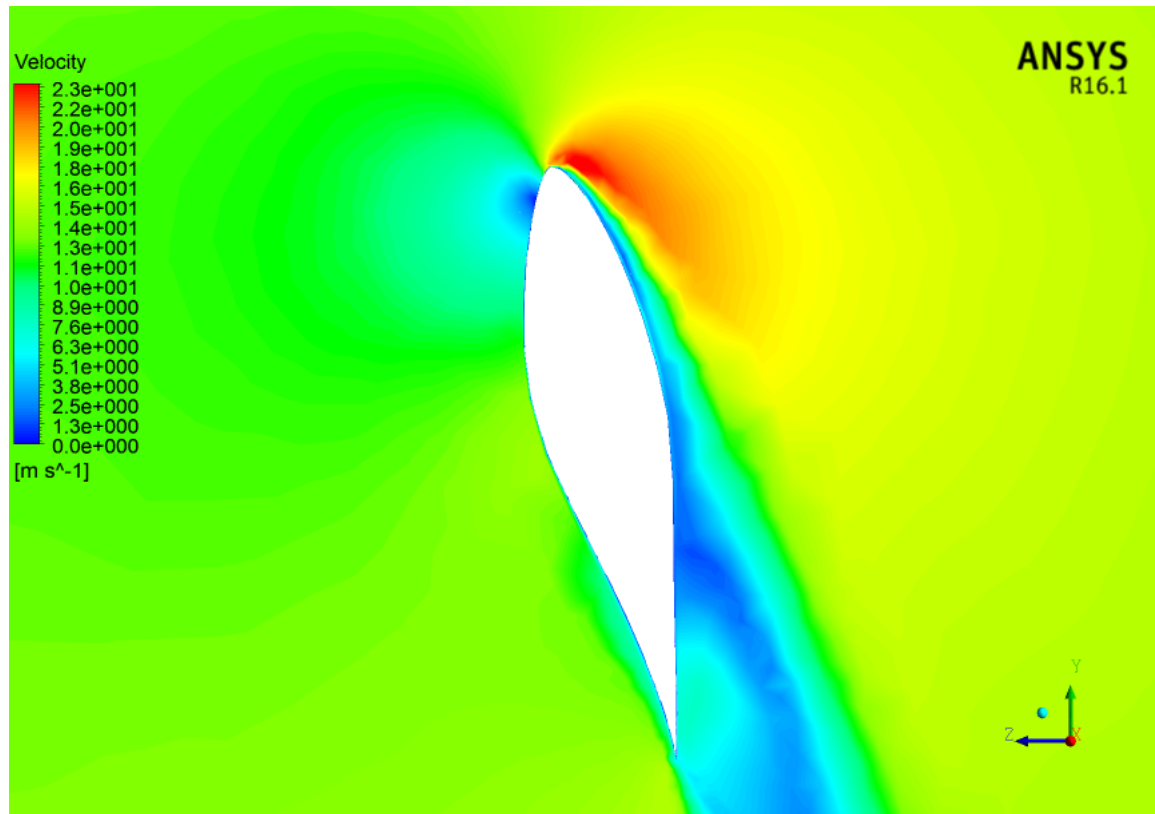


Figure 115: The velocity contour of the smooth WT at 30% span at  $V_\infty = 7m/s$

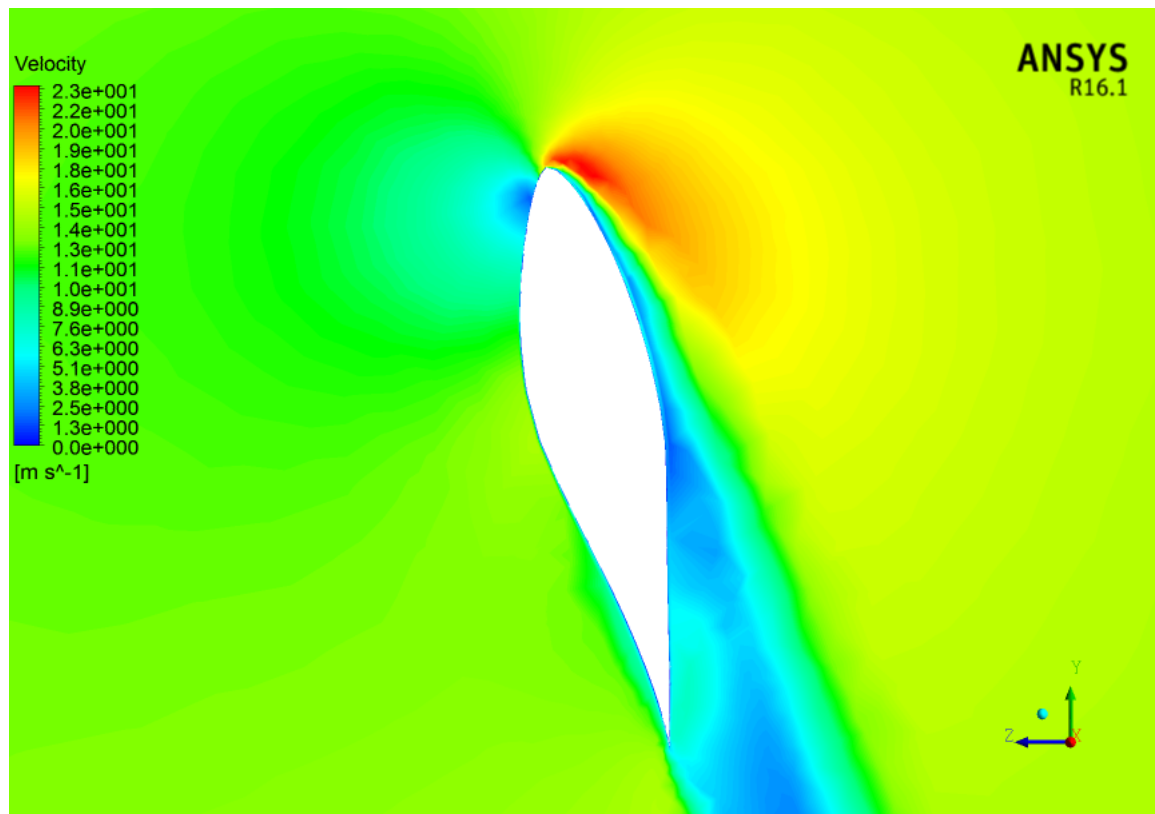


Figure 116: The velocity contour of the tripped WT at 30% span at  $V_\infty = 7m/s$

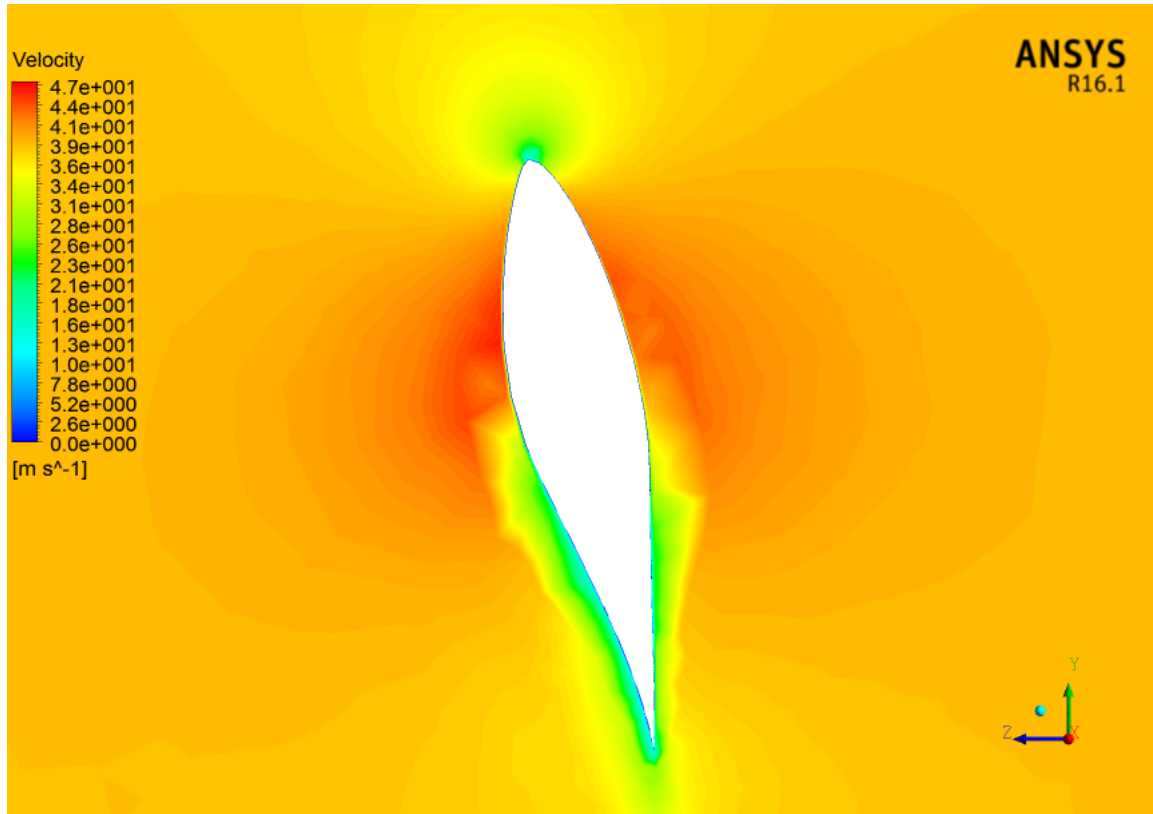


Figure 117: The velocity contour of the smooth WT at 99.7% span (riblets' location) at  $V_\infty = 7m/s$

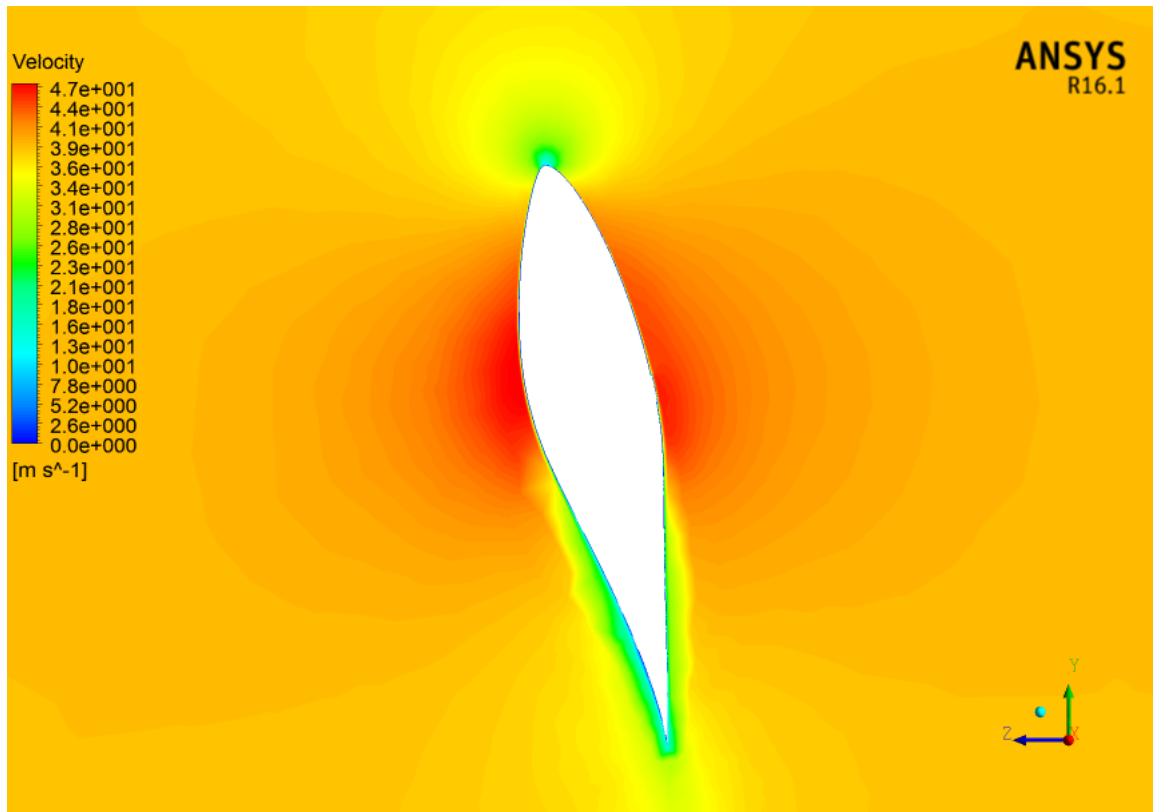


Figure 118: The velocity contour of the tripped WT at 99.7% span (riblets' location) at  $V_\infty = 7m/s$

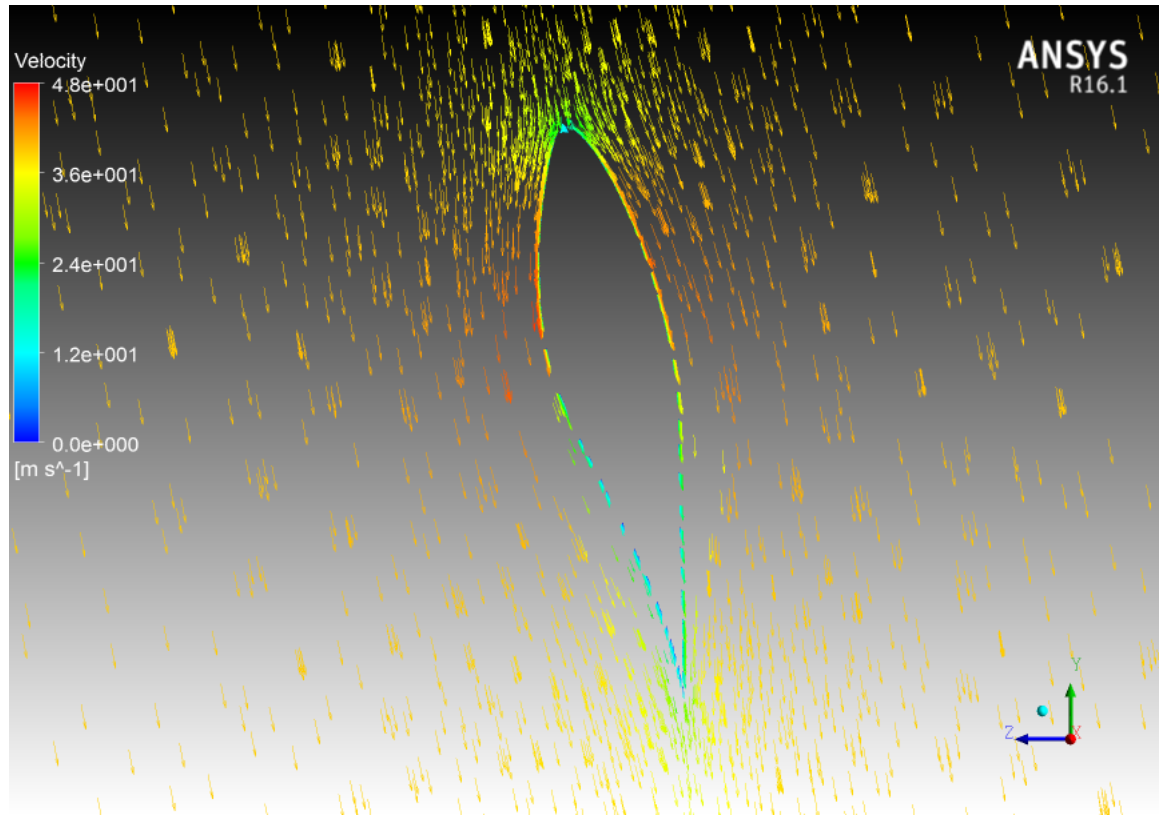


Figure 119: The velocity vector of the smooth WT at 99.7% span (riblets' location) at  $V_\infty = 7m/s$

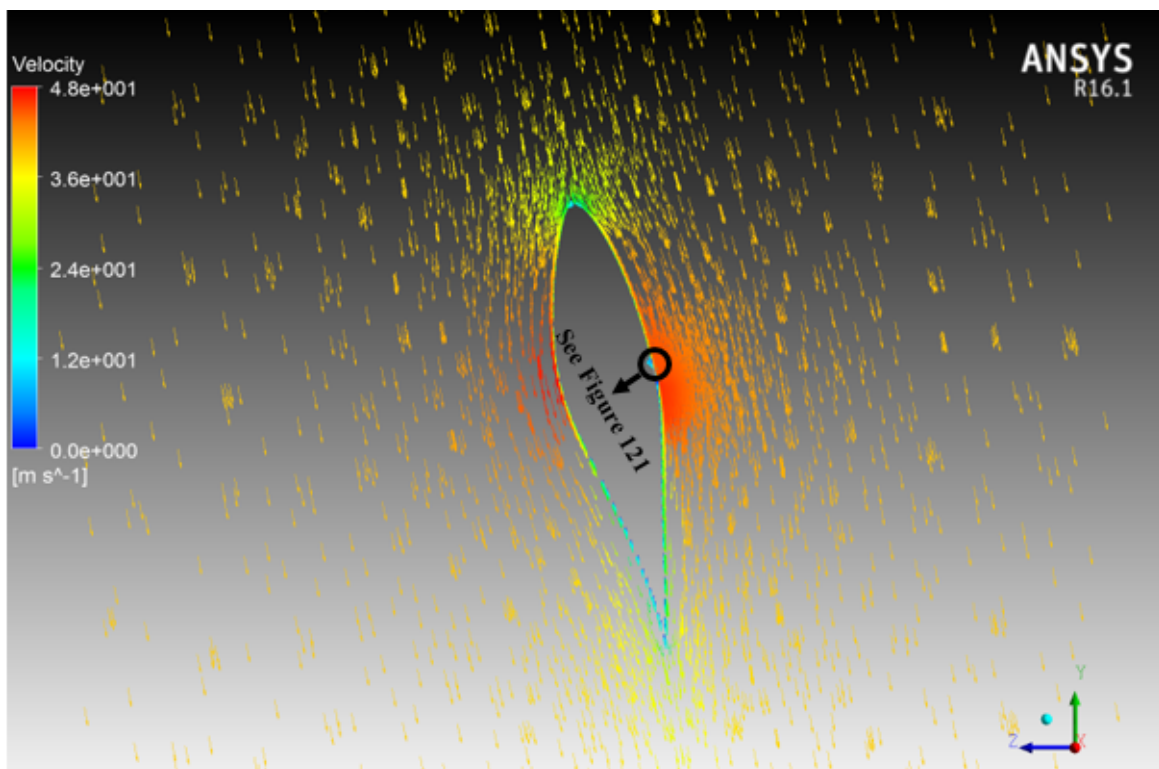


Figure 120: The velocity vector of the tripped WT at 99.7% span (riblets' location) at  $V_\infty = 7m/s$

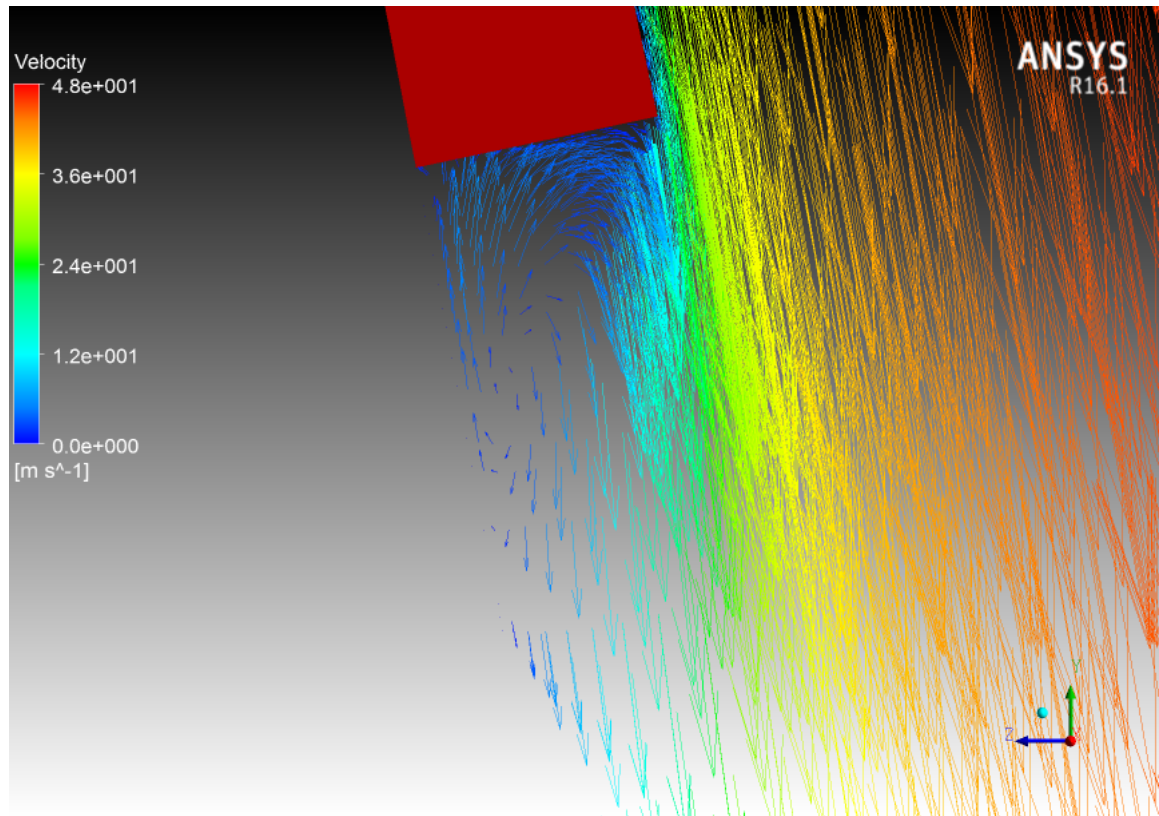


Figure 121: The velocity vector of the tripped WT at 99.7% span (zoom-in) at  $V_\infty = 7\text{m/s}$

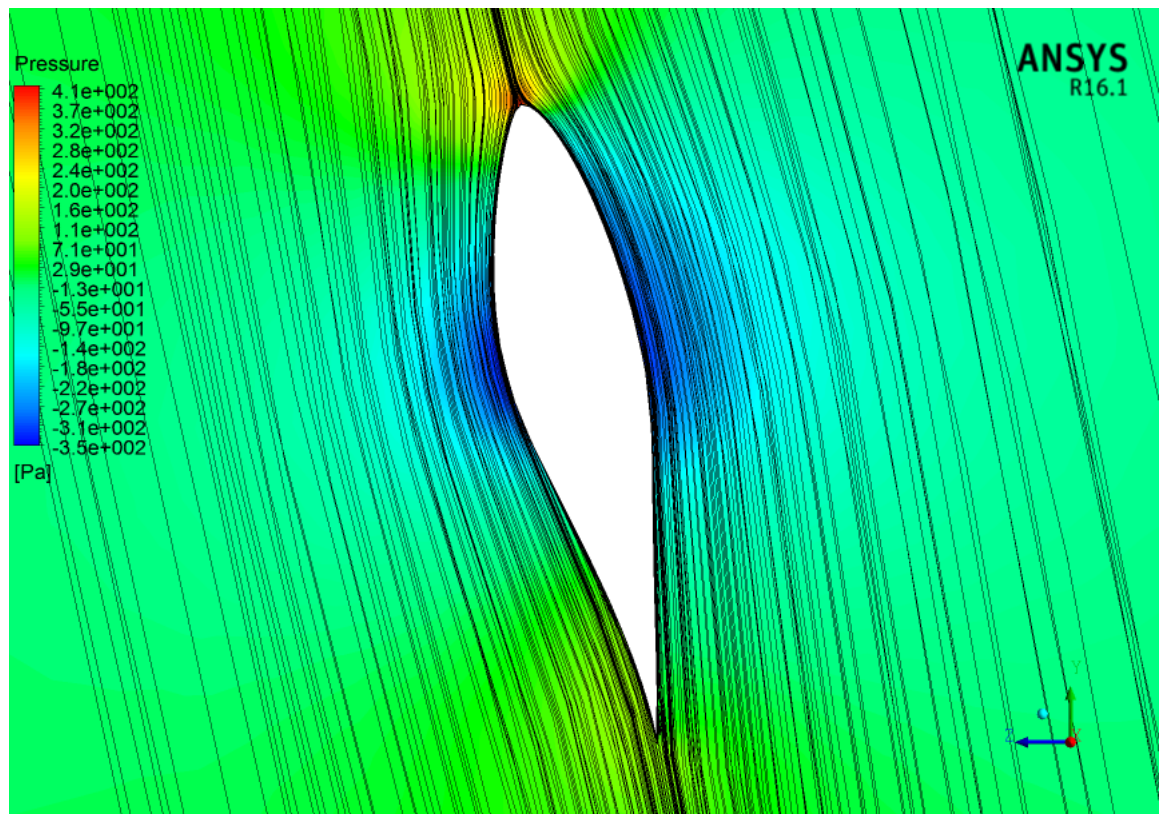


Figure 122: The streamline of the tripped WT at 80% span at  $V_\infty = 7\text{m/s}$

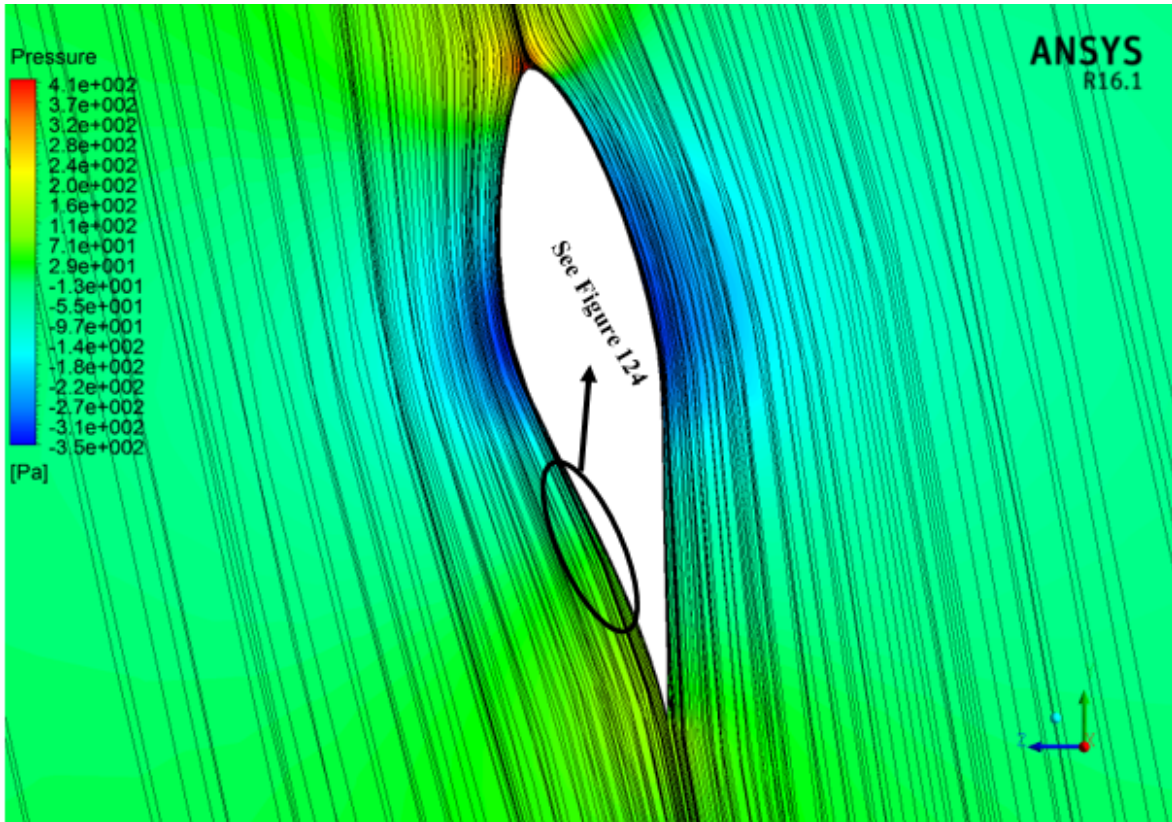


Figure 123: The streamline of the smooth WT at 80% span at  $V_\infty = 7m/s$

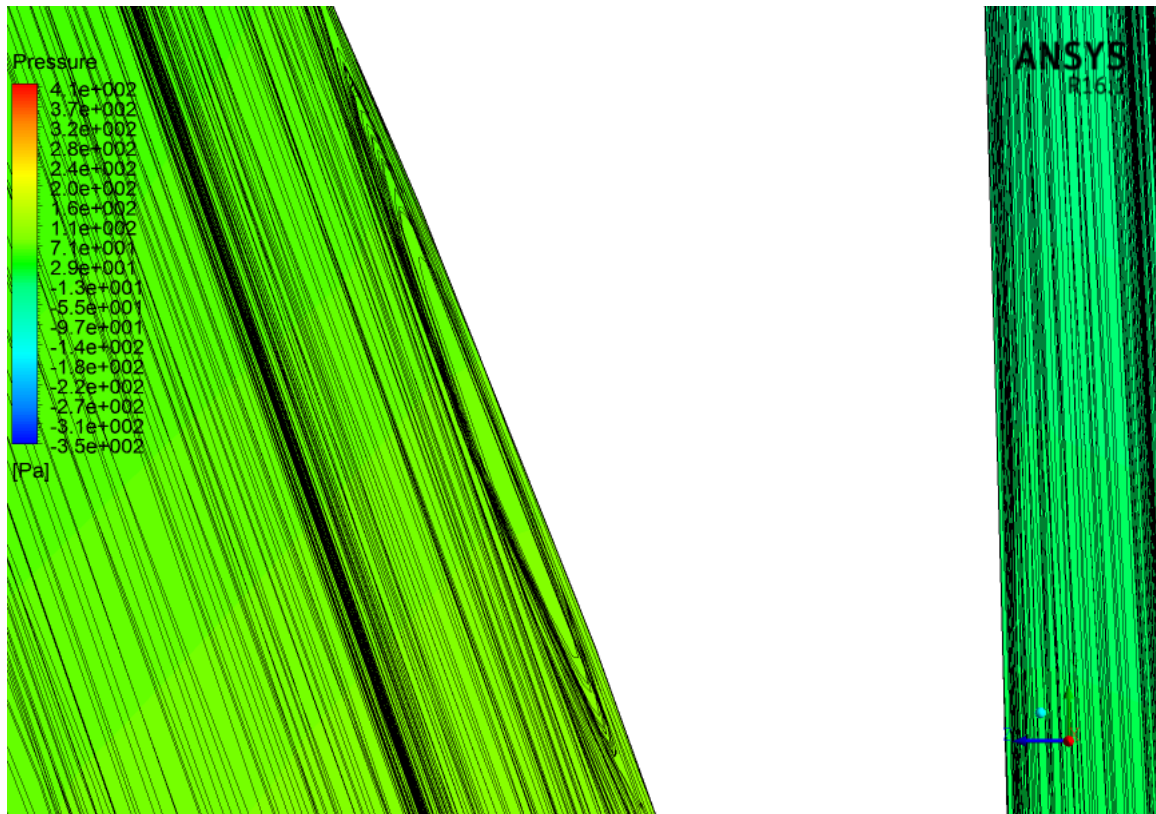


Figure 124: The streamline of the smooth WT at 80% span at  $V_\infty = 7m/s$  (zoom-in)

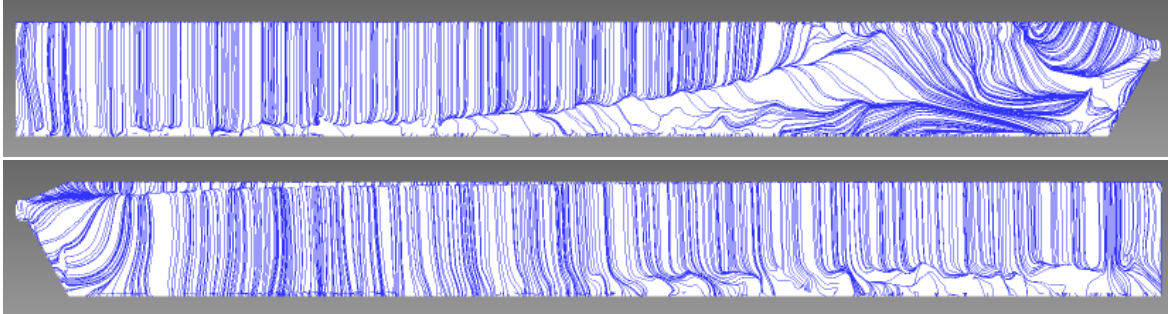


Figure 125: The streamlines (spanwise) of the smooth WT at  $V_\infty = 7\text{ m/s}$  (top: suction, bottom: pressure)

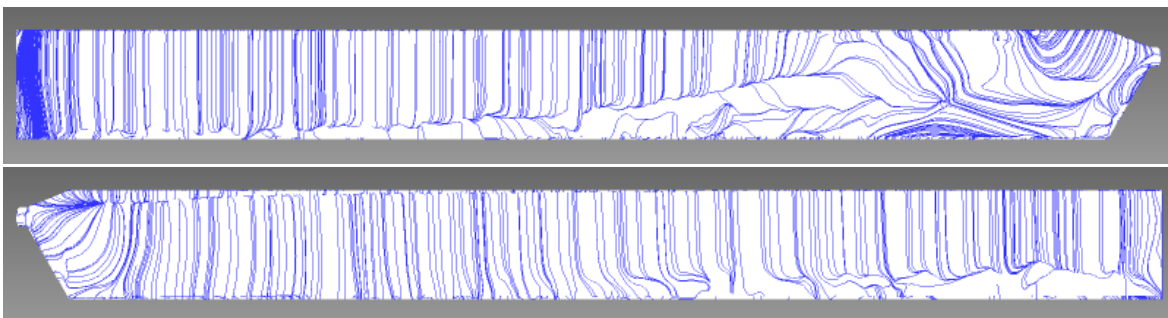


Figure 126: The streamlines (spanwise) of the tripped WT at  $V_\infty = 7\text{ m/s}$  (top: suction, bottom: pressure)

\* **Wind turbine performance degradation:** there are some cases where wind turbine performance is reduced because of applying riblets. At wind speed of  $V_\infty = 18m/s$ , the performance of the tripped wind turbine is decreased by 2.02%. Therefore, this case is taken as an example for wind turbine performance degradation.

1. **Pressure contour & chordwise's streamlines.** The pressure contour and the streamline of the smooth and tripped wind turbines at 80% span are shown in Figures 127 and 128, respectively. The tripped wind turbine shows two flow separation zones rather than one as in the smooth wind turbine. The two flow separation zones are the cause for the wind turbine performance degradation. In addition, the pressure on the suction side of the tripped wind turbine seems to be higher than that of the smooth one, which leads to a reduction of wind turbine performance.
2. **Velocity contour.** The velocity contour of the smooth and tripped wind turbines at 80% span are displayed in Figures 129 and 130, respectively. The flow is more resistant to leading edge separation for the smooth wind turbine. However, the tripped wind turbine shows a flow separation due to the leading edge. Decreasing the flow speed means a reduction in the wind turbine's performance.
3. **Spanwise's streamlines.** Figures 131 and 132 show the streamlines in the spanwise direction of the smooth and tripped WTs, respectively. The streamlines in both WTs are exposed to the same behaviour, resulting in a strong spanwise flow from root to tip of the blade's suction side that is drawn by centrifugal force. This is due to a high wind speed and therefore high AOAs exist. The flows on the pressure side of both WTs are almost not separated.

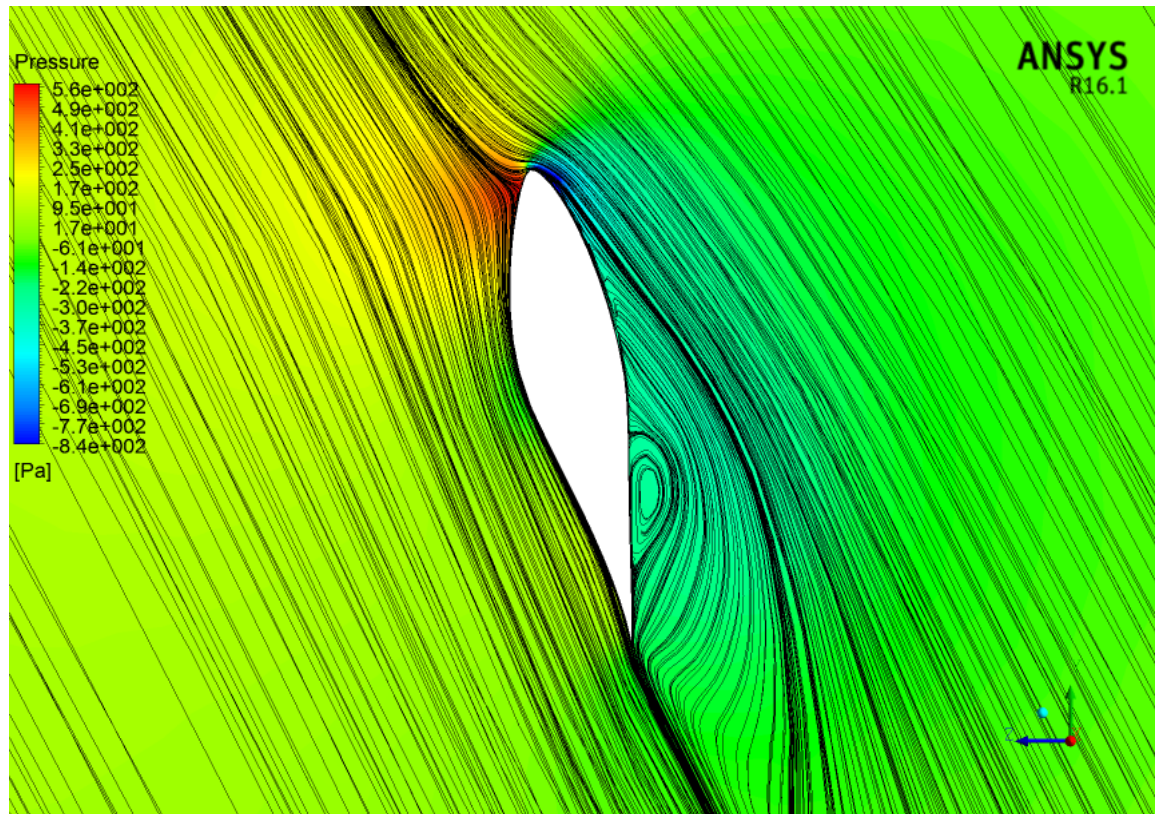


Figure 127: The streamline & pressure contour of the smooth WT at 80% span at  $V_\infty = 18m/s$

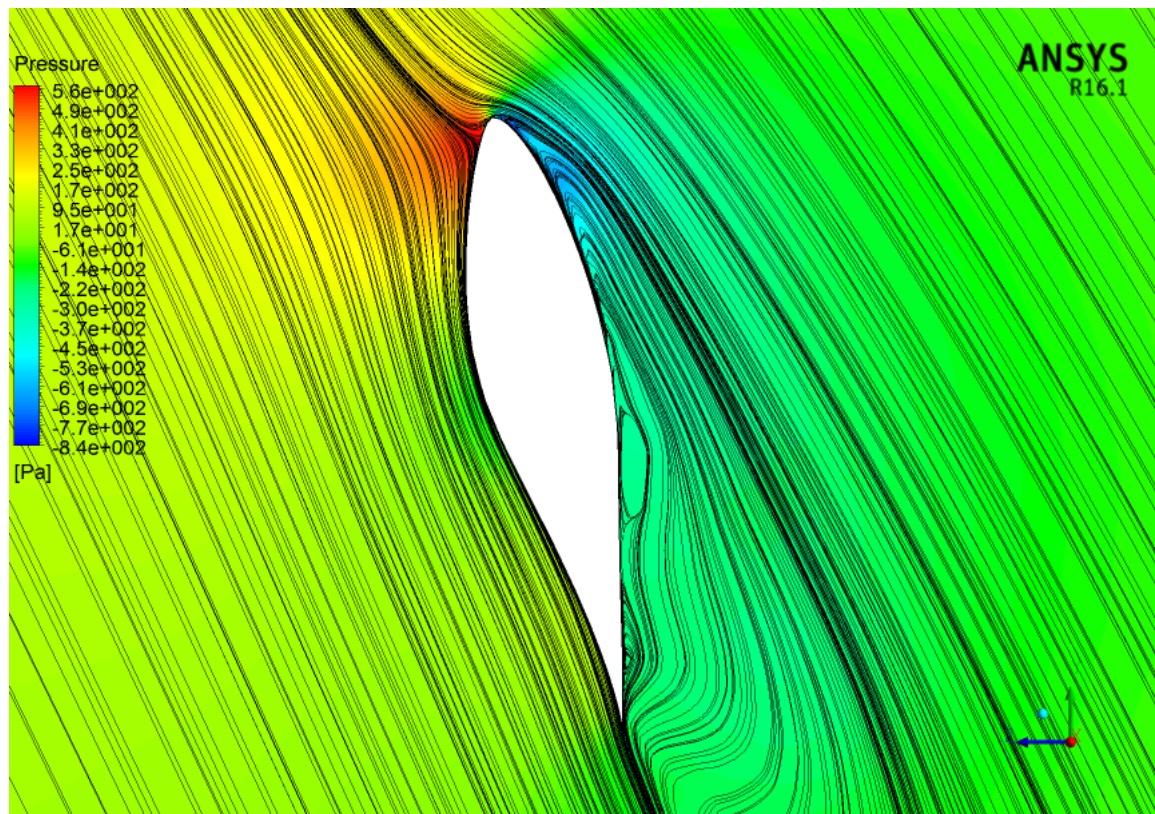


Figure 128: The streamline & pressure contour of the tripped WT at 80% span at  $V_\infty = 18m/s$

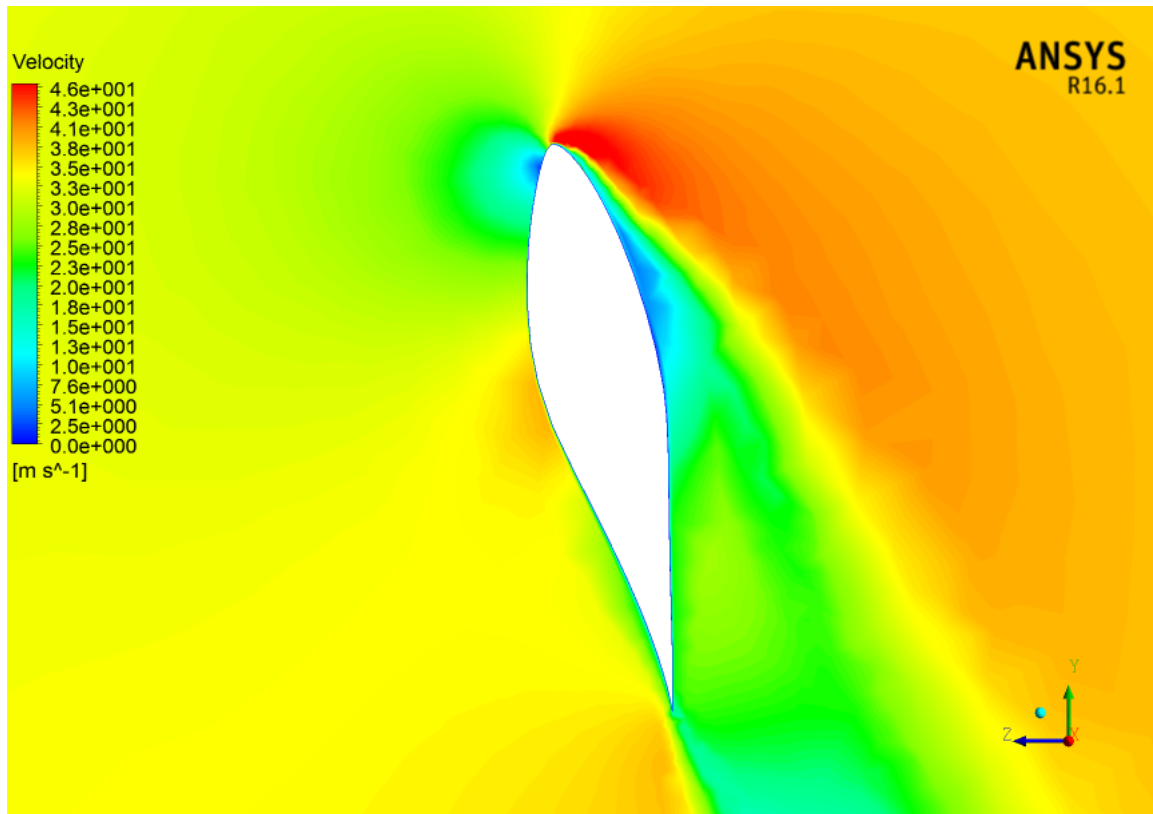


Figure 129: The velocity contour of the smooth WT at 80% span at  $V_\infty = 18\text{m/s}$

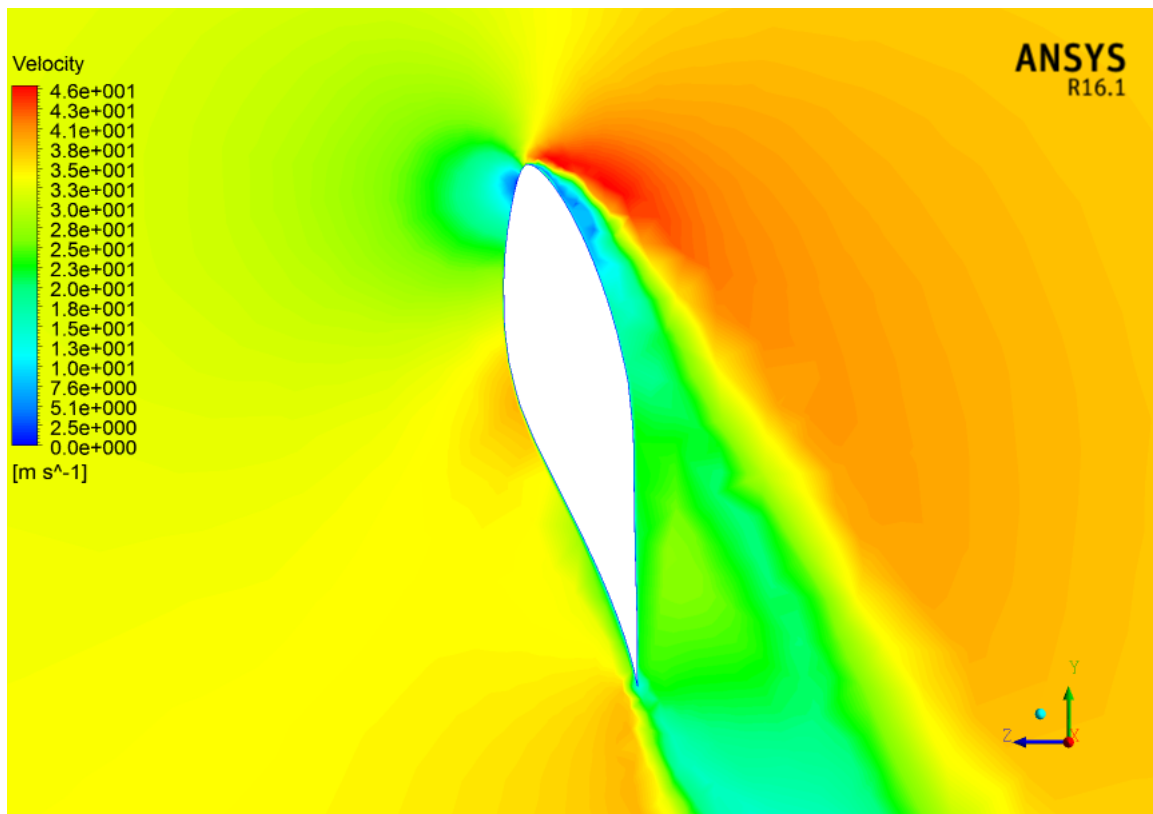


Figure 130: The velocity contour of the tripped WT at 80% span at  $V_\infty = 18\text{m/s}$

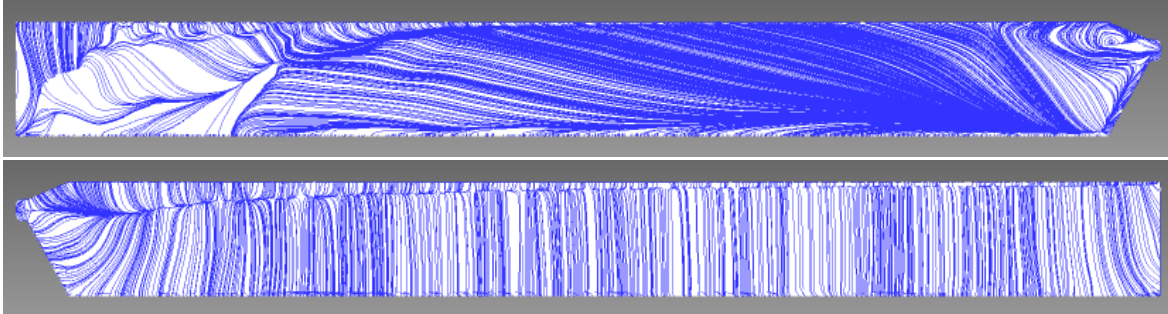


Figure 131: The streamlines (spanwise) of the smooth WT at  $V_\infty = 18m/s$  (top: suction, bottom: pressure)

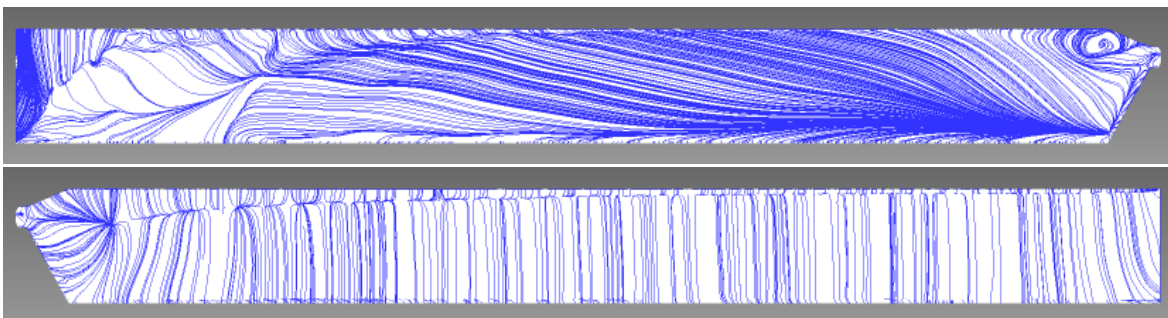


Figure 132: The streamlines (spanwise) of the tripped WT at  $V_\infty = 18m/s$  (top: suction, bottom: pressure)

## 6 IMPROVING PERFORMANCE OF NREL PHASE II

Four separate studies are done to further improve the wind turbine performance for  $l^+ = 114 - 140$ . The four studies are changing number of riblets, applying riblets on both blade sides and only on the pressure side of the blade, and changing the riblets' orientation.

### 6.1 Number of riblets

#### 6.1.1 Geometrical setup

The fluid domain and the wind turbine of this study case are the same as study case 5 (section 8.5.2), that are shown in Figures 221 and 4, respectively. The same riblet configuration of study case 8 (section 5.3.2), as displayed in Figures 96-98, is simulated except that the number of riblets is changed to observe their effect on WT. The tested number of riblets are 40, 30 and 20 riblets.

#### 6.1.2 Mesh element number

The mesh setting of this study case is the same as study case 5 (section 8.5.3), including the element sizes and the inflation layers. Table 25 shows the average number of triangular mesh on each blade of the NREL phase II. Table 26 represents the total mesh elements, including the mesh elements of the fluid domain and the wind turbine. Referring to Tables 25 and 26, increasing the number of riblets requires more mesh elements. Therefore, more simulated time is needed.

#### 6.1.3 Result & discussion

Figure 133 shows the power coefficient of the NREL phase II at various tip speed ratios for different number of riblets. A better wind turbine performance is only recorded for 40 and 30 riblets. This is because different AOAs are existed in this region of the blade. However, this also leads to a negative performance for 20 riblets. The more riblets added in the spanwise

Table 25: Average number of the mesh (triangular faces)

Number of riblets	Average number of triangular mesh faces
Smooth NREL phase II	27, 228
40 riblets	53, 666
30 riblets	47, 727
20 riblets	41, 741

Table 26: Total number of mixed cells

Number of riblets	Number of the mixed cells
Smooth NREL phase II	4, 726, 267
40 riblets	8, 215, 682
30 riblets	7, 458, 388
20 riblets	6, 615, 171

direction, the better performance of wind turbine is obtained. The number of riblets should be selected carefully to minimise the manufacturing cost.

Table 27 represents the percentage change in the NREL phase II power coefficient of different number of riblets compared to the smooth wind turbine. The best improvement for increasing the wind turbine performance is obtained at  $7m/s$  for 40 riblets. However, it is obtained at  $16.4m/s$  for 30 riblets. This is due to different AOAs are existed in this region. Increasing further the number of riblets could lead to a further wind turbine improvement, but mesh elements will hugely increase.

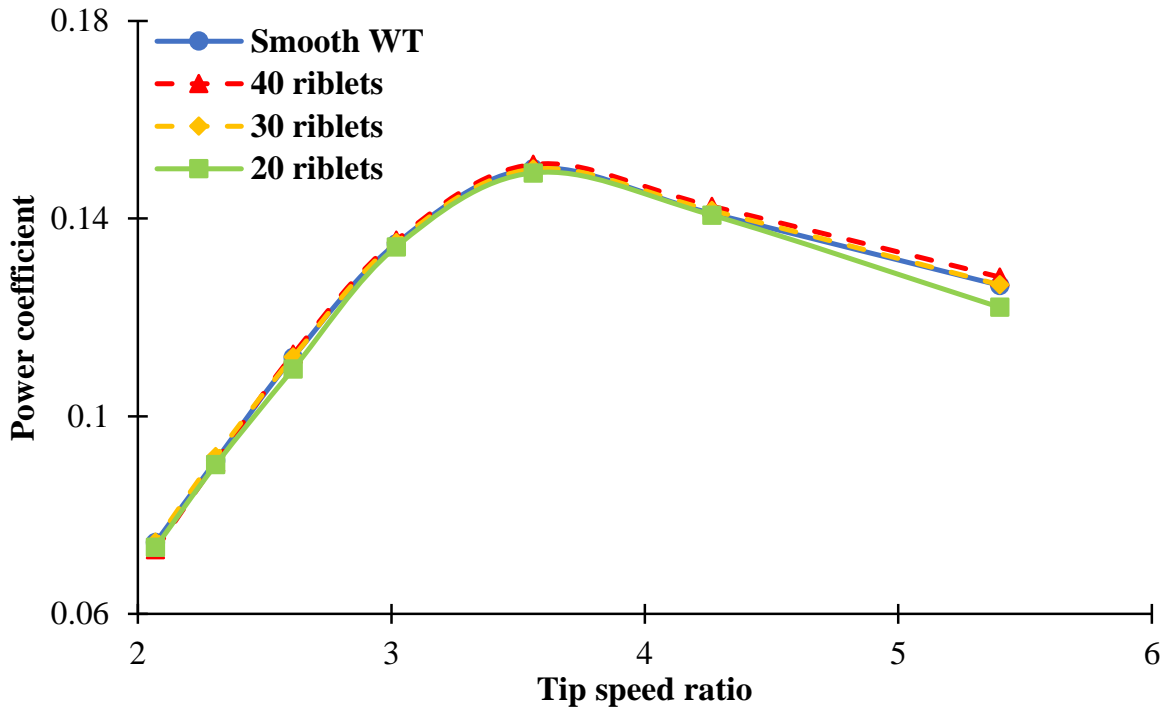


Figure 133: Power coefficient versus tip speed ratio for different number of riblets

Table 27: Percentage change in power coefficient for different number of riblets compared to the smooth WT

Tip speed ratio	40 riblets	30 riblets	20 riblets
5.40	1.32%	0.08%	-3.52%
4.26	1.03%	0.42%	-0.25%
3.56	0.57%	-0.08%	-0.58%
3.02	0.51%	0.18%	-0.47%
2.61	0.54%	0.06%	-2.12%
2.31	-0.41%	0.90%	-0.88%
2.07	-2.02%	0.15%	-1.26%

## 6.2 Riblets Only on Pressure Side

### 6.2.1 Geometrical setup

The geometrical setup for both fluid domain and wind turbine of this study case are displayed in Figures 221 and 4, respectively. Particularly, for this study case, 40 riblets with  $l^+ = 114 - 140$  are only created on the pressure side of the blades, as viewed in Figures 134 and 135. Riblets start at the lowest node of the aerofoil and extend towards the trailing edge. The lowest node is about  $35\%c$ . The spanwise length of riblets is  $80mm$  ( $2.3\%$  span). According to Table 45, the riblets extend from  $0.04955m$  to  $0.04947m$ , which corresponds to  $19mm$ .

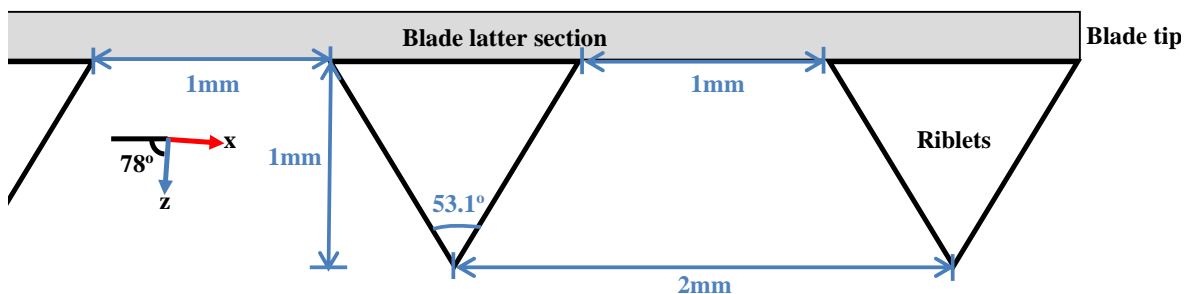


Figure 134: Triangular riblets on the NREL phase II blade's pressure side

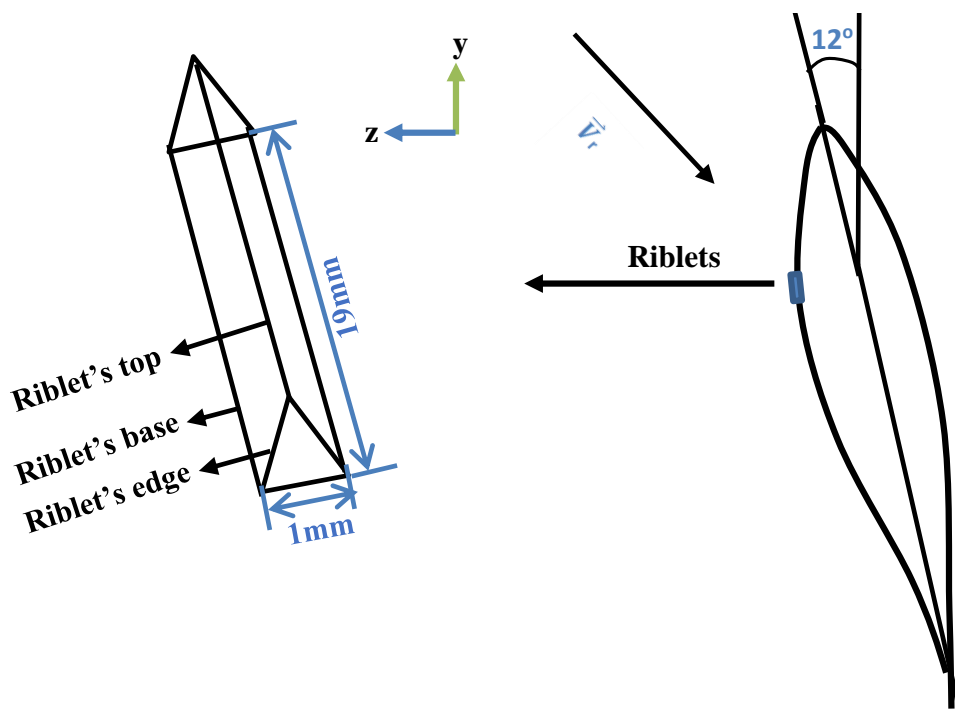


Figure 135: The riblets on the pressure side of the blade at the tip

### 6.2.2 Mesh element number

The mesh setting for this case is the same as the mesh setting that is used for study case 5 (section 8.5.3). This implies that the size of mesh elements as well as the inflation layers settings are the same for both cases. Tables 28 and 29 show the number of the average mesh faces on each blade and the total mixed cells for different riblets locations, respectively. The difference in element number between riblets on suction side and pressure side is due to the location of riblets on each side of the blade.

Table 28: Average number of the mesh (triangular faces)

<b>Riblet length on pressure side</b>	<b>Average number of triangular mesh faces</b>
Smooth NREL phase II	27, 228
Riblets on suction side	53, 666
Riblets on pressure side	53, 898

Table 29: Total number of the mixed cells

<b>Riblet length on pressure side</b>	<b>Number of mixed cells</b>
Smooth NREL phase II	4, 726, 267
Riblets on suction side	8, 215, 682
Riblets on pressure side	8, 439, 829

### 6.2.3 Result & discussion

Figure 136 shows the power coefficient of different riblets' locations on the blade in comparison with the smooth blade. Both configurations have 40 riblets on only either side of the blade. At the lowest wind speed, riblets on the pressure side perform better than riblets on suction side. Considering  $8.88\text{m/s}$  as the average wind speed over the year, riblets only on suction side perform better than riblets on pressure side. Both configurations show poor performance at low tip speed ratios.

Table 30 represents the percentage change in wind turbine performance for riblets that are only applied on either side of the blade compared to smooth WT. The maximum power coefficient of the smooth WT is increased by 0.57% when applying riblets only on the suction side. However, it is decreased by 0.13% when applying riblets only on pressure side of the blade. Consequently, placing riblets only on the blade's top side proves its advantage over the other configuration by showing a better wind turbine performance.

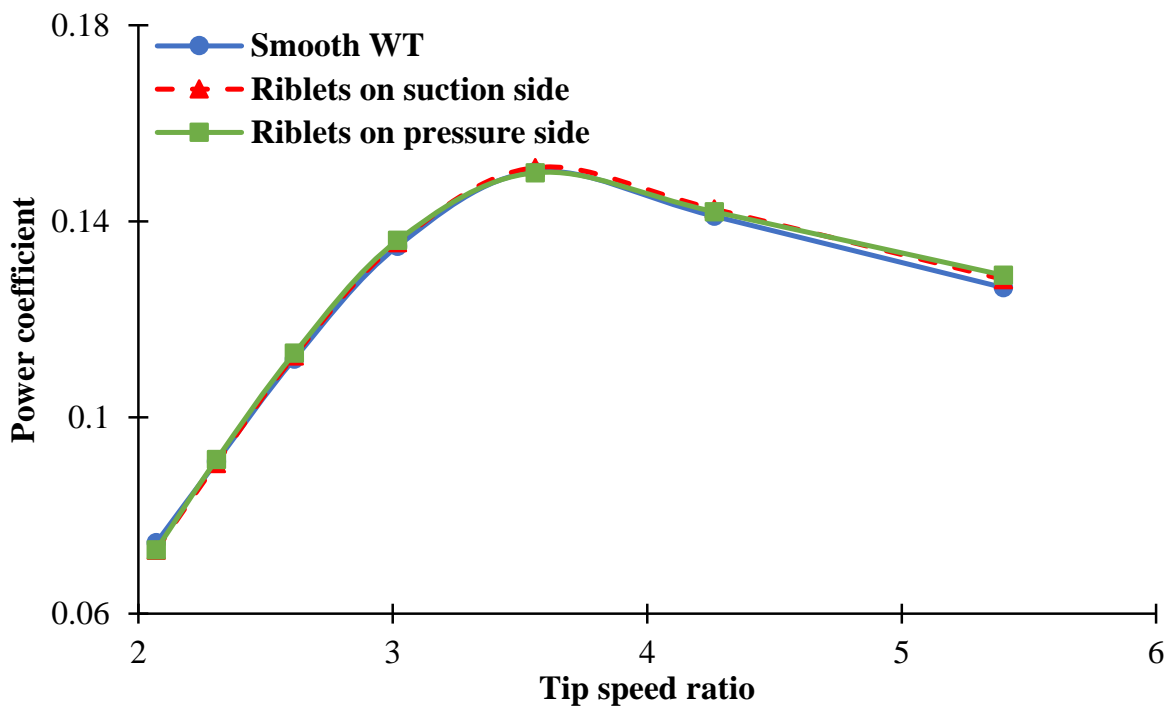


Figure 136: Power coefficient versus tip speed ratio for different riblets's locations on the blade

**Table 30: Percentage change in power coefficient of riblets only on suction or pressure side compared to the smooth side**

<b>Tip speed ratio</b>	<b>Pressure side</b>	<b>Suction side</b>
5.40	2.00%	1.32%
4.26	0.65%	1.03%
3.56	-0.13%	0.57%
3.02	0.88%	0.51%
2.61	1.05%	0.54%
2.31	0.47%	-0.41%
2.07	-1.93%	-2.02%

### 6.3 Riblets on Both Blade Sides

#### 6.3.1 Geometrical setup

This study case's fluid domain is shown in Figure 221 and the wind turbine blade is displayed in Figure 4. For this study case, riblets are applied on both blade sides. 20 riblets with  $l^+ = 114 - 140$  are applied on each side of the blade with spanwise distance of  $40\text{mm}$ . The lengths of riblets on the suction and pressure sides of the blade are  $21\text{mm}$  and  $19\text{mm}$ , respectively. The riblets geometrical setup is displayed in Figures 137 and 138.

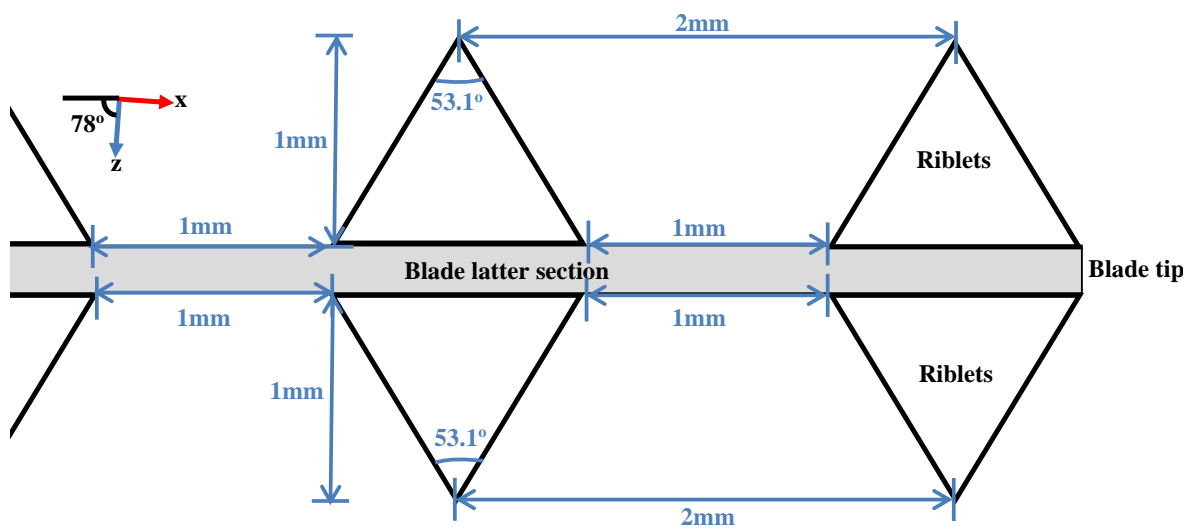


Figure 137: Triangular riblets on both NREL phase II blade sides

#### 6.3.2 Mesh element number

The mesh setting of study case 5 (section 8.5.3) is also used for this study case. This includes the maximum and minimum sizes of mesh elements as well as the inflation layers settings. Tables 31 and 32 show the number of the average mesh faces on each blade and the total mixed cells for different riblets's configurations, respectively. Applying riblets on both blade sides will increase the number of mesh elements. This means more time is needed for running the simulation for applying riblets on both blade sides.

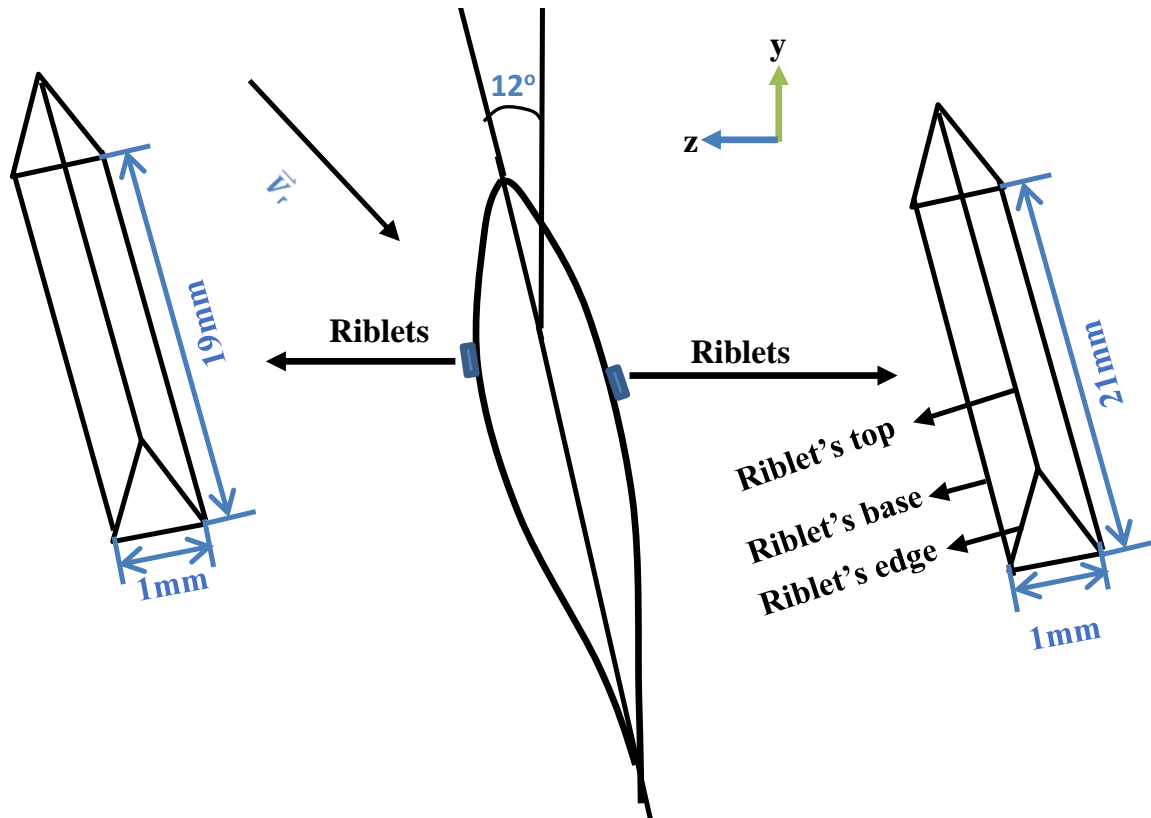


Figure 138: The riblets on both sides of the blade at the tip

Table 31: Average number of the mesh (triangular faces)

Number of riblets	Average number of triangular mesh faces
Smooth NREL phase II	27, 228
Riblets on both sides	56, 026
Riblets on suction side	41, 741

Table 32: Total number of mixed cells

Number of riblets	Number of the mixed cells
Smooth NREL phase II	4, 726, 267
Riblets on both sides	8, 658, 667
Riblets on suction side	6, 615, 171

### 6.3.3 Result & discussion

Figure 139 shows the power coefficient for tripped blades by applying riblets on both sides and only suction side. The number of riblets on the suction side is 20. This means 20 riblets are applied on each blade's side for riblets on both sides. The best improvement is recorded at tip speed ratio of 5.4 for applying riblets on both blade sides. Both configurations show a decrease in the performance of wind turbine at a wind speed of  $18.3\text{m/s}$ . Increasing the number of riblets on both sides is expected to further improve the performance. However, the simulation capacity cannot handle more than this number used in the thesis.

Table 33 describes the increase percentage of the wind turbine performance for riblets on both blade sides and only on suction side compared to the smooth sides of wind turbine. In comparison between the two configurations, applying riblets on both blade sides show an increase in power coefficient at most wind speeds. Comparing 20 riblets on each blade side with 40 riblets on suction side (Table 27), 40 riblets on suction side shows better performance at yearly averaged wind speed. However, if 40 riblets are applied on each blade's side, then a better performance of wind turbine is expected.

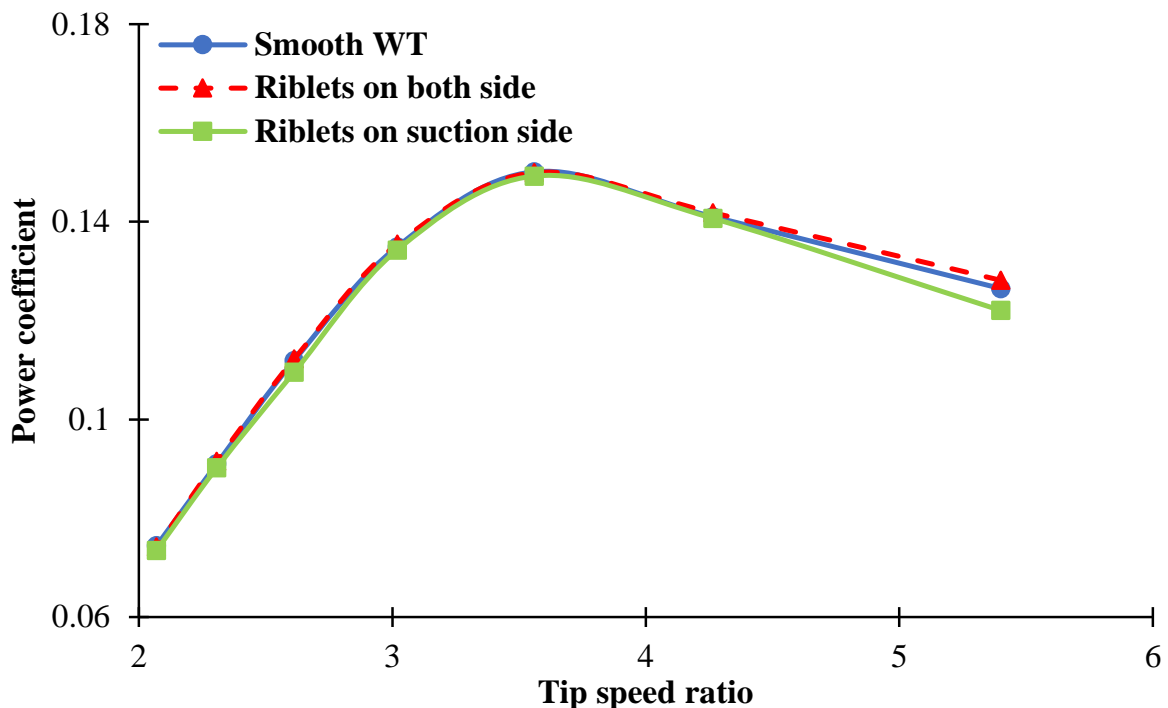


Figure 139: Power coefficient versus tip speed ratio for different riblets' configurations

Table 33: Percentage change in power coefficient for different riblets' configurations compared to the smooth WT

<b>Tip speed ratio</b>	<b>Both sides</b>	<b>Suction side</b>
5.40	1.32%	-3.52%
4.26	0.56%	-0.25%
3.56	-0.12%	-0.58%
3.02	0.40%	-0.47%
2.61	0.26%	-2.12%
2.31	0.60%	-0.88%
2.07	-0.35%	-1.26%

## 6.4 Changing Riblets' Orientation

### 6.4.1 Geometrical setup

The geometrical setup for both fluid domain and wind turbine blades are already described in detail, as shown in Figures 221 and 4, respectively. For this study case, the orientation of riblets are changed by  $90^\circ$  with respect to the riblets baseline of study case 8 (section 5.3.2), so that the incoming wind hits the sides of the riblets rather than the front triangular riblet faces. The riblets' geometrical setup for the chordwise and spanwise directions are displayed in Figures 140 and 141, respectively. The simulated riblet chordwise length is  $21\text{mm}$  and the spanwise length of the riblet is  $80\text{mm}$ , with  $h^+ = 69 - 85$ .

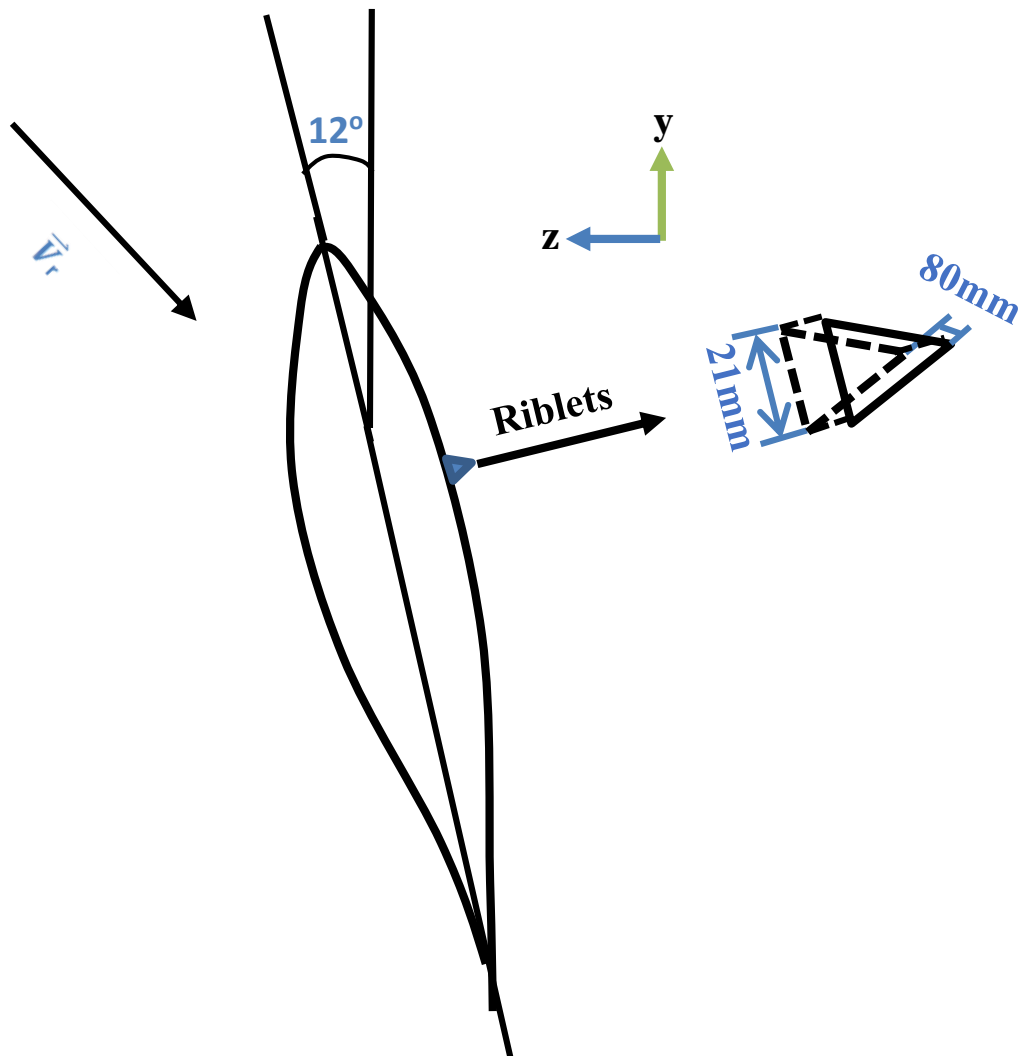


Figure 140: Riblets on the NREL phase II blade in the chordwise direction (not to scale)

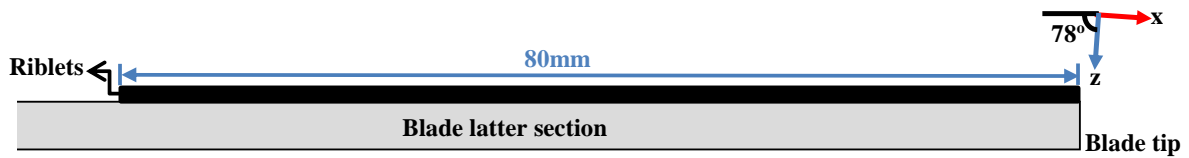


Figure 141: Riblets on the NREL phase II blade in the spanwise direction

### 6.4.2 Mesh element number

The same wind turbine is simulated, which is the NREL phase II, but different riblets' orientation is applied. Therefore, the same mesh is generated for this study case as the smooth case (study case 5, section 8.5.3). However, there are 22, 41 and 41 nodes for each edge, base and top of the riblets, respectively. Tables 34 and 35 show the number of the average mesh faces on each blade as well as the total mixed cells, respectively. Figures 142-146 show the generated mesh of the new riblets' orientation.

Table 34: Average number of the mesh (triangular faces)

Riblet streamwise length	Average number of triangular mesh faces
Smooth NREL phase II	27, 228
New orientation	30, 126
Original orientation	53, 666

Table 35: Total number of the mixed cells

Riblet streamwise length	Number of mixed cells
Smooth NREL phase II	4, 726, 267
New orientation	5, 267, 367
Original orientation	8, 215, 682

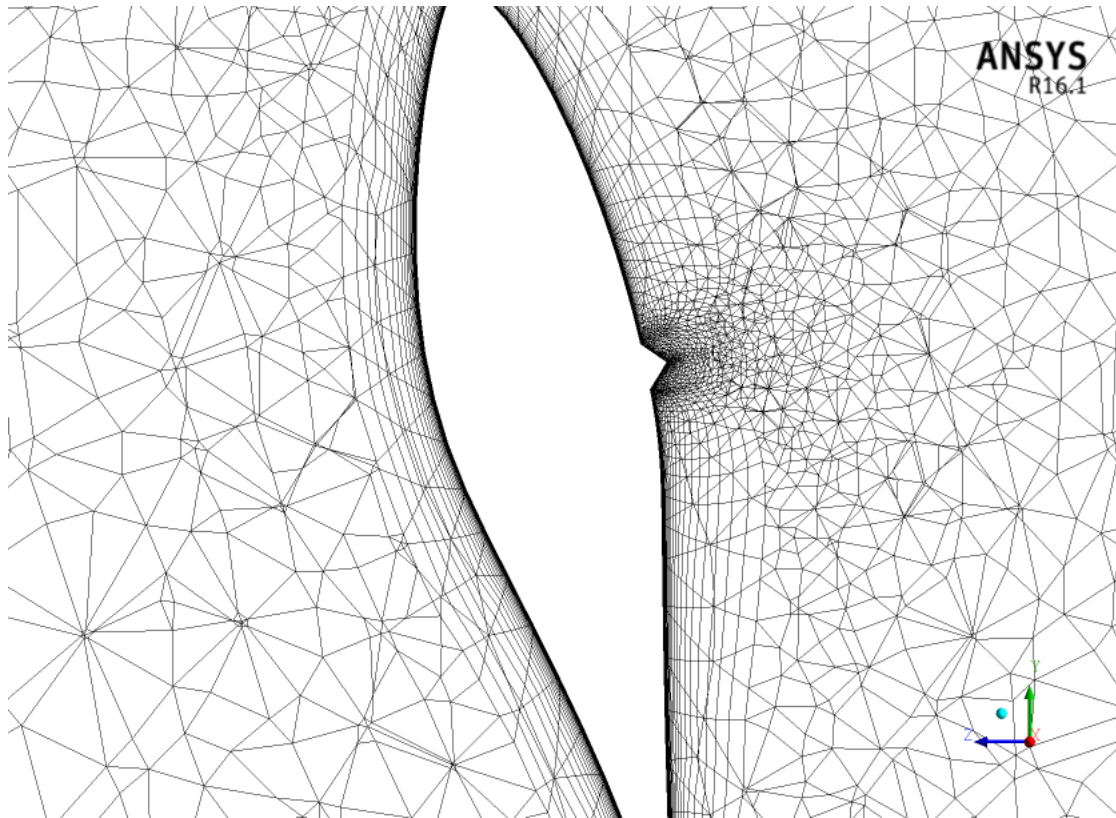


Figure 142: The generated mesh of the riblet for the new orientation

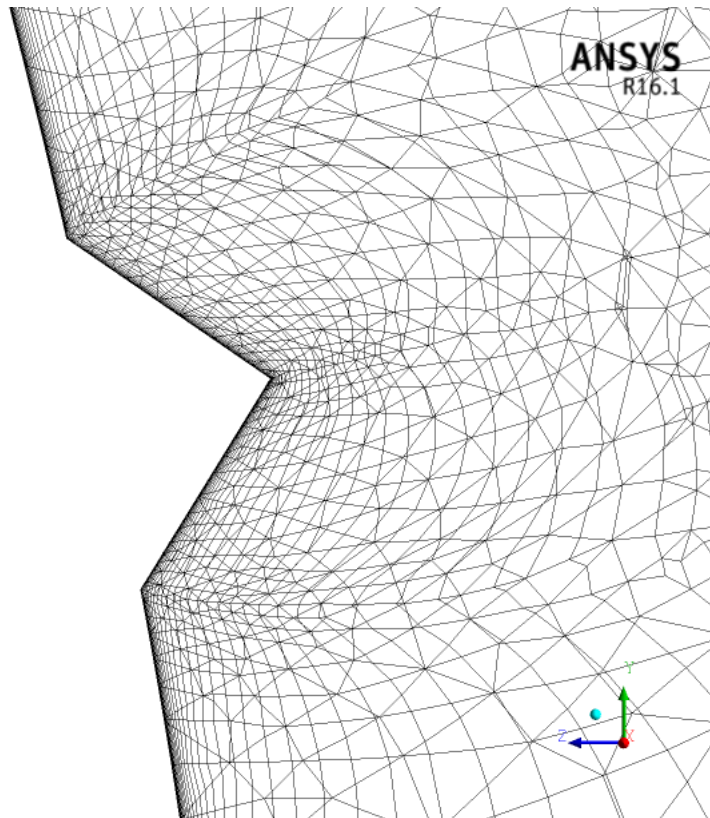


Figure 143: The generated mesh of the riblet for the new orientation (zoom-in)

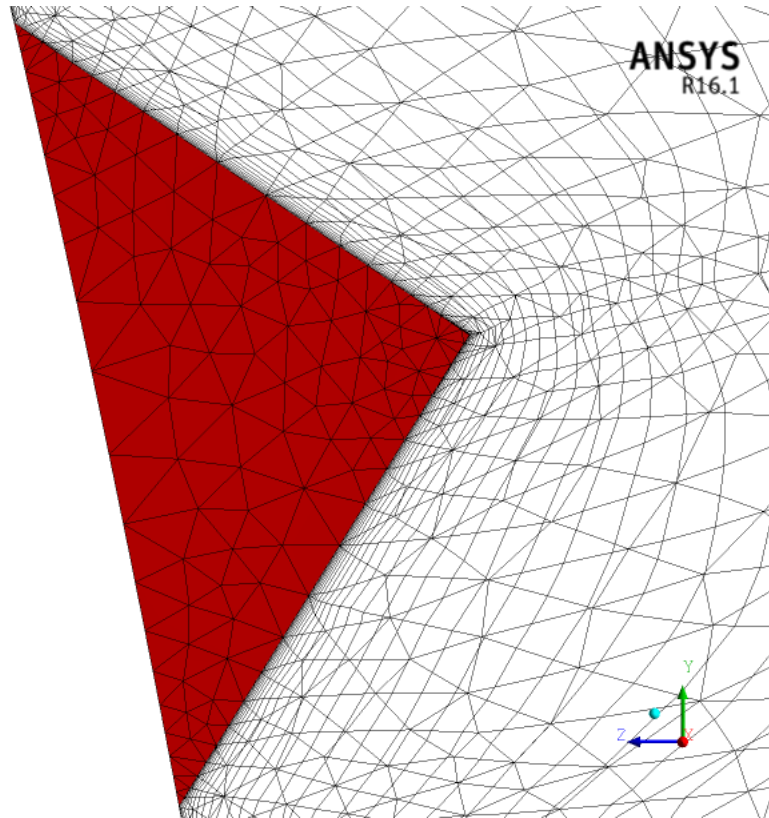


Figure 144: The generated mesh of the riblet's face for the new orientation

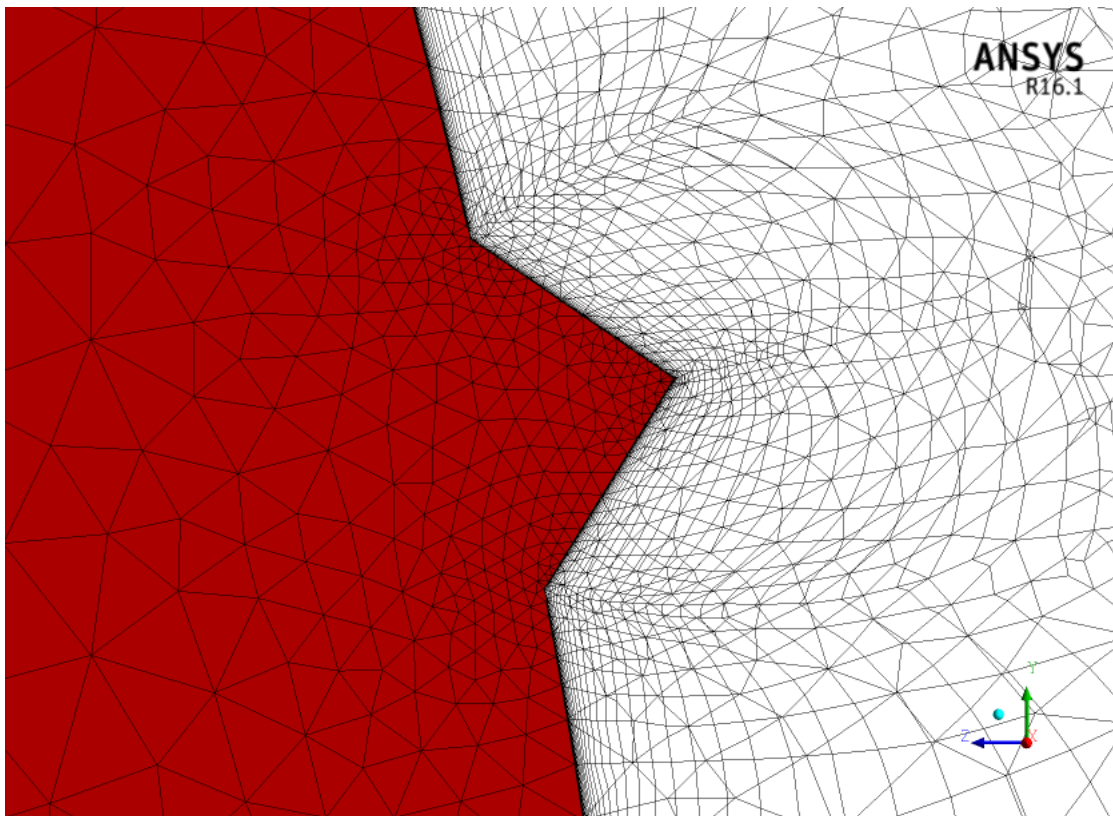


Figure 145: The generated mesh of the riblet and aerofoil for the new orientation

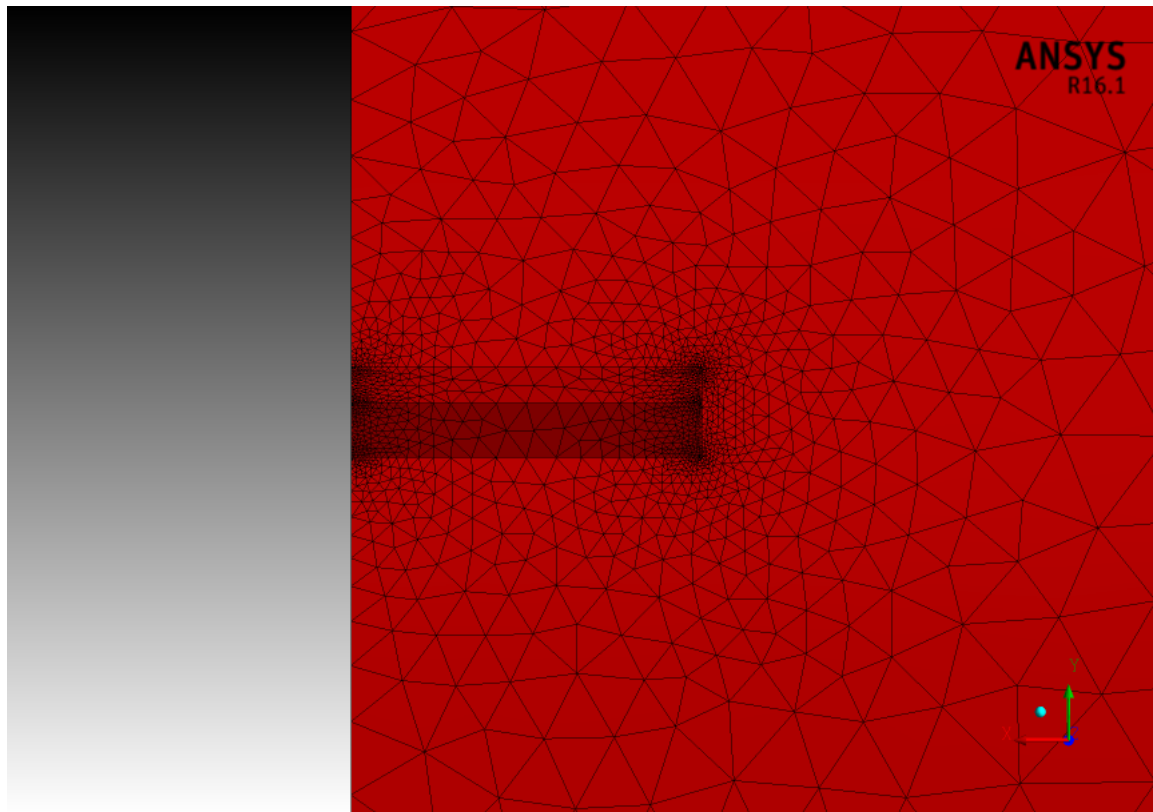


Figure 146: The generated mesh of the riblet on the blade for the new orientation

### 6.4.3 Result & discussion

The effect of changing the orientation of riblets has not been studied in full details before. This section illustrates one of many suggested riblet orientations that can be simulated. Figure 147 displays the power coefficient of the NREL phase II for the original orientation and the new suggested riblets' orientation. Changing riblets' orientation by  $90^\circ$  with respect to the triangular riblets' baseline shows a lower performance of the wind turbine compared to both smooth WT and original orientation (described early in Section 5.3.2). For the new orientation, the performance of WT is decreased by 2.42% at  $8.88m/s$ .

Table 36 shows the percentage change of power coefficient of original and new orientations compared to the smooth NREL phase II. As stated before, it is not recommended to apply  $90^\circ$  riblets' orientation because the results negatively affect the wind turbine performance. The reason behind this decrease is because riblets act as an obstacle and prevent incoming wind to flow through the riblets in the streamwise direction. This means the blades become larger in size. Concluding from this, the spaces between riblets in the streamwise direction is an important factor for increasing the wind turbines performance.

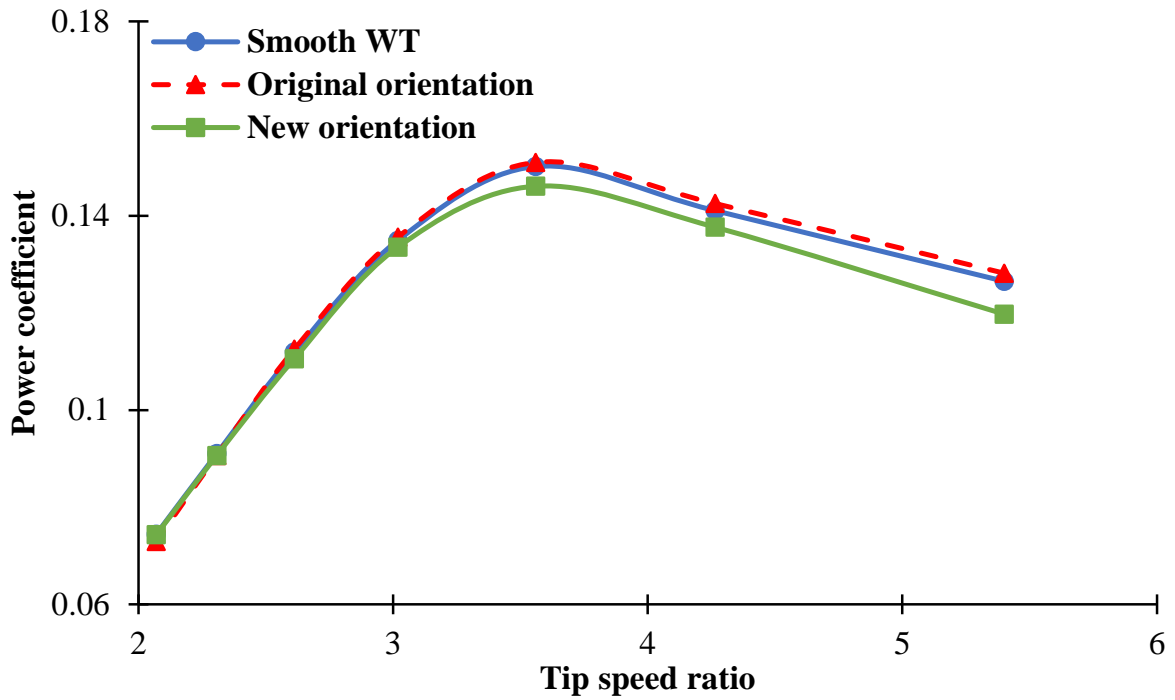


Figure 147: Power coefficient versus tip speed ratio for two orientations of riblets in comparison with the smooth WT

Table 36: Percentage change in power coefficient of two different orientations of riblets compared to the smooth WT

Tip speed ratio	New orientation	Original orientation
5.40	-5.35%	1.32%
4.26	-2.42%	1.03%
3.56	-2.70%	0.57%
3.02	-1.03%	0.51%
2.61	-1.20%	0.54%
2.31	-0.40%	-0.41%
2.07	-0.16%	-2.02%

The pressure contours of the smooth WT and the new riblet's orientation at  $7m/s$  are shown in Figures 148 and 149, respectively. The pressure on the suction side of the blade for the new riblet's orientation is higher than that of the smooth WT resulting in reduction of the lift force, and therefore lower wind turbine performance. The difference in pressure before and after the riblets causes a decrease in the favourable pressure gradient. This means the flow is exposed faster to flow separation, leading to a reduction in the resultant force of the blade.

Figures 150 and 151 display the velocity contour of the smooth and new riblet's orientation at wind speed of  $7m/s$ , respectively. When the relative flow hits the riblets, the flow speed reaches zero. This means the riblets act as an obstacle to prevent a flow favourable direction. The riblets clearly cause a flow separation, which leads to a decrease in the wind turbine performance. Figures 152 and 153 show the velocity vector of the smooth and new riblet's orientation, respectively.

The new orientation of riblets causes a flow separation resulting in a back flow. This can be clearly viewed in Figure 154. A better representation of the flow separation for the tripped wind turbine can be shown via streamlines. Figures 155 and 156 show the streamlines of the smooth and tripped wind turbines at a wind speed of  $V_{\infty} = 7m/s$ , respectively. The flow separation is caused by the new orientation of the riblets. Therefore, this leads to a degradation in the performance of the wind turbine.

The streamlines along the spanwise direction of the smooth and new riblet's orientation WTs are displayed in Figures 157 and 158, respectively. The flow on blade's pressure side of both WTs is the same, showing a flow separation at the blade's root. Similarly, the suction side of both WTs show almost the same behaviour except that a flow separation is clearly displayed near the tip of the blade for the new riblets' orientation. This flow separation is a result of riblets and therefore, a degradation of the wind turbine performance is shown.

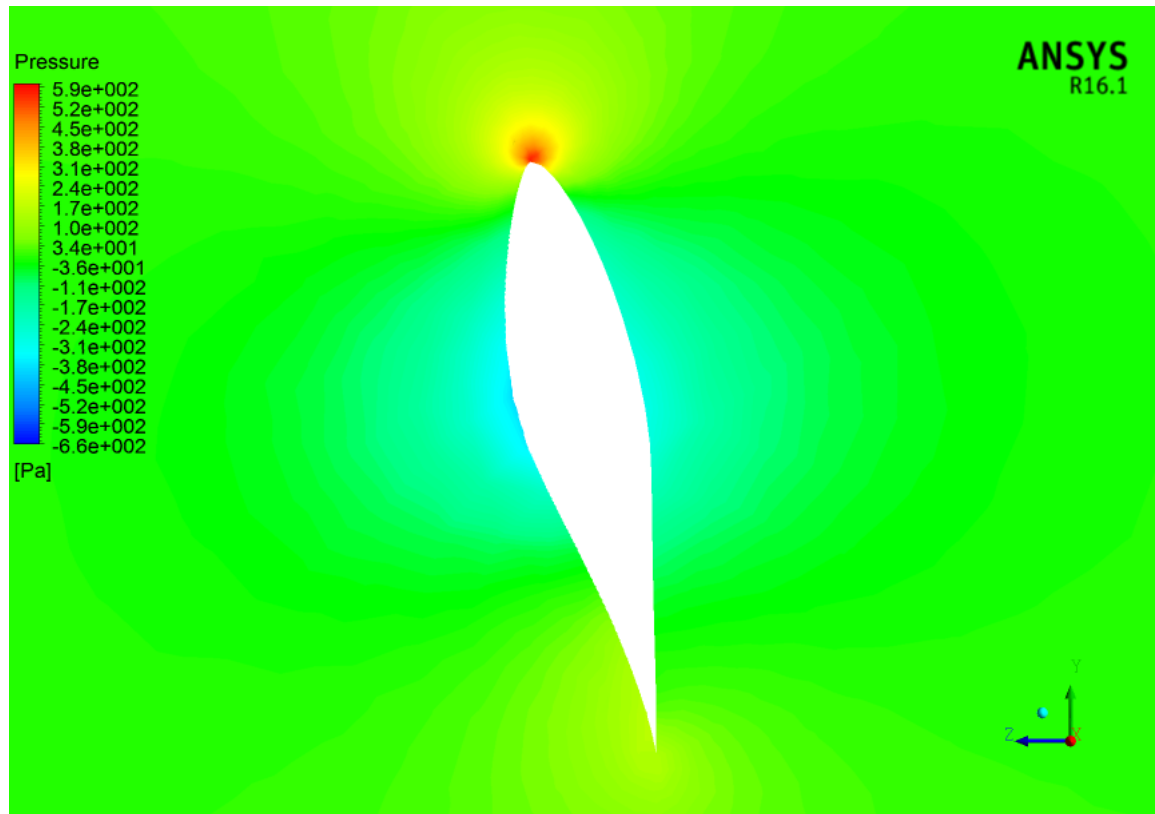


Figure 148: The pressure contour of the smooth WT at 99.7% span (riblets' location) at  $V_\infty = 7m/s$

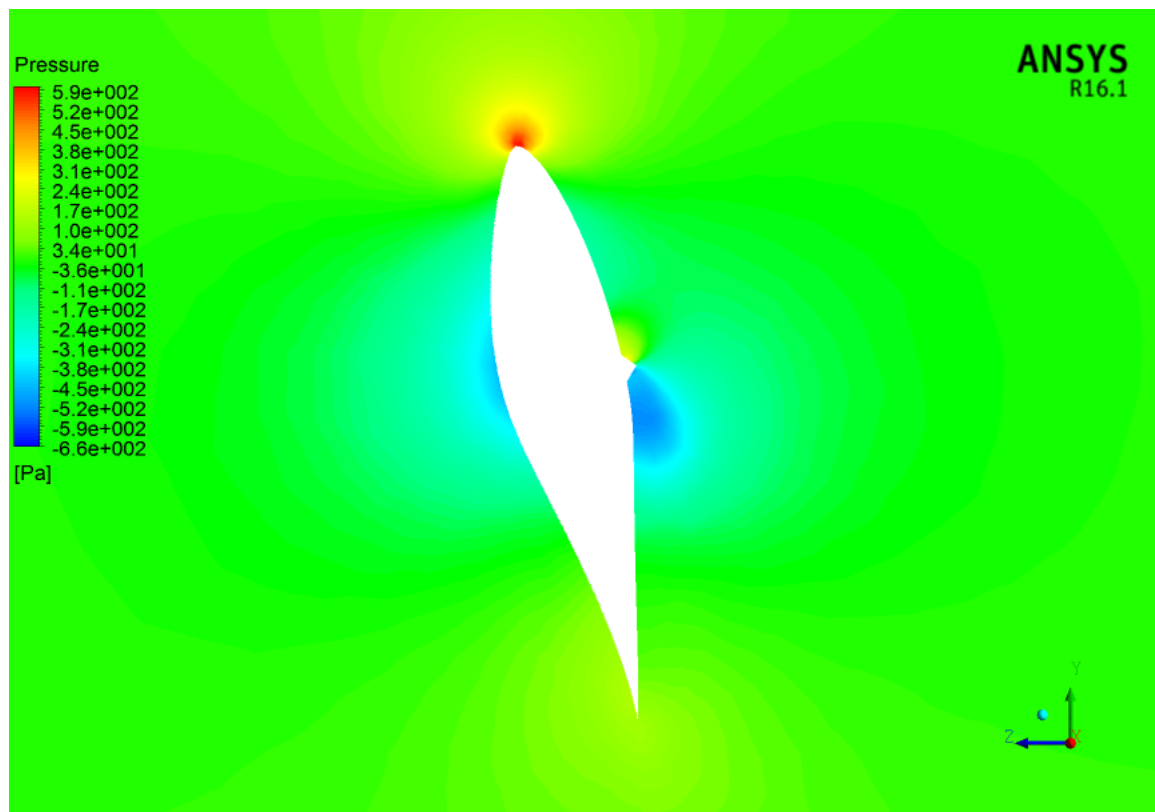


Figure 149: The pressure contour of the new riblet's orientation at 99.7% span (riblets' location) at  $V_\infty = 7m/s$

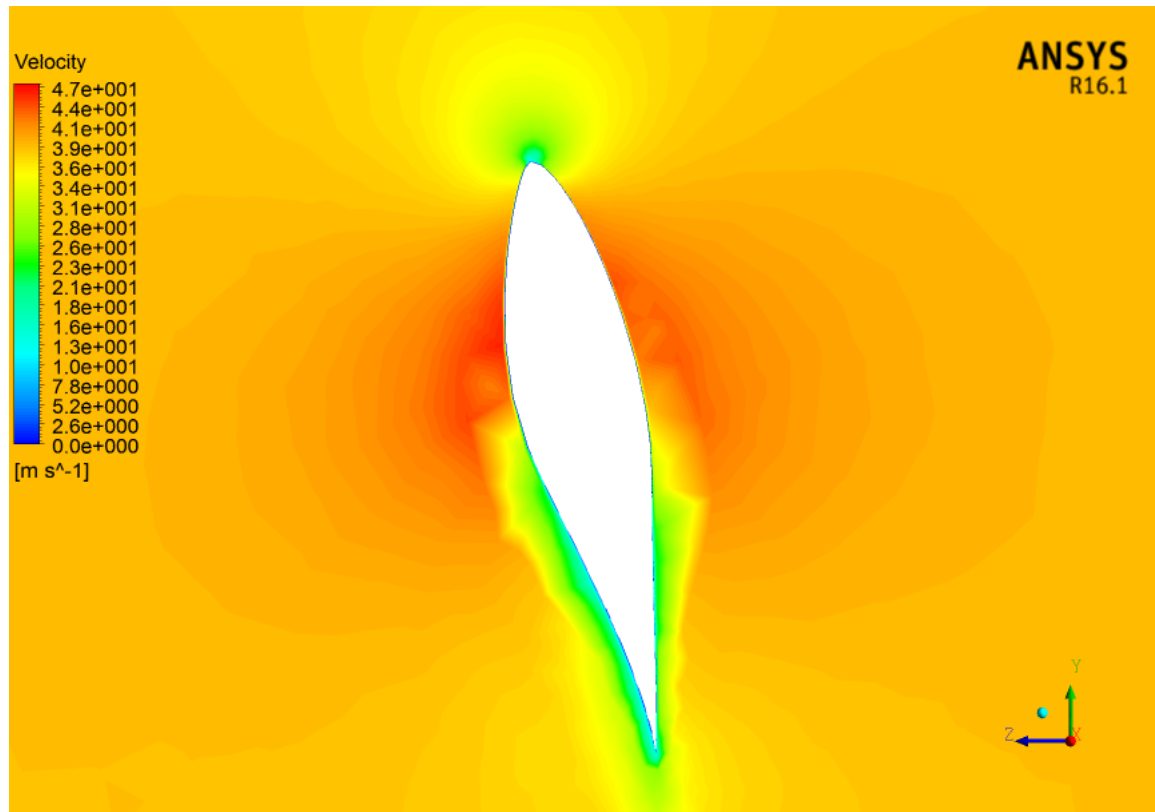


Figure 150: The velocity contour of the smooth WT at 99.7% span (riblets' location) at  $V_{\infty} = 7m/s$

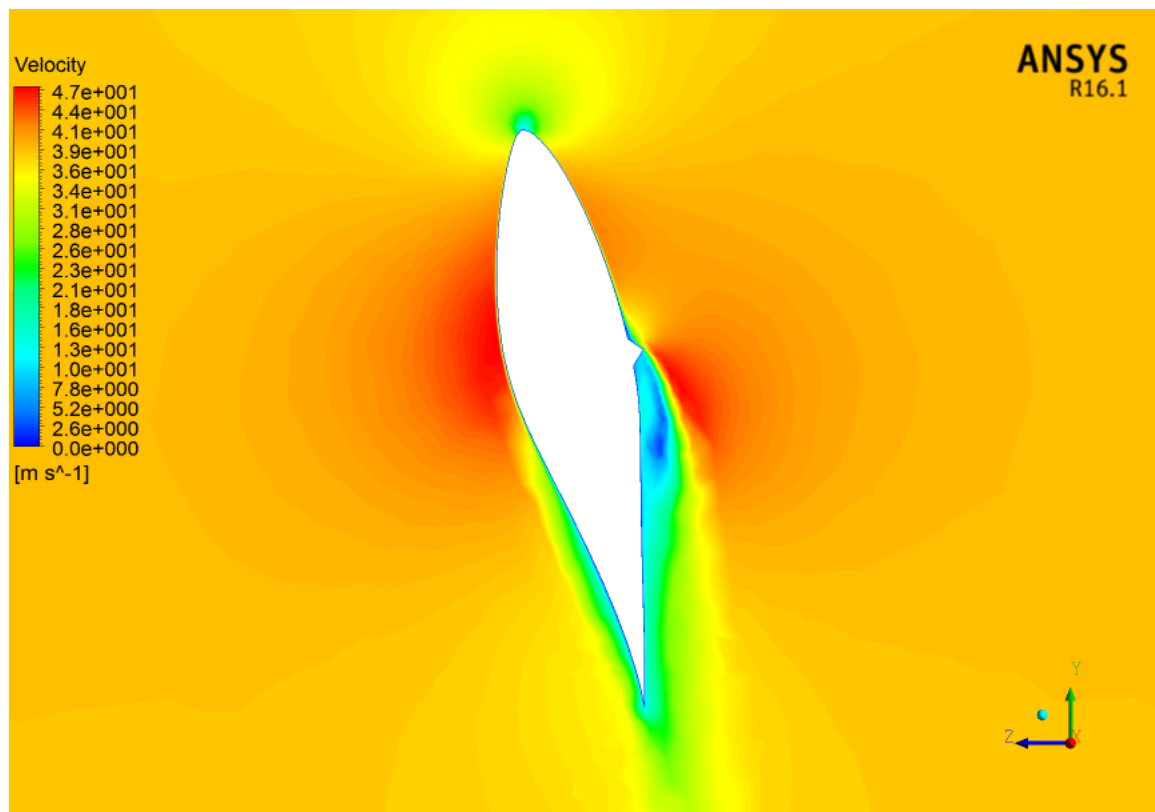


Figure 151: The velocity contour of the new riblet's orientation at 99.7% span (riblets' location) at  $V_{\infty} = 7m/s$

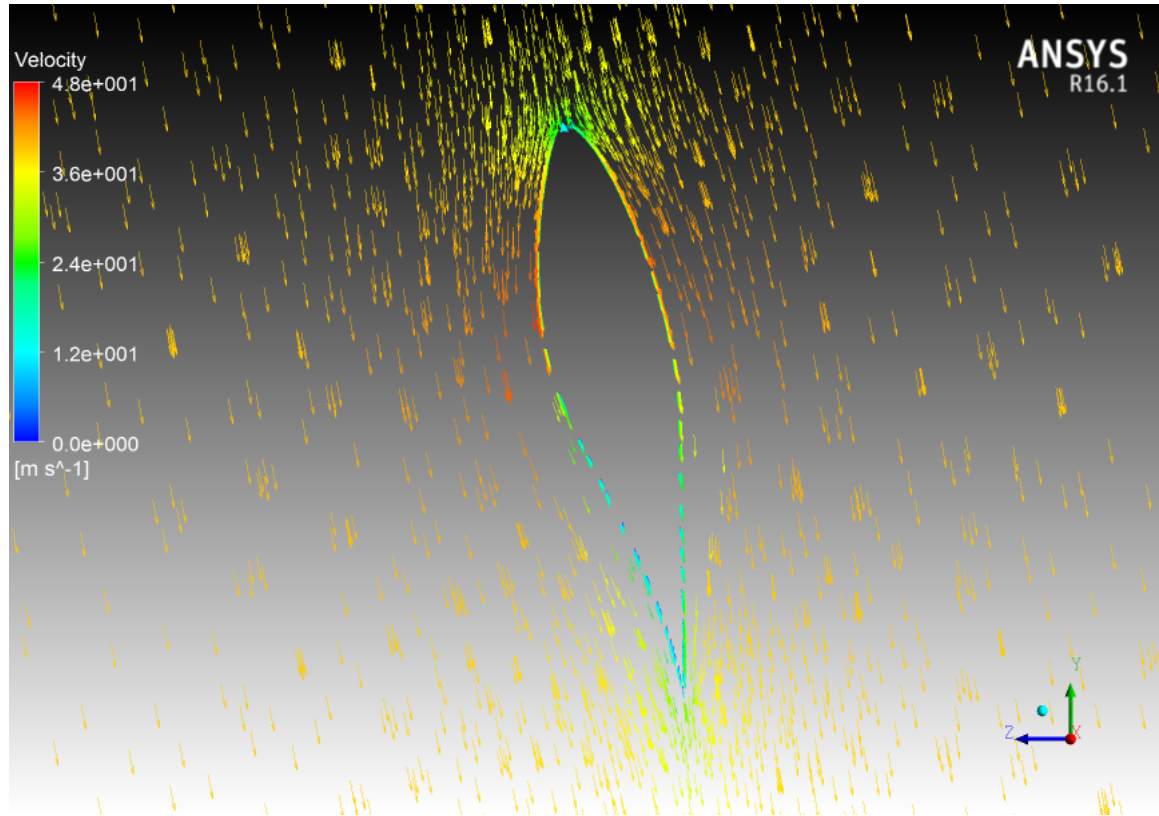


Figure 152: The velocity vector of the smooth WT at 99.7% span at  $V_\infty = 7\text{m/s}$

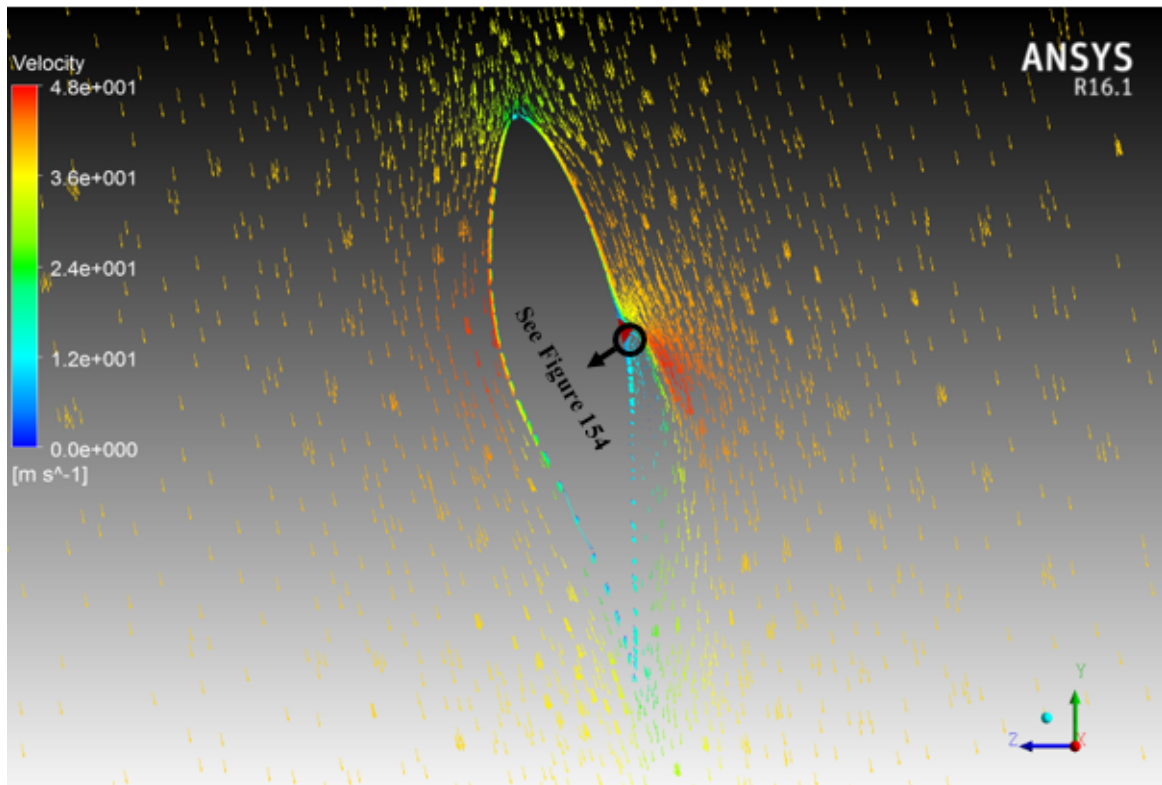


Figure 153: The velocity vector of the new riblet's orientation at 99.7% span at  $V_\infty = 7\text{m/s}$

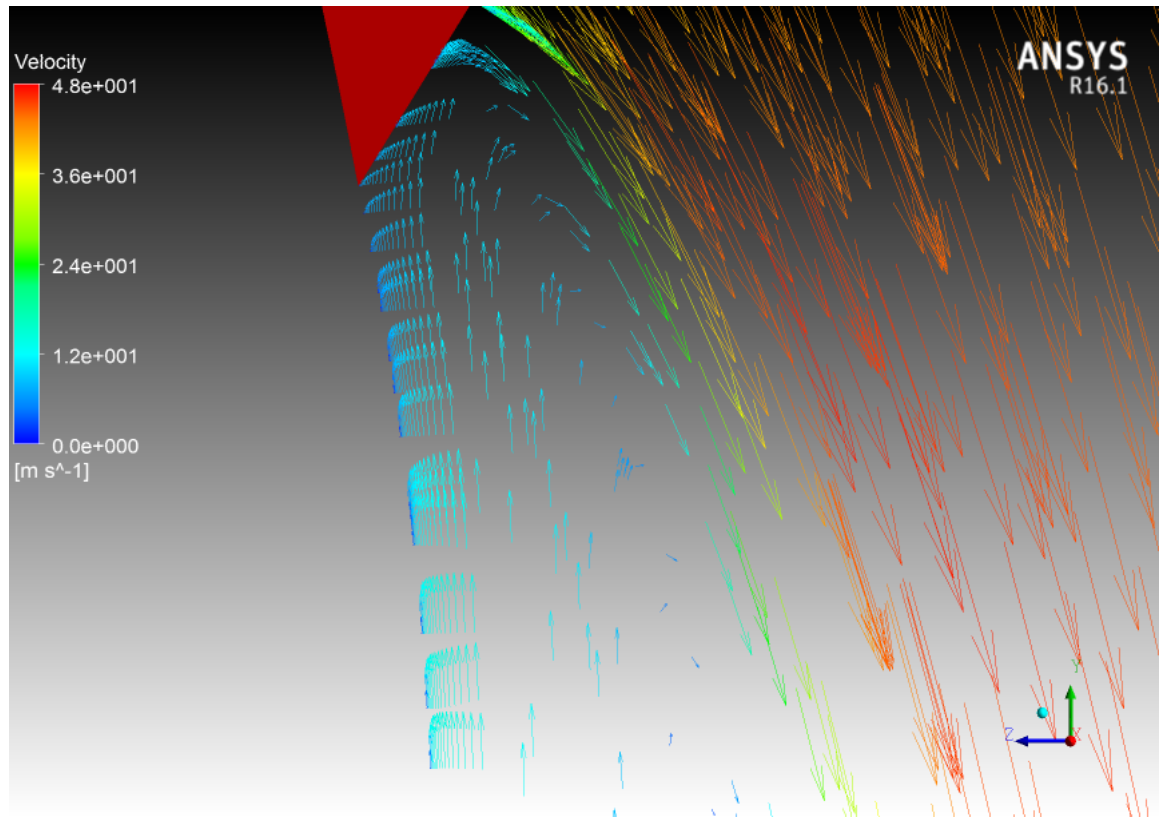


Figure 154: The velocity vector of the new riblet's orientation at 99.7% span (zoom-in) at  $V_\infty = 7m/s$

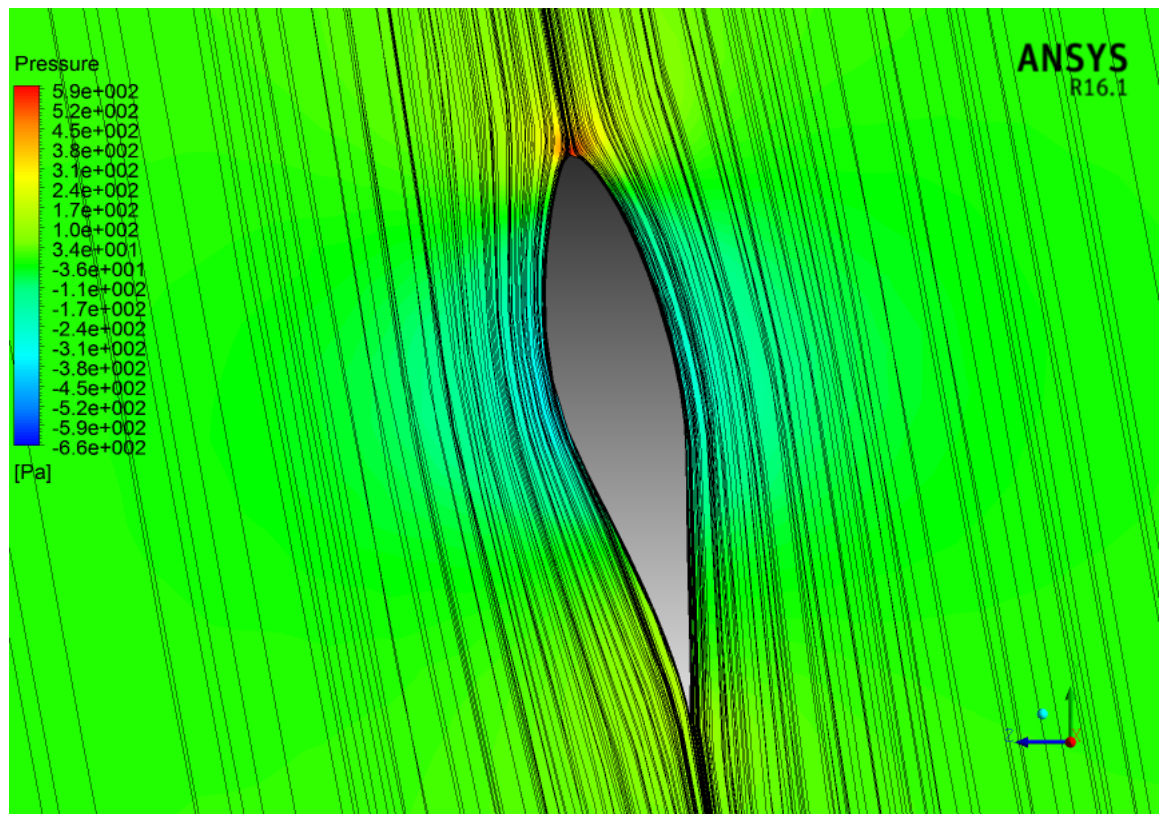


Figure 155: The streamlines of the smooth WT at 99.7% span at  $V_\infty = 7m/s$

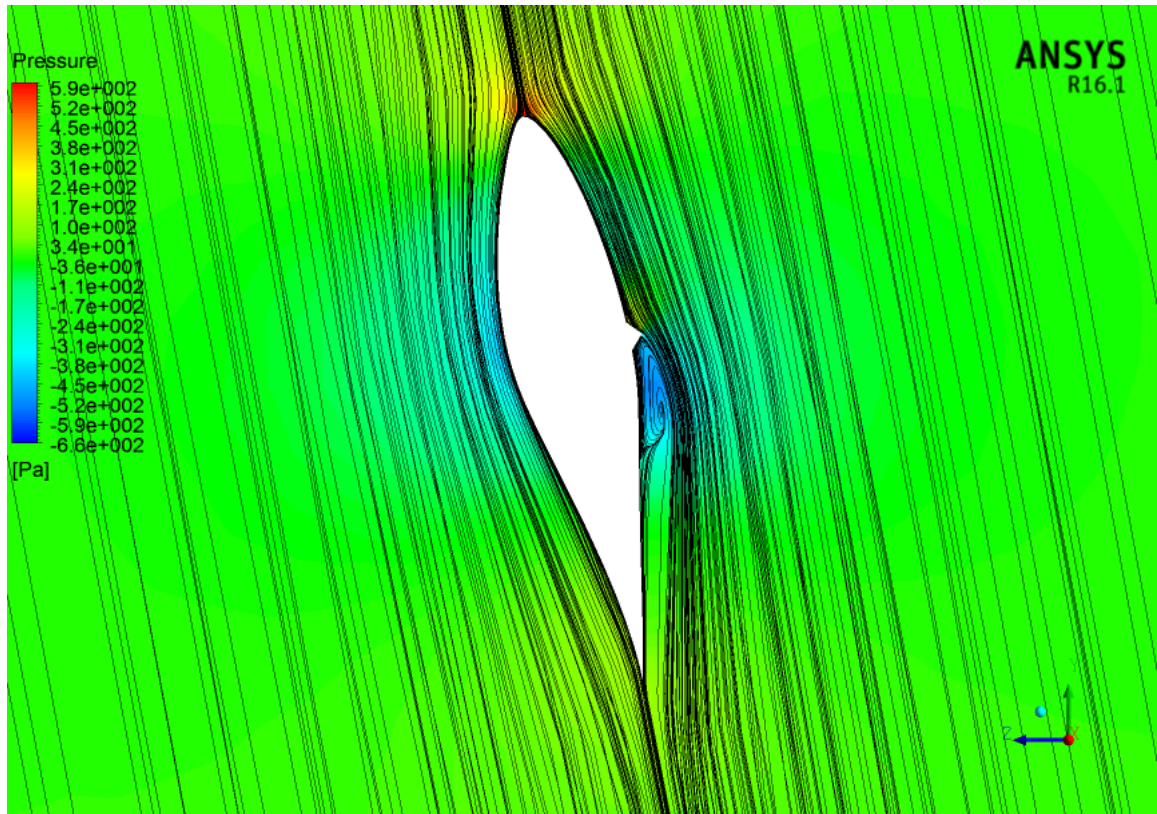


Figure 156: The streamlines of the new riblet's orientation at 99.7% span at  $V_\infty = 7m/s$

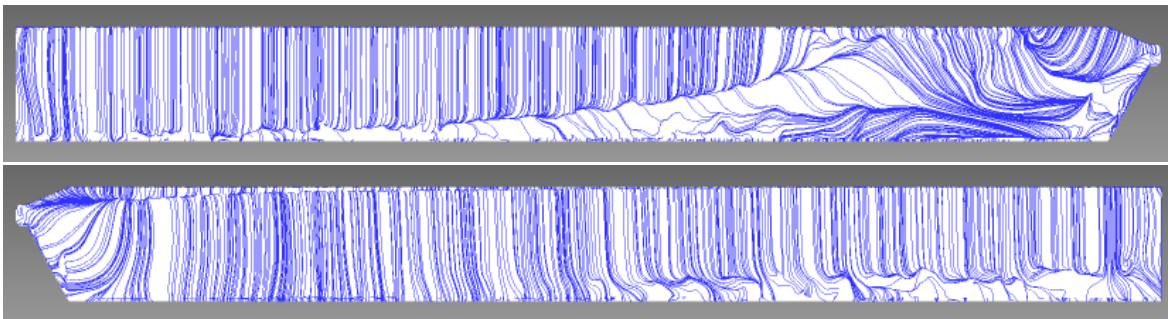


Figure 157: The streamlines (spanwise) of smooth WT at  $V_\infty = 7m/s$  (top: suction, bottom: pressure)

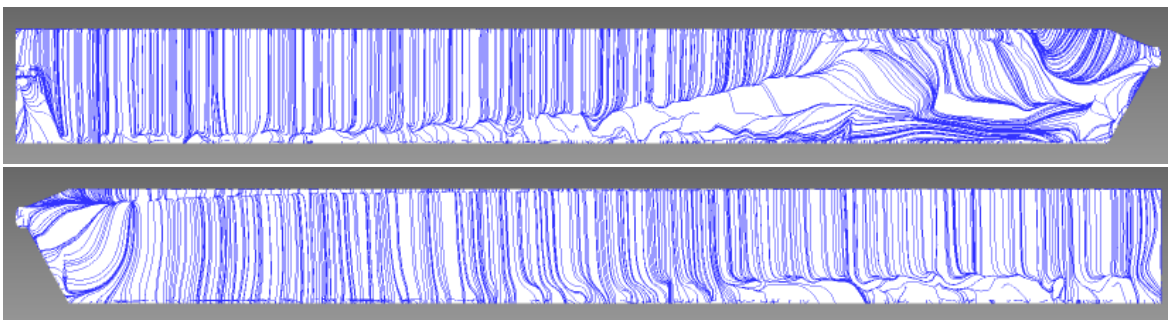


Figure 158: The streamlines (spanwise) of new riblet's orientation at  $V_\infty = 7m/s$  (top: suction, bottom: pressure)

## 7 CONCLUSION & FUTURE WORK

The use of renewable energy, particularly wind energy, is expected to rise in the next decades due to its low risk to the environment and its high availability. Increasing lift force is an important factor that positively affects the performance of wind turbines. Therefore, a passive flow controller, namely riblets, has been applied to aerodynamic applications since the 1970s. The aim of this PhD project is to increase the performance of the NREL phase II by creating triangular riblets on its blades. This is done through two main bodies; one body is the validation of smooth cases against experiment, which includes simulation of a 2D aerofoil, a 3D fixed blade and the NREL phase II. Another body is comparing tripped cases with smooth ones based on experimental validation. Applying triangular riblets on a 2D aerofoil, a 3D fixed blade and the NREL phase II are the subsections of unclean cases.

Within this thesis, there are five smooth study cases and each study case has its own objectives in addition to validation against experiment. The first study case is employed to observe the effect of fluid domain geometry of a rectangular shape and C-shape at an inlet on a 2D NACA 4412 aerofoil. More advanced examination is based on selecting appropriate turbulence models using a 2D S809 aerofoil. Another study is on a 3D S809 blade by computing its force coefficients. It also focuses on showing the separation flow points on a S809 aerofoil profile by computing the pressure distribution. This is done in order to determine the best location of riblets to be placed on the S809 aerofoil. Furthermore, periodic simulation of one-third of the NREL phase II with an offset angle of  $120^\circ$  is performed using the MRF model. In addition, SMM is applied on full rotor scale of the NREL phase II to determine its power coefficient and mechanical torque.

Furthermore, A validation for large-scale riblets on DU 96-W-180 against recent experimental work is done. However, the discrepancy in results is due to the experimental ability of having larger riblets number. Three studies for S809 tripped cases are undertaken. This includes simulating a riblet with  $h^+ = 67 - 69$  on 2D S809 aerofoil. The result demonstrates the importance of the 3D riblets' effect. Another study applies different riblet configurations and wind speeds on a fixed blade. The improved performance is obtained at  $l^+ = 104 - 157$  for a wider range of AOAs and  $Re$ , while  $l^+ = 460$  shows the maximum increase in lift and reduction in drag. The results also show that riblets perform best at low  $Re$  and stall AOAs. The last study simulates riblets with  $l^+ = 114 - 140$  on the blades' upper side of the NREL

phase II. Consequently, the performance is improved, and the rise in power coefficient ranges between 1.32% and 0.51%, depending on tip speed ratio.

Finally, four new riblets' configurations are accomplished. First, the riblet spanwise length is altered (changing number of riblets). Consequently, an improved wind turbine performance is observed when riblets' spanwise length increases. Another new configuration is placing riblets only on a blade's pressure side. In comparison with riblets only on a suction blade side, a better wind turbine performance is obtained for applying riblets only on the blade's upper side. Applying riblets on both blade sides is also attempted. The conclusion states that riblets perform better when they are applied on both blade's sides. Lastly, changing riblets' orientation by  $90^\circ$  negatively affects the performance of the wind turbine. To sum up, riblet configurations, AOAs and tip speed ratio are the factors for increasing the performance of wind turbines.

This work confirms that the large-scale riblets are not only able to reduce drag, but also can increase lift, and therefore improve the performance of wind turbines. Unlike the small-scale riblets, the large-scale ones act as a vortex generator and cause a recirculated zone in the wake of large riblets, which leads to delaying stall to a further chord location of the blade. In addition, and similar to small-scale riblets, the viscous sub-layer thickness of current tripped cases is increased, thus causing an upward shift of the log-law region and a reduction of the turbulence statistics. The drag reduction and lift increase depend on AOAs. However, the riblets positively affect more the skin-friction force for a larger number of riblets at a wider range of AOAs. This means the contribution of riblets in increasing the area of the blade is negligible because of the small riblets size compared to the blade size.

In the future, the findings from this thesis should be practically performed, that is applying riblets experimentally. This can be done using a small wind turbine scale but with the same aerofoil characteristic and Reynolds number settings as in this document. Furthermore, employing other different riblets' orientations rather than  $90^\circ$  orientation is recommended. This may also include changing the angle of riblet tip as well as the size of riblet heights. A potential improvement would be simulation of riblets with zero space between each other. However, this would require a more aggressive mesh in between the riblets (riblets' base). Moreover, creating riblets all over the blade's suction side might be another potential solution to increase the performance of wind turbines. However, the computational and manufacturing costs and time should be considered carefully.

## References

- [1] W. Zhong, H. An, L. Shen, T. Dai, W. Fang, X. Gao, and D. Dong, “Global pattern of the international fossil fuel trade: The evolution of communities”, *Energy*, vol. 123, pp. 260–270, 2017.
- [2] M. M. Mateus, M. do Vale, A. Rodrigues, J. C. Bordado, and R. G. dos Santos, “Is biomass liquefaction an option for the viability of poplar short rotation coppices? a preliminary experimental approach”, *Energy*, vol. 124, pp. 40–45, 2017.
- [3] D. Bonalumi and A. Giuffrida, “Investigations of an air-blown integrated gasification combined cycle fired with high-sulphur coal with post-combustion carbon capture by aqueous ammonia”, *Energy*, vol. 117, pp. 439–449, 2016.
- [4] O. Y. Edelenbosch, K. Kermeli, W. Crijns-Graus, E. Worrell, R. Bibas, B. Fais, S. Fujimori, P. Kyle, F. Sano, and D. van Vuuren, “Comparing projections of industrial energy demand and greenhouse gas emissions in long-term energy models”, *Energy*, vol. 122, pp. 701–710, 2017.
- [5] S. Naderi and F. Torabi, “Numerical investigation of wake behind a HAWT using modified actuator disc method”, *Energy Conversion and Management*, vol. 148, pp. 1346–1357, 2017.
- [6] C. L. Archer and M. Z. Jacobson, “Evaluation of global wind power”, *Journal of Geophysical Research: Atmospheres*, vol. 110, no. D12, 2005.
- [7] J. Thé and H. Yu, “A critical review on the simulations of wind turbine aerodynamics focusing on hybrid RANS-LES methods”, *Energy*, vol. 138, pp. 257–289, 2017.
- [8] US Energy Information Administration, *Annual Energy Outlook 2010: With Projections to 2035*. Government Printing Office, 2010.
- [9] US Energy Information Administration, *Annual Energy Outlook 2011: With Projections to 2035*. Government Printing Office, 2011.
- [10] J. Conti, P. Holtberg, J. Diefenderfer, A. LaRose, J. T. Turnure, and L. Westfall, “International energy outlook 2016 with projections to 2040”, tech. rep., USDOE

- Energy Information Administration (EIA), Washington, DC (United States). Office of Energy Analysis, 2016.
- [11] C. J. Bai and W. C. Wang, “Review of computational and experimental approaches to analysis of aerodynamic performance in horizontal-axis wind turbines (HAWTs)”, *Renewable and Sustainable Energy Reviews*, vol. 63, pp. 506–519, 2016.
- [12] M. Ó. Óskarsdóttir, “A General Description and Comparison of Horizontal Axis Wind Turbines and Vertical Axis Wind Turbines”, PhD thesis, 2014.
- [13] E. Sun, “Spinning electricity out of thin, moving air”, 15-12-2012. Accessed on: 04-04-2018. [Online]. Available: <http://sitn.hms.harvard.edu/flash/2012/wind/>.
- [14] S. M. Larwood and R. Chow, “Comparison of upwind and downwind operation of the NREL phase VI experiment”, in *Journal of Physics: Conference Series*, vol. 753, p. 022041, IOP Publishing, 2016.
- [15] J. Schepers, A. Brand, A. Bruining, M. Hand, D. Infield, H. Madsen, T. Maeda, J. Paynter, R. van Rooij, Y. Shimizu, D.A. Simms, and N. Stefanatos, “Final report of IEA Annex XVIII: enhanced field rotor aerodynamics database”, *Energy Research Center of the Netherlands, ECN-C-02-016, February, 2002*.
- [16] D. A. Simms, M. Hand, L. Fingersh, and D. Jager, “Unsteady aerodynamics experiment phases II-IV test configurations and available data campaigns”, tech. rep., National Renewable Energy Lab., Golden, CO (US), 1999.
- [17] C. P. Butterfield, W. P. Musial, and D. A. Simms, “Combined experiment phase 1. Final report”, tech. rep., National Renewable Energy Lab., Golden, CO (US), 1992.
- [18] J. D. Anderson, *Introduction to flight*, 8th ed. McGraw-Hill Higher Education, 2016.
- [19] A. Fluent, “12.0 user’s guide”, *Ansys Inc, New Hampshire*, 2009.
- [20] D. A. Spera, “Wind turbine technology, fundamental concepts of wind turbine engineering”, *New York: ASME*, 1994.
- [21] A. Betz, “Wind energy and its extraction through wind mills”, *Vieweg, Gottingen*, 1926.
- [22] H. Glauert, “Airplane propellers”, in *Aerodynamic theory*, pp. 169–360, Springer, 1935.

- [23] L. Prandtl, A. Betz “Vier Abhandlungen zur Hydrodynamik und Aerodynamik”, *Universitätsverlag Göttingen*, 1927.
- [24] W. Z. Shen, R. Mikkelsen, J. N. Sørensen, and C. Bak, “Tip loss corrections for wind turbine computations”, *Wind Energy*, vol. 8, no. 4, pp. 457–475, 2005.
- [25] J. G. Leishman and T. Beddoes, “A semi-empirical model for dynamic stall”, *Journal of the American Helicopter society*, vol. 34, no. 3, pp. 3–17, 1989.
- [26] H. M. Lee and Y. Wu, “An experimental study of stall delay on the blade of a horizontal-axis wind turbine using tomographic particle image velocimetry”, *Journal of Wind Engineering and Industrial Aerodynamics*, vol. 123, pp. 56–68, 2013.
- [27] Y. Li, K.-J. Paik, T. Xing, and P. M. Carrica, “Dynamic overset CFD simulations of wind turbine aerodynamics”, *Renewable Energy*, vol. 37, no. 1, pp. 285–298, 2012.
- [28] B. Sanderse, S. Pijl, and B. Koren, “Review of computational fluid dynamics for wind turbine wake aerodynamics”, *Wind energy*, vol. 14, no. 7, pp. 799–819, 2011.
- [29] Y. Song and J. B. Perot, “CFD simulation of the NREL phase VI rotor”, *Wind engineering*, vol. 39, no. 3, pp. 299–309, 2015.
- [30] J. Y. You, D. O. Yu, and O. J. Kwon, “Effect of turbulence models on predicting HAWT rotor blade performances”, *Journal of Mechanical Science and Technology*, vol. 27, no. 12, pp. 3703–3711, 2013.
- [31] K. Mansour and M. Yahyazade, “Effects of turbulence model in computational fluid dynamics of horizontal axis wind turbine aerodynamic”, *WSEAS Trans. Appl. Theor. Mech*, vol. 3, no. 6, 2011.
- [32] N. Tachos, A. Filios, D. Margaris, and J. Kaldellis, “A computational aerodynamics simulation of the NREL phase II rotor”, *Open Mechanical Engineering Journal*, vol. 3, pp. 9–16, 2009.
- [33] C. Thumthae and T. Chitsomboon, “Optimal angle of attack for untwisted blade wind turbine”, *Renewable energy*, vol. 34, no. 5, pp. 1279–1284, 2009.

- [34] M. A. Elfarrar, N. Sezer-Uzol, and I. S. Akmandor, “NREL VI rotor blade: numerical investigation and winglet design and optimization using CFD”, *Wind Energy*, vol. 17, no. 4, pp. 605–626, 2014.
- [35] L. Daróczy, G. Janiga, K. Petrasch, M. Webner, and D. Thévenin, “Comparative analysis of turbulence models for the aerodynamic simulation of H-darrieus rotors”, *Energy*, vol. 90, pp. 680–690, 2015.
- [36] N. Sørensen and J. Michelsen, “Aerodynamic predictions for the unsteady aerodynamics experiment phase-II rotor at the national renewable energy laboratory”, in *2000 ASME Wind Energy Symposium*, p. 37, 2000.
- [37] R. Lanzafame, S. Mauro, and M. Messina, “Wind turbine CFD modeling using a correlation-based transitional model”, *Renewable Energy*, vol. 52, pp. 31–39, 2013.
- [38] N. N. Sørensen, F. Zahle, K. Boorsma, and G. Schepers, “CFD computations of the second round of mexico rotor measurements”, in *Journal of Physics: Conference Series*, vol. 753, p. 022054, IOP Publishing, 2016.
- [39] J. Newman, *Marine hydrodynamics*, 40th ed. The MIT Press, 2018.
- [40] H. Chen and N. Qin, “Trailing-edge flow control for wind turbine performance and load control”, *Renewable Energy*, vol. 105, pp. 419–435, 2017.
- [41] N. N. Sørensen, J. Michelsen, and S. Schreck, “Navier–stokes predictions of the NREL phase VI rotor in the NASA Ames 80 ft× 120 ft wind tunnel”, *Wind Energy*, vol. 5, no. 2-3, pp. 151–169, 2002.
- [42] D. P. Raymer, *Aircraft Design: A Conceptual Approach*, 5th ed. American Institute of Aeronautics and Astronautics, 2012
- [43] P. J. Schubel and R. J. Crossley, “Wind turbine blade design”, *Energies*, vol. 5, no. 9, pp. 3425–3449, 2012.
- [44] A. G. Domel, M. Saadat, J. C. Weaver, H. Haj-Hariri, K. Bertoldi, and G. V. Lauder, “Shark skin-inspired designs that improve aerodynamic performance”, *Journal of The Royal Society Interface*, vol. 15, no. 139, p. 20170828, 2018.

- [45] M. Amitay, B. Smith, and A. Glezer, “Aerodynamic flow control using synthetic jet technology”, in *36th AIAA Aerospace Sciences Meeting and Exhibit*, p. 208, 1998.
- [46] A. Sareen, R. W. Deters, S. P. Henry, and M. S. Selig, “Drag reduction using riblet film applied to airfoils for wind turbines”, in *49th AIAA Aerospace Sciences Meeting*, p. 558, 2011.
- [47] L. P. Chamorro, R. Arndt, and F. Sotiropoulos, “Drag reduction of large wind turbine blades through riblets: Evaluation of riblet geometry and application strategies”, *Renewable energy*, vol. 50, pp. 1095–1105, 2013.
- [48] B. S. Sidhu, M. R. Saad, K. Z. K. Ahmad, and A. C. Idris, “Riblets for airfoil drag reduction in subsonic flow”, *ARPJ Journal of Engineering and Applied Sciences*, pp. 7694–7698, 2016.
- [49] M. Ghazali, Z. Harun, W. Wan Ghopa, and A. Abbas, “Computational fluid dynamic simulation on NACA 0026 airfoil with V-groove riblets”, *International Journal on Advanced Science, Engineering and Information Technology*, vol. 6, no. 4, pp. 529–533, 2016.
- [50] Y. Yang, “The characteristics of typical riblets on drag reduction”, *DEStech Transactions on Environment, Energy and Earth Sciences*, 2017.
- [51] R. T. Whitcomb, “A design approach and selected wind tunnel results at high subsonic speeds for wing-tip mounted winglets”, *NASA*, 1976.
- [52] J. E. Guerrero, D. Maestro, and A. Bottaro, “Biomimetic spiroid winglets for lift and drag control”, *Comptes Rendus Mecanique*, vol. 340, no. 1-2, pp. 67–80, 2012.
- [53] C. P. Van Dam, R. Chow, J. R. Zayas, and D. E. Berg, “Computational investigations of small deploying tabs and flaps for aerodynamic load control”, *Journal of Physics: Conference Series*, vol. 75, no. 1, pp. 012027, 2007.
- [54] M. Walsh, “Turbulent boundary layer drag reduction using riblets”, in *20th aerospace sciences meeting*, p. 169, 1982.
- [55] M. Walsh and A. Lindemann, “Optimization and application of riblets for turbulent drag reduction”, in *22nd Aerospace Sciences Meeting*, p. 347, 1984.

- [56] D. Bechert, M. Bruse, and W. Hage, “Experiments with three-dimensional riblets as an idealized model of shark skin”, *Experiments in fluids*, vol. 28, no. 5, pp. 403–412, 2000.
- [57] B. Dean and B. Bhushan, “Shark-skin surfaces for fluid-drag reduction in turbulent flow: a review”, *Philosophical Transactions of the Royal Society of London A: Mathematical, Physical and Engineering Sciences*, vol. 368, no. 1929, pp. 4775–4806, 2010.
- [58] J. Oeffner and G. V. Lauder, “The hydrodynamic function of shark skin and two biomimetic applications”, *Journal of Experimental Biology*, vol. 215, no. 5, pp. 785–795, 2012.
- [59] L. Wen, J. C. Weaver, and G. V. Lauder, “Biomimetic shark skin: design, fabrication and hydrodynamic function”, *Journal of Experimental Biology*, vol. 217, no. 10, pp. 1656–1666, 2014.
- [60] G. V. Lauder, D. K. Wainwright, A. G. Domel, J. C. Weaver, L. Wen, and K. Bertoldi, “Structure, biomimetics, and fluid dynamics of fish skin surfaces”, *Physical Review Fluids*, vol. 1, no. 6, p. 060502, 2016.
- [61] H. Choi, P. Moin, and J. Kim, “Direct numerical simulation of turbulent flow over riblets”, *Journal of fluid mechanics*, vol. 255, pp. 503–539, 1993.
- [62] J. Tiainen, A. Grönman, A. Jaatinen-Värri and L. Pyy, “Effect of non-ideally manufactured riblets on airfoil and wind turbine performance”, *Renewable Energy*, vol. 155, pp. 79–89, 2020.
- [63] D. Bechert and M. Bartenwerfer, “The viscous flow on surfaces with longitudinal ribs”, *Journal of fluid mechanics*, vol. 206, pp. 105–129, 1989.
- [64] P. Luchini, F. Manzo, and A. Pozzi, “Resistance of a grooved surface to parallel flow and cross-flow”, *Journal of fluid mechanics*, vol. 228, pp. 87–109, 1991.
- [65] S. Martin and B. Bhushan, “Fluid flow analysis of continuous and segmented riblet structures”, *Rsc Advances*, vol. 6, pp. 10962–10978, 2016.
- [66] R. Garcia-Mayoral and J. Jiménez, “Hydrodynamic stability and breakdown of the viscous regime over riblets”, *Journal of Fluid Mechanics*, vol. 678, pp. 317–347, 2011.

- [67] D. Bechert, M. Bruse, W. V. Hage, J. T. Van der Hoeven, and G. Hoppe, “Experiments on drag-reducing surfaces and their optimization with an adjustable geometry”, *Journal of fluid mechanics*, vol. 338, pp. 59–87, 1997.
- [68] B. E. Launder and S. Li, “On the prediction of riblet performance with engineering turbulence models”, in *Further Developments in Turbulence Management*, pp. 283–298, Springer, 1993.
- [69] D. C. Chu and G. E. Karniadakis, “A direct numerical simulation of laminar and turbulent flow over riblet-mounted surfaces”, *Journal of fluid mechanics*, vol. 250, pp. 1–42, Cambridge University Press, 1993.
- [70] F. Beibei, L. Xiaodi, C. Darong, and W. Jiadao, “Characteristics of flow over thin triangular riblet surface”, *Recent Advances in Fluid Mechanics, Heat & Mass Transfer and Biology*, 2011.
- [71] L. Djenidi, L. Squire, and A. Savill, “High resolution conformal mesh computations for V, U or L groove riblets in laminar and turbulent boundary layers”, in *Recent Developments in Turbulence Management*, pp. 65–92, Springer, 1991.
- [72] P. A. Leitl, V. Stenzel, A. Flanschger, H. Kordy, C. Feichtinger, Y. Kowalik, S. Schreck, and D. Stübing, “Riblet surfaces for improvement of efficiency of wind turbines”, in *AIAA Scitech 2020 Forum*, p. 0308, 2020.
- [73] S. B. Pope, *Turbulent flows*. IOP Publishing, 2001.
- [74] J. O. Hinze, *Turbulence*. McGraw-Hill Publishing Co, New York, 1959.
- [75] P. Spalart and S. Allmaras, “A one-equation turbulence model for aerodynamic flows”, in *30th aerospace sciences meeting and exhibit*, p. 439, 1992.
- [76] F. R. Menter, “Two-equation eddy-viscosity turbulence models for engineering applications”, *AIAA journal*, vol. 32, no. 8, pp. 1598–1605, 1994.
- [77] B. E. Launder and D. B. Spalding, *Mathematical models of turbulence*. Academic Press, 1972.
- [78] J. O. Mo, A. Choudhry, M. Arjomandi, R. Kelso, and Y.-H. Lee, “Effects of wind speed changes on wake instability of a wind turbine in a virtual wind tunnel using large

- eddy simulation”, *Journal of Wind Engineering and Industrial Aerodynamics*, vol. 117, pp. 38–56, 2013.
- [79] G. Bachelor, *An introduction to fluid dynamics*, 3rd ed. Cambridge University Press, 2000.
- [80] J. Luo and A. Gosman, “Prediction of impeller-induced flow in mixing vessels using multiple frames of reference”, *Institute of Chemical Engineers Symposium Series*, 1994.
- [81] A. A. Matyushenko, E. V. Kotov, and A. V. Garbaruk, “Calculations of flow around airfoils using two-dimensional RANS: an analysis of the reduction in accuracy”, *St. Petersburg Polytechnical University Journal: Physics and Mathematics*, vol. 3, no. 1, pp. 15–21, 2017.
- [82] A. J. Wadcock, “Investigation of low-speed turbulent separated flow around airfoils”, NASA, 1987.
- [83] H. Y. Xu, C. L. Qiao, H. Q. Yang, and Z. Y. Ye, “Delayed detached eddy simulation of the wind turbine airfoil S809 for angles of attack up to 90 degrees”, *Energy*, vol. 118, pp. 1090–1109, 2017.
- [84] C. P. Butterfield, G. Scott, and W. Musial, “Comparison of wind tunnel airfoil performance data with wind turbine blade data”, *Journal of solar energy engineering*, vol. 114, no. 2, pp. 119–124, 1992.
- [85] M. Keating, “ANSYS Advantage”, *ANSYS, Inc*, vol. 1, p. 48, 2011.
- [86] C. P. Butterfield, W. Musial, G. Scott, and D. Simms, “NREL combined experimental final report—phase II”, tech. rep., National Renewable Energy Laboratory (NREL), Golden, CO., 1992.
- [87] E. L. Blades and D. L. Marcum, “A sliding interface method for unsteady unstructured flow simulations”, *International Journal for Numerical Methods in Fluids*, vol. 53, no. 3, pp. 507–529, 2005.
- [88] S. A. Abdulqadir, H. Iacovides, and A. Nasser, “The physical modelling and aerodynamics of turbulent flows around horizontal axis wind turbines”, *Energy*, vol. 119, pp. 767–799, 2017.

- [89] M. Hand, D. Simms, L. Fingersh, D. Jager, J. Cotrell, S. Schreck, and S. Larwood, “Unsteady aerodynamics experiment phase VI: wind tunnel test configurations and available data campaigns”, tech. rep., National Renewable Energy Lab., Golden, CO. (US), 2001.
- [90] D. Simms, S. Schreck, M. Hand, and L. J. Fingersh, “NREL unsteady aerodynamics experiment in the NASA-Ames wind tunnel: a comparison of predictions to measurements”, tech. rep., National Renewable Energy Lab., Golden, CO (US), 2001.
- [91] E. P. Duque, W. Johnson, C. VanDam, R. Cortes, and K. Yee, “Numerical predictions of wind turbine power and aerodynamic loads for the NREL phase II combined experiment rotor”, tech. rep., National Aeronautics And Space Administration Moffett Field Ca Ames Research Center, 2000.

## Appendix A (Smooth Study Cases)

### 8 SMOOTH STUDY CASES

#### 8.1 Study Case 1 (2D, RANS, NACA 4412, $Re_c = 1.64 \times 10^6$ )

##### 8.1.1 Purpose

The main purpose of this study case is to test two different shapes of fluid domain to observe their effect on the lift and drag coefficients of an aerofoil. The result is shown in terms of a relation between AOAs and lift and drag coefficients at a constant wind speed of  $29.1m/s$  for a 2D NACA 4412 aerofoil.

##### 8.1.2 Geometrical setup

Two different fluid domains are created to study the shape effect on an aerofoil. The two fluid domain setups are shown in Figure 159 (rectangular shape) and Figure 160 (semi-circle shape at inlet). In both geometries, the domain boundaries are placed at 15 chord ( $c$ ) measured from the leading edge of the aerofoil. The aerofoil is set to be stationary with no slip condition. Other boundary conditions are velocity-inlet, walls, and pressure-outlet.

##### 8.1.3 Mesh study & simulation setup

The mesh dependency of this study case is represented in Figure 161 for  $\alpha = 12^\circ$ . From Figure 161, a mesh of  $1 \times 10^5$  elements is selected as lift coefficient becomes approximately independent of mesh size. Figure 162 displays how the  $y^+$  changes with lift coefficient. The selected mesh has an average value of  $y^+ = 1.15$ . The mesh study is based on changing the number of nodes on perpendicular and parallel directions to the flow.

There are 80 and 130 nodes in the normal and streamwise axes respectively for freestream boundary layers. There are 600 nodes on the aerofoil edge with 30 inflation layers. The

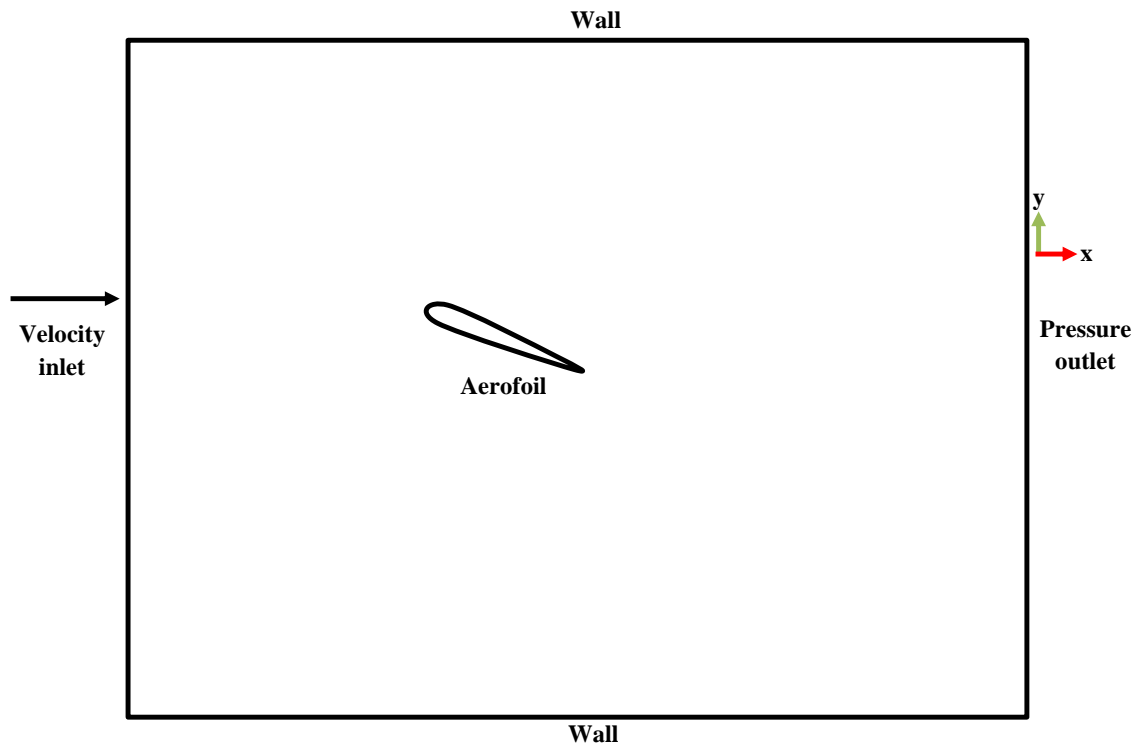


Figure 159: Study case 1 rectangular shape fluid domain (not to scale)

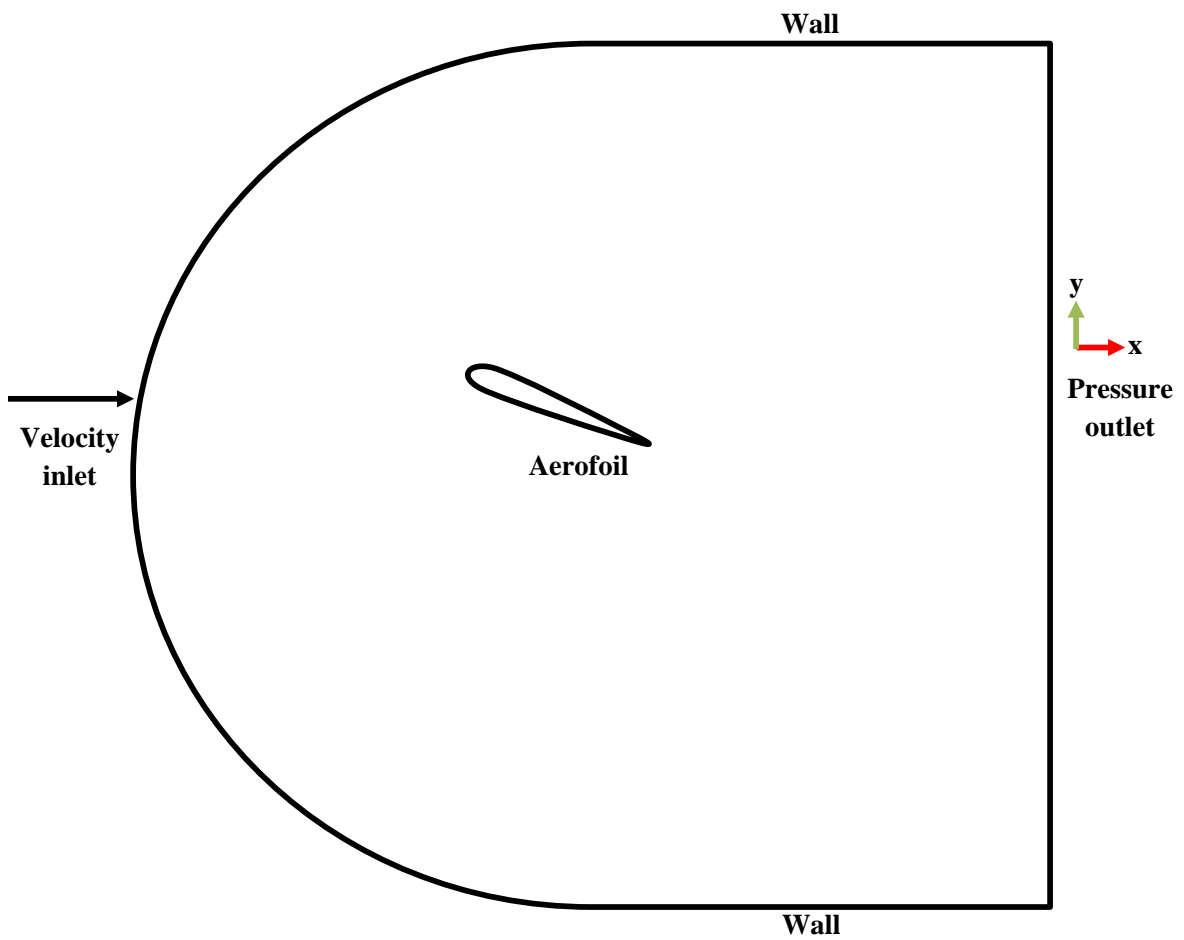


Figure 160: Study case 1 C-shaped fluid domain (not to scale)

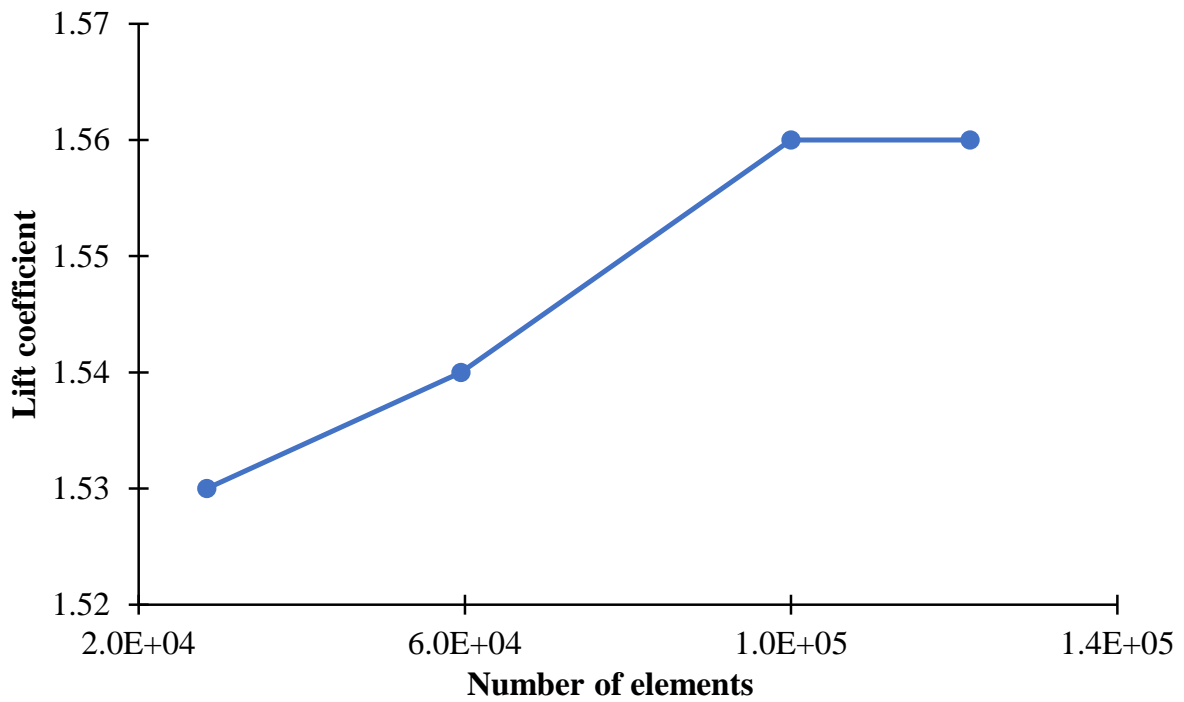


Figure 161: Mesh dependency for study case 1

mesh metric is displayed in Figures 163 and 164 for skewness and orthogonality, respectively. Minimising skewness and maximising orthogonality are achieved for better mesh quality. Figures 165-168 show the generated mesh. The simulation algorithm is shown in Table 37.

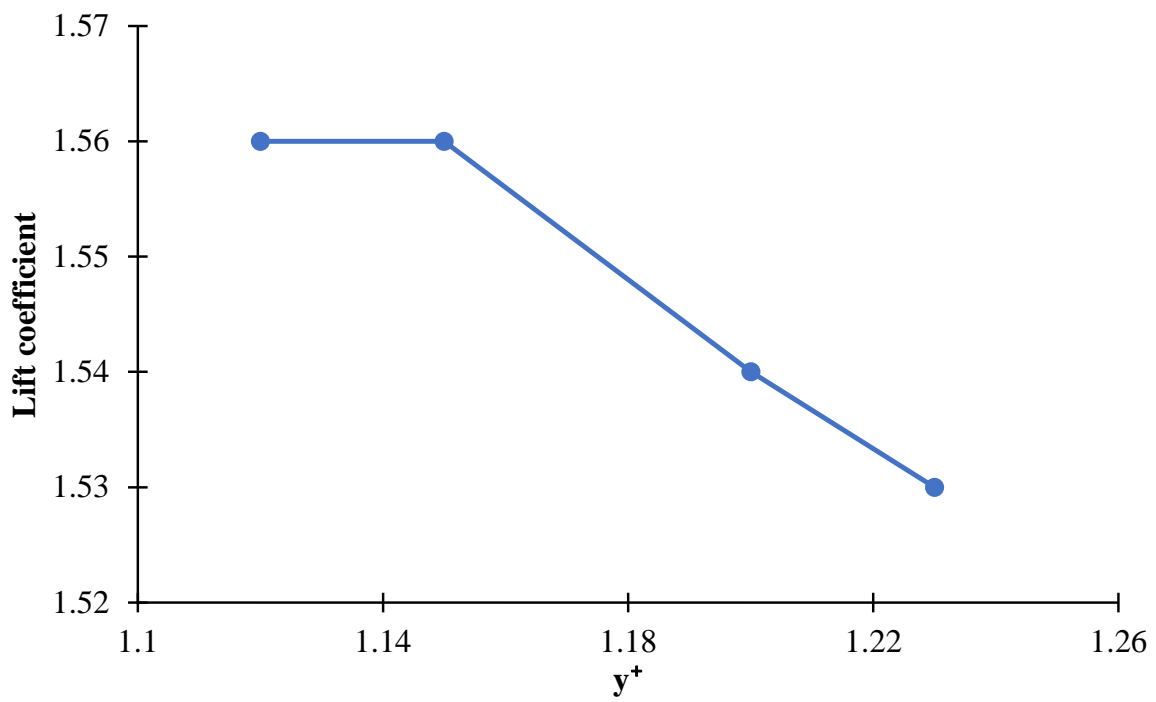


Figure 162:  $y^+$  values for different meshes of study case 1

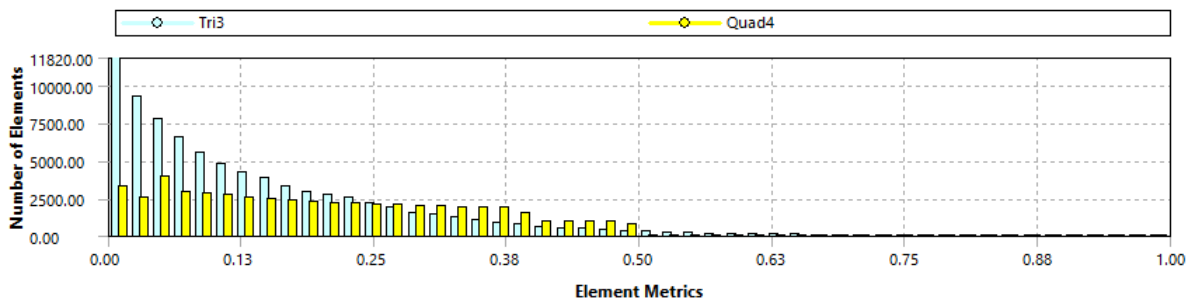


Figure 163: The skewness of study case 1

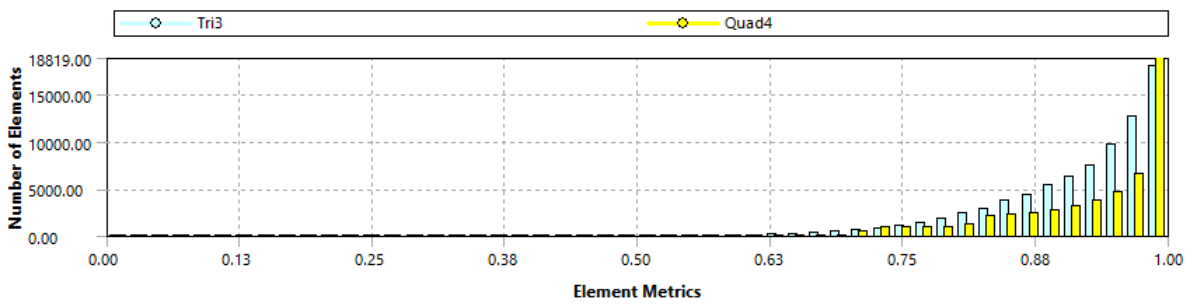


Figure 164: The orthogonality of study case 1

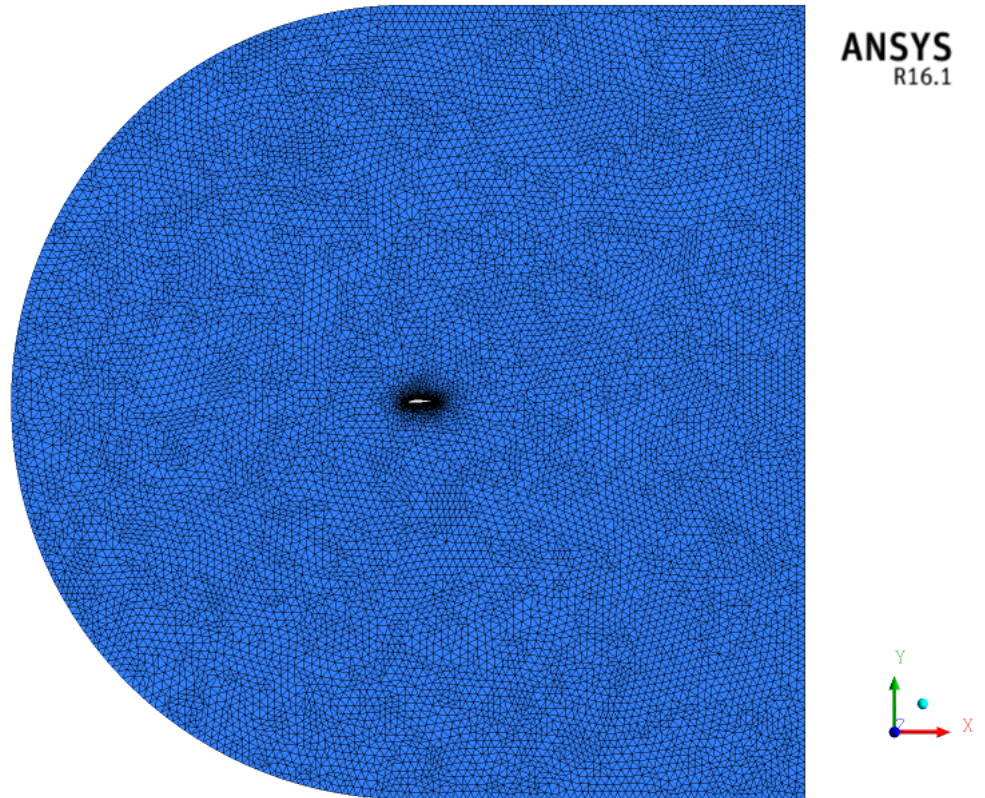


Figure 165: The generated mesh of fluid domain and aerofoil for case 1

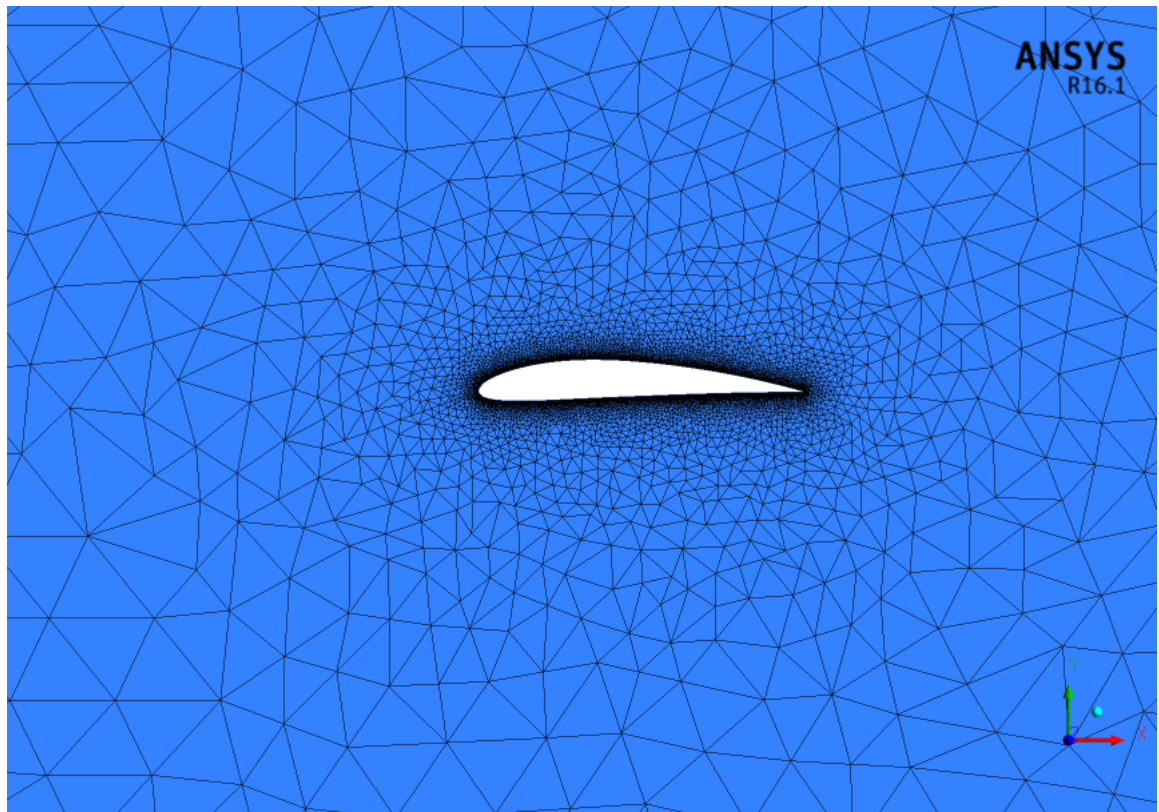


Figure 166: The generated mesh of the aerofoil for case 1

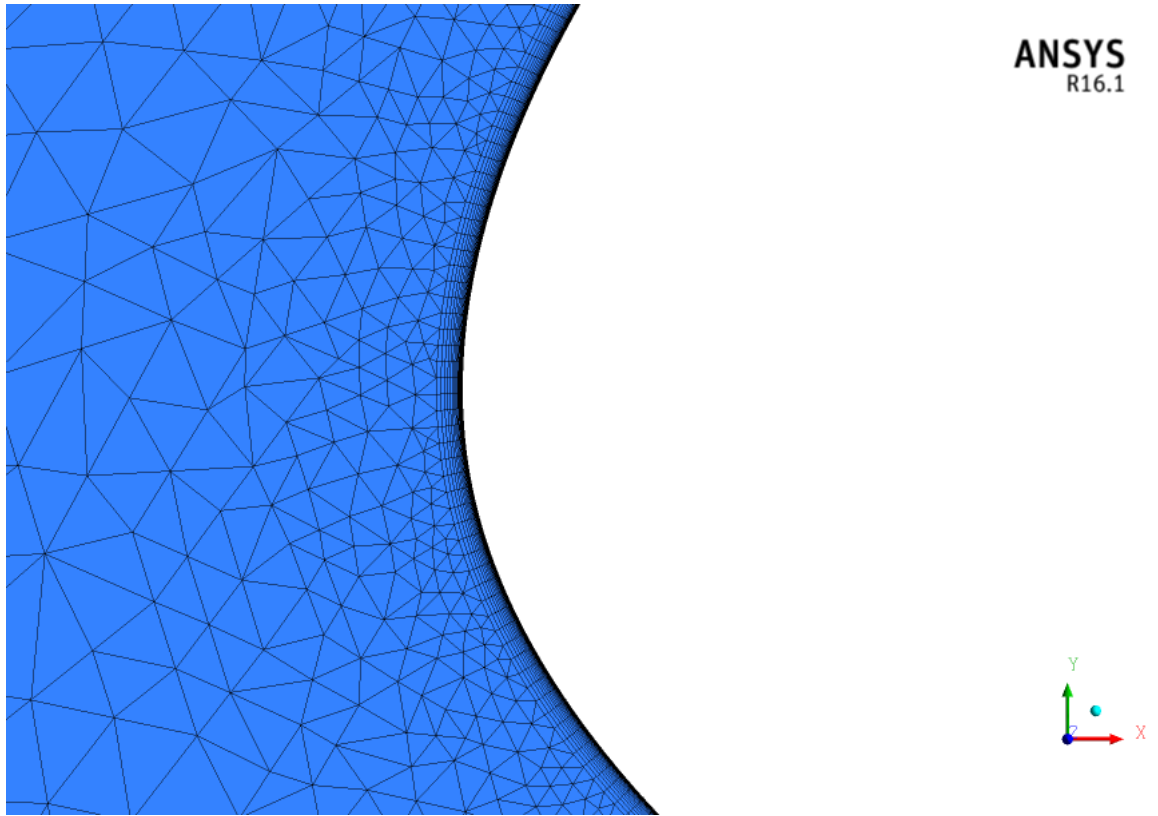


Figure 167: The generated mesh of the aerofoil's leading edge for case 1

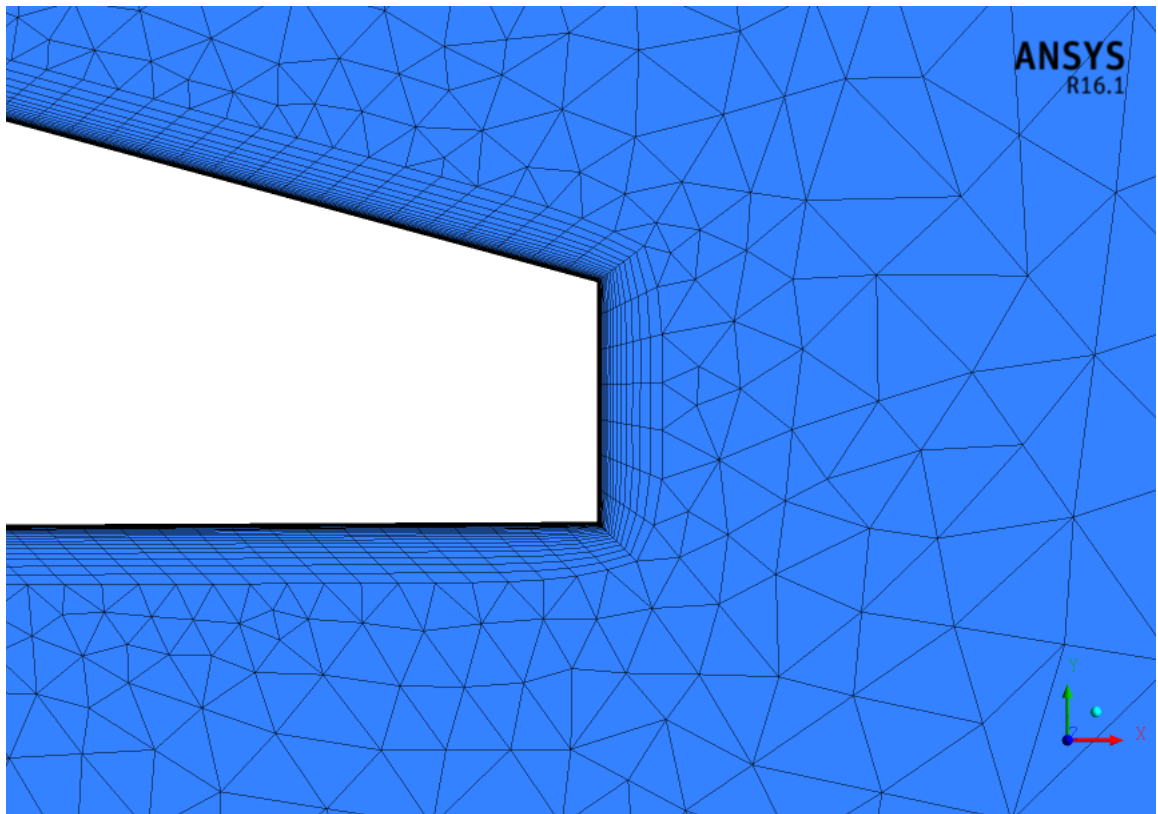


Figure 168: The generated mesh of the aerofoil's trailing edge for case 1

Table 37: Study case 1 simulation algorithm

<b>Algorithm</b>	<b>Function Used</b>
Turbulence Model	<i>SST</i> $k - \omega$
Turbulence Intensity	$I = 0.1\%$ [81]
Viscosity Ratio	$\nu_t/\nu = 1$ [81]
Wind Velocity	$V_\infty = 29.1m/s$ [82]
Pressure-Velocity Coupling	Coupled
Interpolating Scheme	Second Order

### 8.1.4 Results & discussion

The convergence history of the lift coefficient is shown in Figure 169. At about 2000 iterations, the lift coefficient does not change as the simulation continues to run therefore, study case 1 is converged. The  $y^+$  distribution along the chord line of the aerofoil is displayed in Figure 170. The values of  $y^+$  at different aerofoil locations are below 2, which means the generated mesh is able to resolve the viscous sub-layer.

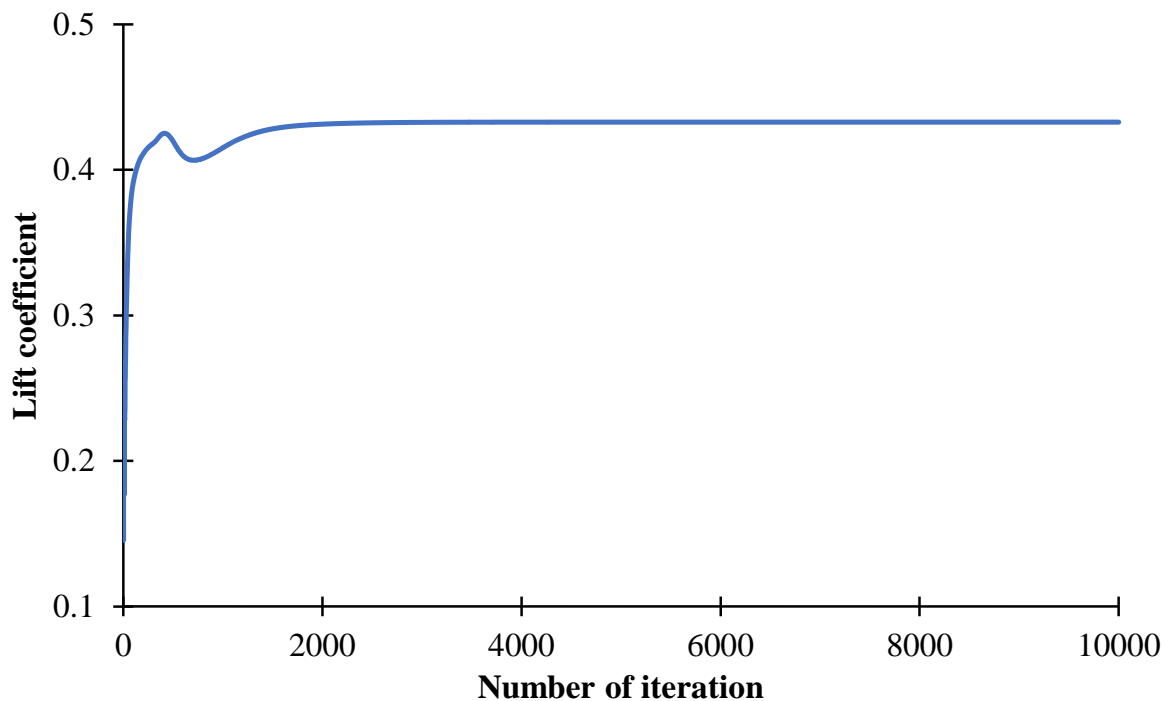


Figure 169: The convergence history of study case 1

The simulation is assumed 2D and steady state using the *SST*  $k - \omega$  turbulence model. The result is compared to a simulation by Matyushenko *et al.* [81], who used the same turbulence model. Both numerical simulations are plotted and validated against experimental work that was conducted by Wadcock [82], as displayed in Figure 171. Referring to Figure 171, C-shaped domain shows a slightly better agreement with referenced simulation than rectangular shaped domain at most flow conditions. This is because the C-shaped domain has a very similar pattern to the aerofoil leading edge. Both simulations overpredict the lift coefficients at high AOAs, where flow separation occurs.

This work's simulation poorly predict the AOA at maximum lift coefficient. According to experiment, the maximum lift coefficient is at  $\alpha = 12^\circ$ , while the computed maximum lift

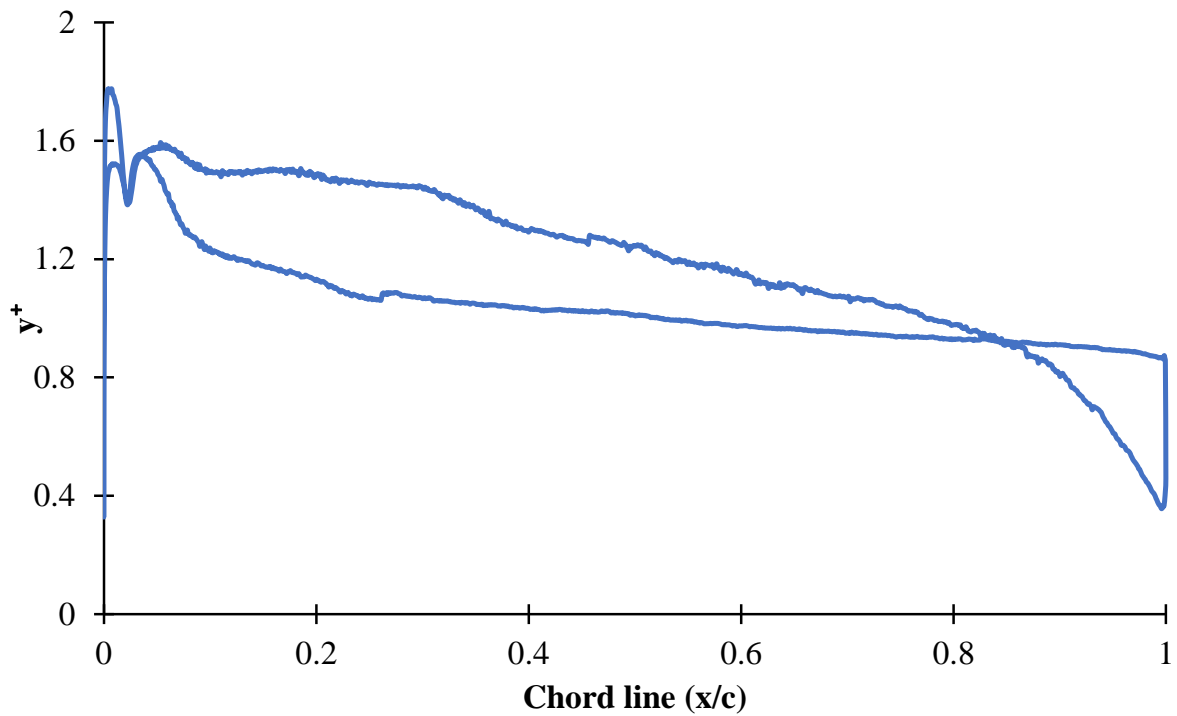


Figure 170: The  $y^+$  distribution of study case 1

coefficient is at  $\alpha = 16^\circ$ . An additional simulation is run using SIMPLE algorithm. The result is displayed in Figure 172 with better matching with experiment by showing the maximum lift coefficient at  $\alpha = 12^\circ$ . Figure 173 shows the computed drag coefficient versus AOAs. In general, a good agreement of computed drag coefficient with experiment at low AOAs. However, as AOA increases, the computed values differ from experiment, particularly at stall and post-stall AOAs.

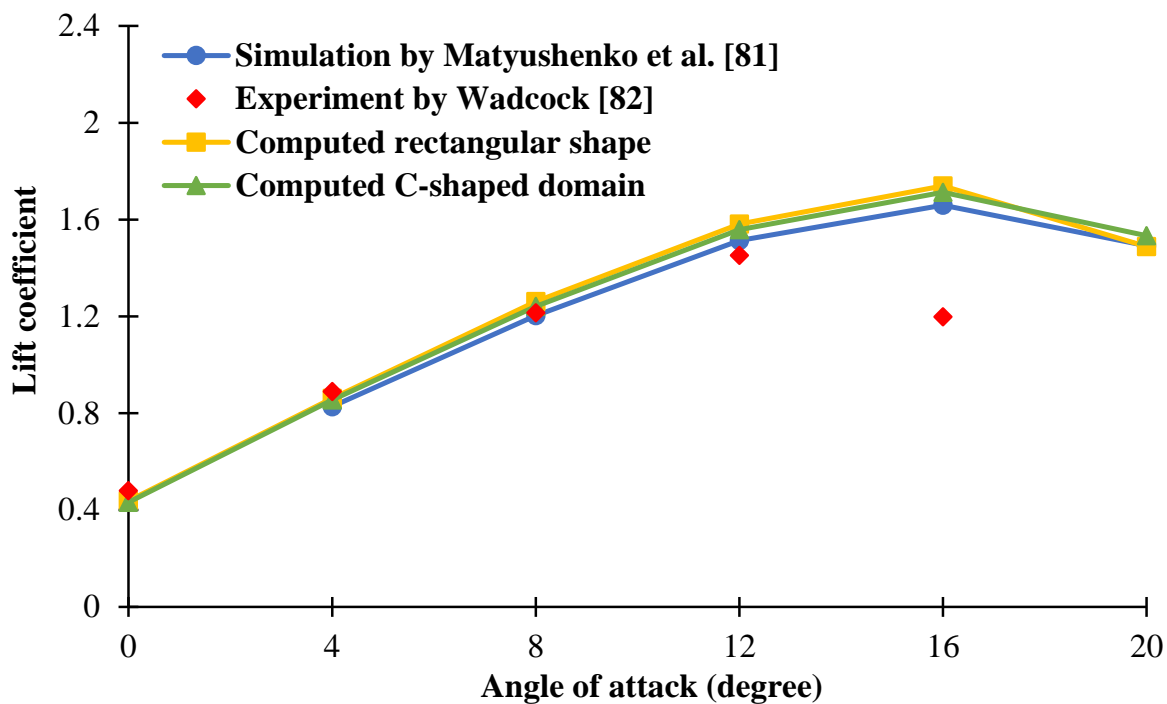


Figure 171: Lift coefficient versus angle of attack for study case 1

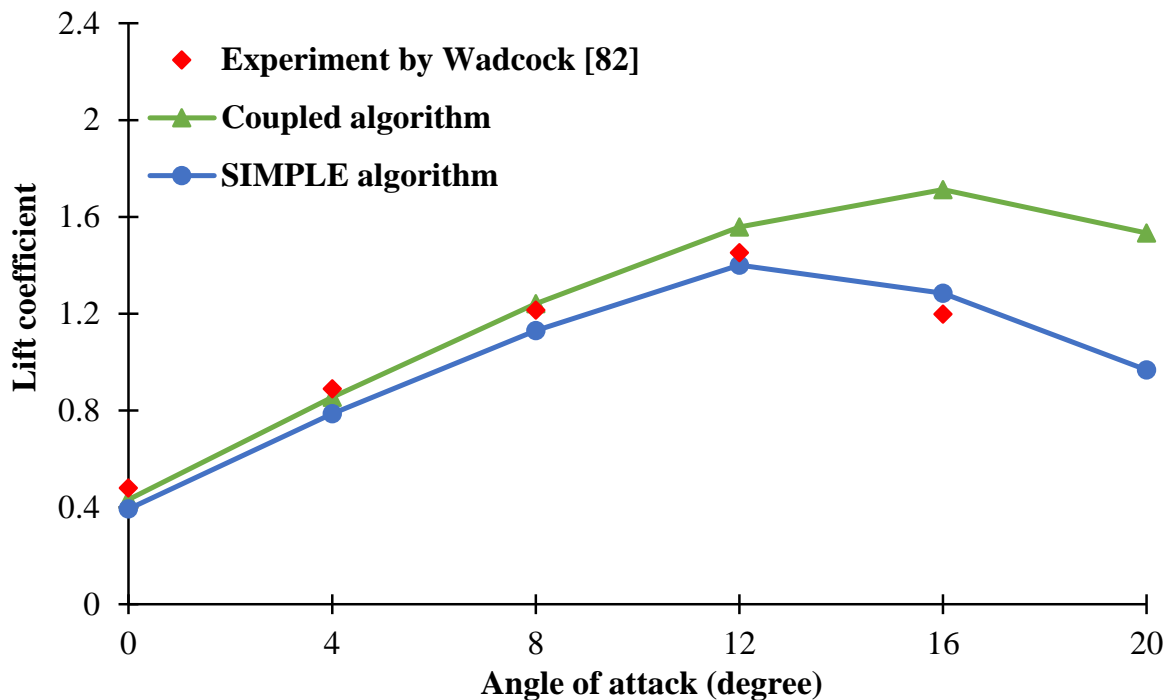


Figure 172: Lift coefficient versus angle of attack for different pressure-velocity couplings (study case 1)

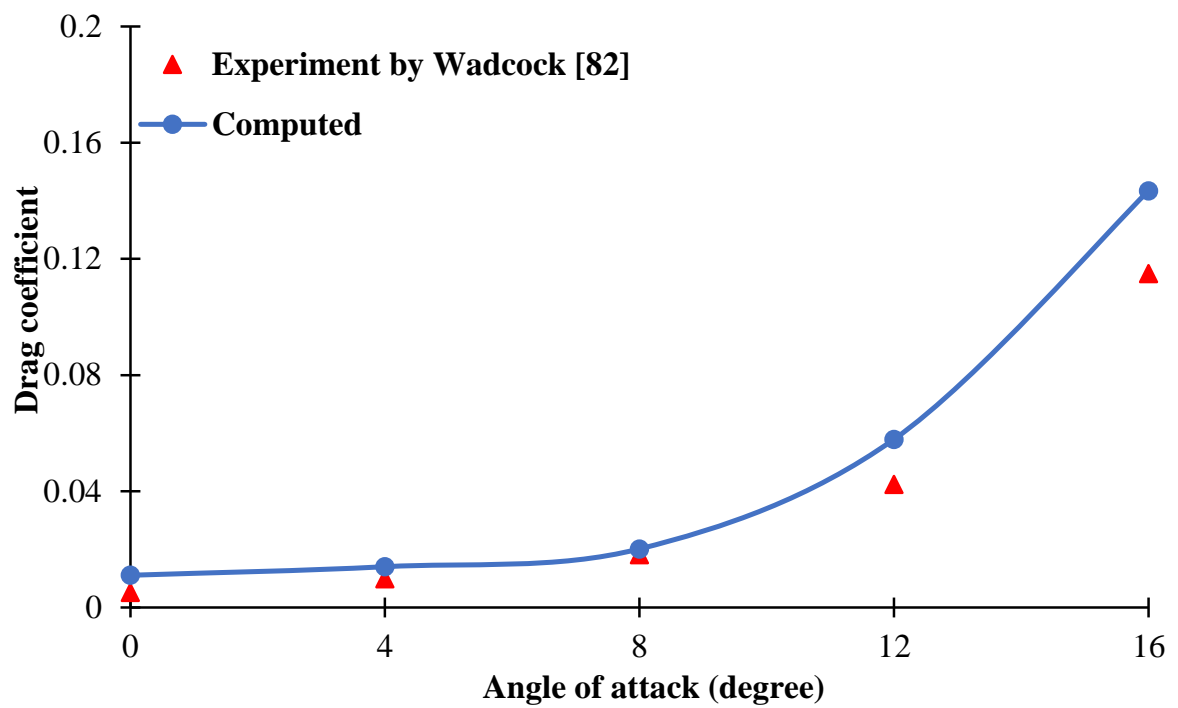


Figure 173: Drag coefficient versus angle of attack for study case 1

## 8.2 Study Case 2 (2D, URANS, S809, $Re_c = 6.5 \times 10^5$ )

### 8.2.1 Purpose

Examining two different turbulence models' effect on 2D force coefficients of S809 aerofoil is the core of this study case. The two models are  $S - A$  and  $SST k - \omega$ . The computational conditions are the same for both models, including mesh and simulation settings. The result is compared to  $S - A$  turbulence model that was performed by Xu *et al.* [83] and it is validated against wind tunnel experiment that was conducted by Butterfield *et al.* [84].

### 8.2.2 Geometrical setup

The fluid domain of study case 2 has a rectangular shape with dimensions of  $3.66m$  and  $25.83m$  in height and length respectively, as shown in Figure 174. This is the same dimensions that was used for wind tunnel experiment by Butterfield *et al.* [84]. However, the fluid domain of the referenced simulation by Xu *et al.* [83] is not clearly provided in the literature. The boundary conditions for this study case are also specified in Figure 174.

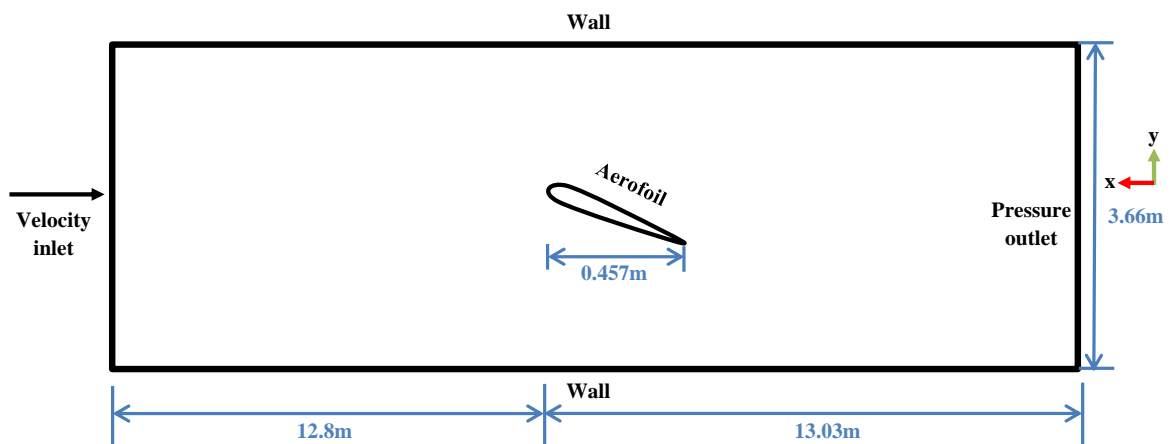


Figure 174: Study case 2 rectangular fluid domain (not to scale)

### 8.2.3 Mesh study & computational setup

Mesh dependency study of this case at AOA of  $\alpha = 0^\circ$  is displayed in Figure 175. It shows how drag coefficient changes as the mesh elements change. Therefore, a mesh of about  $1.25 \times 10^5$  elements is selected as the result becomes independent on mesh elements. Figure 176 displays how the  $y^+$  changes with drag coefficient. The selected mesh has an average value of  $y^+ = 1.625$ . For this selected mesh, there are about 80 and 300 nodes in normal and parallel directions to the freestream, respectively.

The aerofoil edge has about 400 nodes with 30 inflation layers and growth rate of 1.2. The first layer is placed at  $50\mu m$  to resolve laminar region as well as validate riblet effect for later study. The mesh metric of study case 2 for skewness and orthogonality are shown in Figures 177 and 178, respectively. The generated mesh pictures of this case are displayed in Figures 179-182. The simulation settings are shown in Table 38.

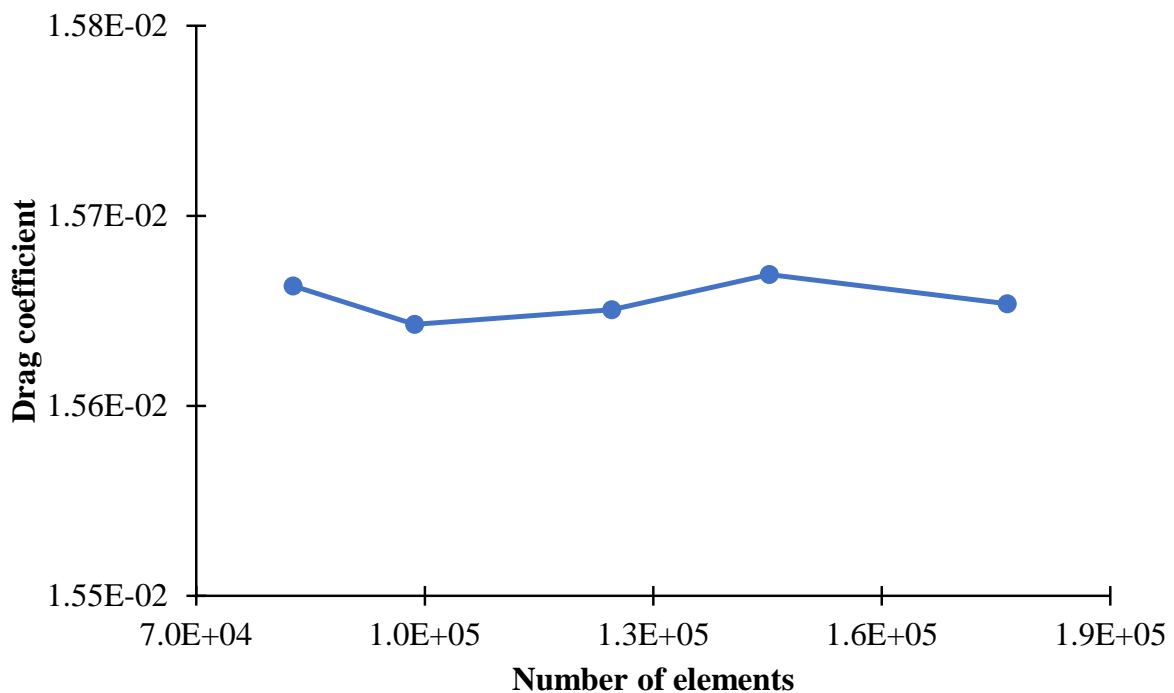


Figure 175: Mesh dependency for study case 2

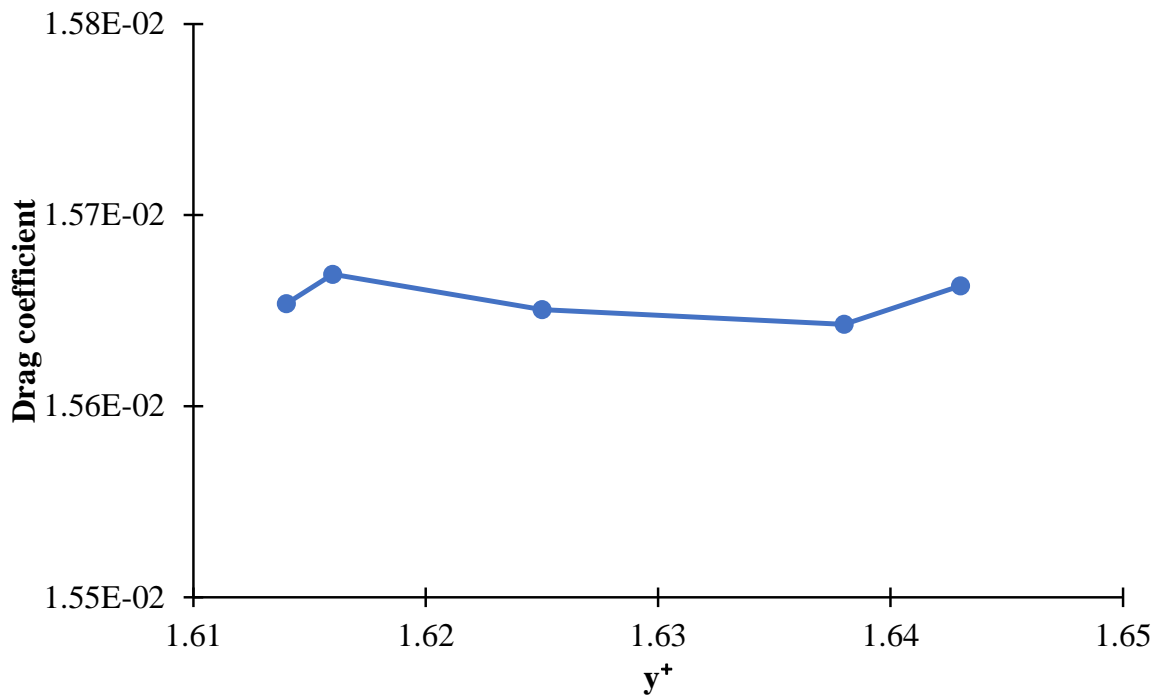


Figure 176:  $y^+$  values for different meshes of study case 2

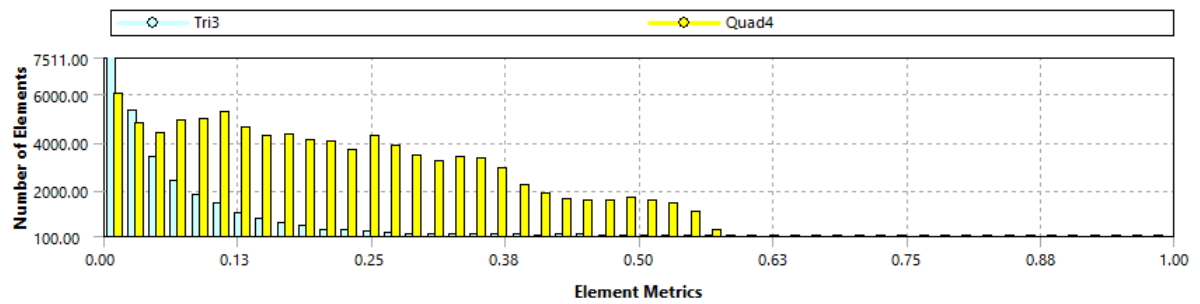


Figure 177: The skewness of study case 2

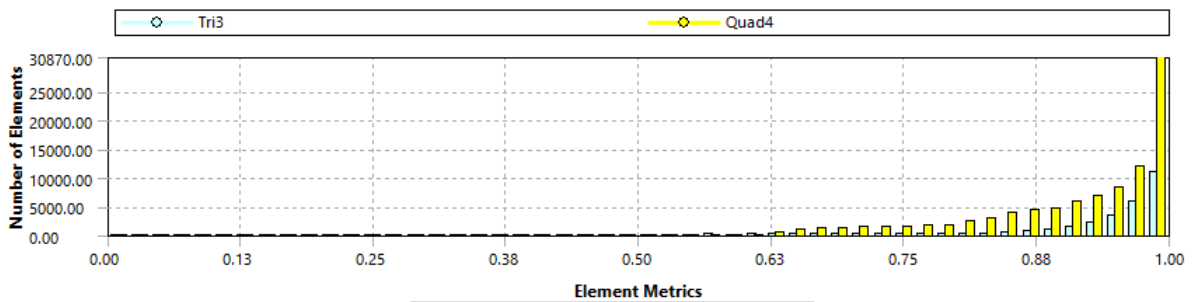


Figure 178: The orthogonality of study case 2

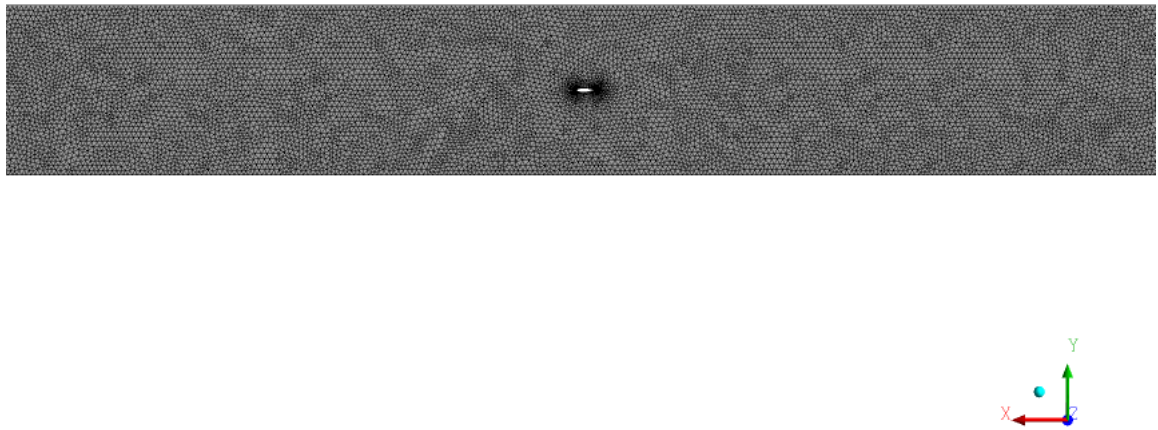


Figure 179: The generated mesh of fluid domain and aerofoil for case 2

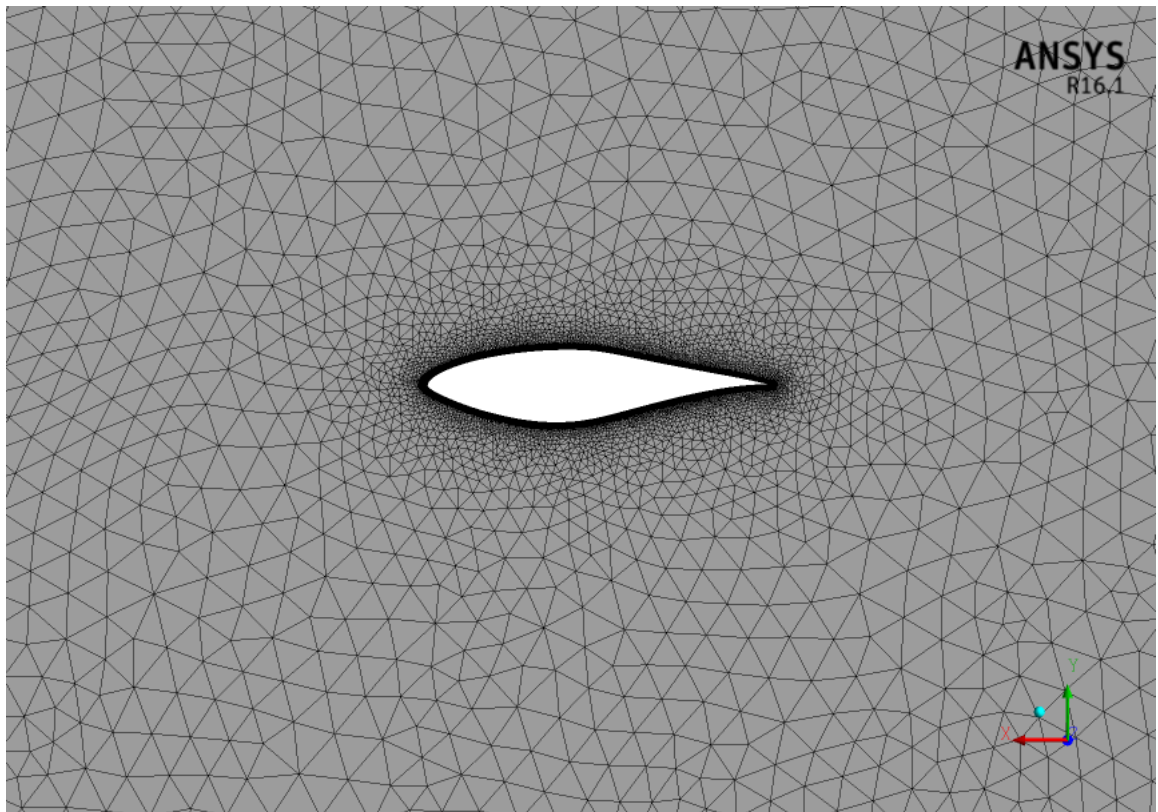


Figure 180: The generated mesh of the aerofoil for case 2

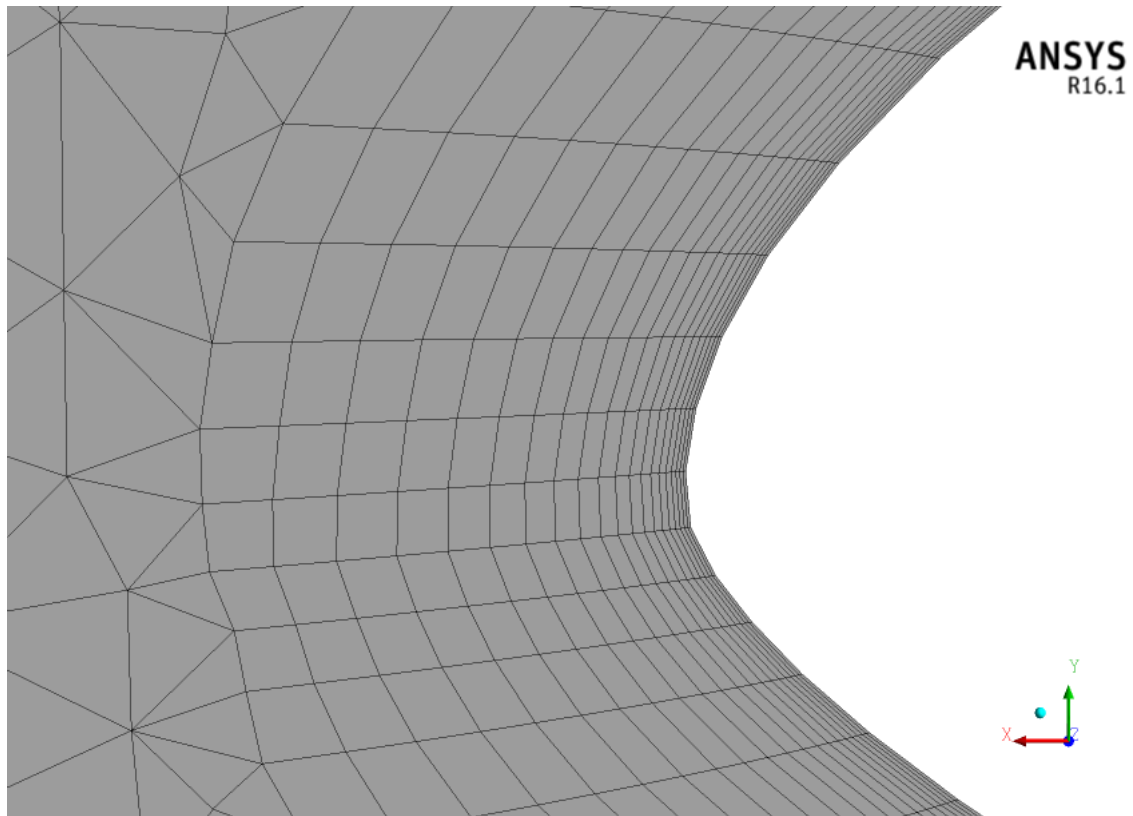


Figure 181: The generated mesh of the aerofoil's leading edge for case 2

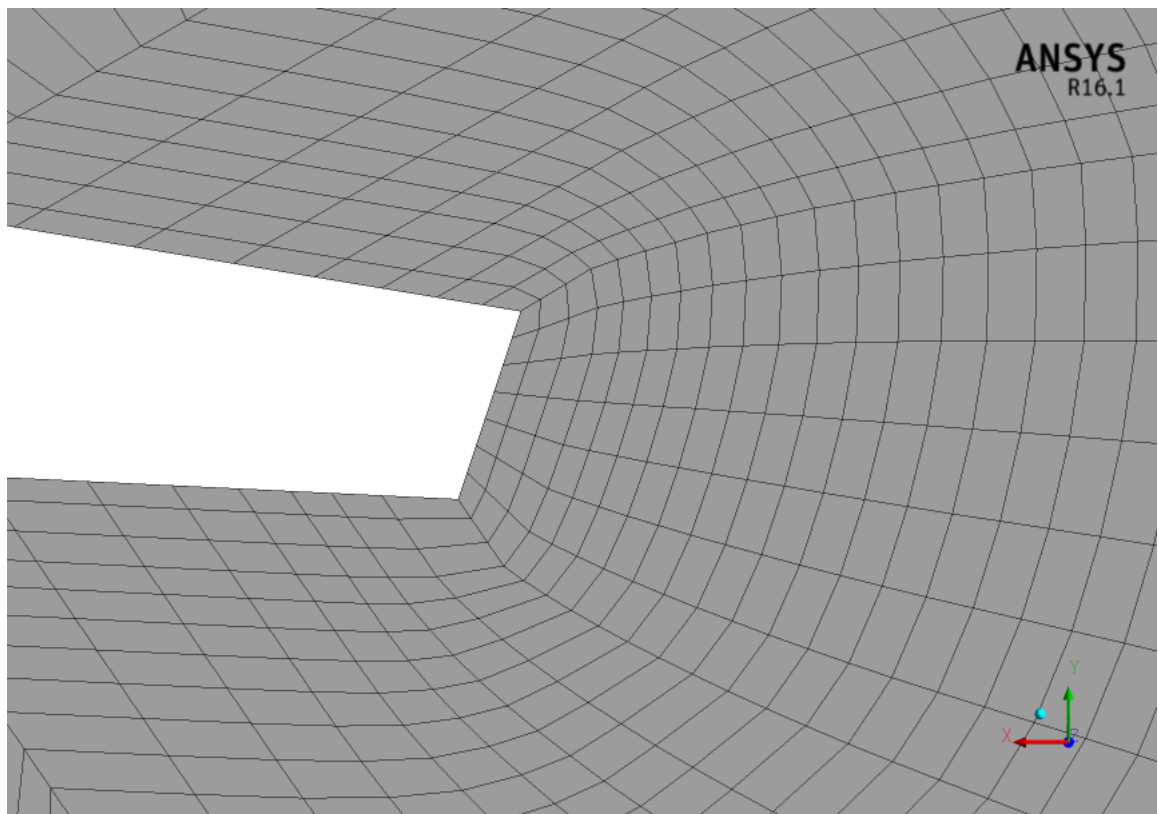


Figure 182: The generated mesh of the aerofoil's trailing edge for case 2

Table 38: Simulation settings for study case 2

<b>Algorithm</b>	<b>Function Used</b>
Time State	Transient
Turbulence Model	<i>SST <math>k - \omega</math> &amp; <math>S - A</math></i>
Turbulence Intensity	$I = 1\%$ [84]
Length Scale	$l = 0.02m$
Time Step	$0.002s$
Wind Velocity	$V_\infty = 26m/s$
Pressure-Velocity Coupling	SIMPLE
Interpolating Scheme	(Momentum) Second Order
Residual Error	$10^{-5}$

### 8.2.4 Results & discussion

The lift coefficient is shown in Figure 183 as a function of time. According to Figure 183, the use of unsteady state is worthless for a 2D flow as the lift coefficient does not change with time. The  $y^+$  distribution along the chord line of the aerofoil is displayed in Figure 184. The values of  $y^+$  at different aerofoil locations are below 3, which means the generated mesh is able to resolve the viscous sub-layer.

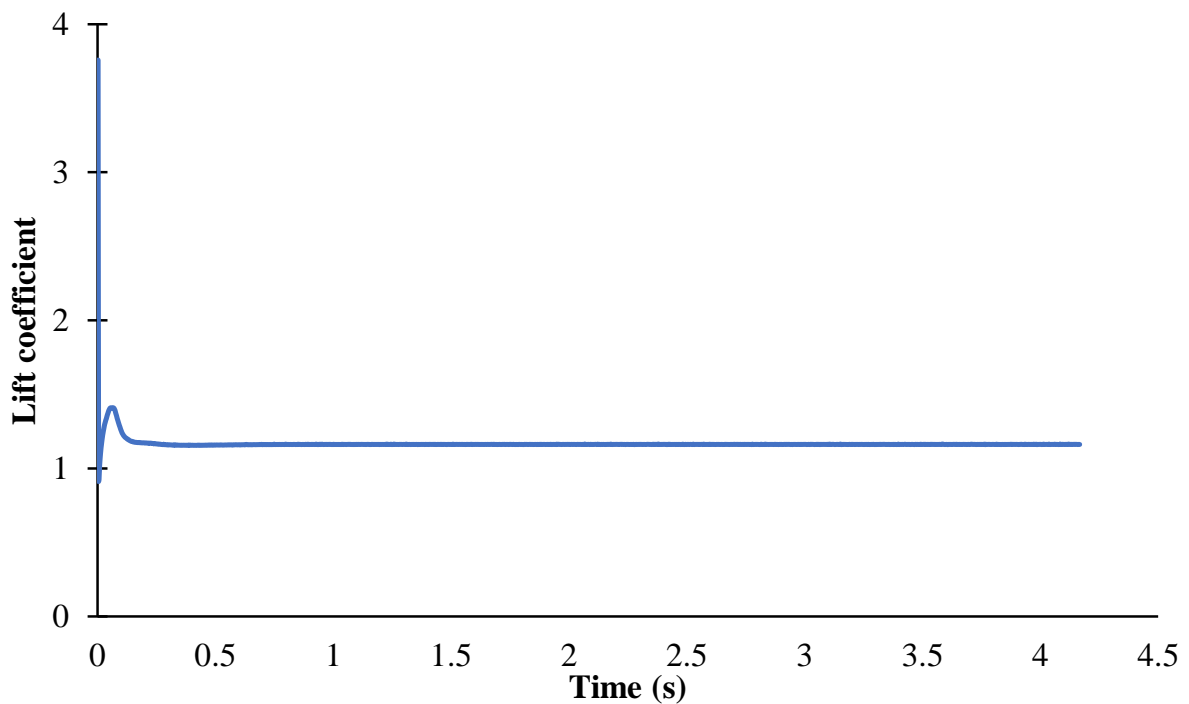


Figure 183: The simulated time of study case 2

Figure 185 shows lift coefficient versus AOAs for 2D smooth aerofoil. In general, the computed values are in good agreement with experimental work at low AOAs. However, large differences at higher AOAs are recorded for both turbulence models. The method of this case mesh and referenced simulation mesh are not the same, as Xu *et al.* [83] generated structured grids, while this work uses unstructured grids thus, computed values are similar at low AOAs but slightly different at high AOAs.

This work's results have an advantage over referenced simulation because of using the *SST*  $k-\omega$  turbulence model. This advantage is clearly shown at stall condition ( $\alpha = 16^\circ$ ) therefore, better lift coefficient value is obtained. At post-stall, the *SST*  $k-\omega$  turbulence model still performs better than the other two simulations. This is also a proof of what was previously

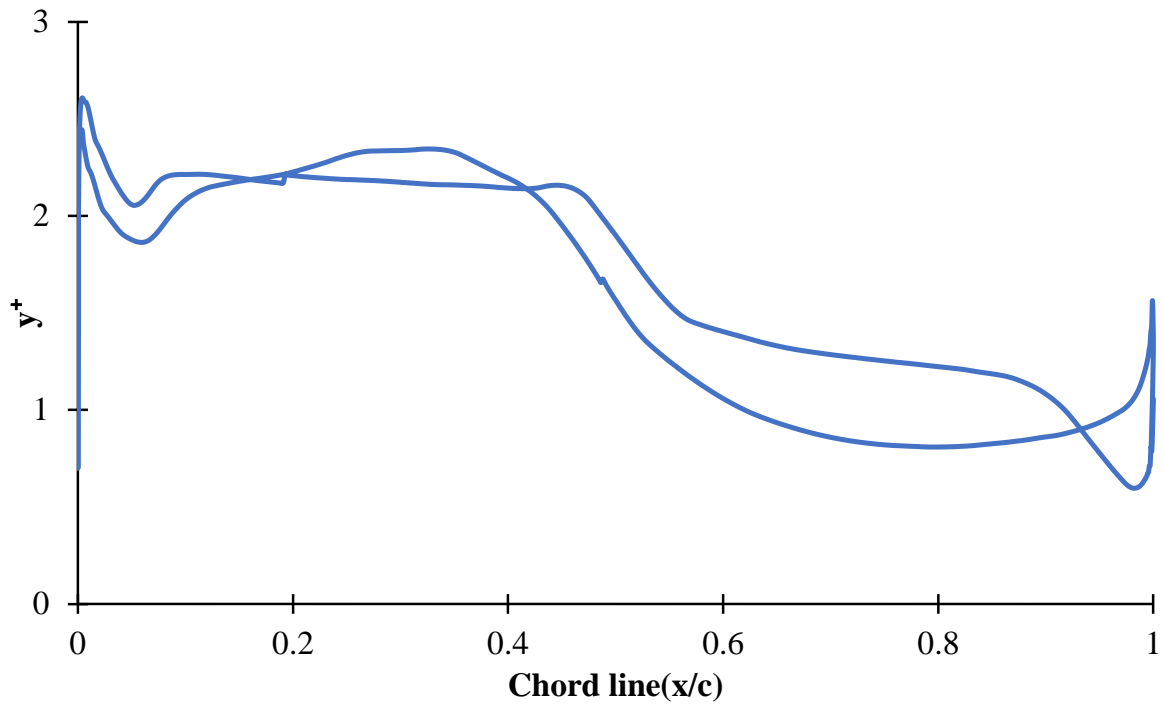


Figure 184: The  $y^+$  distribution of study case 2

reported by other researchers [29–32] that the  $S - A$  turbulence model showed less accuracy at high AOAs.

Pressure drag coefficient values against various AOAs of smooth aerofoil are displayed in Figure 186. Both simulations show a good agreement with experiment except at  $\alpha = 16^\circ$  and  $\alpha = 20^\circ$ , where flow separation is believed to start. However, the  $SST k - \omega$  model proves its ability to resolve flow better than the  $S - A$  model at stall and post-stall conditions. Based on these results, the  $SST k - \omega$  model will be the selected turbulence model for further simulations of this thesis, including smooth and tripped cases.

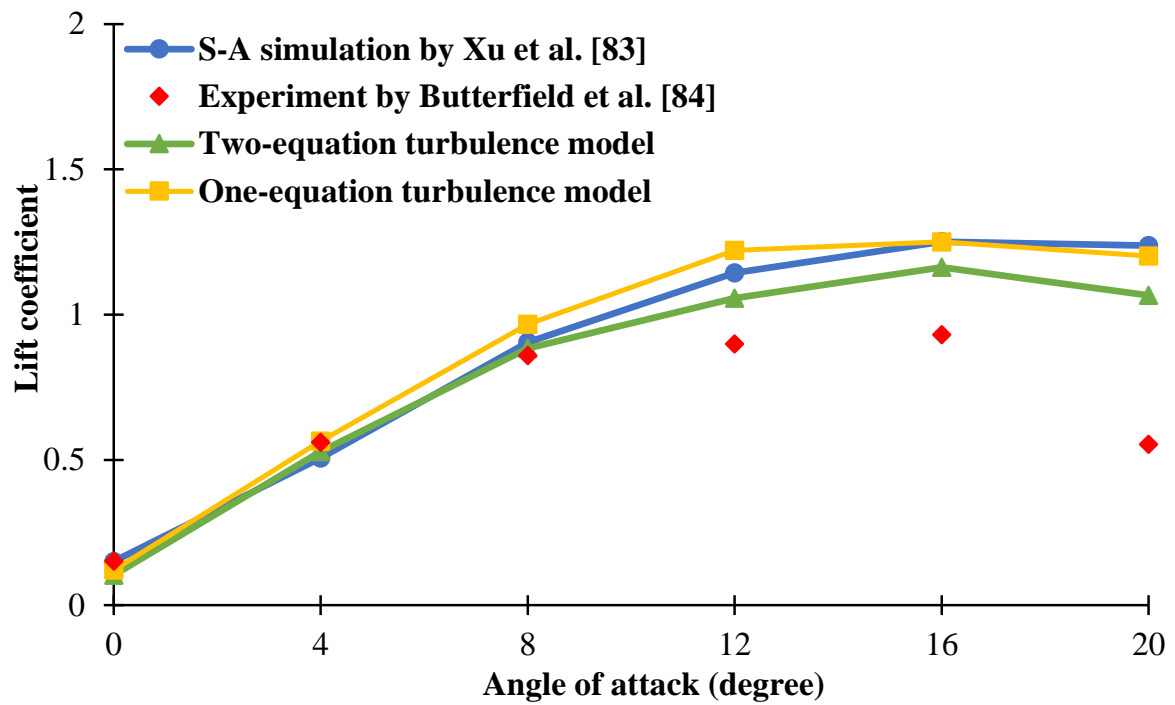


Figure 185: Lift coefficient against angle of attacks for study case 2

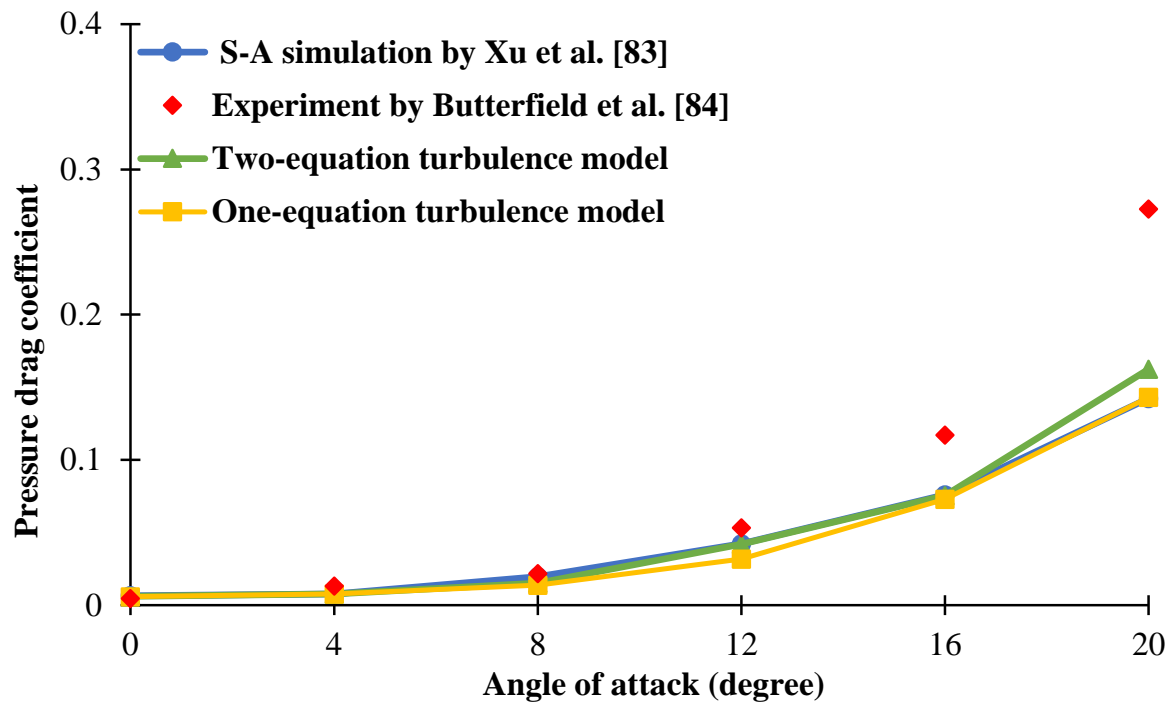


Figure 186: Pressure drag coefficient against angle of attacks for study case 2

### 8.3 Study Case 3 (3D, URANS, S809, $Re_c = 6.5 \times 10^5$ )

#### 8.3.1 Purpose

There are two aims for this study case. First, calculating drag-to-lift ratio at different AOAs for 3D blade with S809 aerofoil profile by computing lift and drag coefficients. In addition, it aims to determine the flow separation point by showing the pressure distribution along the blade chord. The result is compared to numerical simulation by Xu *et al.* [83] and it is validated against experimental dataset by Butterfield *et al.* [84]. The dimensionality is the difference between study case 2 (2D) and 3 (3D).

#### 8.3.2 Geometrical setup

The fluid domain geometry is the same as the wind tunnel that was conducted by Butterfield *et al.* [84] therefore, the height and width are  $3.66m$  and  $1m$  respectively. The inlet and outlet boundaries are  $12.8m$  and  $13.03m$  away from the aerofoil leading edge, respectively. The fluid domain is viewed as in Figure 187. The boundary conditions of this study case are also shown in Figure 187. The blade has a length chord of  $0.46m$  and length span of  $0.99m$ , and it is divided into three sections for later riblets' study as displayed in Figure 188.

#### 8.3.3 Mesh study & computational setup

A mesh dependency test is displayed in Figure 189. Both drag and lift coefficients become independent of mesh size after  $1.4 \times 10^6$  elements. The mesh varies as the nodes on the blade change. The mesh is refined in all three directions. The selected mesh has 20, 80 and 300 nodes in the spanwise, normal and streamwise directions of the freestream, respectively. The number of nodes on the blade are 120 and 270 in the chordwise and spanwise directions.

There are 30 inflation layers in the normal direction with growth rate of 1.2 and first layer at  $50\mu m$ . Figure 190 displays how the  $y^+$  changes with lift coefficient. The selected mesh has an average value of  $y^+ = 1.4$ . The mesh metric for skewness and orthogonality are shown in Figures 191 and 192, respectively. The generated mesh is displayed in Figures 193-196. Table 39 shows the simulation algorithm of this study case.

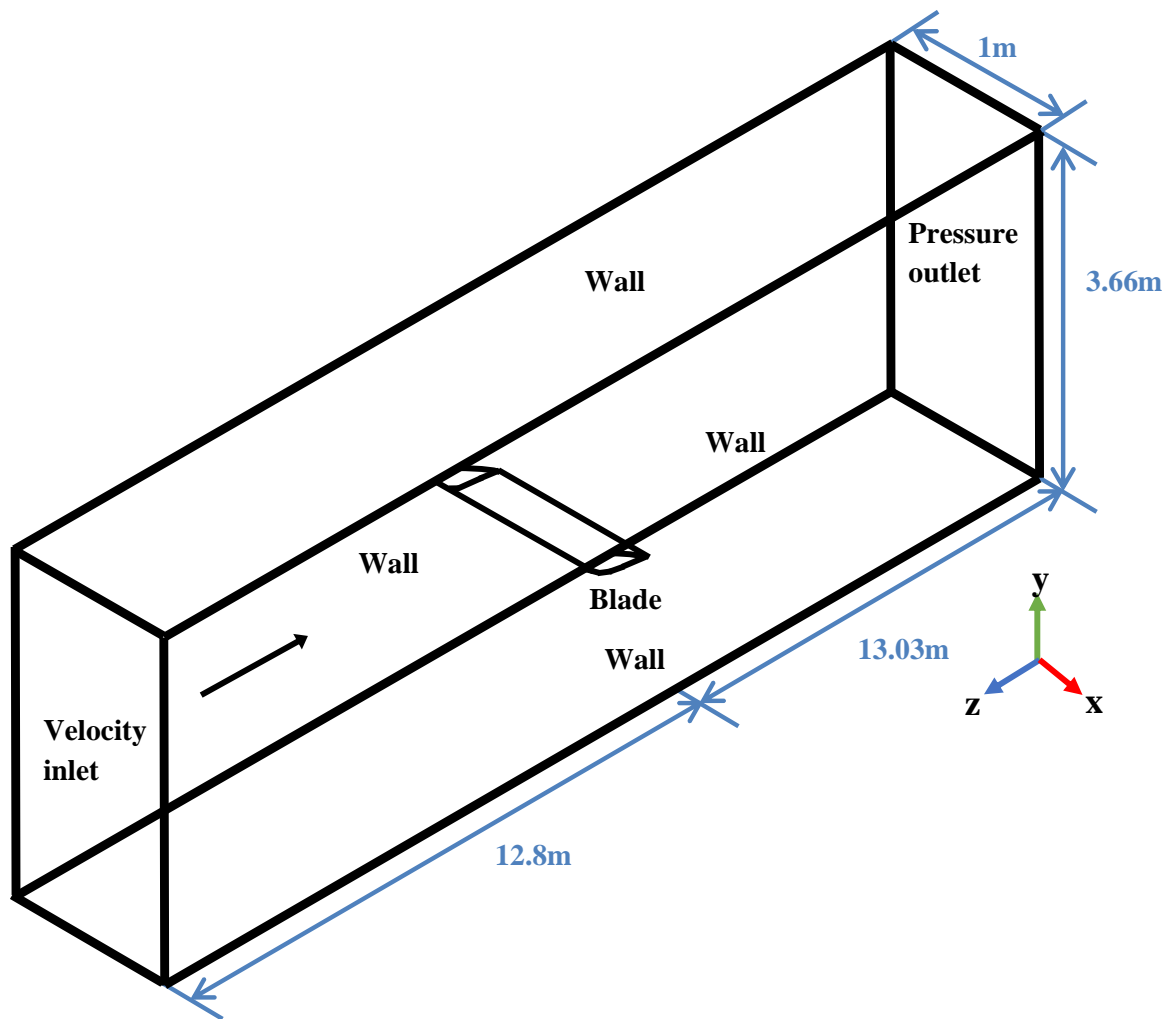


Figure 187: Study case 3 fluid domain (not to scale)

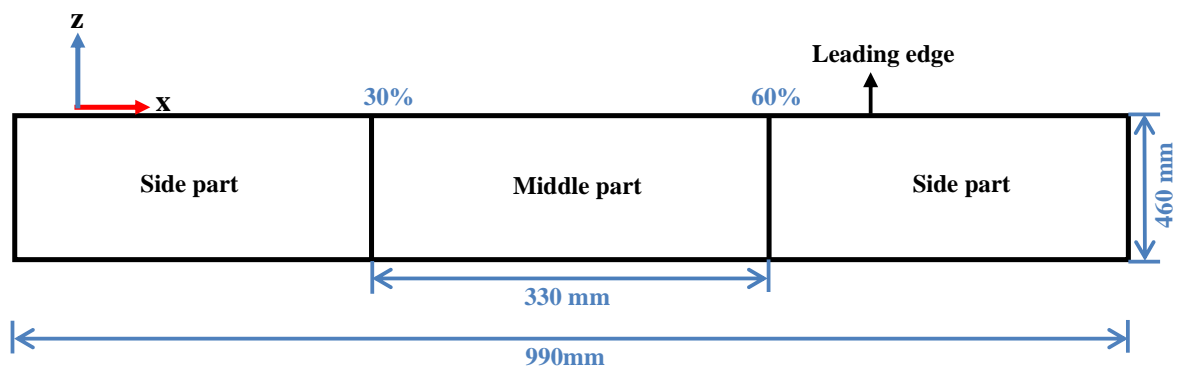


Figure 188: Study case 3 simulated blade (not to scale)

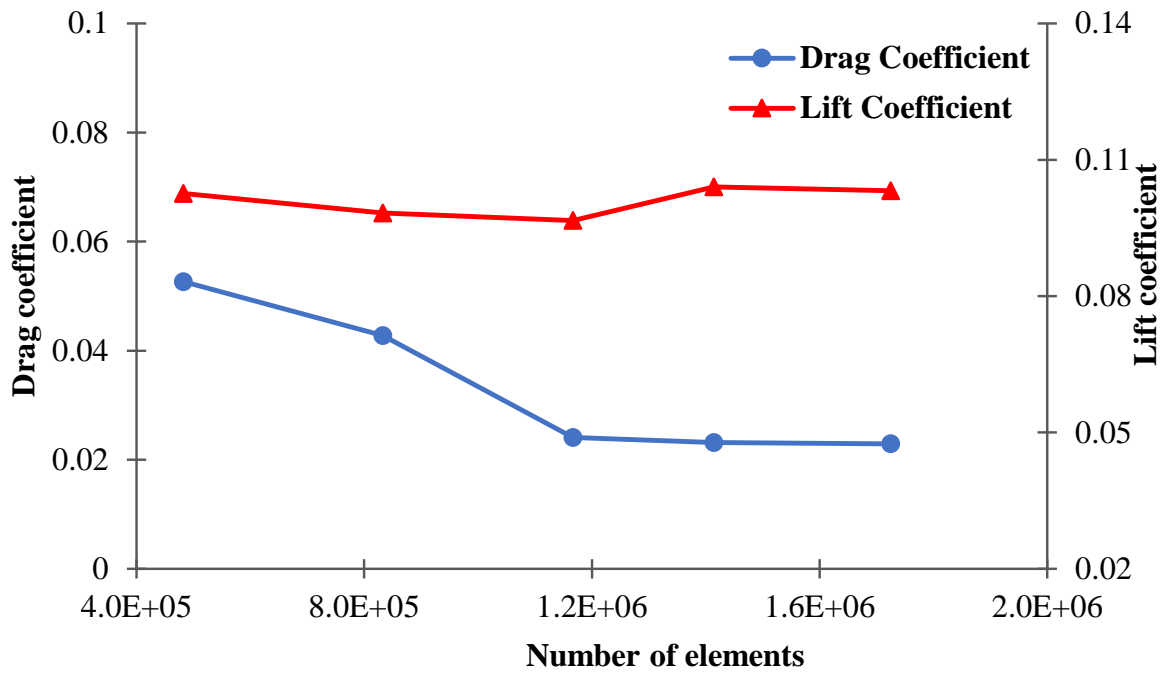
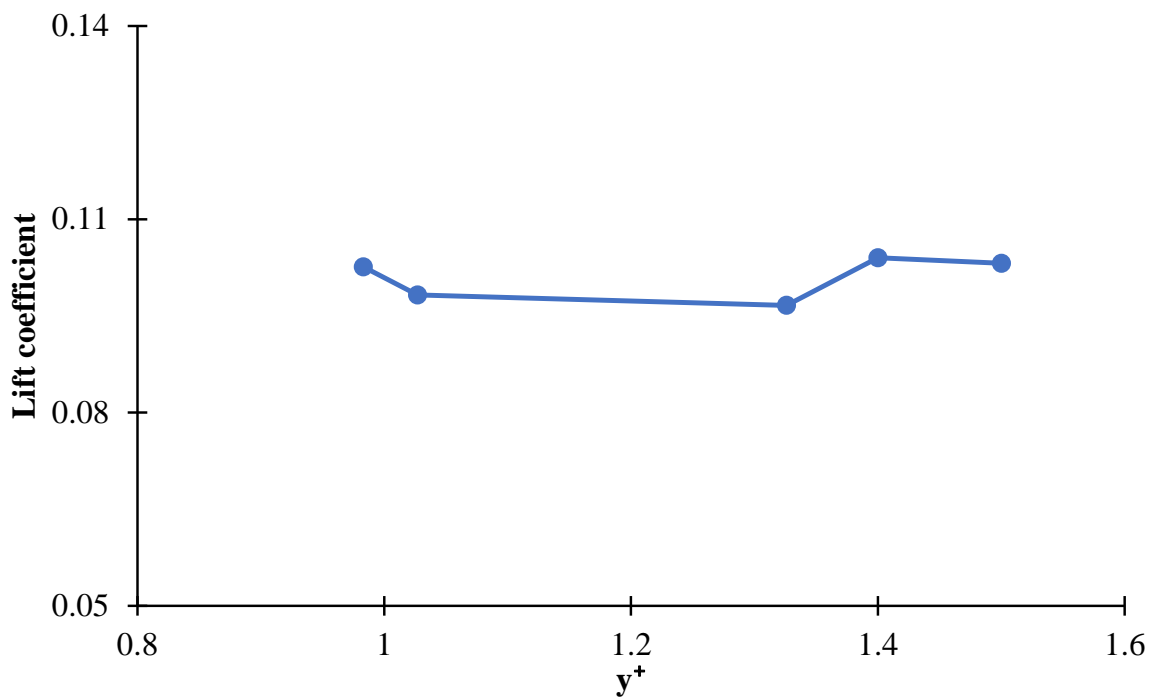


Figure 189: Mesh dependency for study case 3

Figure 190:  $y^+$  values for different meshes of study case 3

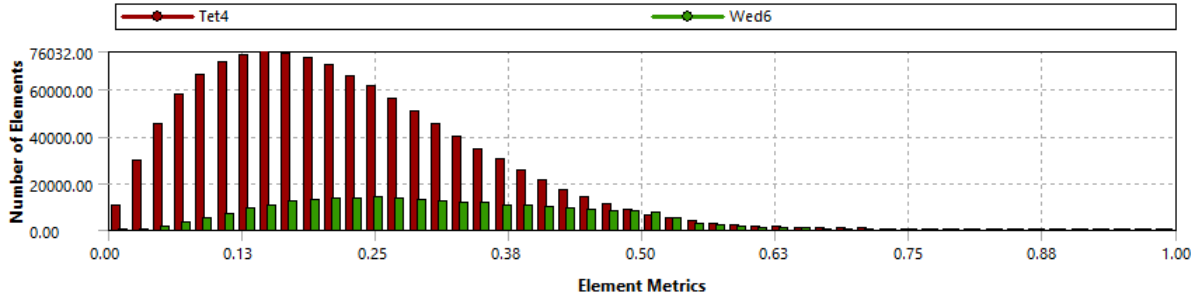


Figure 191: The skewness of study case 3

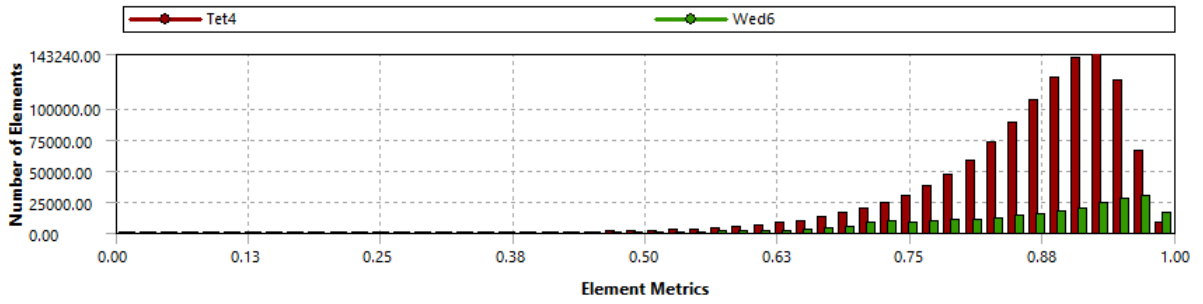


Figure 192: The orthogonality of study case 3

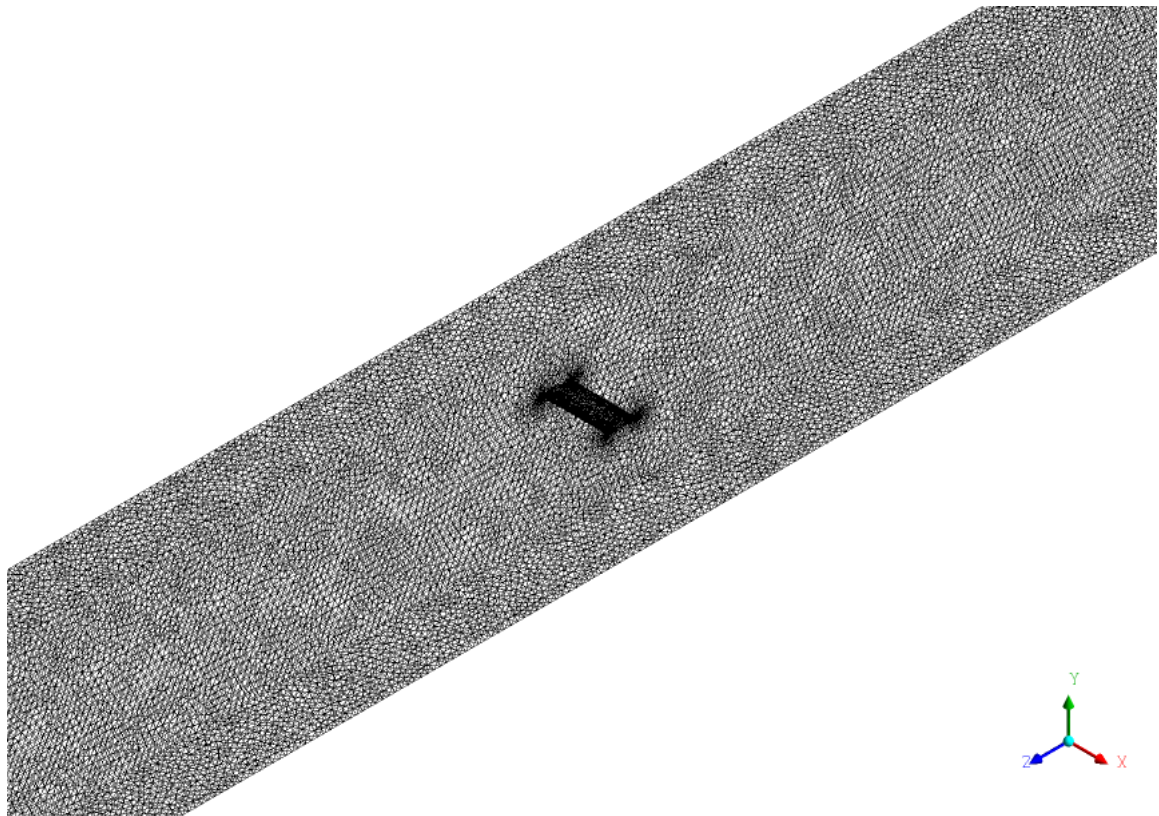


Figure 193: The generated mesh of fluid domain and blade for case 3

ANSYS  
R16.1

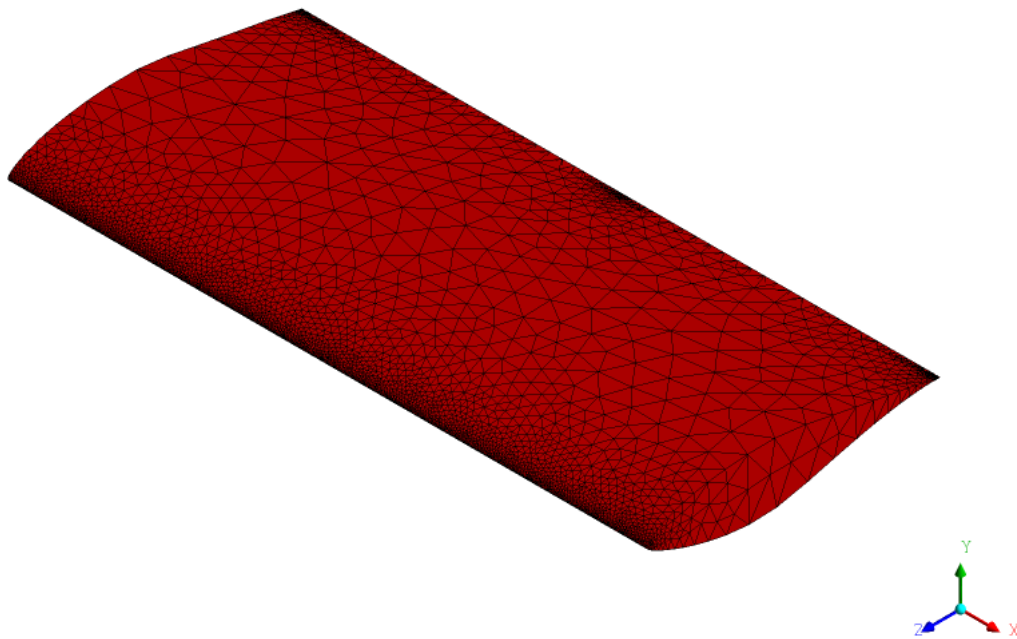
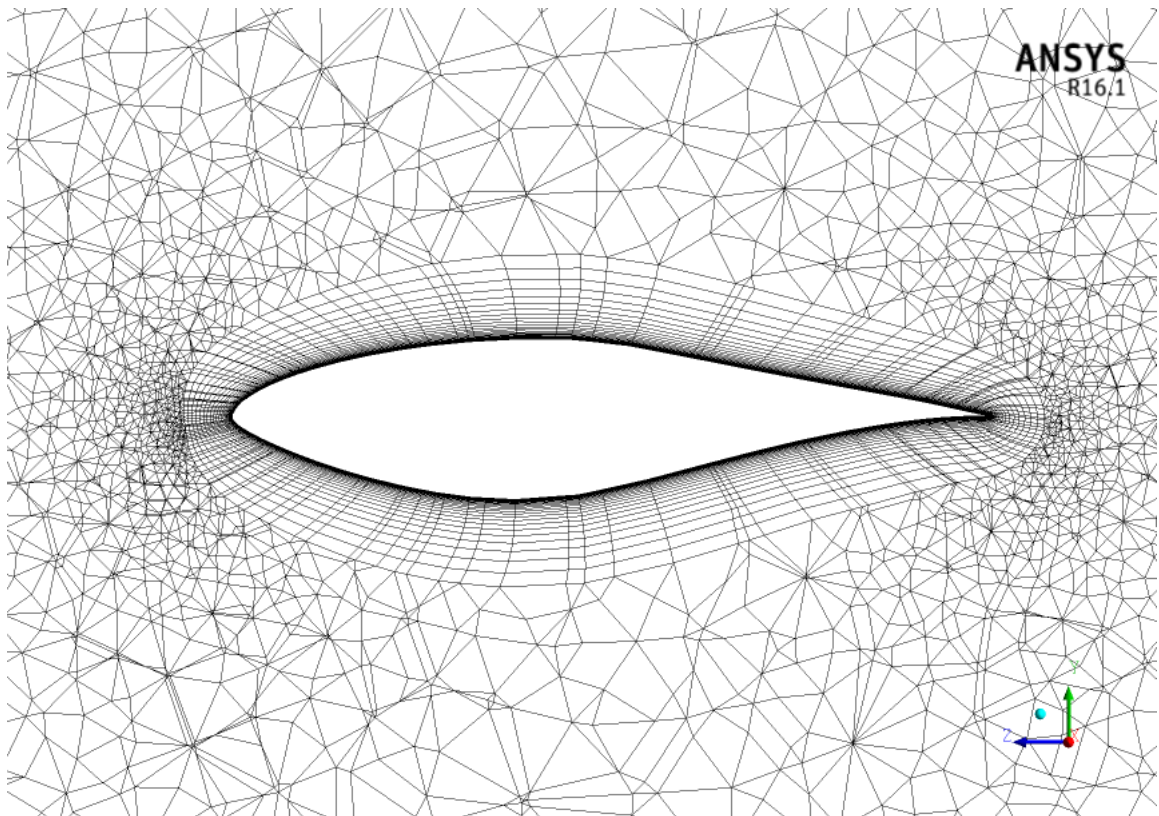


Figure 194: The generated mesh of the blade for case 3



ANSYS  
R16.1

Figure 195: The inflation layers on the blade for case 3

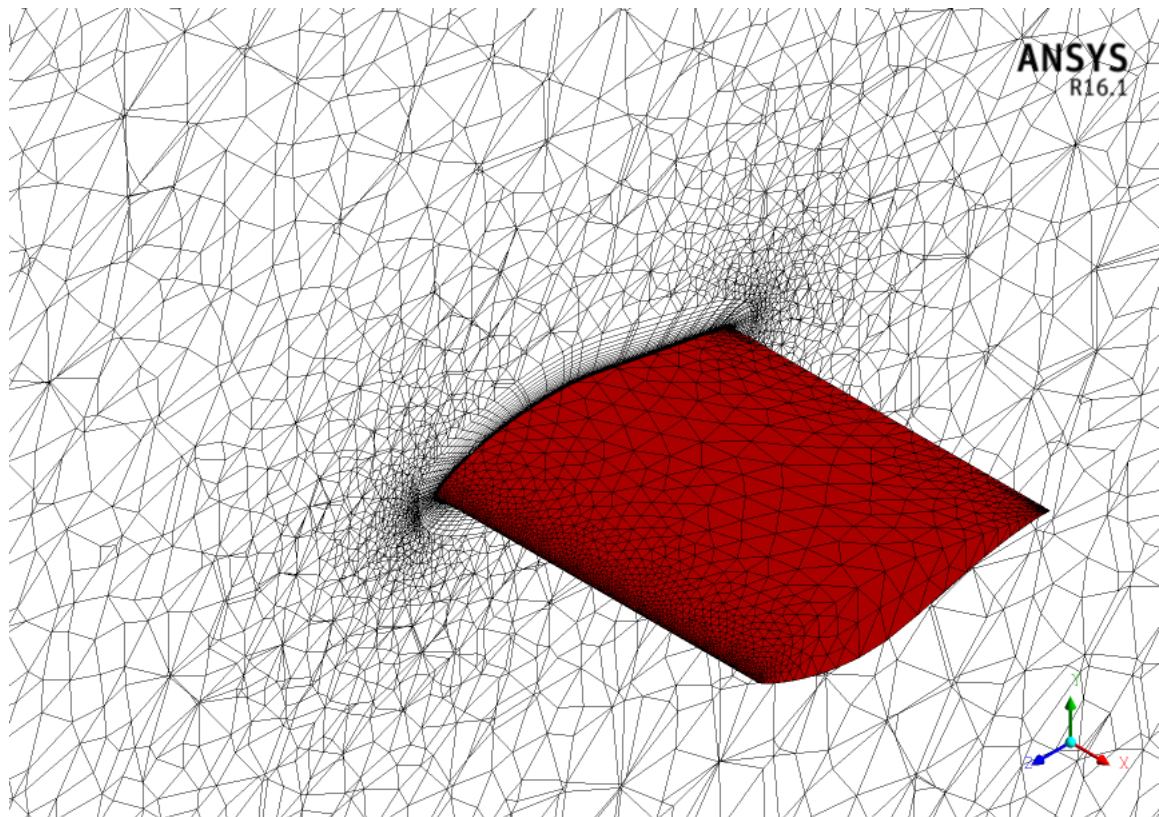


Figure 196: The generated mesh of the cross section of the blade for case 3

Table 39: Study case 3 simulation algorithm

Algorithm	Function Used
Time State	Transient
Turbulence Model	<i>SST</i> $k - \omega$
Turbulence Intensity	$I = 1\%$ [84]
Length Scale	$l = 0.02m$
Time Step	$0.002s$
Pressure-Velocity Coupling	SIMPLE
Interpolating Scheme	(Momentum) Second Order
Residual Error	$10^{-5}$

### 8.3.4 Results & discussion

The simulation is run in transient state so that calculating the variation of aerodynamic coefficients as a function of time. Figure 197 shows the drag coefficient of study case 3 as a function of time. The calculation of aerodynamic coefficients is based on averaging the last cycle of the simulated time, as shown in Figure 197. Figure 198 shows the distribution of  $y^+$  along blade's chord at 50% span.  $y^+ < 3$  is achieved for all blade's locations therefore, resolving viscous sub-layer.

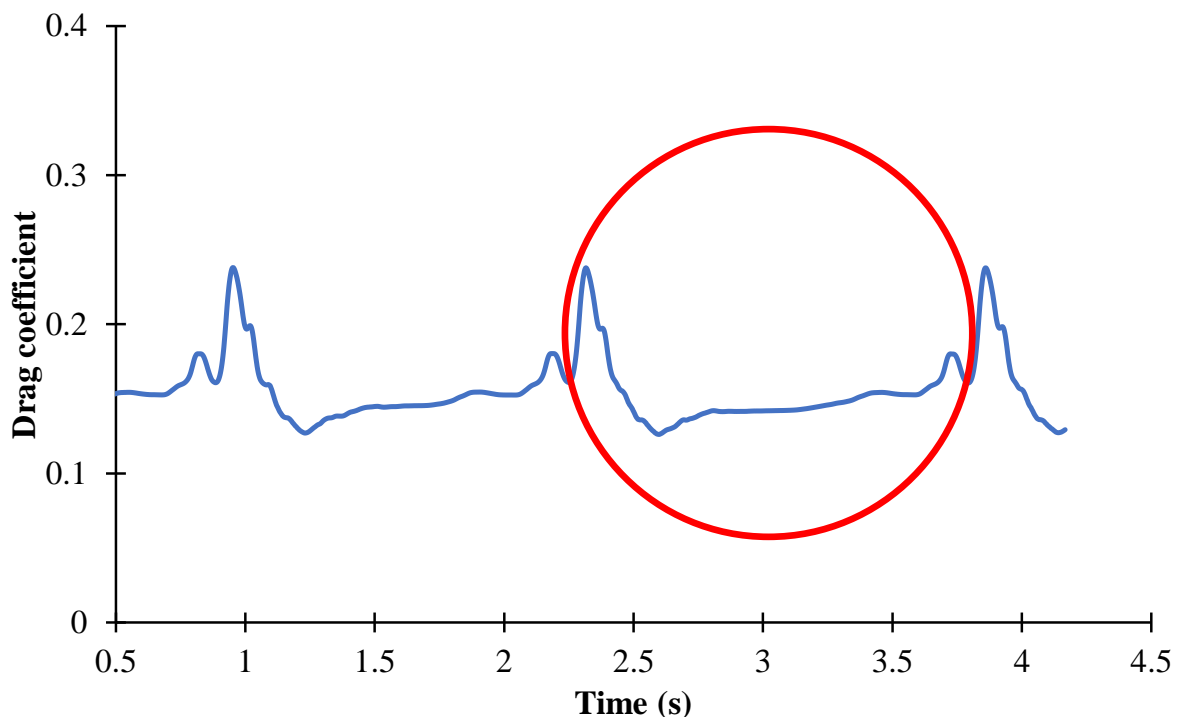


Figure 197: The simulated time of study case 3

As a result from study case 2, the *SST*  $k - \omega$  turbulence model is preferred for this simulation. However, Xu *et al.* [83] used the *S - A* turbulence model. Referring to Xu *et al.* [83], the air was assumed compressible, so that the ideal gas law was considered along with RANS equations to evaluate the change in density, although  $Ma < 0.3$ . Because the flow was assumed incompressible in the conducted experiment by Butterfield *et al.* [84], it is decided to neglect compressibility effect for this work.

Graph of drag coefficient versus AOAs is plotted in Figure 199. According to Butterfield *et al.* [84], only pressure drag coefficient was measured experimentally. However, both total drag and pressure drag coefficients are computed for this work. The referenced simulation

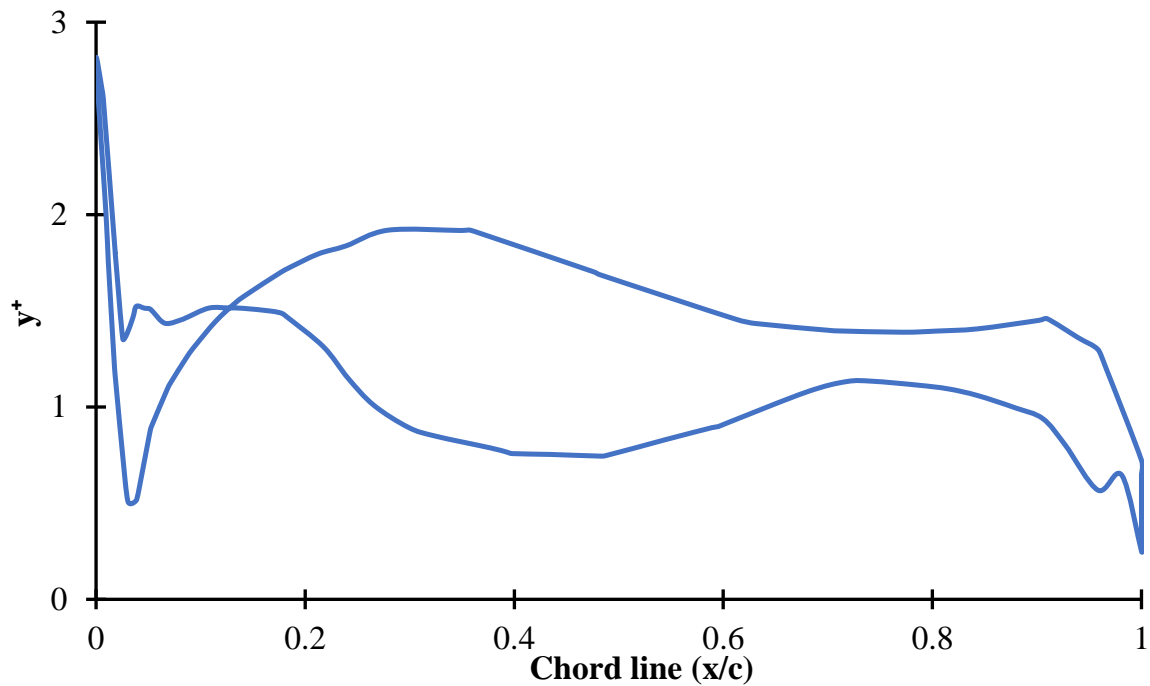


Figure 198: The  $y^+$  distribution of study case 3

did not report about whether pressure drag or total drag was computed. The simulation seems to accurately predict the value of drag coefficients at pre-stall condition. Nevertheless, the computed drag coefficients start to differ from measured values at stall and post-stall conditions, where flow separation occurs.

A graph of lift coefficient against different AOAs is displayed in Figure 200. The lift coefficient plot shows the same trend as the experiment, particularly after stall occurs, but it overpredicts the lift coefficient values. Once again, the  $SST\ k - \omega$  turbulence model proves its advantage over the  $S - A$  turbulence model in predicting aerodynamic forces at stall. A graph of drag-to-lift ratio against AOA is plotted in Figure 201. The purpose of showing this graph is to observe the effects of riblets on the S809 aerofoil for later study.

The pressure distribution along the blade chord at 50% blade span is validated against experiment's pressure distribution for various AOAs, as shown in Figures 202, 203 and 204. At pre-stall condition (Figure 202) and post-stall condition (Figure 203), good agreement is observed except at the beginning of the suction side due to the leading-edge separation. At pre-stall condition, no flow separation is recorded however, the flow is fully de-attached for post-stall condition. The flow separation point starts where the pressure coefficient is flattened.

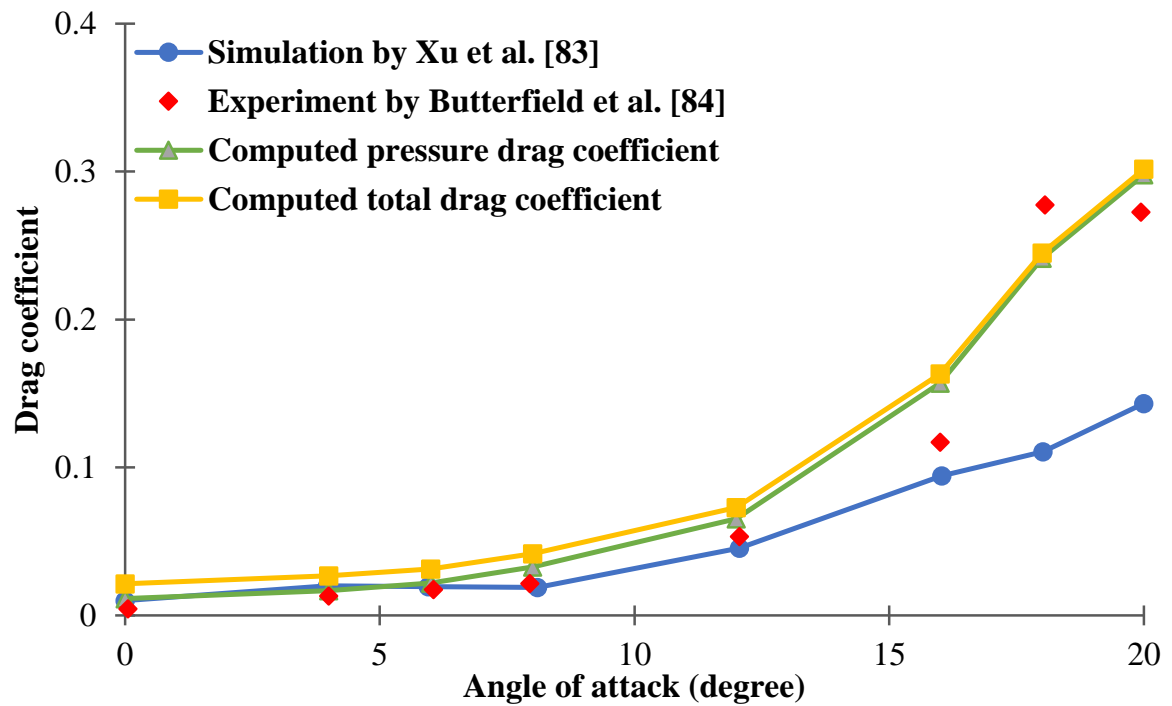


Figure 199: Drag coefficient against angle of attack for study case 3

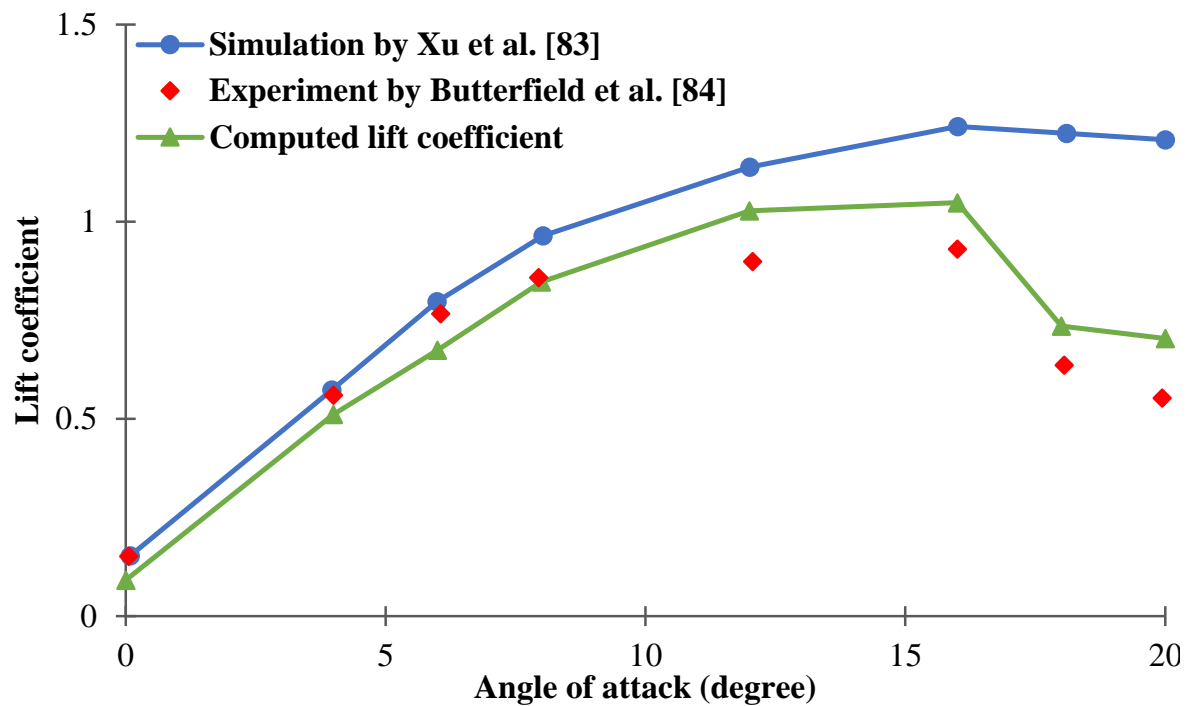


Figure 200: Lift coefficient against angle of attack for study case 3

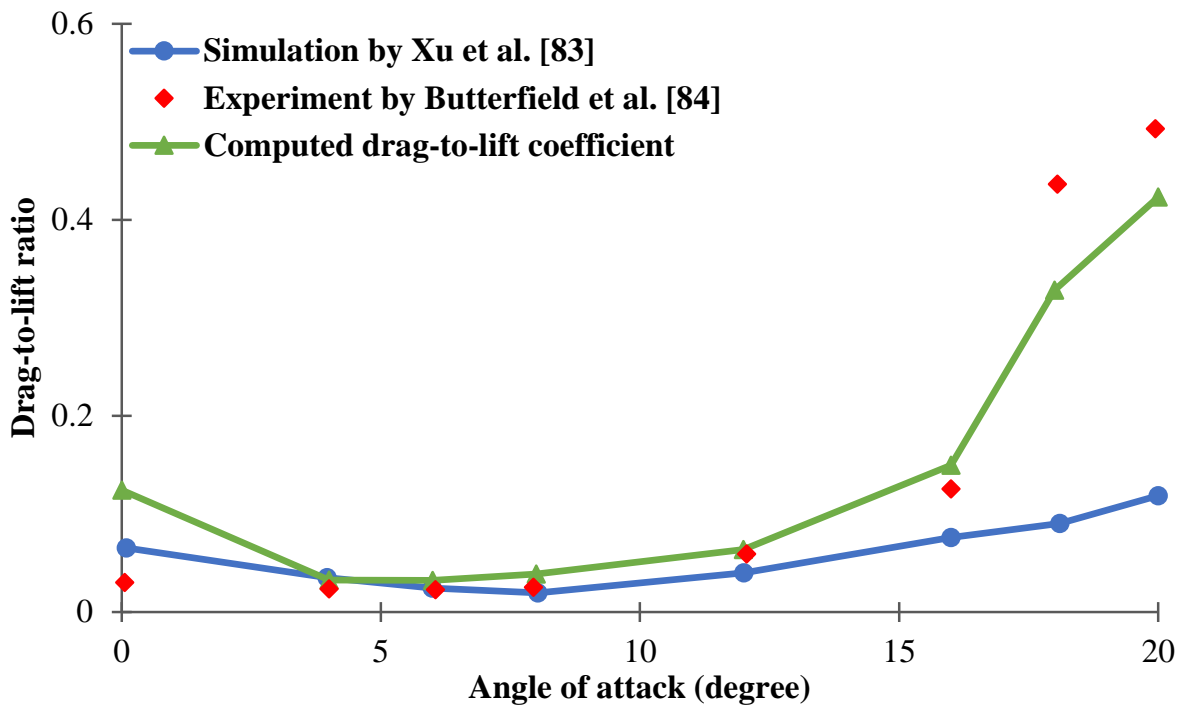
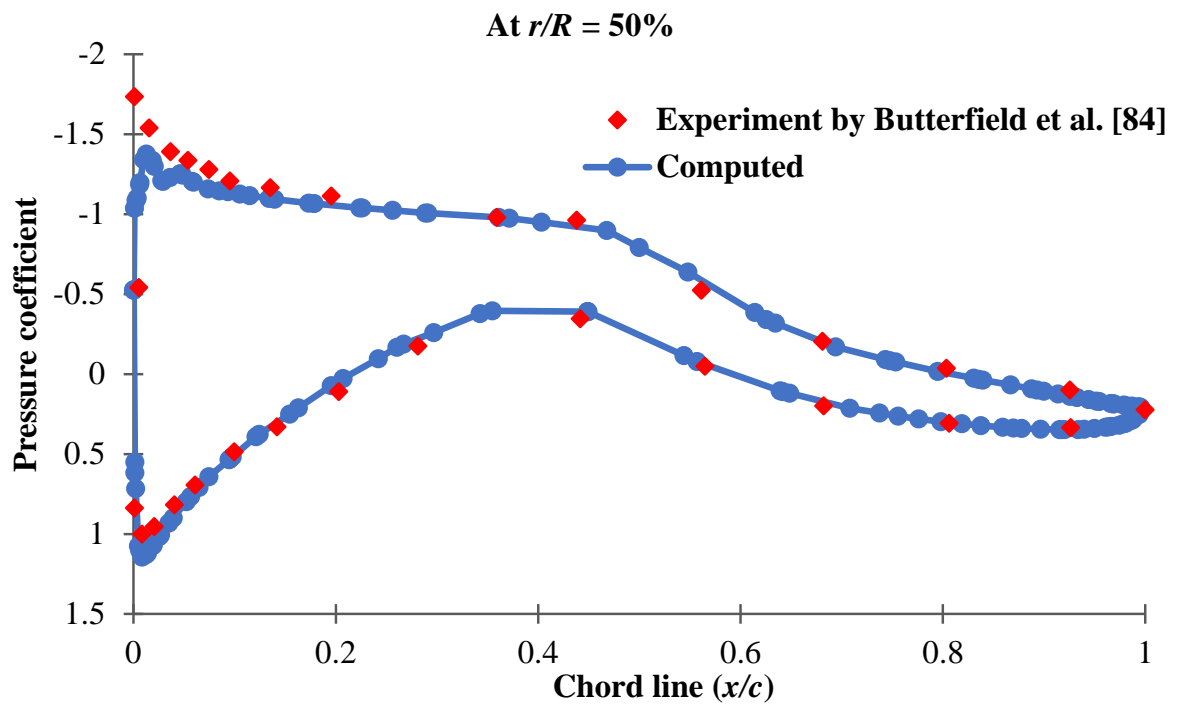
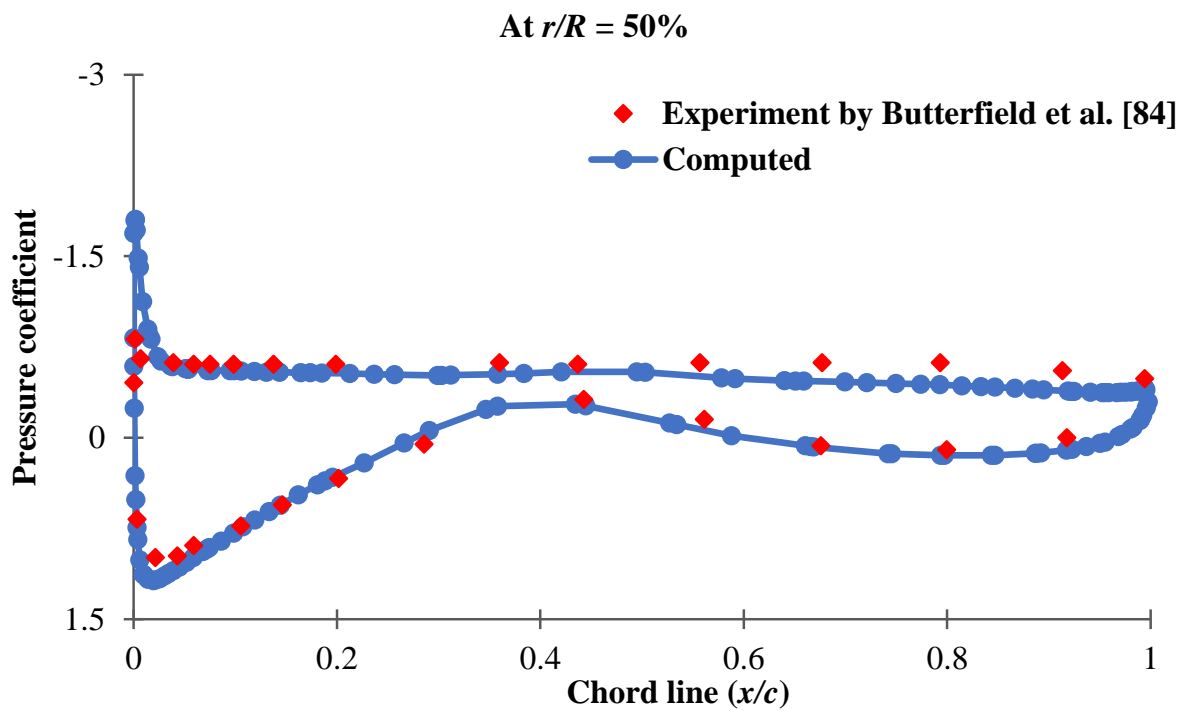


Figure 201: Drag-to-lift ratio against angle of attack for study case 3

At stall condition (Figure 204), *SST*  $k - \omega$  turbulence model fails to accurately predict the pressure distribution. Computationally, the flow separation begins at 21% chord on the blade upper side. However, the separation point experimentally occurs at 35% chord on the same blade side. As a result, the triangular riblets should start at further location of the chord on upper side of the blade. This means riblets should be placed within the region of flow separation, particularly after 35% chord, according to experiment.

Figure 202: Pressure distribution along the blade chord at  $\alpha = 6^\circ$  (pre-stall)Figure 203: Pressure distribution along the blade chord at  $\alpha = 18^\circ$  (post-stall)

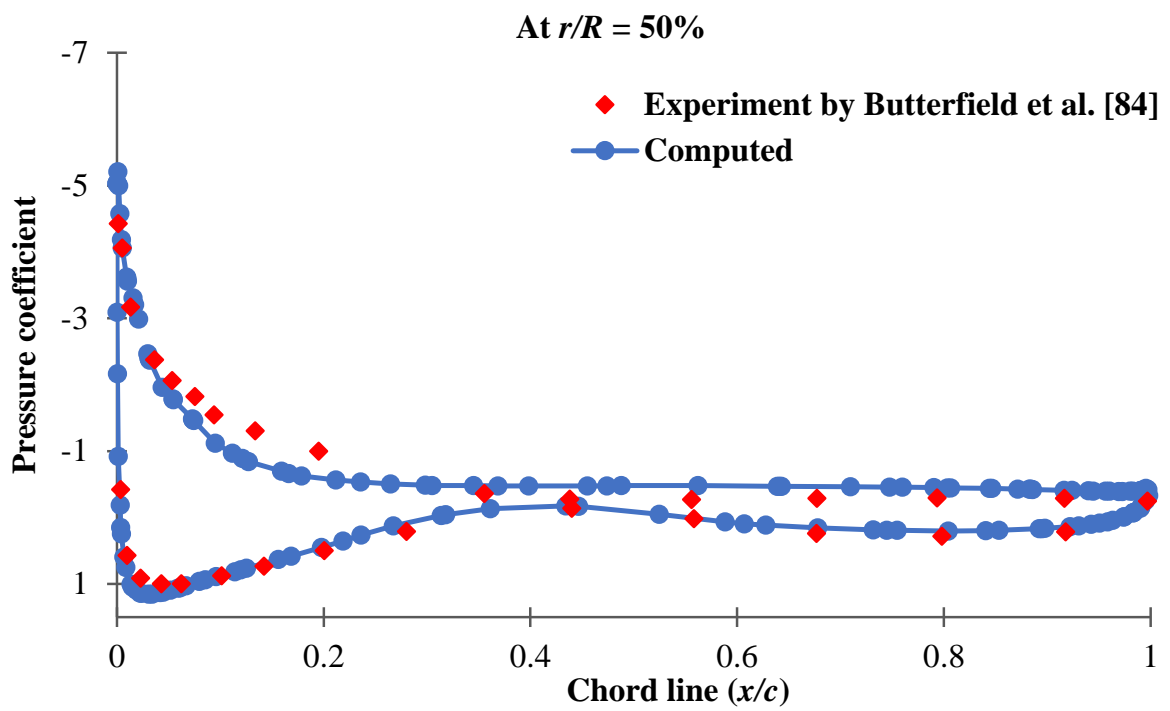


Figure 204: Pressure distribution along the blade chord at  $\alpha = 16^\circ$  (stall)

## 8.4 Study Case 4 (3D, RANS, NREL phase II, MRF, $Re_c = 9.4 \times 10^5$ )

### 8.4.1 Purpose

This study case shows a comparison of two commonly used turbulence models, which are the *SST*  $k - \omega$  and the standard  $k - \epsilon$ . A comparison is done by showing the steady mechanical torque of the NREL phase II at wind speed of  $10.5m/s$ . It also illustrates the ability of using symmetrical assumption for predicting wind turbine aerodynamic quantities to save computational cost and time. The velocity along the blades and the velocity variations through the wind turbine are also shown for verification.

### 8.4.2 Geometrical Setup

Study case 4 simulates one-third of the NREL phase II blades, so that using one blade instead of three blades with rotational periodic boundary condition with offset angle of  $120^\circ$  to account for the other two blades, as shown in Figure 205. Three points to be noted from Figure 205. First point is that the spar and hub are neglected, but the blade is translated by a distance of  $1m$  from origin to arbitrary account for the existence of spar and hub.

In addition, the periodic faces must have a conformal mesh, so that both faces have the same number of nodes at the interface for connection purpose. Lastly, the outlet boundary size is three times larger than the inlet boundary size because of the wind diffusion behind the blades. Figure 205 also displays the NREL phase II blade however, details of the blade can be found in section 2.2.1.

### 8.4.3 Mesh study & computational setup

In terms of meshing process, less intensive mesh is generated near the blade surfaces for the standard  $k - \epsilon$  model because of using wall function. The reason of applying wall function is to model sub-viscous region therefore,  $y^+$  should be between 30 and 300. For this simulation,  $y_{ave}^+ = 117$  is computed. However,  $y_{ave}^+ = 1.77$  is achieved for the *SST*  $k - \omega$  turbulence model thus, more aggressive mesh is generated around the blade. Figure 206 shows how the  $y^+$  changes with refining of the generated mesh.

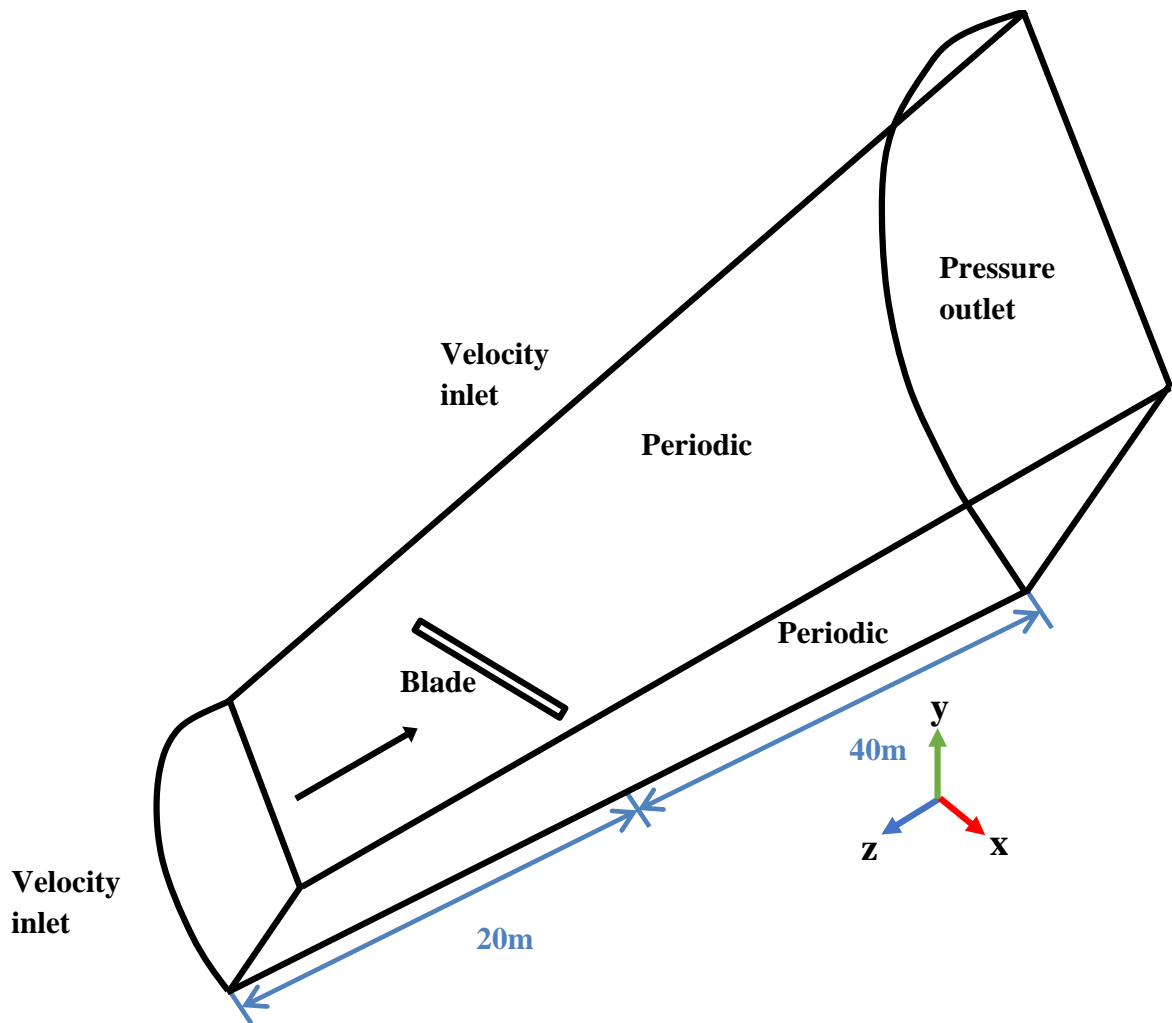


Figure 205: Study case 4 fluid domain (not to scale)

Based on the selected mesh, there are 200, 45 and 135 on the parallel lines, inlet and outlet of the freestream, respectively. The number of nodes on the aerofoil are 500 and 200 in spanwise and chordwise directions, respectively. The inflation layers are applied on the blade with a first layer of  $50\mu m$  and growth rate of 1.2. The mesh metric for skewness and orthogonality are shown in Figures 207 and 208, respectively. The generated mesh of this study case are displayed in Figures 209-212. The computational settings including air properties and simulation algorithm are shown in Table 40.

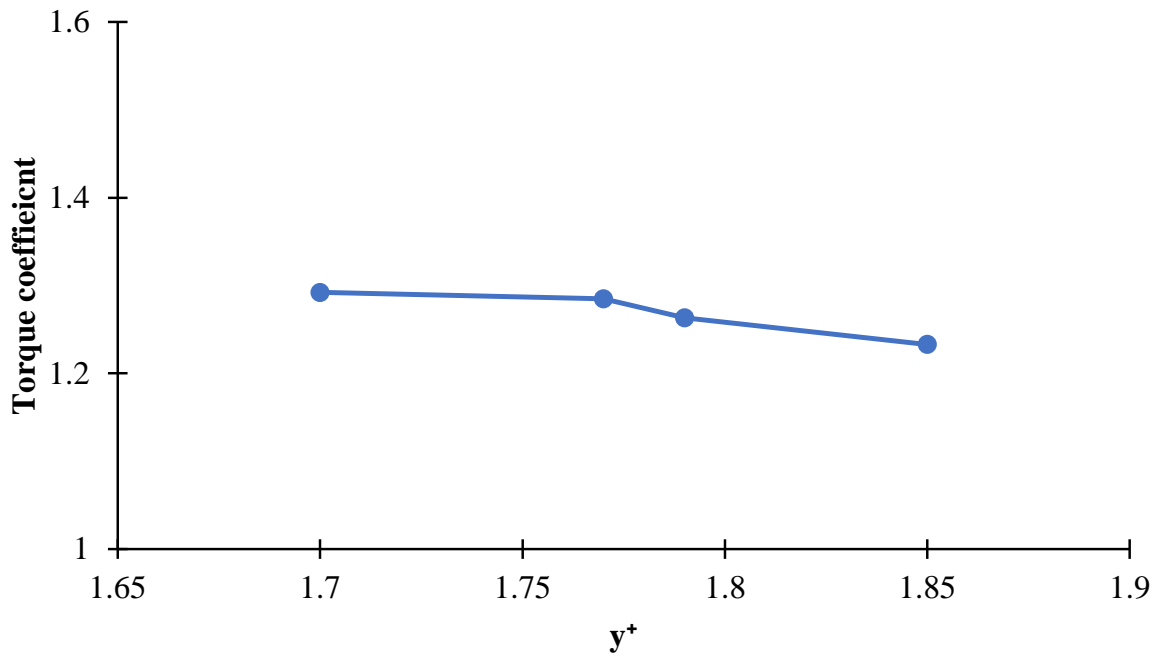


Figure 206:  $y^+$  values for different meshes of study case 4

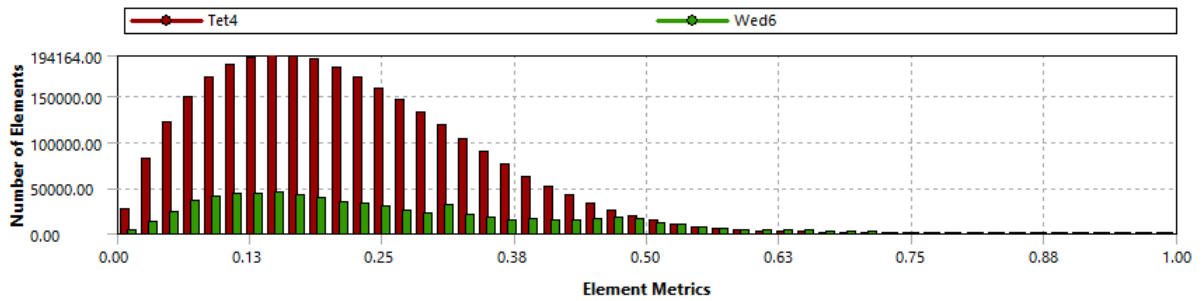


Figure 207: The skewness of study case 4

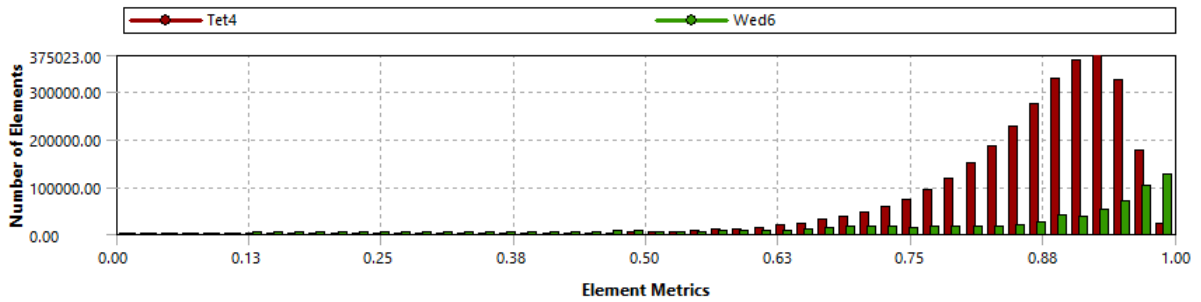


Figure 208: The orthogonality of study case 4

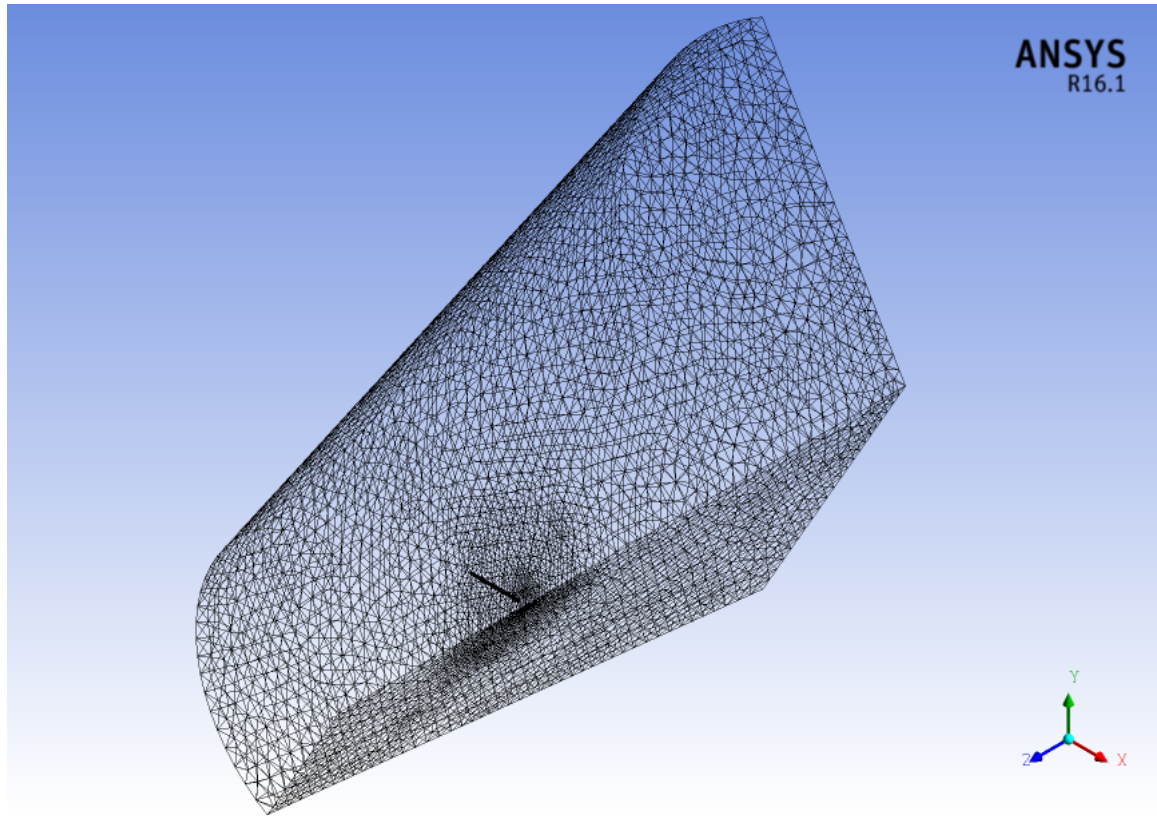


Figure 209: The generated mesh of fluid domain and blade for case 4

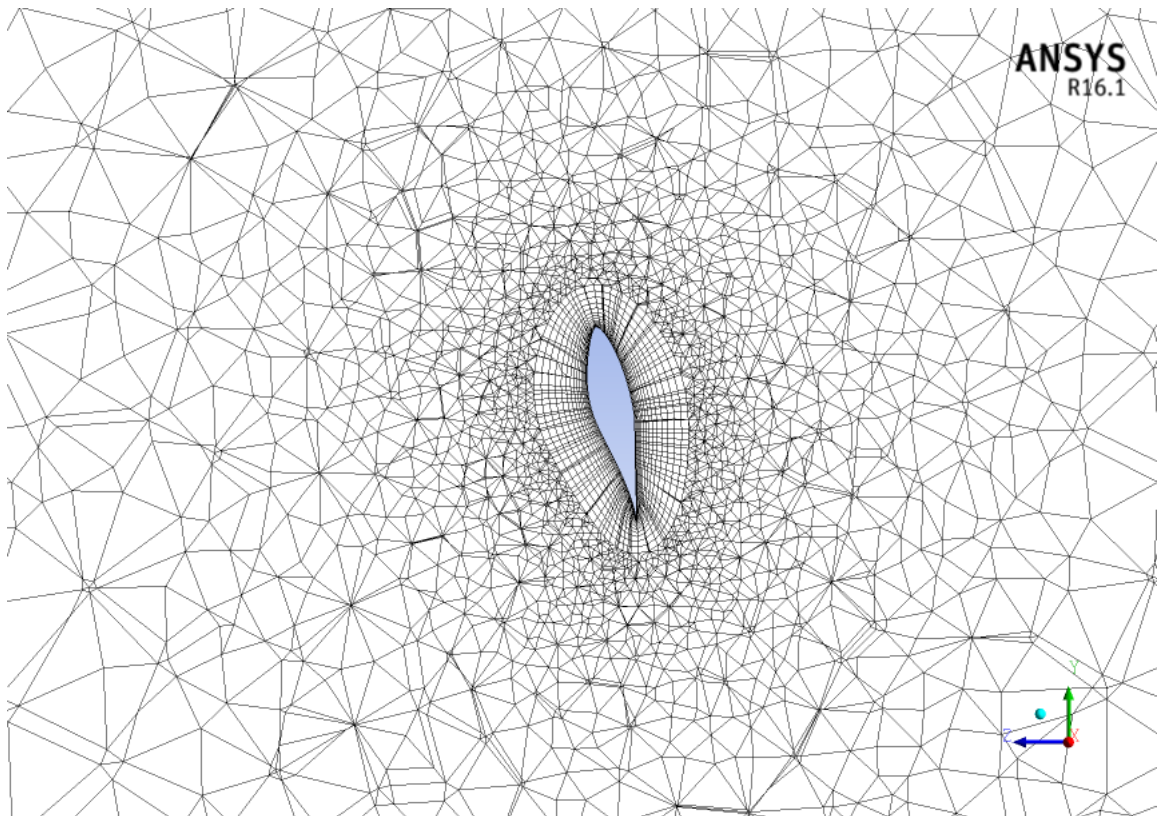


Figure 210: The generated mesh of the cross plane of the blade for case 4

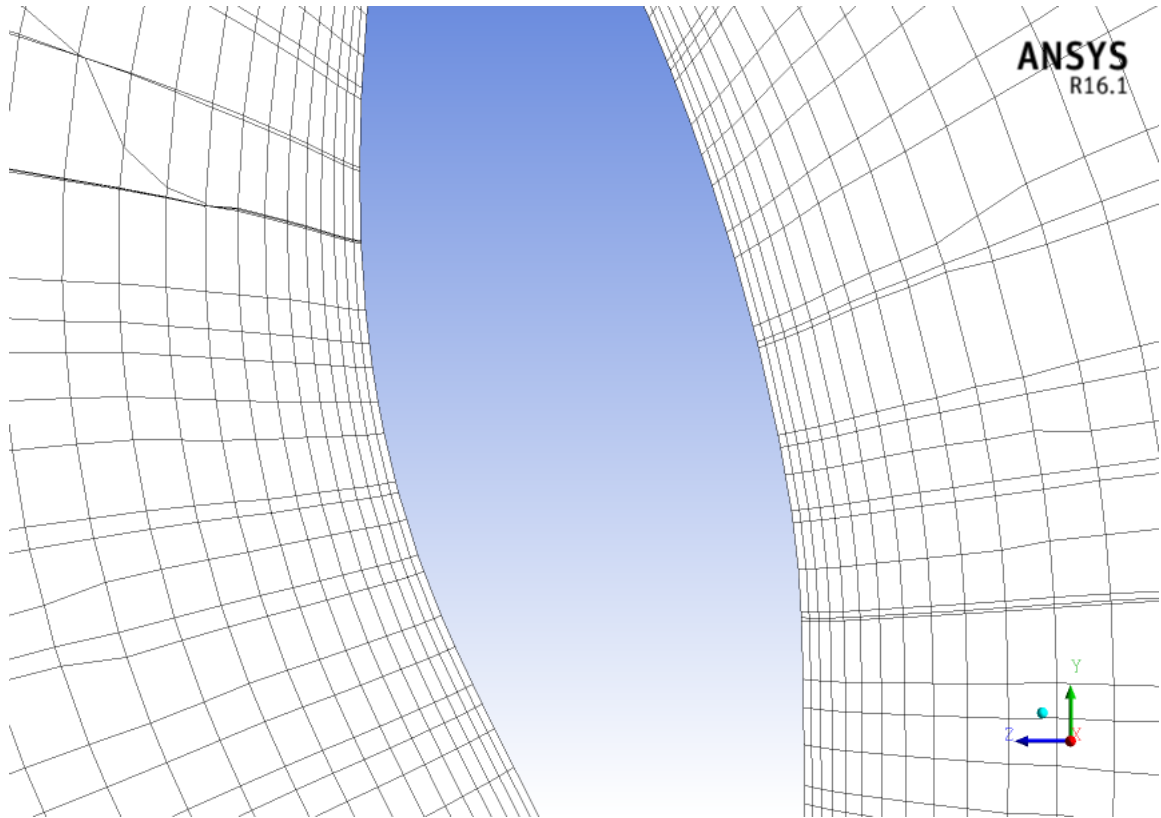


Figure 211: The inflation layers around the blade for case 4

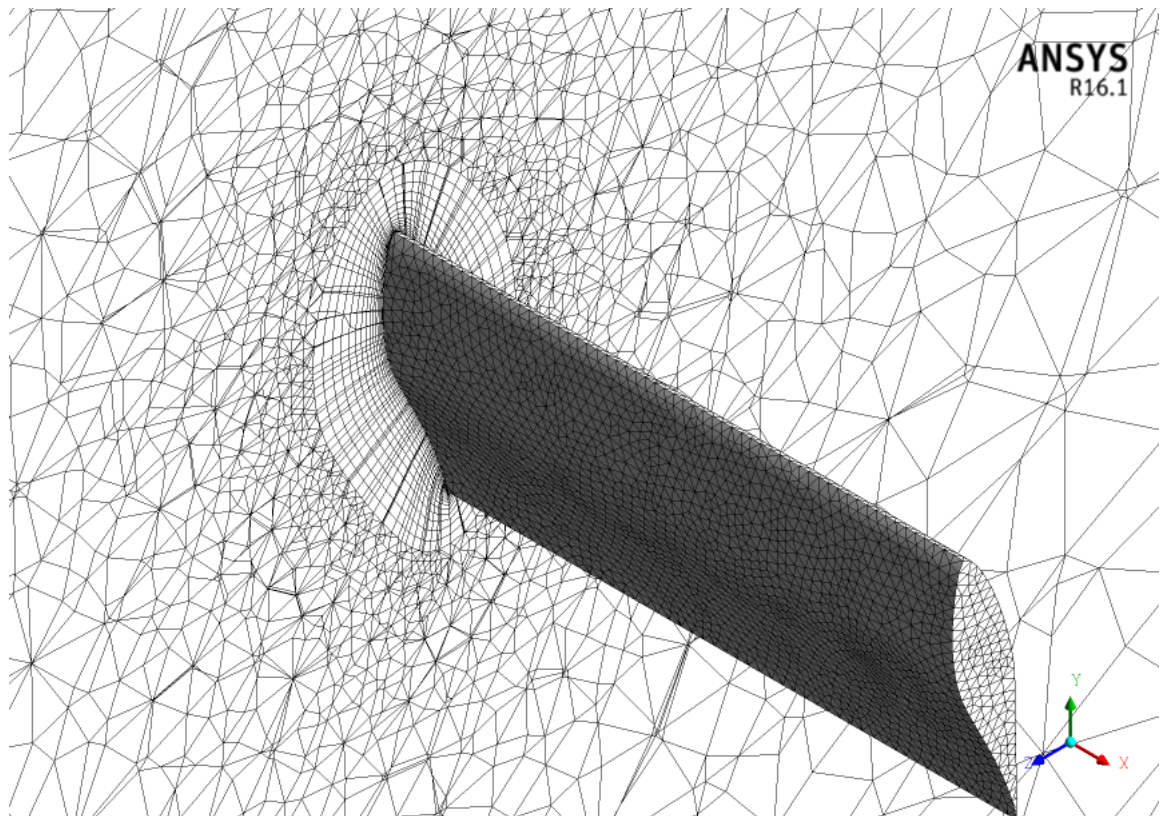


Figure 212: The generated mesh of the blade for case 4

Table 40: Study case 4 simulation algorithm

---

<b>Algorithm</b>	<b>Function Used</b>
Time State	Steady
Turbulence Model	Standard $k - \epsilon$ & <i>SST</i> $k - \omega$
Density	$\rho = 0.976 \text{ kg/m}^3$ [33]
Turbulence Intensity	$I = 0.1\%$ [40]
Length Scale	$l = 0.02 \text{ m}$ [40]
Operating Pressure	$p = 80.592 \text{ kPa}$ [33]
Wind Velocity	$V_\infty = 10.5 \text{ m/s}$
Pressure-Velocity Coupling	Coupled
Interpolating Scheme	1 <sup>st</sup> Order Upwind (Turbulence Models) QUICK (Momentum)

---

#### 8.4.4 Results & discussion

The convergence history of the torque coefficient at  $10.5\text{m/s}$  is shown in Figure 213. At about 1000 iterations, the torque coefficient does not change as the simulation continues to run therefore, study case 4 is converged. The  $y^+$  distribution along the chord line of the blade at 80% span for *SST*  $k - \omega$  turbulence model is displayed in Figure 214. The values of  $y^+$  at different blade locations are below 3, which means the generated mesh is able to resolve the viscous sub-layer.

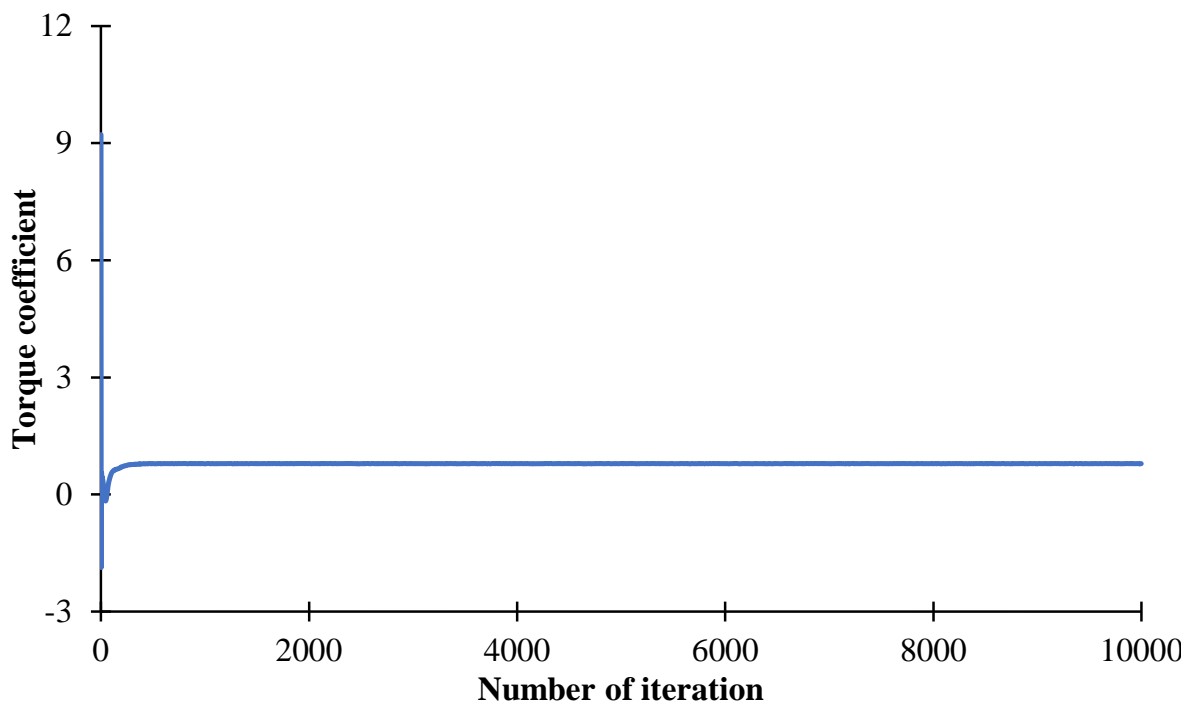


Figure 213: The convergence history of study case 4

One-third of the NREL phase II is simulated using the advantage of rotational periodic boundary condition, as shown in Figure 205. This study case involves rotation of the blade therefore, it is modelled with assistance of MRF due to steady state flow. To accelerate the convergence process by 30% to 50%, pseudo-transient solution method is performed, which is only allowed to be used in pressure-velocity coupling [85].

Regarding to the turbulence models used, standard  $k - \epsilon$  turbulence model is employed because the result is compared computationally to Mansour and Yahyazade [31] and Thumthae and Chitsomboon [33], who used the same turbulence model. *SST*  $k - \omega$  turbulence model is also used for further comparison with standard  $k - \epsilon$  in computing wind turbine torque.

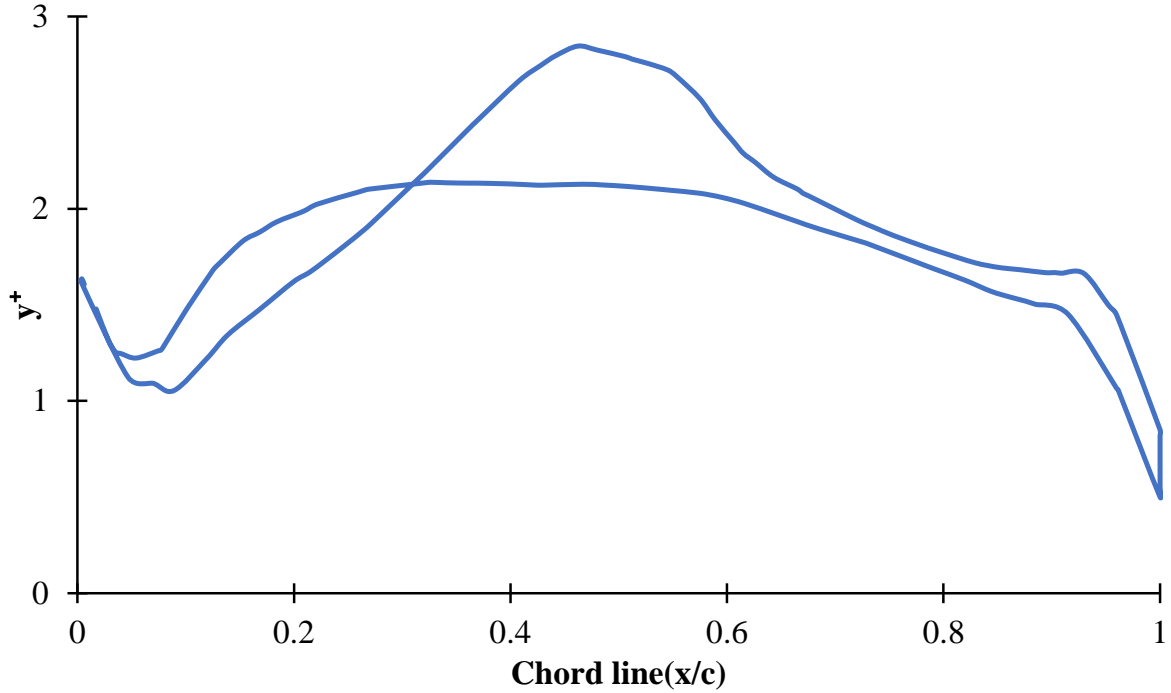


Figure 214: The  $y^+$  distribution of study case 4

Figure 215 displays the blade velocity at different spanwise locations. Theoretically, the maximum blade velocity must be at the tip of the blade, as it has the maximum blade radius according to Equation (34) [43].

$$\vec{V}_B = \vec{\omega}_B \times \frac{\vec{d}}{2} \quad (34)$$

Where:  $\vec{V}_B$  is the blade velocity ( $m/s$ ).

Referring to Equation (34), the blade velocity at the tip is therefore  $45.6m/s$ . This value is calculated as in Equation (35), where  $1m$  accounts for the hub and spar existence. According to Fluent as shown in Figure 215, the blade velocity at the tip is  $45.7m/s$ , which is very close to the value obtained by the theory.

$$\vec{V}_B = \vec{\omega}_B \times \frac{\vec{d}}{2} = -7.54(rad/s)\hat{k} \times -(5.05 + 1)(m)\hat{i} = 45.6(m/s)\hat{j} \quad (35)$$

Figure 216 shows the velocity streamlines through the blades of the NREL phase II. There are three main regimes with wind velocity variations. Region 1 is at inlet, which has a wind velocity of  $10.5m/s$  as estimated for the inlet boundary condition. Once the wind hits the blades, a sharp decrease in wind velocity behind the blades at the near wake is shown and it is indicated by dark blue streamlines. However, the maximum velocity of wind is found around

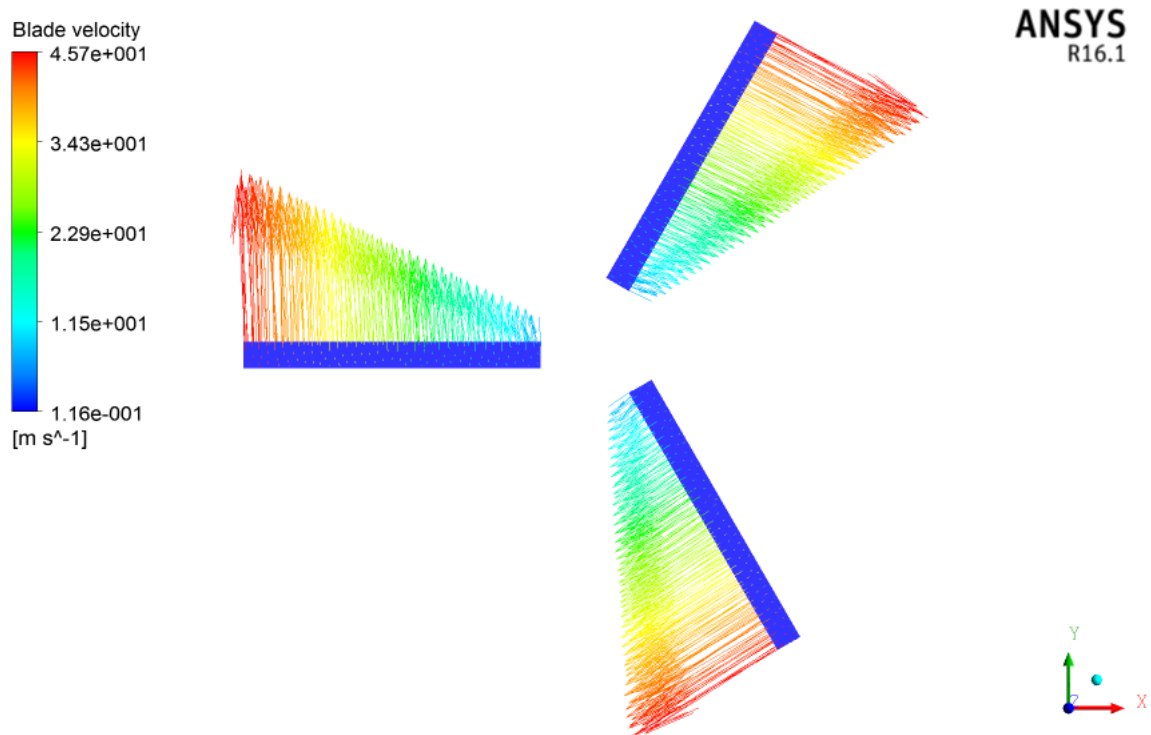


Figure 215: Study case 4: the blade velocity at different spanwise locations

the wake region and it is shown as a red streamline. This is expected according to the mass conservation law. The flow must recover the loss existed in continuity that occurs in the wake region after hitting the blades.

Figures 217 and 218 represent the relative velocity vectors at 30% and 80% span, respectively. Wind accelerates at the suction side of the blade after leading edge separation. This can be clearly seen at 30% span. This acceleration is due to that air on the suction side has to travel longer distance. At 80% span, the relative velocity is increased because of the rise in the blade velocity according to Equation 34. The pressure contour of the blade at 30% and 80% span are displayed in Figures 219 and 220, respectively. The maximum pressure is found to be towards the blade tip acting on the lower side of the blade to create lift force and therefore, rotation of the blades.

The required torque of the three blades at wind speed of  $10.5\text{m/s}$  is computed via Ansys Fluent which evaluates the torque according to Equation (5). The validation of torque that is calculated in this study case and experiment by Butterfield *et al.* [86] are measured in both strain gauge (produced by the rotor) and electrical generator is shown in Table 41. The torque of study case 4 is also compared to other simulation studies, such as computational

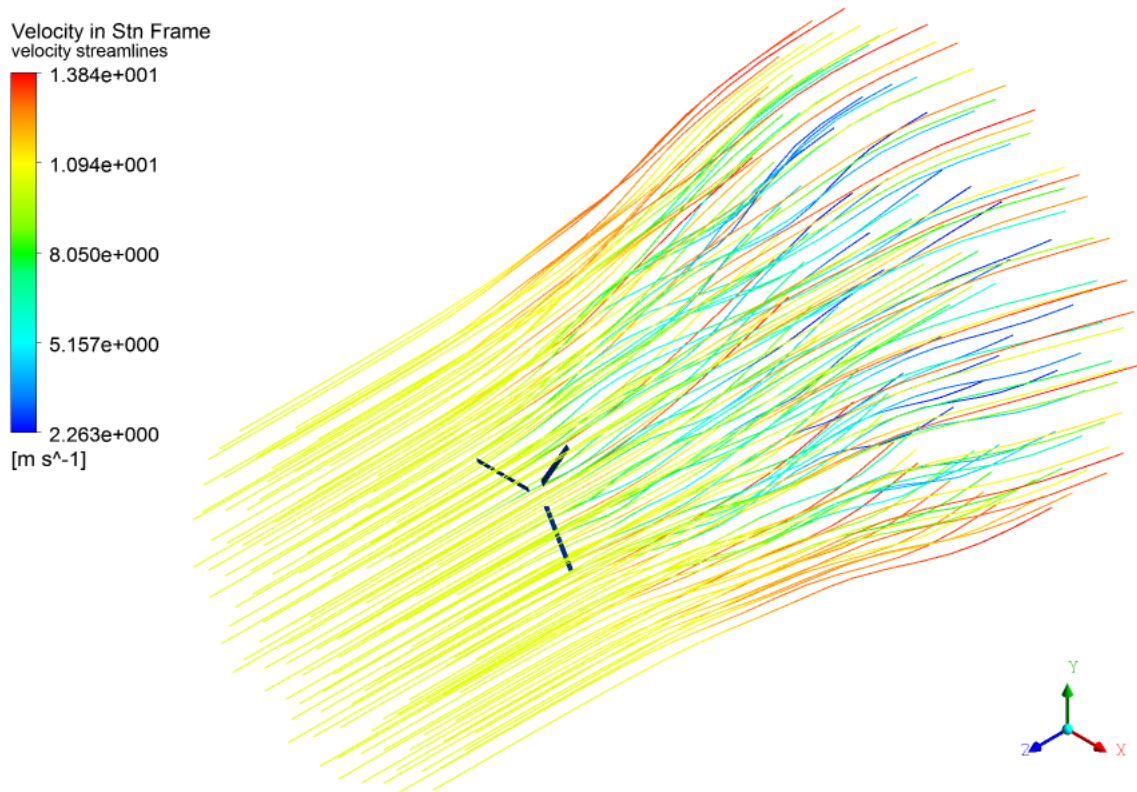


Figure 216: Study case 4: the velocity streamlines

study by Mansour and Yahyazade [31] and Thumthae and Chitsomboon [33]. The numerical simulation comparison is also recorded in Table 41.

The results of Table 41 prove that the *SST*  $k - \omega$  turbulence model can simulate the flow around wind turbine blades better than the standard  $k - \epsilon$  turbulence model. The reason behind this discrepancy is that the standard  $k - \epsilon$  turbulence model cannot handle highly swirling flow, such as the flows behind the wind turbines. Based on these findings, the *SST*  $k - \omega$  turbulence model is selected for further simulations for both smooth and tripped cases. Table 41 also shows that this study case result has smaller difference compared to the referenced simulations. This could be due to a better resolved flow around the blades.

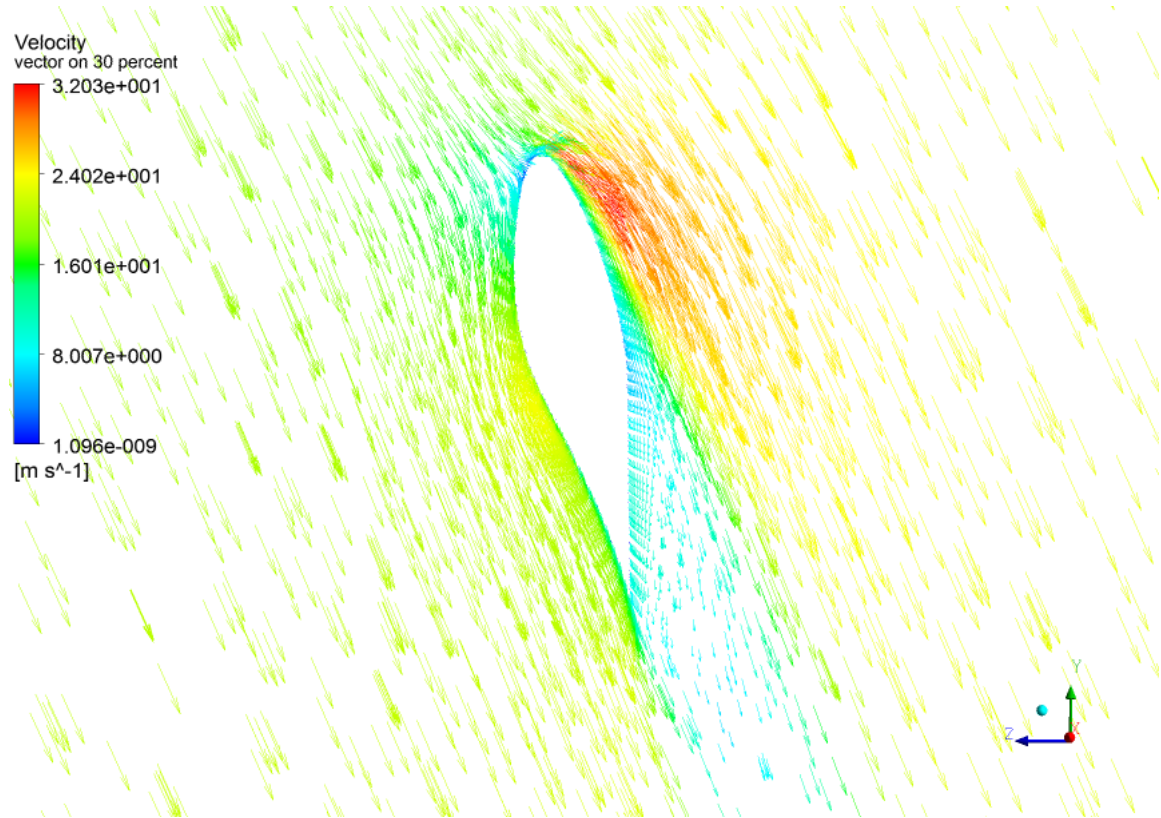


Figure 217: Relative velocity vector at 30% span for case 4

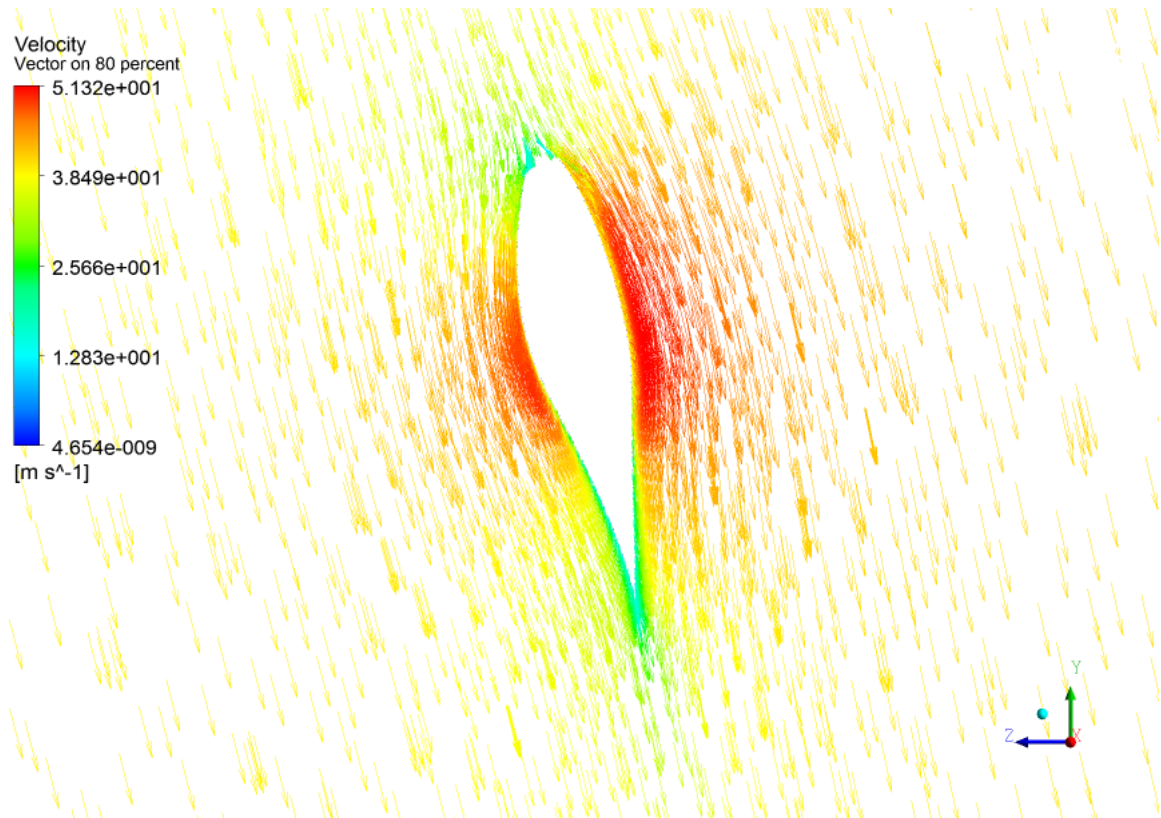


Figure 218: Relative velocity vector at 80% span for case 4

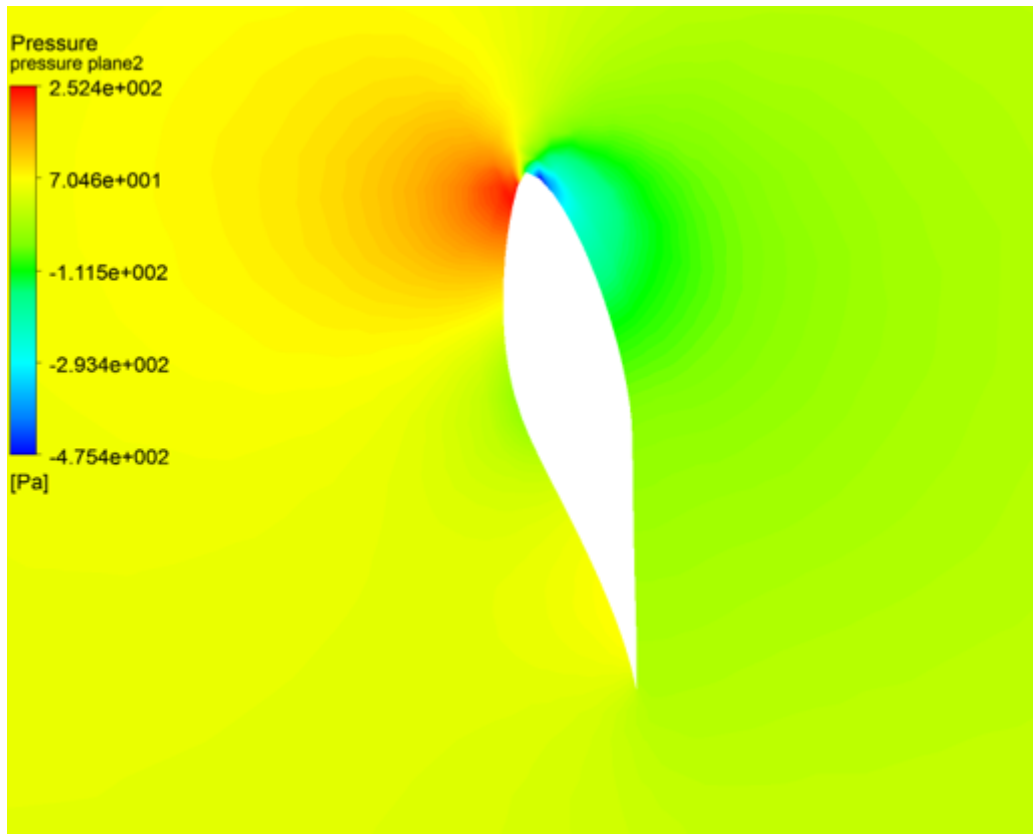


Figure 219: Pressure contour at 30% span for case 4

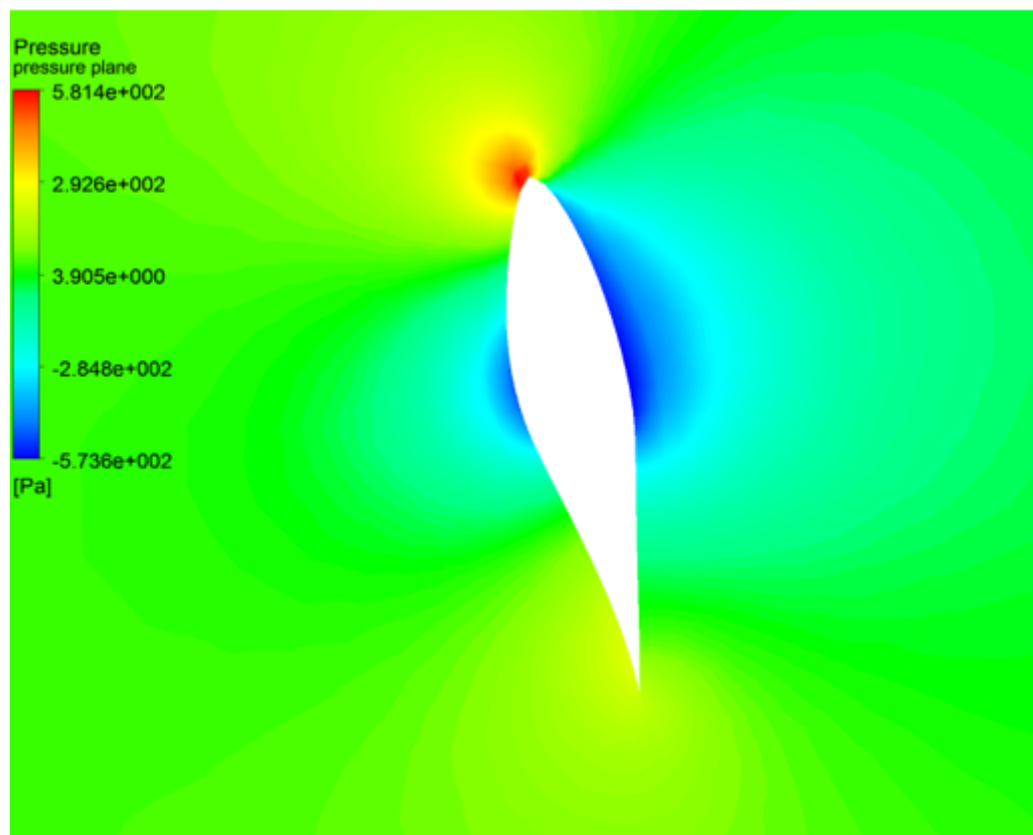


Figure 220: Pressure contour at 80% span for case 4

Table 41: Study case 4: torque ( $N.m$ ) at  $10.5m/s$  calculation comparison

CFD		Experimental Measurements [86]			
Ansys Fluent		Mechanical		Generator	
Turbulence Model	Torque	Torque	Difference %	Torque	Difference %
<i>SST</i> $k - \omega$	1219.8	1207.4	1.03	1190.0	2.50
Standard $k - \epsilon$	1157.4	1207.4	4.14	1190.0	2.74
Standard $k - \epsilon$ [31]	1078.7	1207.4	10.7	1190.0	9.35
Standard $k - \epsilon$ [33]	1144.4	1207.4	5.22	1190.0	3.84

## 8.5 Study Case 5 (3D, URANS, NREL phase II, SMM, $Re_c = 9.4 \times 10^5$ )

### 8.5.1 Purpose

Study case 5 is very similar to study case 4 (section 8.4) in terms of simulating the same WT (NREL phase II). However, there are two main differences regarding to computational settings. One difference is that study case 5 models full rotor scale instead of simulating one-third rotor scale. The tower is not included in study case 5, as it has a very low effect on power output of HAWTs [28]. In addition, the existence of tower leads to higher computational time and cost due to the increase in the number of mesh elements.

Another difference is that study case 5 include the time variation in the calculation. Therefore, SMM is required to be implemented instead of MRF to account for the rotation of the rotor. SMM is one of the rotational techniques that is available in Fluent. It was recommended by Blades and Marcum [87] if the rotational motion is already known. It was well explained by Abdulqdir *et al.* [88], such that it applies a cyclic rotational mesh at the interface between the rotational components and the stationary domain.

The reason of modelling full rotor scale is related to the simulation difficulty. Although study case 4 uses less mesh, it cannot be run in supercomputer due to unknown reasons. Alternatively, it is run on author's personal laptop, thereby, it is very hard and time consuming to run transient cases on personal laptop. However, full rotor scale is smoothly simulated via supercomputer. In addition, the computational sources availability provides an opportunity to simulate full rotor scale for future work on non-uniform flow around HAWT.

Study case 5 computes the performance of the NREL phase II in terms of mechanical torque and power coefficient. This study case also examines the difference between computed steady and transient torque and power coefficient by showing a validation against experiment. The results are validated against experiment by Butterfield *et al.* [86] at the range of various wind speeds. Furthermore, study case 5 shows the effect of hub on the computed torque as well as showing the computed blade velocity at different blade locations.

### 8.5.2 Geometrical setup

The fluid domain of study case 5 is selected to be the very well-known NASA Ames wind tunnel that was proposed by Hands *et al.* [89]. The wind tunnel has a test section of  $24.4$  by  $36.6\text{m}^2$ . NASA Ames wind tunnel is believed to have negligible blockage effect for span length of  $5\text{m}$  [90]. The wind turbine with origin at the hub centre is placed  $2d$  from inlet and  $3d$  from outlet to capture near wake effects on resulting mechanical torque and power coefficient. Figure 221 displays the fluid domain of study case 5.

The blades and hub of the NREL phase II are also shown in Figure 221. The geometrical details of the blades and hub are illustrated in section 2.2.1. Referring to Figure 221, the boundary conditions are as following: the lateral and vertical faces of the fluid domain are assumed as no slip walls. Beside this, the blades and hub are set as stationary wall with no slip condition is applied. The frontal and back faces of the wind tunnel are velocity inlet and pressure outlet, respectively.

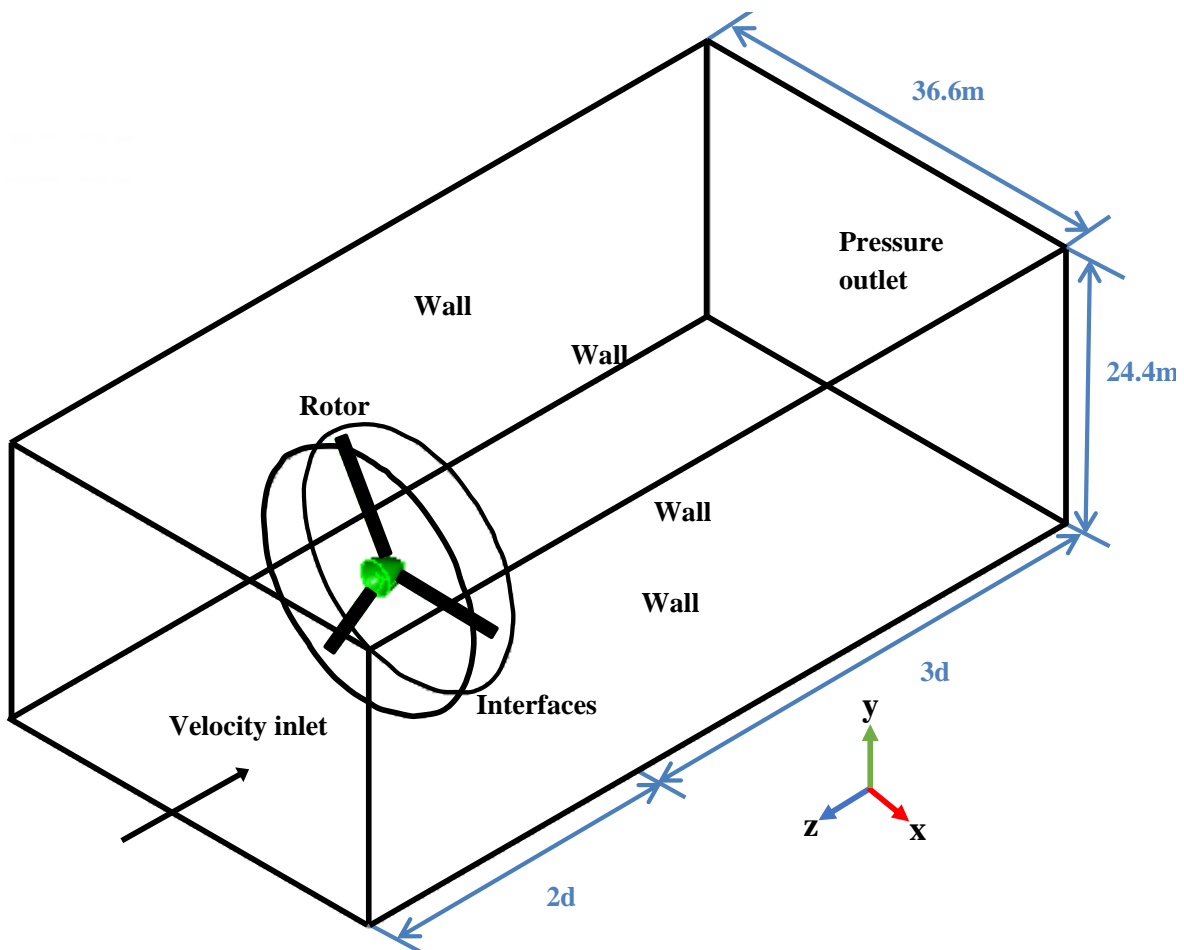


Figure 221: Study case 5 fluid domain (not to scale)

Because of employing SMM, inner and outer interfaces between rotor and fluid domain are created, as shown in Figure 221. Only the inner interface involves a rotation based on angular velocity of  $71.63rpm$ , while the outer interface is set stationary. The dimensions of the cylindrical interfaces are  $10.5m$  and  $2m$  in diameter and length, respectively. The diameter and length of the interfaces are assumed to ensure that the interfaces have a minimal effect on the rotor performance therefore, higher accuracy.

### 8.5.3 Mesh study & computational setup

A mesh study is carried out for the rotating body and wind tunnel separately. First, the rotating body's mesh elements are conserved, and a mesh study is performed on the wind tunnel. A tetrahedral mesh of  $6 \times 10^5$  elements is preferred for the wind tunnel, as displayed in Figure 222. The mesh of the fluid domain is refined in all three directions. The selected fluid domain's mesh has 150, 80 and 80 nodes in streamwise, spanwise and normal directions of the freestream boundary layers.

Furthermore, a mesh dependency on the rotating body is tested, while maintaining constant wind tunnel's mesh elements, as shown in Figure 223. The blades' mesh is refined in all three directions. The selected mesh of the blades has 120 and 800 nodes in the chordwise and spanwise directions, respectively. The first layer of mesh is placed at  $50\mu m$  with 30 inflation layers and 1.2 growth rate. Consequently, a mesh of  $4.1 \times 10^6$  elements is selected, which corresponds to an average of  $27 \times 10^3$  triangular faces for each blade. Both mesh studies contribute to a total mesh of  $4.7 \times 10^6$  elements.

Figure 224 shows how the  $y^+$  changes with refining of the generated mesh. An average value of  $y^+ = 1.2$  is selected for this study case. The mesh metrics of the selected mesh are shown in Figures 225 and 226 for skewness and orthogonality, respectively. The generated mesh of the fixed part and rotating part are displayed in Figures 227-231. The simulation setting and air properties of study case 5 are shown in Table 42. The time step is selected based on  $1^\circ$  for each blade rotation, which corresponds to  $0.002315s$ .

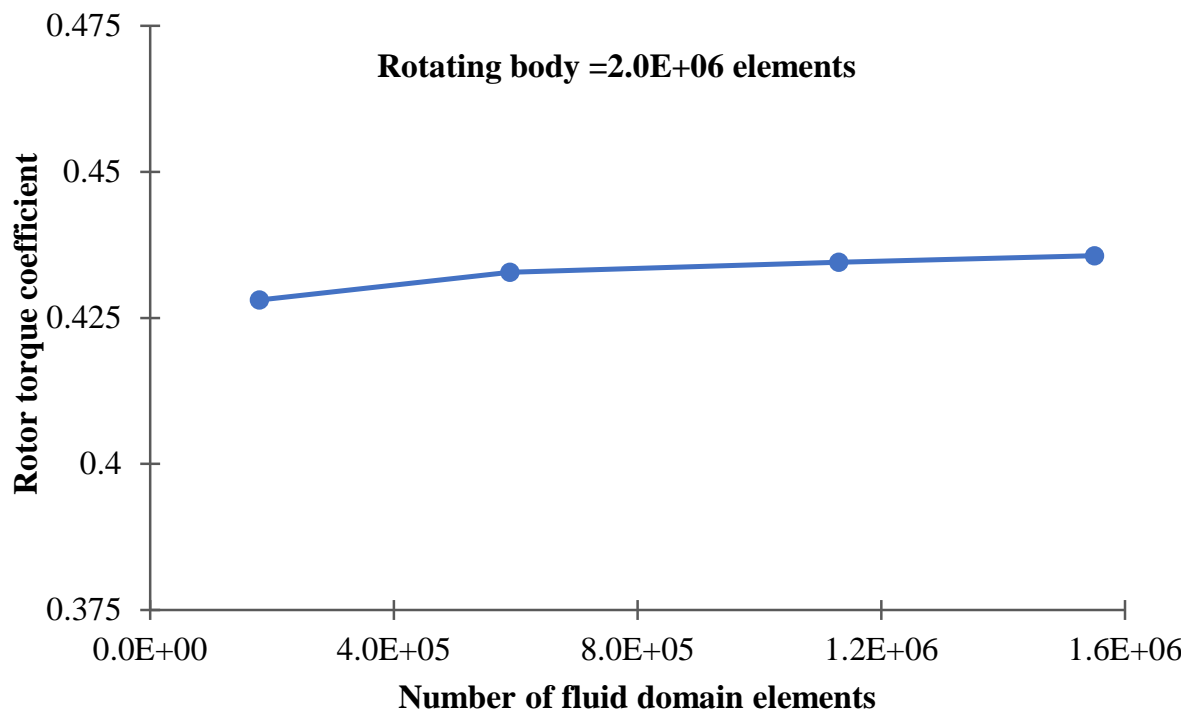


Figure 222: Mesh dependency of fluid domain (study case 5)

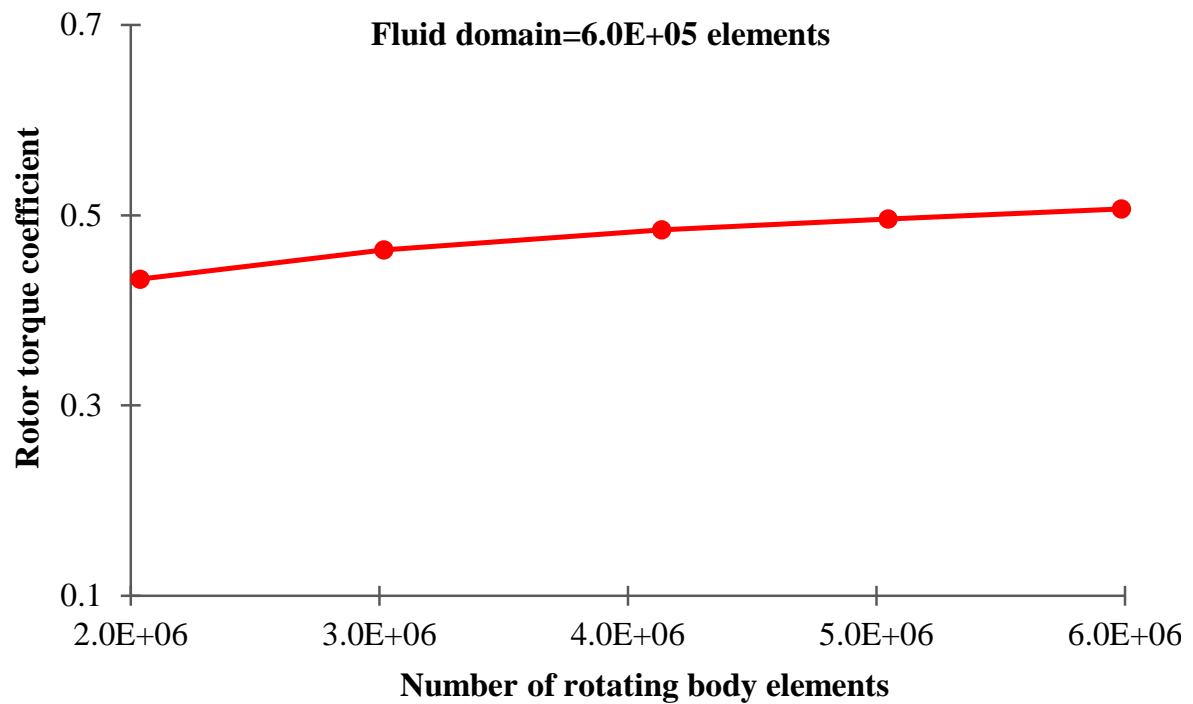


Figure 223: Mesh dependency of rotating body (study case 5)

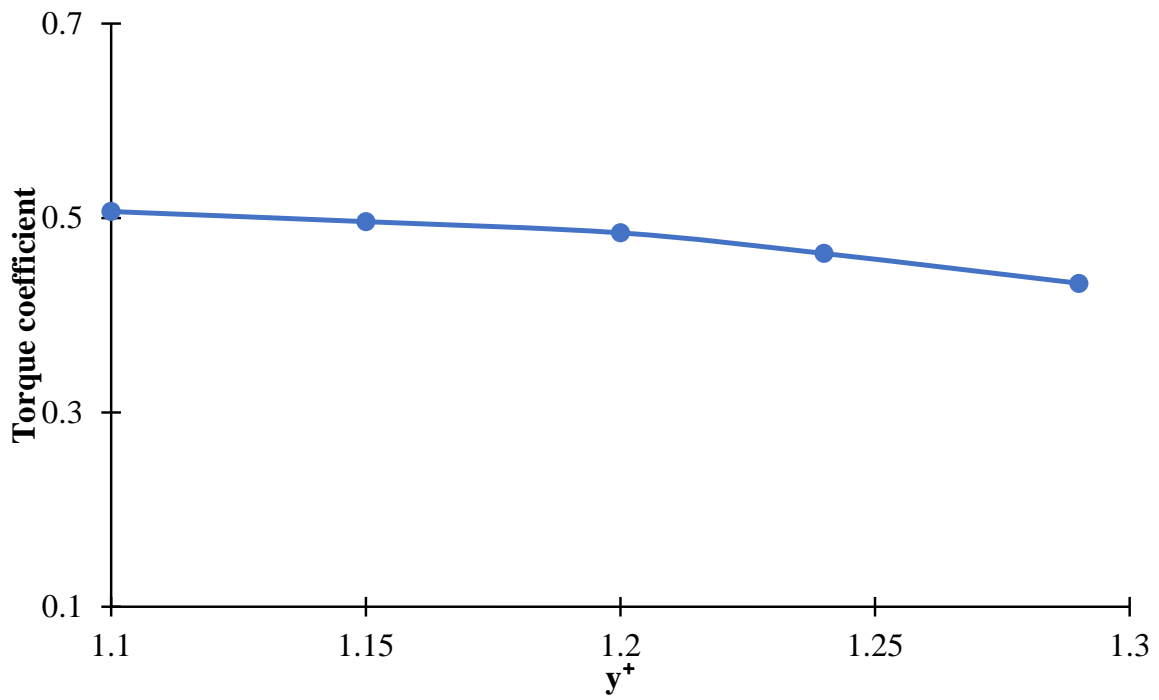


Figure 224:  $y^+$  values for different meshes of study case 5

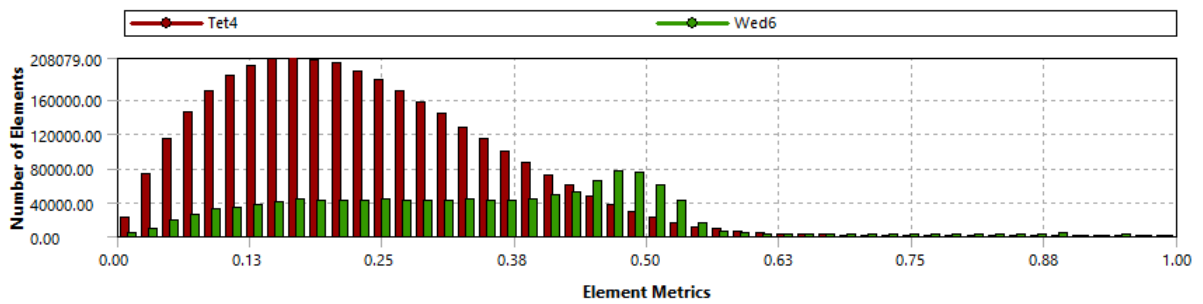


Figure 225: The skewness of study case 5

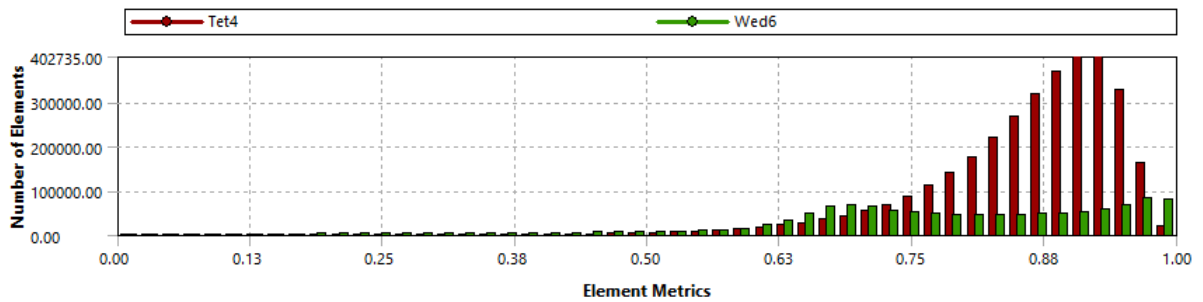


Figure 226: The orthogonality of study case 5

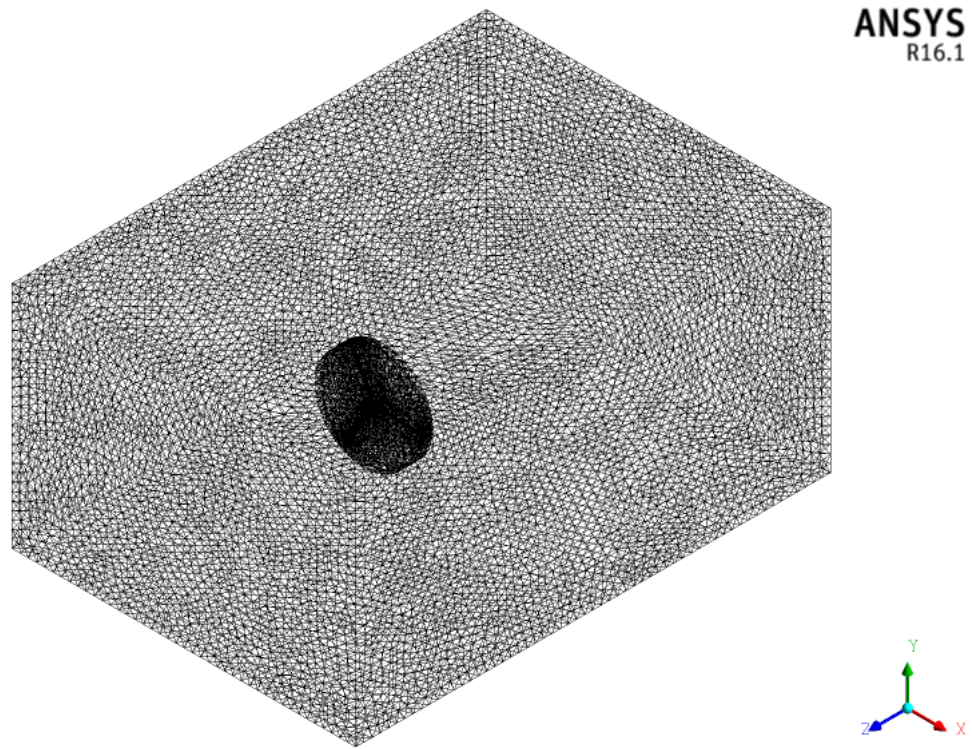


Figure 227: The generated mesh of fluid domain and rotor for case 5

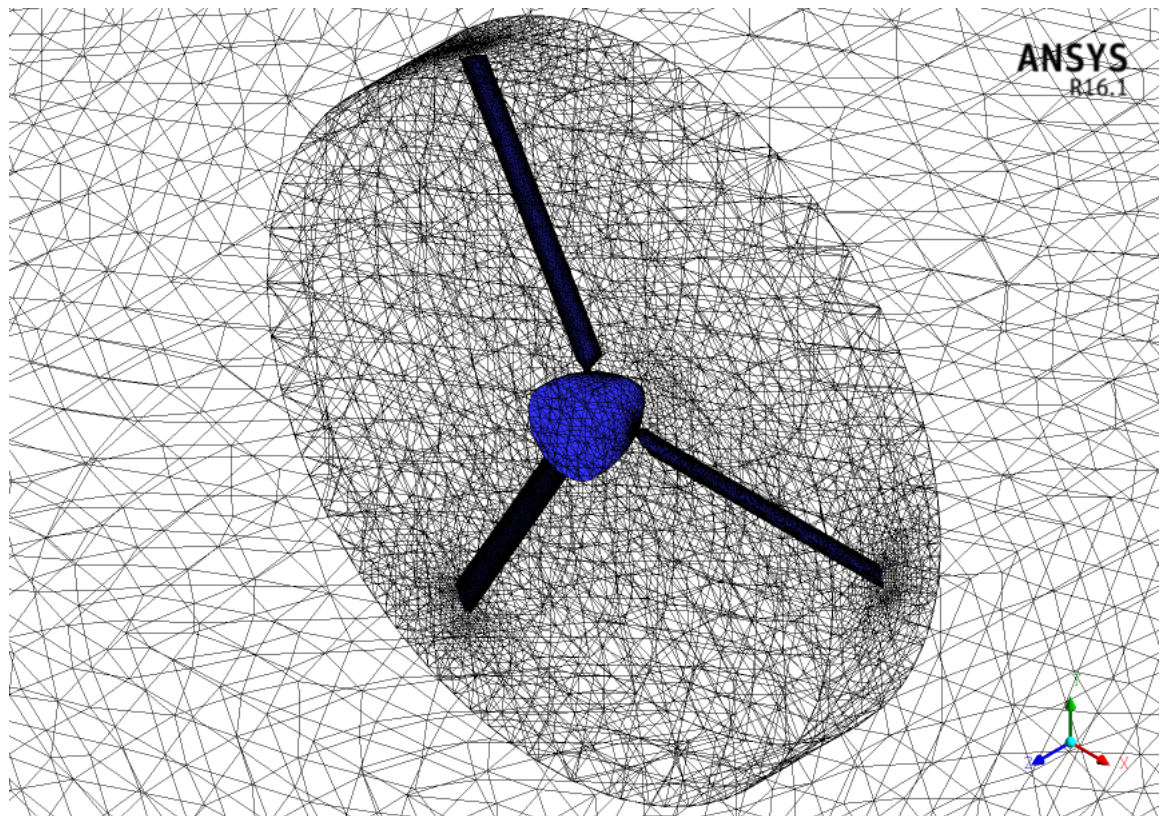


Figure 228: The generated mesh of the rotor for case 5

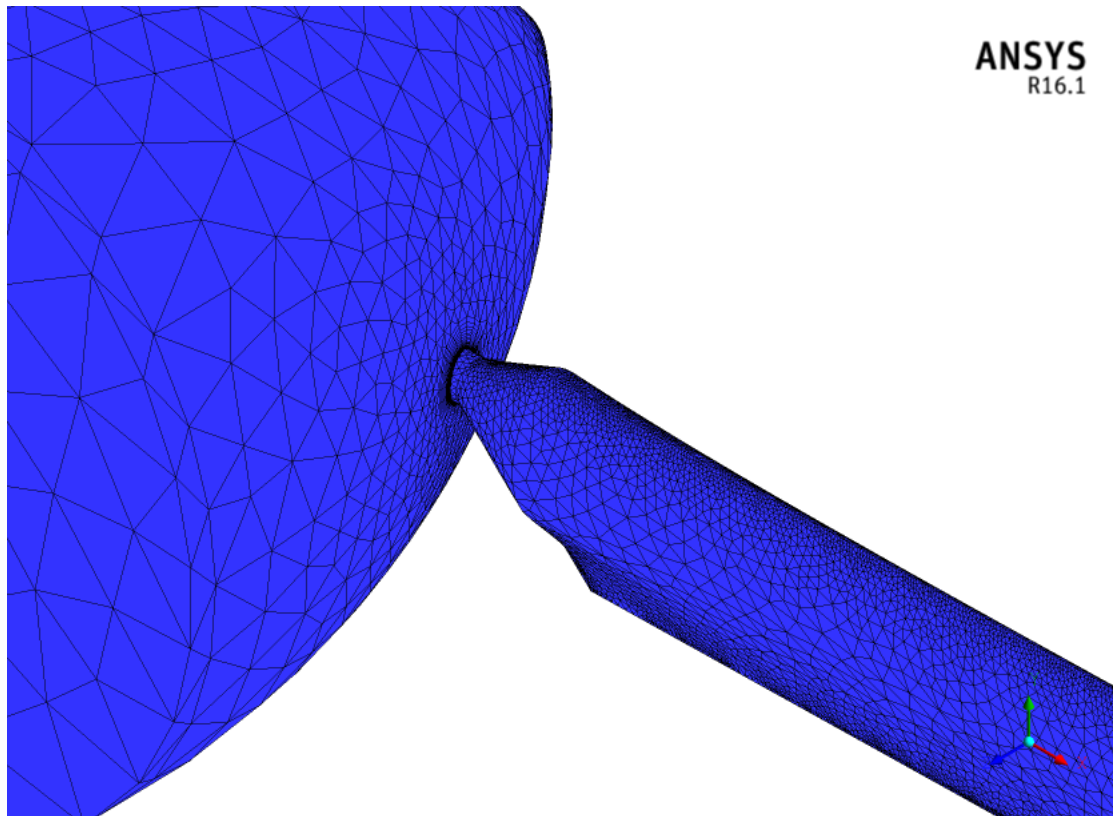


Figure 229: The generated mesh of the hub and one blade for case 5

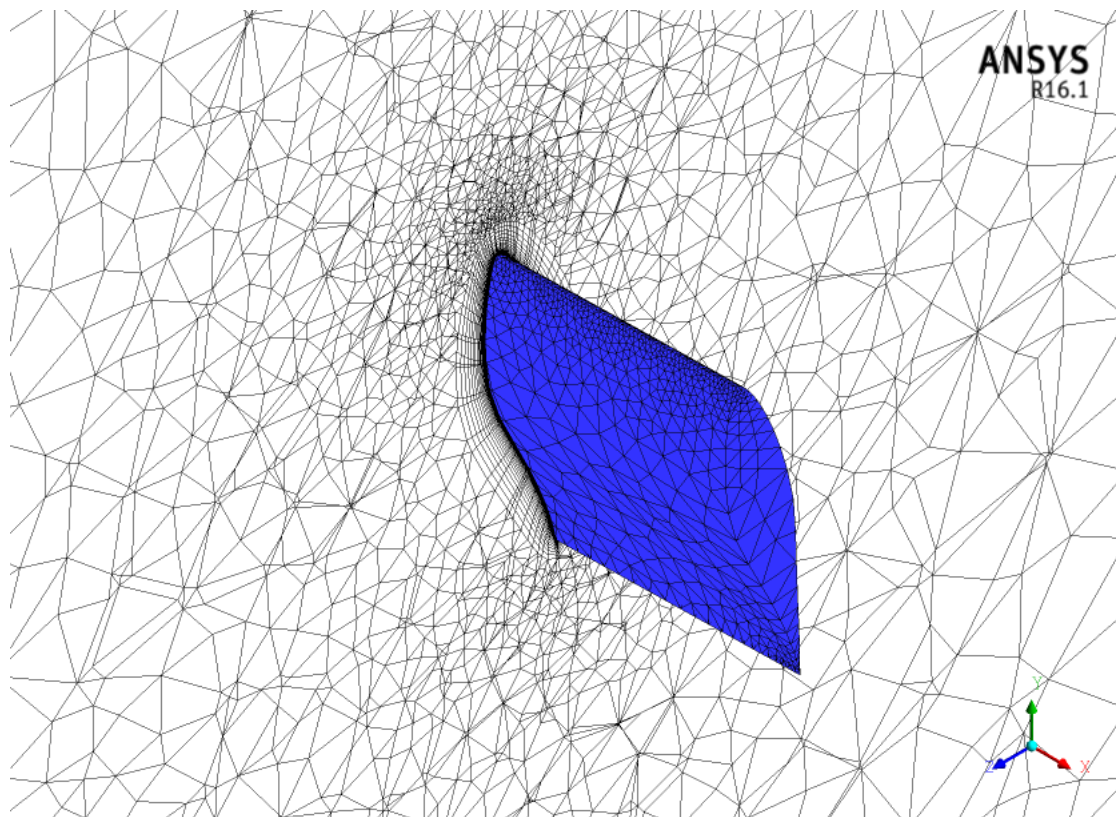


Figure 230: The generated mesh of a cross section with one blade for case 5

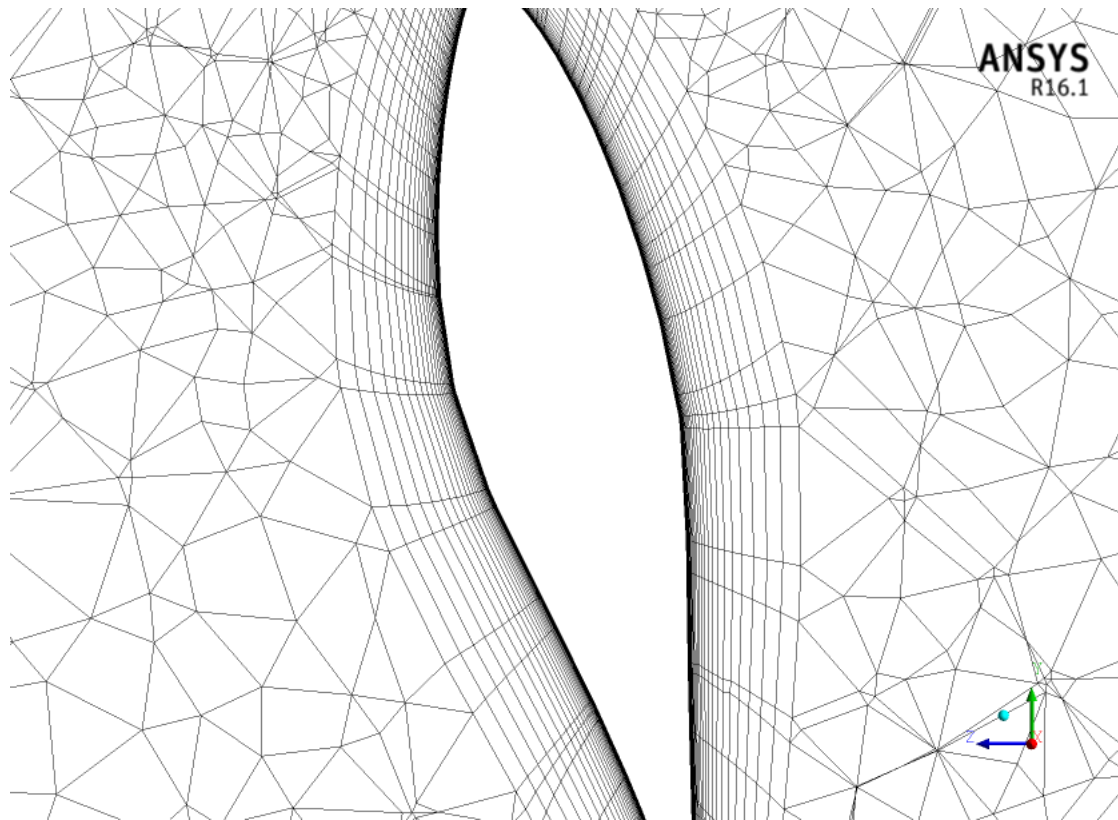


Figure 231: The inflation layers around the blade for case 5

Table 42: Study case 5 Simulation Algorithm

Algorithm	Function Used
Time State	Transient
Turbulence Model	<i>SST k - <math>\omega</math></i>
Density	$\rho = 0.976 \text{ kg/m}^3$ [33]
Turbulence Intensity	$I = 0.2\%$
Length Scale	$l = 0.02 \text{ m}$ [40]
Operating Pressure	$p = 80.592 \text{ kPa}$ [33]
Time Step	$0.002315 \text{ s}$
Pressure-Velocity Coupling	SIMPLE
Interpolating Scheme	1 <sup>st</sup> Order Upwind

### 8.5.4 Results & discussion

The state of study case 5 is set transient however, divergent result is obtained due to high number of mesh elements. Alternatively, a steady condition is applied for the first 10000 iterations with residual error of  $1 \times 10^{-5}$  to ensure solution stability, and then the computation continues for five revolutions as transient state. Because SMM can be only used for transient state, MRF is modelled first for steady state. The simulation is run with 40 processors via supercomputer and it is approximately lasted for 15 hours per case.

The simulated time of torque coefficient for study case 5 is shown in Figures 232 and 233. The calculation of the torque coefficient is based on averaging the last circle of the simulated time, as marked in Figure 233. The  $y^+$  distribution over the chord line of the blade at 80% span is displayed in Figure 234. The  $y^+$  is ensured to be less than 3 at all blade locations therefore, resolving viscous sub-layer. This is also important when comparing this smooth study case with tripped study case.

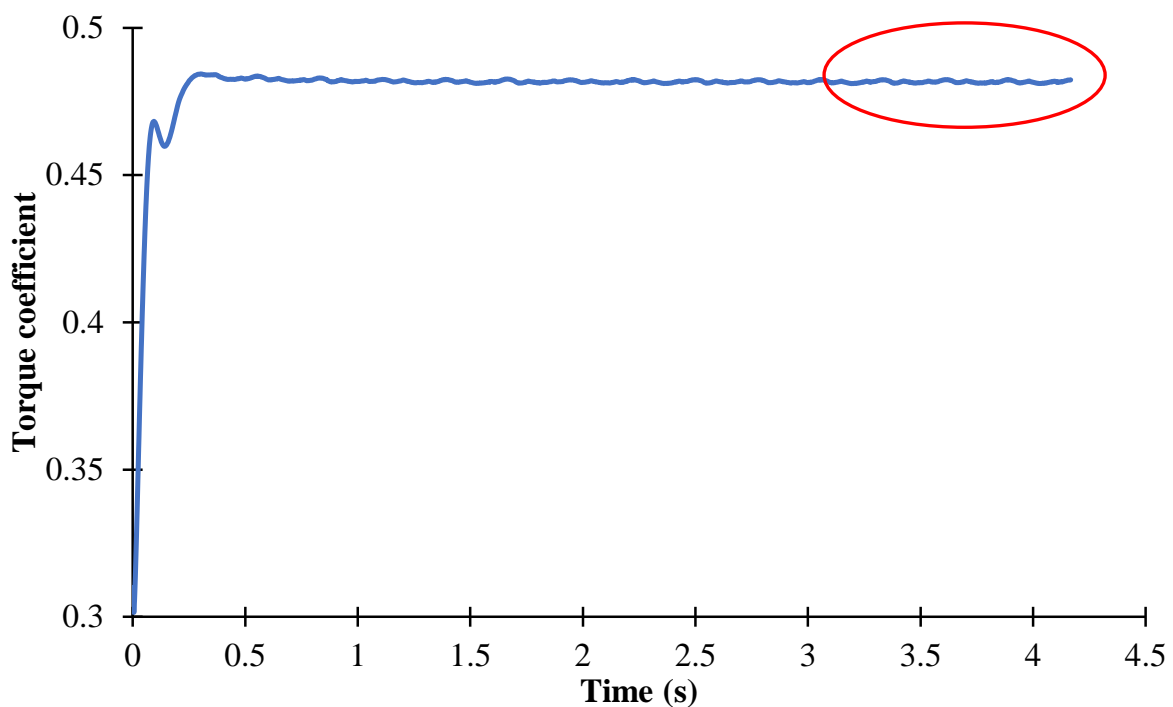


Figure 232: The simulated time of study case 5

Figure 235 displays the velocity of the blade at different blade locations as well as showing the direction of rotation as clockwise. According to Figure 235, the maximum blade velocity is at the blade tip that is  $37.8m/s$ . Referring to Equation (34), the blade tip velocity is calculated

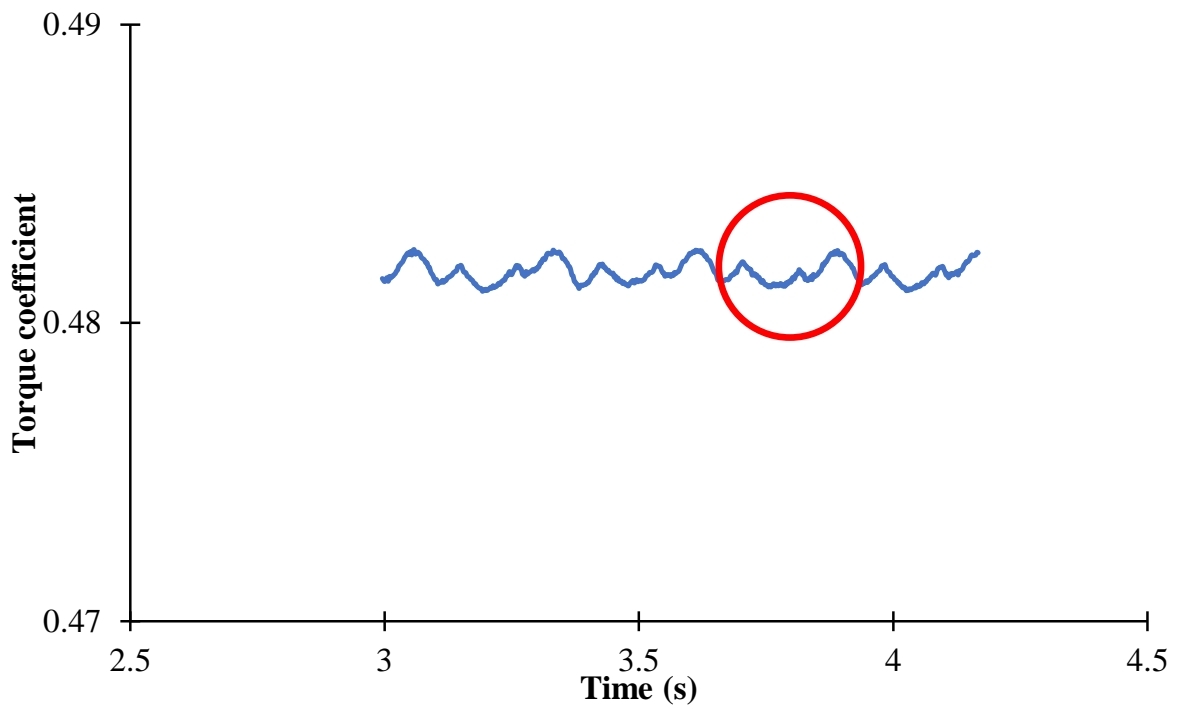


Figure 233: The simulated time of study case 5 (zoom-in)

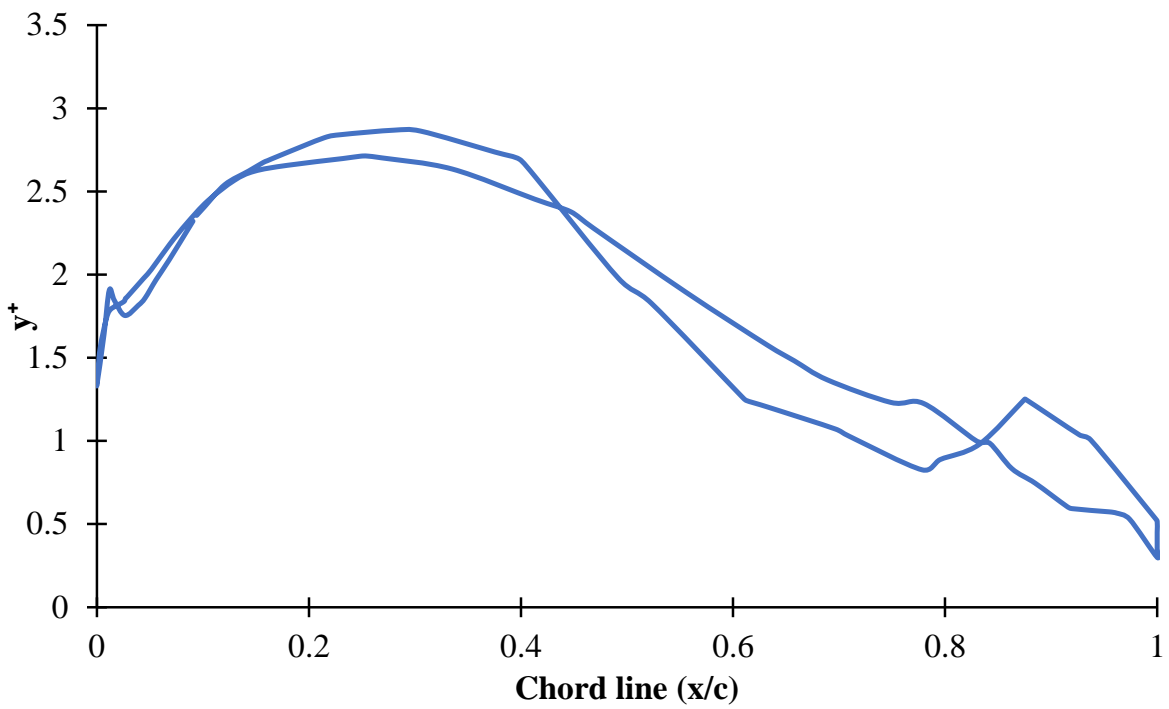


Figure 234: The  $y^+$  distribution of study case 5

theoretically as in Equation (36). The difference in blade tip velocity answers between study case 4 (Equation (35)) and study case 5 (Equation (36)) is that study case 4 accounts for  $1m$  displacement because of assuming the existence of hub and spar.

$$\vec{V}_B = \vec{\omega}_B \times \frac{\vec{d}}{2} = -7.54(\text{rad/s})\hat{k} \times -(5.05)(m)\hat{i} = 38.1(m/s)\hat{j} \quad (36)$$

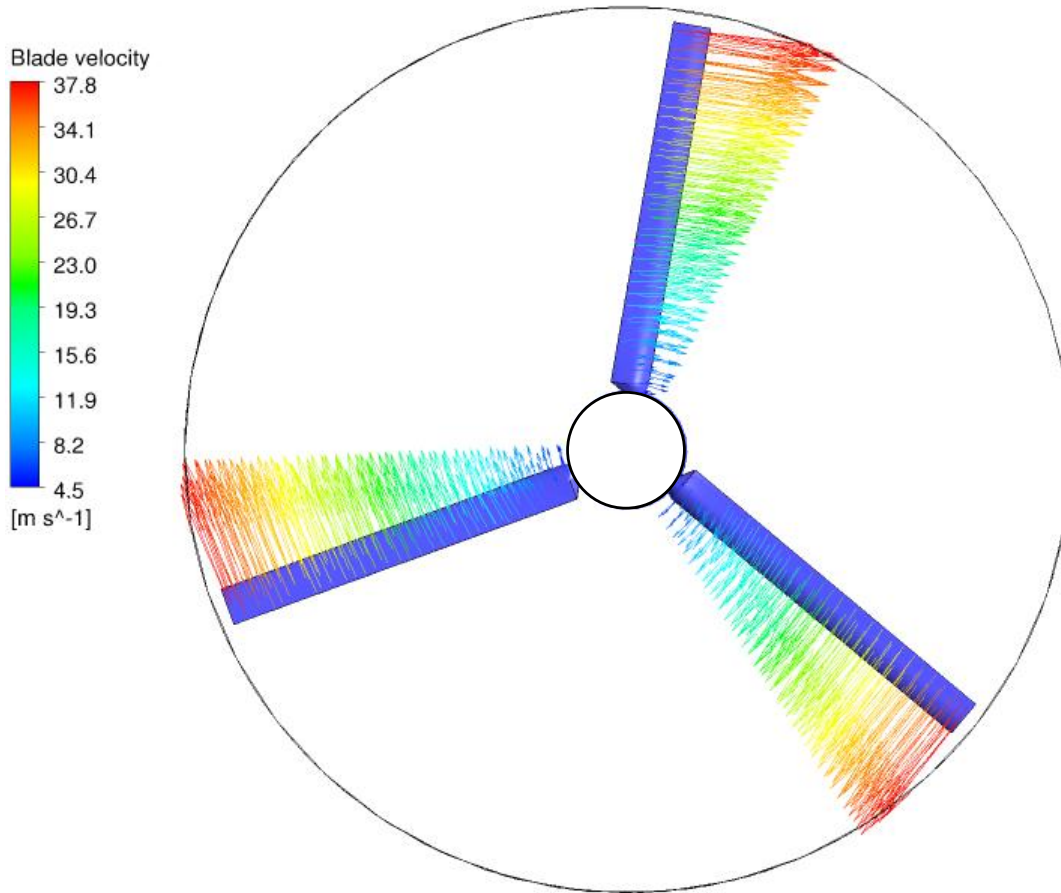


Figure 235: The velocity of the blades (study case 5)

The performance of the NREL phase II is computed using the *SST*  $k - \omega$  model and validated against field experiment [86]. According to Figure 236, the computed mechanical torque is approximately in a good agreement with experiment. However, the percentage error rises from one to another. The reason behind this increase is believed because of the flow conditions for each run were impossible to be controlled as the experiment was conducted in a field rather than a lab, while they are kept constant computationally for all runs.

Figure 237 shows the power coefficient of the NREL phase II at different tip speed ratios. The power coefficient is calculated based on the generator, which is different to mechanical power

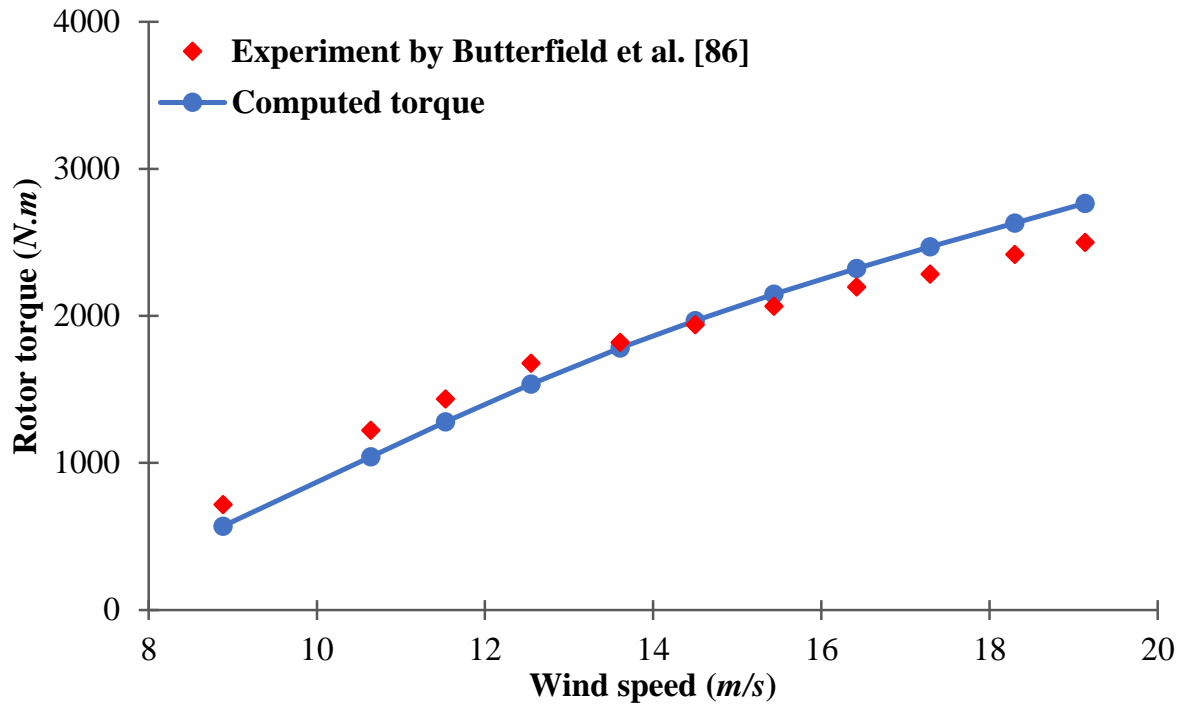


Figure 236: Rotor torque for different wind speeds (study case 5)

by the rotor due to the nacelle losses. Therefore, the computed generator power is corrected using Equation (37) [91]. According to Figure 237, the maximum power coefficient occurs at  $\lambda = 3.6$  for both calculations. The maximum power coefficient is computed as 15.0%, while the maximum measured power coefficient is about 15.2%.

$$P_g = 0.9036P_m - 0.847 \quad (37)$$

To fully understand the effects of including time changes in the simulations, steady (MRF) and unsteady (SMM) torques are computed separately and recorded in Table 43 and compared to the measured torque. At the lowest wind speed, the mechanical torque of the steady flow proves its advantage over the unsteady flow. However, as wind speed increases, the transient flow shows much better results. Consequently, more accurate wind turbine performance is obtained by considering time changes in the calculation.

Due to the lack of information about the dimension of the NREL phase II hub in the literature, the hub geometry is estimated by the author. However, Table 44 represents the effect of hub on the computed mechanical torque by showing a comparison of hub and no hub effects on the mechanical torque. Referring to Table 44, the difference shown is almost negligible at most computed wind speeds. Resulting from this, the existence of hub is not very important in computing the torque of wind turbines.

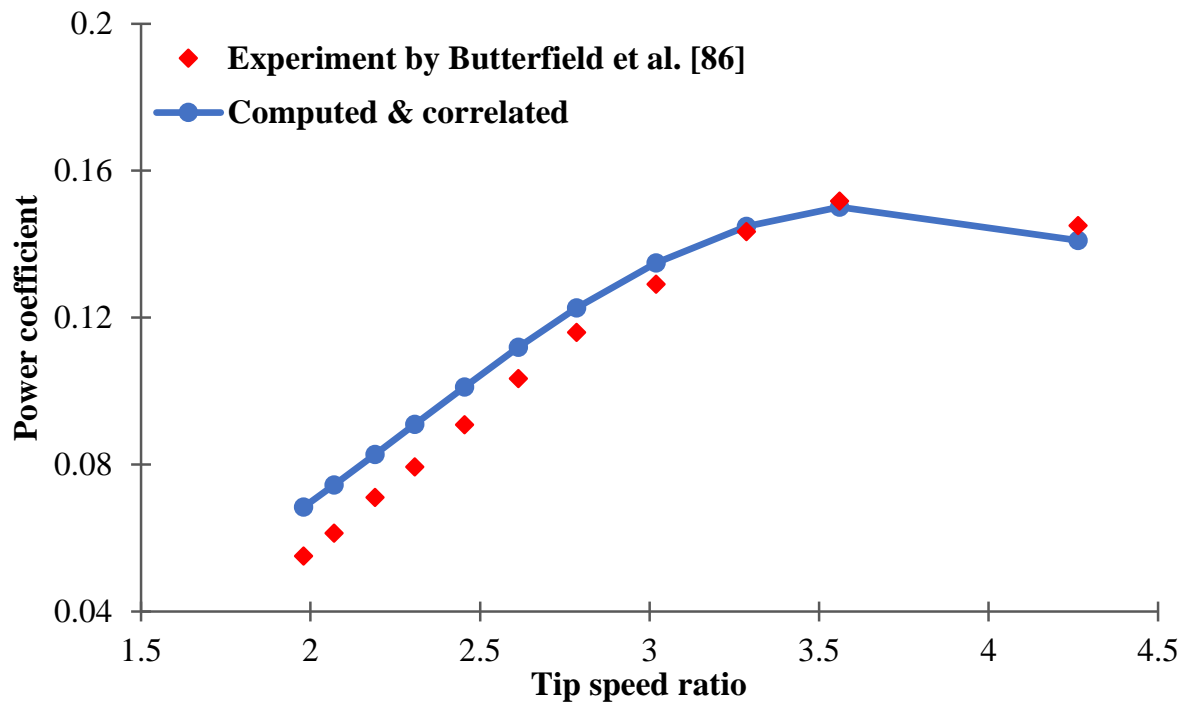


Figure 237: Power coefficient versus tip speed ratio (study case 5)

Table 43: Steady and transient torques validated against experiment

Wind speed ( $m/s$ )	MRF ( $N.m$ )	Difference%	SMM ( $N.m$ )	Difference%
8.88	642.3	10.4	570.4	20.4
10.6	1018.6	16.8	1043.4	14.7
11.5	1169.6	19.2	1280.7	10.7
12.5	1272.0	24.2	1537.6	8.43
13.6	1386.4	23.9	1782.5	2.10
14.5	1495.1	23.0	1968.3	1.43
15.4	1483.5	28.2	2147.4	3.94
16.4	1471.8	33.0	2323.4	5.74
17.3	1599.3	30.0	2470.1	8.10
18.3	1567.6	35.2	2632.1	8.87
19.1	1666.7	33.3	2766.3	10.6

Table 44: Effect of hub on the computed mechanical torque

Wind speed ( $m/s$ )	Hub ( $N.m$ )	No hub ( $N.m$ )	Difference%
8.88	570.4	562.7	1.35
10.6	1043.4	1023.6	1.90
11.5	1280.7	1255.4	1.98
12.5	1537.6	1505.1	2.11
13.6	1782.5	1742.3	2.26
14.5	1968.3	1886.2	4.17
15.4	2147.4	2102.6	2.09
16.4	2323.4	2276.1	2.04
17.3	2470.1	2423.3	1.90
18.3	2632.1	2585.9	1.76
19.1	2766.3	2720.2	1.67

## Appendix B (Aerofoil Coordinates)

Table 45: The 21% chord aerofoil coordinates

Upper surface ( <i>m</i> )				Lower surface ( <i>m</i> )			
y-axis	Chord	y-axis	Chord	y-axis	Chord	y-axis	Chord
0.00022	-0.45700	0.00109	-0.45122	-0.00082	-0.00001	-0.00159	-0.00048
0.00273	-0.44327	0.00505	-0.43284	-0.00171	-0.00055	-0.00241	-0.00110
0.00780	-0.42021	0.01074	-0.40546	-0.00527	-0.00427	-0.00934	-0.01064
0.01387	-0.38859	0.01730	-0.36982	-0.01386	-0.01938	-0.01870	-0.03017
0.02106	-0.34947	0.02513	-0.32791	-0.02378	-0.04279	-0.02889	-0.05684
0.02947	-0.30552	0.03399	-0.28274	-0.03377	-0.07221	-0.03827	-0.08873
0.03852	-0.26007	0.04272	-0.23808	-0.04234	-0.10622	-0.04576	-0.12432
0.04552	-0.21720	0.04661	-0.19624	-0.04822	-0.14288	-0.04955	-0.16184
0.04664	-0.17524	0.04583	-0.15447	-0.04947	-0.18106	-0.04788	-0.20073
0.04429	-0.13418	0.04209	-0.11461	-0.04458	-0.22072	-0.03965	-0.24179
0.03932	-0.09598	0.03604	-0.07851	-0.03388	-0.26390	-0.02777	-0.28675
0.03233	-0.06237	0.02826	-0.04775	-0.02173	-0.30995	-0.01608	-0.33306
0.02392	-0.03482	0.01940	-0.02373	-0.01109	-0.35561	-0.00694	-0.37706
0.01479	-0.01461	0.01021	-0.00760	-0.00376	-0.39692	-0.00154	-0.41466
0.00578	-0.00276	0.00171	-0.00030	-0.00022	-0.42982	0.00034	-0.44201
0.00089	-0.00009	0.00000	0.00000	0.00035	-0.45089	0.00013	-0.45700

Table 46: The 43% chord aerofoil coordinates

Upper surface ( <i>m</i> )				Lower surface ( <i>m</i> )			
y-axis	Chord	y-axis	Chord	y-axis	Chord	y-axis	Chord
0.00046	-0.45700	0.00223	-0.45122	-0.00168	-0.00010	-0.00326	-0.00048
0.00559	-0.44327	0.01034	-0.43284	-0.00349	-0.00055	-0.00494	-0.00110
0.01597	-0.42021	0.02200	-0.40546	-0.01078	-0.00427	-0.01913	-0.01064
0.02840	-0.38859	0.03542	-0.36982	-0.02839	-0.01938	-0.03828	-0.03017
0.04311	-0.34947	0.05146	-0.32791	-0.04869	-0.04279	-0.05916	-0.05684
0.06035	-0.30552	0.06960	-0.28274	-0.06914	-0.07221	-0.07837	-0.08873
0.07887	-0.26007	0.08747	-0.23808	-0.08669	-0.10622	-0.09369	-0.12432
0.09321	-0.21720	0.09543	-0.19624	-0.09873	-0.14288	-0.10145	-0.16184
0.09551	-0.17524	0.09385	-0.15447	-0.10129	-0.18106	-0.09805	-0.20073
0.09069	-0.13418	0.08619	-0.11461	-0.09129	-0.22072	-0.08119	-0.24179
0.08051	-0.09599	0.07379	-0.07851	-0.06938	-0.26390	-0.05687	-0.28675
0.06619	-0.06237	0.05786	-0.04775	-0.04449	-0.30995	-0.03292	-0.33306
0.04898	-0.03482	0.03972	-0.02373	-0.02270	-0.35561	-0.01422	-0.37706
0.03029	-0.01461	0.02090	-0.00760	-0.00769	-0.39692	-0.00315	-0.41466
0.01183	-0.00276	0.00349	-0.00030	-0.00046	-0.42982	0.00070	-0.44201
0.00182	-0.00009	0.00000	0.00000	0.00073	-0.45089	0.00027	-0.45700

## Appendix C (Turbulence Models)

- The  $S - A$  turbulence model [75]:

$$\frac{\partial}{\partial t}(\rho\tilde{\nu}) + \frac{\partial}{\partial x_i}(\rho\tilde{\nu}u_i) = G_\nu + \frac{1}{\sigma_{\tilde{\nu}}} \left[ \frac{\partial}{\partial x_j} \left\{ (\mu + \rho\tilde{\nu}) \frac{\partial \tilde{\nu}}{\partial x_j} \right\} + C_{b2}\rho \left( \frac{\partial \tilde{\nu}}{\partial x_j} \right)^2 \right] - Y_\nu + S_{\tilde{\nu}} \quad (38)$$

$$\nu_t = \tilde{\nu}f_{\nu 1} \quad (39)$$

$$f_{\nu 1} = \frac{\chi^3}{\chi^3 + C_{\nu 1}^3} \quad (40)$$

$$\chi \equiv \frac{\tilde{\nu}}{\nu} \quad (41)$$

$$G_\nu = C_{b1}\rho\tilde{S}\tilde{\nu} \quad (42)$$

$$\tilde{S} \equiv S + \frac{\tilde{\nu}}{\kappa^2 d^2} f_{\nu 2} \quad (43)$$

$$S \equiv \sqrt{2\Omega_{ij}\Omega_{ij}} \quad (44)$$

$$\Omega_{ij} = \frac{1}{2} \left( \frac{\partial u_i}{\partial x_j} - \frac{\partial u_j}{\partial x_i} \right) \quad (45)$$

$$Y_\nu = C_{w1}\rho f_w \left( \frac{\tilde{n}u}{d} \right)^2 \quad (46)$$

$$f_w = g \left[ \frac{1 + C_{w3}^6}{g^6 + C_{w3}^6} \right]^{1/6} \quad (47)$$

$$g = r + C_{w2}(r^6 - r) \quad (48)$$

$$r \equiv \frac{\tilde{\nu}}{\tilde{S}\kappa^2 d^2} \quad (49)$$

Where:

$\tilde{\nu}$  is transported variable.

$G_\nu$  is the production of turbulent viscosity.

$Y_\nu$  is the destruction of turbulent viscosity that occurs in the near-wall region due to wall blocking and viscous damping.

$S_\nu$  is a user-defined source term.

$f_{\nu 1}$  is the viscous damping function.

$d$  is the distance from the wall.

$S$  is a scalar measure of the deformation tensor.

$\Omega_{ij}$  is the mean rate-of-rotation tensor.

Table 47:  $S - A$  turbulence model constants

$C_{b1}$	$C_{b2}$	$\sigma_\nu$	$C_{nu1}$	$C_{w1}$	$C_{w2}$	$C_{w3}$	$\kappa$
0.1355	0.622	$\frac{2}{3}$	7.1	$\frac{C_{b1}}{\kappa^2} + \frac{(1+C_{b2})}{\sigma_\nu}$	0.3	2.0	0.4187

• **The SST  $k - \omega$  turbulence model [76]:**

$$\frac{\partial}{\partial t}(\rho k) + \frac{\partial}{\partial x_i}(\rho k u_i) = \frac{\partial}{\partial x_j} \left( \Gamma_k \frac{\partial k}{\partial x_j} \right) + \tilde{G}_k - Y_k + S_k \quad (50)$$

$$\frac{\partial}{\partial t}(\rho \omega) + \frac{\partial}{\partial x_i}(\rho \omega u_i) = \frac{\partial}{\partial x_j} \left( \Gamma_\omega \frac{\partial \omega}{\partial x_j} \right) + G_\omega - Y_\omega + D_\omega + S_\omega \quad (51)$$

$$\nu_t = \frac{k}{\omega} \frac{1}{\max \left[ \frac{1}{\alpha^*}, \frac{SF_2}{a_1 \omega} \right]} \quad (52)$$

$$\Gamma_k = \mu + \frac{\mu_t}{\sigma_k} \quad (53)$$

$$\Gamma_\omega = \mu + \frac{\mu_t}{\sigma_\omega} \quad (54)$$

$$\sigma_k = \frac{1}{F_1/\sigma_{k,1} + (1 - F_1)/\sigma_{k,2}} \quad (55)$$

$$\sigma_\omega = \frac{1}{F_1/\sigma_{\omega,1} + (1 - F_1)/\sigma_{\omega,2}} \quad (56)$$

$$\alpha^* = \alpha_\infty^* \left( \frac{\alpha_0^* + Re_t/R_k}{1 + Re_t/R_k} \right) \quad (57)$$

$$Re_t = \frac{\rho k}{\mu \omega} \quad (58)$$

$$\alpha_0^* = \frac{\beta_i}{3} \quad (59)$$

$$F_1 = \tanh(\phi_1^4) \quad (60)$$

$$\phi_1 = \min \left[ \max \left( \frac{\sqrt{k}}{0.09\omega y}, \frac{500\mu}{\rho y^2 \omega} \right), \frac{4\rho k}{\sigma_{\omega,2} D_{\omega}^+ y^2} \right] \quad (61)$$

$$D_{\omega}^+ = \max \left[ 2\rho \frac{1}{\sigma_{\omega,2}} \frac{1}{\omega} \frac{\partial k}{\partial x_j} \frac{\partial \omega}{\partial x_j}, 10^{-10} \right] \quad (62)$$

$$F_2 = \tanh(\phi_2^2) \quad (63)$$

$$\phi_1 = \max \left[ 2 \frac{\sqrt{k}}{0.09\omega y}, \frac{500\mu}{\rho y^2 \omega} \right] \quad (64)$$

$$\tilde{G}_k = \min(G_k, 10\rho\beta^*k\omega) \quad (65)$$

$$G_k = \mu_t S^2 \quad (66)$$

$$S^2 \equiv \sqrt{2S_{ij}S_{ij}} \quad (67)$$

$$S_{ij} = \frac{1}{2} \left( \frac{\partial u_j}{\partial u_i} + \frac{\partial u_i}{\partial u_j} \right) \quad (68)$$

$$G_{\omega} = \frac{\alpha}{\nu_t} G_k \quad (69)$$

$$\alpha = \frac{\alpha_{\infty}}{\alpha^*} \left( \frac{\alpha_0 + Re_t/R_{\omega}}{1 + Re_t/R_{\omega}} \right) \quad (70)$$

$$\alpha_{\infty} = F_1 \alpha_{\infty,1} + (1 - F_1) \alpha_{\infty,2} \quad (71)$$

$$\alpha_{\infty,1} = \frac{\beta_{i,1}}{\beta_{\infty}^*} - \frac{\kappa^2}{\sigma_{\omega,1}\sqrt{\beta_{\infty}^*}} \quad (72)$$

$$\alpha_{\infty,2} = \frac{\beta_{i,2}}{\beta_{\infty}^*} - \frac{\kappa^2}{\sigma_{\omega,2}\sqrt{\beta_{\infty}^*}} \quad (73)$$

$$Y_k = \rho\beta^*k\omega \quad (74)$$

$$\beta^* = \beta_i^*[1 + \zeta^*F(M_t)] \quad (75)$$

$$\beta_i^* = \beta_{\infty}^* \left( \frac{4/15 + (Re_t/R_{\beta})^4}{1 + (Re_t/R_{\beta})^4} \right) \quad (76)$$

$$Y_{\omega} = \rho\beta\omega^2 \quad (77)$$

$$\beta = \beta_i \left[ 1 - \frac{\beta_i^*}{\beta_i} \zeta^* F(M_t) \right] \quad (78)$$

$$\beta_i = F_1\beta_{i,1} + (1 - F_1)\beta_{i,2} \quad (79)$$

$$F(M_t) = \begin{cases} 0, & M_t \leq M_{t0} \\ M_t^2 - M_{t0}^2, & M_t > M_{t0} \end{cases} \quad (80)$$

$$M_t^2 = \frac{2k}{a^2} \quad (81)$$

$$a \equiv \sqrt{\gamma RT} \quad (82)$$

$$D_{\omega} = 2(1 - F_1)\rho\sigma_{\omega,2} \frac{1}{\omega} \frac{\partial k}{\partial x_j} \frac{\partial \omega}{\partial x_j} \quad (83)$$

Where:

$\Gamma_k$  is the effective diffusivity of  $k$ .

$\tilde{G}_k$  is the generation of turbulence kinetic energy due to mean velocity gradients.

$Y_k$  is the dissipation of  $k$ .

$S_k$  is user-defined source term.

$\omega$  is the specific dissipation rate.

$\Gamma_\omega$  is the effective diffusivity of  $\omega$ .

$G_\omega$  is the generation of  $\omega$ .

$Y_\omega$  is the dissipation of  $\omega$ .

$D_\omega$  is the cross-diffusion term.

$S_\omega$  is user-defined source term.

$\alpha^*$  damps the turbulent viscosity causing a low-Reynolds-number correction.

$S$  is the modulus of the mean rate-of-strain tensor.

$S_{ij}$  is the mean strain rate.

$F_2$  is The blending function.

$\sigma_k$  is the turbulent Prandtl number for  $k$ .

$\sigma_\omega$  is the turbulent Prandtl number for  $\omega$ .

$Re_t$  is turbulent Reynold's number.

$y$  is the distance to the next surface.

$D_\omega^+$  is the positive portion of the cross-diffusion term.

$G_k$  is production of turbulence kinetic energy.

$M_t$  is the turbulent Mach number.

Table 48: *SST*  $k - \omega$  turbulence model constants

$\sigma_{k,1}$	$\sigma_{\omega,1}$	$\sigma_{k,2}$	$\sigma_{\omega,2}$	$a_1$	$\beta_{i,1}$	$\beta_{i,2}$	$\zeta^*$
1.176	2.0	1.0	1.168	0.31	0.075	0.0828	1.5
$\alpha_\infty^*$	$\alpha_\infty$	$\alpha_0$	$\beta_\infty^*$	$R_\beta$	$R_k$	$R_\omega$	$M_{t0}$
1	0.52	$\frac{1}{9}$	0.09	8	6	2.95	0.25

- **The standard  $k - \epsilon$  turbulence model [77]:**

$$\frac{\partial}{\partial t}(\rho k) + \frac{\partial}{\partial x_i}(\rho k u_i) = \frac{\partial}{\partial x_j} \left[ \left( \mu + \frac{\mu_t}{\sigma_k} \right) \frac{\partial k}{\partial x_j} \right] + G_k + G_b - \rho \epsilon - Y_M + S_k \quad (84)$$

$$\frac{\partial}{\partial t}(\rho \epsilon) + \frac{\partial}{\partial x_i}(\rho \epsilon u_i) = \frac{\partial}{\partial x_j} \left[ \left( \mu + \frac{\mu_t}{\sigma_\epsilon} \right) \frac{\partial \epsilon}{\partial x_j} \right] + C_{1\epsilon} \frac{\epsilon}{k} (G_k + C_{3\epsilon} G_b) - C_{2\epsilon} \rho \frac{\epsilon^2}{k} + S_\epsilon \quad (85)$$

$$\nu_t = C_\mu \frac{k^2}{\epsilon} \quad (86)$$

$$G_b = \beta g_i \frac{\mu_t}{Pr_t} \frac{\partial T}{\partial x_i} \quad (87)$$

$$\beta = -\frac{1}{\rho} \left( \frac{\partial \rho}{\partial T} \right)_P \quad (88)$$

$$Y_M = 2\rho\epsilon M_t^2 \quad (89)$$

$$M_t = \sqrt{\frac{k}{a^2}} \quad (90)$$

Where:

$\sigma_k$  is the turbulent Prandtl number for  $k$ .

$G_k$  is the generation of turbulence kinetic energy due to the mean velocity gradients.

$\epsilon$  is turbulence dissipation rate.

$Y_M$  is the contribution of the fluctuating dilatation in compressible turbulence to the overall dissipation rate.

$\sigma_\epsilon$  is the turbulent Prandtl numbers for  $\epsilon$ .

$S_\epsilon$  is user-defined source term.

$C_\mu$  is constant.  $Pr_t$  is the turbulent Prandtl number for energy.

$g_i$  is the component of the gravitational vector in the  $i$ th direction.

$\beta$  is the coefficient of thermal expansion.

Table 49:  $k - \epsilon$  turbulence model constants

$Pr_t$	$C_{1\epsilon}$	$C_{2\epsilon}$	$C_\mu$	$\sigma_k$	$\sigma_\epsilon$
0.85	1.44	1.92	0.09	1	1.3